UNIVERSITY OF CALIFORNIA,
IRVINE

Engineered MEMS microenvironments for studying stem cells and microorganisms

DISSERTATION

submitted in partial satisfaction of the requirements
for the degree of

DOCTOR OF PHILOSOPHY

in Physics

by

Alexandra Perebikovsky

Dissertation Committee:
Professor Marc Madou, Chair
Professor Zuzanna Siwy
Professor Albert Siryaporn
Professor James Nowick

2020

TABLE OF CONTENTS

LIST OF FIGURES

LIST OF TABLES

ACKNOWLEDGMENTS

First and foremost, I would like to thank the chair of my thesis committee, Marc Madou, for more than seven years of mentorship and friendship throughout my undergraduate and graduate career. I would also like to thank the other members of my thesis committee, Zuzanna Siwy, Albert Siryaporn, and James Nowick, for their invaluable instruction and for the many thoughtful conversations we have had.

I would also like to thank my lab members, in particular Alexander Hwu, without whom this work would not be possible. His work ethic, organized experimental manner, and insight into the subject have made him one of my most trusted colleagues and an absolute pleasure to work with. I would also like to thank Yujia Liu, Ehsan Shamloo, Sunshine Holmberg, Lawrence Kulinsky, and Horacio Kido for always being their to help with experiments, generate thoughful observations, and just generally have my back in everything. Finally, I want to acknowledge everyone else in the lab who I have become so close to over the years and who have always been their to help as friends and colleagues (you know who you are!).

On a personal note, I would like to acknowledge my family, especially my husband, Michiel, my parents, Tina and Victor, and my brother, Sam, who have always pushed me to do more than I think I think I am capable of and who inspire me everyday to become a better person.

I would like to acknowledge the Laser Spectroscopy Lab for assistance with Raman Spectroscopy and Dr. Lisa Flanagan's Lab at the Sue and Bill Gross Stem Cell Center at UC Irvine for assisting with obtaining neural stem cells used in this project. I would also like to acknowledge Couryn Beleck and Keyence for help with obtaining high quality fluorescent images. SEM and XPS work was performed at the UC Irvine Materials Research Institute (IMRI) using instrumentation funded in part by the National Science Foundation Major ResearchInstrumentation Program [CHE-1338173]. I would also like to acknowledge the UC Irvine Institute for Design and Manufacturing Innovation for their funding and support.

I would like to acknowledge MDPI, Elsevier Ltd., the Electrochemical Society, and the American Chemical Society for granting permission to incorporate some of my previously published work into my dissertation.

CURRICULUM VITAE

Alexandra Perebikovsky

Education

University of California, Irvine
Ph.D. in Physics (2020)
Concentration: Chemical and Material Physics
Advisor: Marc Madou

University of California, Irvine
B.S. in Physics (2016)
Senior Thesis: "Electrical and Magnetic Stimulation of Neural Stem Cells Grown on 3D Carbon Scaffolds" Advisor: Zuzanna Siwy

Research Experience

Graduate Student Researcher
UC Irvine and UC Los Angeles (April 2016-Present)

- Developed a smart stem cell scaffold for applications in neurodegenerative disorders. The device could simultaneously grow, stimulate, and sense differentiated stem cells. As a part of this project, set up a complete stem cell culture laboratory in the BioMEMS lab at UC Irvine and headed up new research directions for several graduate and undergraduate students in this field.
- Led a collaborative project between researchers at UCI, UCLA, and a startup company, MicrobeDX, to develop an ultrafast antibiotic susceptibility test on a spinning microfluidic platform. In less than one year, not only fully automated and improved the performance of the test, but presented at over a dozen investor meetings, helping to raise more than three million dollars for the project.
- Worked under a Bill Gates Foundation Grant to design and test a microfluidic system for performing quantitative detection of organic contaminants in wastewater. The system included sample preperation, droplet generation, DNA amplification, and detection.

Undergraduate Researcher and multi-discipinary design fellow
UC Irvine (April 2012-2016)

- Worked to design, fabricate, and test CD microfluidic devices for development of complex "lab-on-a-chip" assays. Headed the CD Microfluidics section of the BioMEMS lab.
- Recieved three UROP and two SURP grants for research into the effects of hypergravity on C. elegans and effects of electromagnetic fields on neural stem cells.
- Received a multi-disciplinary design fellowship to develop a microfluidic device that uses an enzymatic cascade for DNA testing.
- Fabricated intricate carbon MEMS scaffolds for dual stem cell culture and electrochemical detection of cell byproducts.

Refereed Journal Publications

1. **Perebikovsky, A.**, Liu, Y., Hwu, A.T., Monti, G., Kido, H., Shamloo, E., Song, D., Shoval, O., Gussin, D., Haake, D., and Madou, M., Rapid sample preparation for detection of antibiotic resistance on a microfluidic disc platform, Lab on a Chip, submitted.

2. **Perebikovsky, A.**, Hwu, A., Yale, A., Ghazinejad, M., Madou, M. J. (2019). Nanofibrous Carbon Multi-functional Smart Scaffolds for Simultaneous Cell Differentiation and Dopamine Detection. ACS Biomaterials Science Engineering.

3. Holmberg, S., Ghazinejad, M., Cho, E., George, D., **Perebikovsky, A.**, Pollack, B., Ragan, R., Madou, M. (2018) Stress-activated pyrolytic carbon nanofibers for electrochemical platforms. Electrochimica Acta, 290, 639-648.

4. Cho, E., **Perebikovsky, A.**, Benice, O., Holmberg, S., Madou, M., Ghazinejad, M. (2018). Rapid Iodine Sensing on Mechanically Treated Carbon Nanofibers.Sensors,18(5), 1486.

5. S. Smith, D. Mager, **A. Perebikovsky**, E. Shamloo, D. Kinahan, R. Mishra, S. M. Torres Del- gado, H. Kido, S. Saha, J. Ducre, M. Madou, K. Land, and J. G. Korvink. CD-Based Microfluidics for Primary Care in Extreme Point-of-Care Settings. Micromachines, 7(2):22, 2016.

6. L. X. Kong, **A. Perebikovsky**, J. Moebius, L. Kulinsky, and M. Madou, Lab-on-a-CD: A Fully Integrated Molecular Diagnostic System, J. Lab. Autom., Jun. 2015.

7. **A. Perebikovsky**, S. Holmberg, L. Kulinsky, and M. Madou, "3-D Micro and Nano Technologies for Improvements in Electrochemical Power Devices," Micromachines, vol. 5, no. 2, pp. 171–203, Apr. 2014.

Conference Publications

1. **Perebikovsky, A.**, Hwu, A. T., Holmberg, S., Ghazinejad, M., Madou, M. J. (2018, April). Porous Graphitic Carbon As a Smart Scaffold for Neural Stem Cells. In Meeting Abstracts(No. 6, pp. 666-666). The Electrochemical Society

2. **A. Perebikovsky**, Y. Liu, C. Halford, G. Monti, A.T. Hwu, D.A. Haake, and M.J. Madou, Rapid Bacterial Growth using a Microuidic Centrifugal Incubator Spinstand, Miniaturized Systems for Chemistry and Life Sciences, 2017.

3. L. Kong, J. M. Rodriguez, **A. Perebikovsky**, J. Moebius, R. Mitchell, L. Kulinsky, and M. Madou, "Novel heating and cooling techniques on a centrifugal fluidic platform for polymerase chain reaction," Microtechnologies in Medicine and Biology, 2013.

Conference Presentations and Posters

1. **Perebikovsky, A.**, CD Microfluidics: Barriers to Commercialization, Select Biosciences, Inc. 10th Annual Lab-on-a-Chip and Microfluidics World Congress, 2018. (Invited Talk)

2. **Alexandra Perebikovsky**, Alexander T. Hwu, Sunshine Holmberg, Maziar Ghazinejad, Marc J. Madou, (2018, August) Engineering the micro- and macro-structure of carbon scaffolds for smart stem cell growth. SPIE Proceedings

3. **Perebikovsky, A.**, Hwu, A. T., Holmberg, S., Ghazinejad, M., Madou, M. J. (2018, April). Porous Graphitic Carbon As a Smart Scaffold for Neural Stem Cells. In Meeting Abstracts(No. 6, pp. 666-666). The Electrochemical Society. (Invited Talk)

4. **Perebikovsky, A.**, M. Madou, Keynote Presentation: CD Fluidics for Extreme Point of Care, Select Biosciences, Inc. 9th Annual Lab-on-a-Chip and Microfluidics World Congress, 2017.

5. **Perebikovsky, A.**, Liu Y., Halford C., Monti G., Hwu A.T., Haake D., and Madou M., Rapid Bacterial Growth using a Microfluidic Centrifugal Incubator Spinstand, MicroTAS2017, Oct. 22-26, 2017.

6. M.M. Aeinehvand, A. Palermo, **Perebikovsky, A.**, L.K. Weber, F.F. Loeffler, A.E. Carvajal, D. Mager, M.J. Madou, and S.O. Martinez-Chapa, Active pnuematic microballoon mixing on centrifugal microfluidic platforms, MicroTAS2017, Oct. 22-26, 2017.

7. **Alexandra Perebikovsky**, and Marc J. Madou. "Pyrolized 3D Carbon Scaffolds and Electrical Stimulation Enhance Differentiation of Neurons." Meeting Abstracts. No. 7. The Electrochemical Society, 2016.

Patents/Invention Disclosures

1. Apparatus for Automatic Sampling of Biological Species Employing Disk Microfluidics System. US 2019/0285029.
2. Device for Optimization of Microorganism Growth in Liquid Culture. Filing 2018-08-30, Publication 2019-03-07 WO2019046613A1.
3. Methods for Lysis of Cells Within a Sample. Filing 2018-08-03, Publication 2019-02-07. WO2019028381A1.
4. Methods for antimicrobial susceptibility testing. Filing 2018-08-20, Publication 2019-02-21. WO2019036715A1.
5. RiboSystem: A Centrifugal Microfluidic Device for Bacterial Identification and Antibiotic Susceptibility Testing. UC Case 2019-204-1.
6. Storage and Release of Liquid Reagents on a CD Microfuidic Device. Tech ID 23585, UC Case 2014-145-0.

Awards and Honors

1. Public Impact Fellowship
2. ARCS Scholars Fellowship
3. NSF Graduate Research Fellowship (honorable mention)
4. Artiman B.E.T.A. Fellow 2016
5. Dean's Honors List (2014-2016)
6. Multidisciplinary Design Fellow (2014)
7. Undergraduate Research Opportunities Program Award (2014-2015)
8. Summer Undergraduate Research Program Award (2014, 2015)

Skills

Laboratory Skills: Electrophoresis, Polymerase Chain Reaction, Immunoassay, Tissue Culture, Electrochemistry, Lab Safety and Ethics
Microfabrication: CNC Microfabrication, Photolithography, SEM, XPS, Wet Etch, Plasma Etch, sputtering, critical point dryer
Software/Programming: Mathematica, Matlab, Comsol Multiphysics, Solidworks, AutoCAD, Python
Media and Animation: Adobe Photoshop, Adobe After Effects, Adobe Flash, Adobe Premier, Adobe InDesign, Final Cut Pro, Sony Vegas Pro

ABSTRACT OF THE DISSERTATION

Engineered MEMS microenvironments for studying stem cells and microorganisms

By

Alexandra Perebikovsky

Doctor of Philosophy in Physics

University of California, Irvine, 2020

Professor Marc Madou, Chair

Advances in miniaturization and nanofabrication techniques have led to significant medical breakthroughs, especially in the fields of stem cell therapy and medical diagnostics. In this contribution, we use MEMS techniques to develop two different tools that allow us to study different biological organisms: 1.) a multi-functional smart scaffold for studying stem cells, and 2.) a centrifugal microfluidic platform for studying microorganisms like bacteria. In Part II, we use the multi-functional smart scaffold to control neural stem cell growth/differentiation and simultaneously monitor Dopamine released from the cells. In Part III, we use the centrifugal microfluidic platform to optimize the incubation of multiple bacteria species. We then use the same platform to develop a sample-to-answer phenotypic antibiotic susceptbility test that successfully identifies resistance in 11 different species of E. Coli in under 2 hours.

Part I

A bit of motivation

In 1959, Richard Feynman invited scientists to enter a new field of physics in his now famous talk titled, "There's plenty of room at the bottom" [35]. Inspired by the complexity and remarkable efficiency of biological systems, Feynman described the new science of miniaturization and set the stage for decades of advances in nanotechnology and Microelectromechanical systems (MEMS). Taking inspiration from how DNA stores billions of pieces of cellular information, Feynman talked about fitting all of the literary works of human history on a cube the size of the smallest speck of dust discernible by the human eye. Fascinated by how small cells could maneuver and accomplish intricate tasks in laminar flow environments, he envisioned tiny robotic machines that could perform complex surgical procedures and, like the human brain, make critical decisions and judgements on the fly to accomplish their task. He even described the exciting advances in biology that would come about from developing an electron microscope 100 times more powerful than any light microscope existing at the time or the advances in chemical synthesis that could be accomplished by fabricating any molecule one can think of from the ground up by selectively rearranging the very atoms it consists of.

Since then, a lot of time and research effort has focused on miniaturization in the area of integrated circuits and computing. In accordance with Moore's law, scientists have roughly doubled the amount of transistors that fit on a single chip every 18 months since the 1950s, and consequently have decreased the footprint of a computer down from the size of a large classroom [44] to the portable smartphone most of us hold in our hands. To accomplish this, there have been incredible advancements in the fields of scalable manufacturing, material physics, microfluidics, and electrochemistry.

While the science of miniaturization has, up to now, primarily focused on computational and hardware applications, these advancements have also recently found exciting and revolutionary applications in biological systems, the original inspiration for Feynman's talk. The advances in MEMS and nanoelectromechanical systems (NEMS) has provided a unique

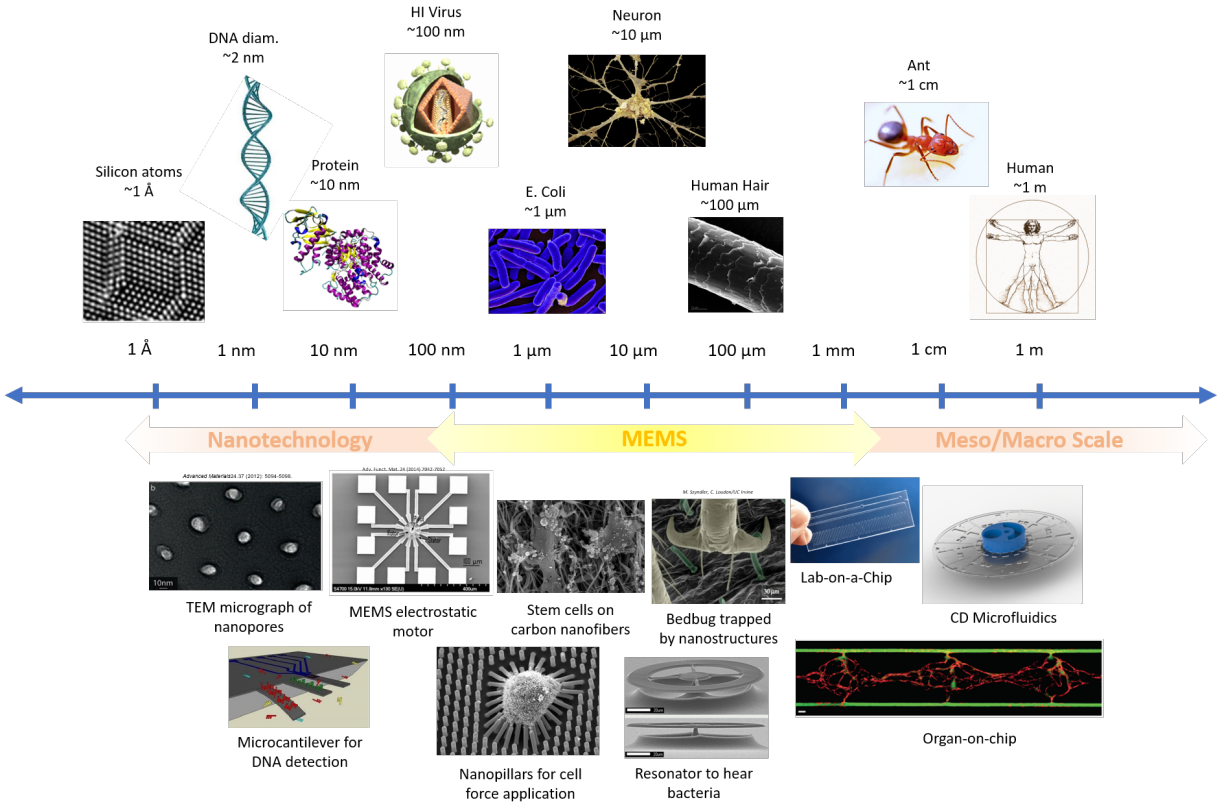

Figure 1: Scaling in MEMS devices and interaction with biological systems.

toolbox for the development of engineered microsystems to study and manipulate molecules, cells, tissues, and microorganisms. Figure 1 shows a small subsection of the unique engineered environments that have been developed in this domain, including nanopores for sequencing DNA [20], carbon scaffolds for directing differentiation of stem cells [144], microstructures that trap bedbugs, and lab-on-a-chip systems that grown entire miniature organs for drug development and analysis [199].

During my academic career, I have had the great fortune of working in this highly interdisciplinary and exciting field. While this work is not comprehensive enough to include all of the projects I have worked on or been exposed to, I have focused on two main projects I have worked on throughout my graduate career: developing nanomaterial MEMS scaffolds for the study of stem cells and developing a comprehensive CD microfluidic-based platform for the study of microorganisms, like bacteria. The remainder of this work is separated into

these two main projects. Each section has an introduction that describes the main theory contributing to the development of the MEMS platform and delves into how each tool has been used to study and/or control the biological organisms in question.

In Part II, we use the multi-functional smart scaffold to control neural stem cell growth/differentiation and simultaneously monitor Dopamine released from the cells. In Part III, we use the centrifugal microfluidic platform to optimize the incubation of multiple bacteria species. We then use the same platform to develop a sample-to-answer phenotypic antibiotic susceptbility test that successfully identifies resistance in 11 different species of E. Coli in under 2 hours.

Part II

Multi-functional smart scaffolds for stem cell-based regenerative medicine

Chapter 1

Introduction

Engineered materials play a pivotal role in stem cell-based regenerative medicine. In addition to providing physical and chemical cues that guide stem cell growth and differentiation, new, multi-functional smart scaffolds (MSS) are being developed for simultaneous sensing and detection of cell metabolites [117, 18, 38, 48]. One especially promising application is using MSS for neurodegenerative disorders like Alzheimer's disease, spinal cord injuries, and Parkinson's disease, which require targeted cell organization, electrical or mechanical stimulation, and non-destructive monitoring of released neurotransmitters like Dopamine (DA) to identify cells ready for transplantation [6, 83, 102]. However, fabricating scaffolds capable of both functions in an efficient and scalable manner remains very challenging.

Conventional methods to control stem cell differentiation using only chemical cues, growth factors, and cytokines have shown limited success in achieving selective differentiation [83, 102, 202]. As a result, scientists are developing additional biophysical cues to guide growth. For example, the surface topography of a scaffold can not only promote cellular adhesion and influence differentiation toward neuronal lineages but can also facilitate alignment of cellular cytoskeletons, critical in spinal cord injuries where aligned axons are required to

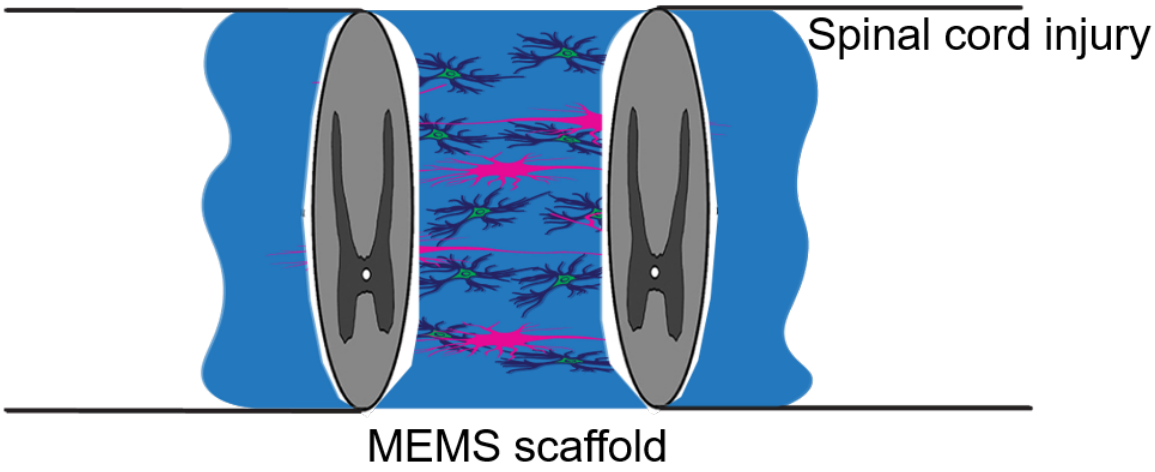

Figure 1.1: Schematic diagram depicting how a scaffold can be used at the site of spinal cord injury to facilitate alignment and growth of stem cells to bridge nerve gaps..

bridge nerve gaps and to form new neural networks [158, 183], see Figure 1.1.

Once cells are ready for implantation, a critical step to avoid complex immune responses and to ensure effective therapy is the robust characterization of the cells grown on scaffolds. Traditional characterization methods such as immunocytochemistry (ICC), polymerase chain reaction (PCR), and high-performance liquid chromatography (HPLC), are labor intensive and generally require destruction of the cell membrane through cell fixation or lysis. An attractive alternative is to use highly sensitive electrochemical sensors, detecting cell metabolites in real-time. For example, one could use an electroactive sensor to verify the production of sufficient quantities of the redox species, Dopamine, a critical neurotransmitter lacking in patients diagnosed with Parkinson's disease, where the degeneration of dopaminergic neurons results in deteriorating motor function [11]. Unfortunately most available electrochemical sensors use expensive noble metals or require time-consuming functionalization or activation that fades over time [155, 123, 194]. No commercially available electrochemical sensors exist that are also capable of simultaneously supporting and guiding stem cell growth.

To tackle these challenges, we developed a carbon multi-functional smart scaffold (MSS) (see Figure 1.2 with a biomimetic macrostructure that guides cell orientation and growth,

and with a nanostructure that enhances electrochemical performance, enabling sensitive, non-invasive and real-time detection of redox active neurotransmitters. Furthermore, the nature of the carbon MSS material makes it suitable for both electrical stimulation, due to its conductive properties, and mechanical stimulation, due to its flexibile and non-brittle nature. In the following chapters, we describe the background and theory behind the carbon MSS and demonstrate the ability of the carbon MSS to:

1. Enhance growth and differentiation of mouse neural stem/progenitor cells (mNSPCs) derived from different regions of the developing brain.

2. Simultaneously detect dopamine from a dopaminergic cell line (rat adrenal PC12 cells) growing on the carbon MSS.

3. Act as a simultaneous mechanical cell stimulation system for application of different mechanical forces during stem cell growth.

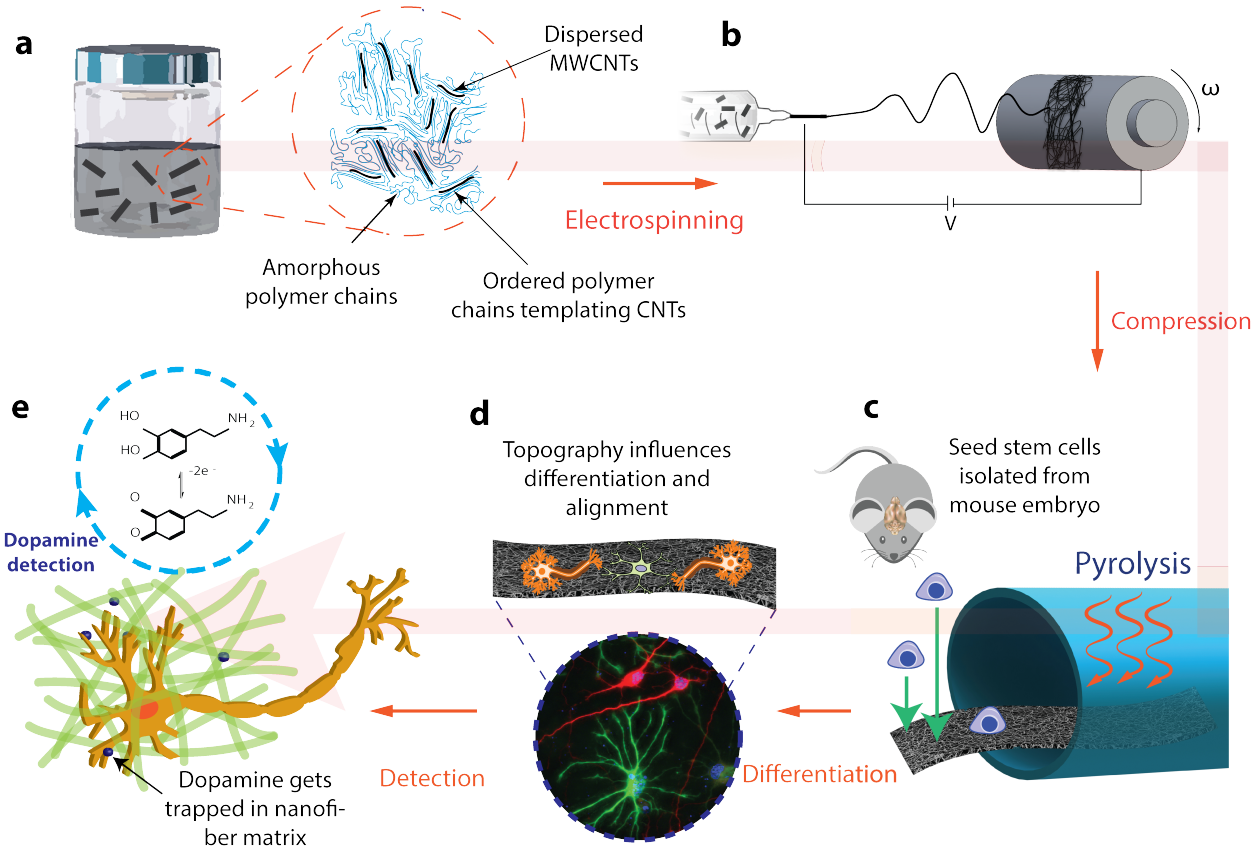

Figure 1.2: Schematic diagram depicting fabrication and application of the carbon multi-functional smart scaffold (MSS) for growth and monitoring of cells. (a) MWCNTs are mixed with polyacrylonitrile (PAN) polymer solution, templating and aligning PAN polymer chains around CNTs. (b) The solution is electrospun into a nanofiber mat and compressed to further organize polymer chains. (c) Immediately upon pyrolysis of the mat into carbon, stem cells are seeded onto the scaffold and (d) allowed to differentiate. (e) The carbon MSS is used as an electrode to detect cellular metabolites, such as dopamine.

Chapter 2

Background and Theory

2.1 The stem cell niche

In ecology, the term niche refers to a habitat where an organism can grow and reside. An organism's niche refers to both its role in an ecosystem and the conditions necessary for the persistance of it's species. In this sense, the niche is a dynamic environment both influencing the fate of an organism and also being influenced and redeveloped by the organism itself. While this active symbiosis between organism and environment has long been understood in regards to organisms, it has only recently been applied to investigating individual cells, and in particular, stem cells in the body [159].

In 1978, Schofield first proposed the hypothesis of the stem cell niche as an in-vivo microenvironment where stem cells not only reside but also receive external stimuli that influence their behavior, identity, and self-renewal ability [162]. The first experimental evidence in support of the active niche hypothesis occurred by examining stem cell populations in the invertebrate model of Drosophila melanogaster and Caenorhabditis elegans gonads [203, 22, 73].

For example, C. elegans has a stem cell population that resides in a niche created by one single cell, called the distal tip cell. This cell emits signals through long fibrils that surround the niche and prevents stem cells from turning into eggs for the worm. If the cell is destroyed or removed from the area, the stem cells differentiate into eggs. If the cell is moved to a different location, the nearby cells receive signals to turn into stem cells. Examination of systems such as this in less complex animals has led to crucial insights into niche structure in more complex animals. Over the years, researchers have found that fundamental components and pathways in the niche environment are conserved among species, making it possible to identify common niche components associated with similar functions in different animals.

Since Schofield's original concept, researchers have expanded the concept of the stem cell niche and identified the following common features that are shared between different niche environments [129, 97], illustrated in Figure 2.1:

1. Direct interactions between stem cells and neighboring cellular components.
2. Physical factors such as shear forces associated with fluid movement, tissue stiffness and elasticity, and mechanical stresses
3. Extracellular matrix topography and composition.
4. Secreted and membrane-bound factors
5. Environmental signals such as hypoxia, metabolism, and circadian oscillations.
6. Inflammation and scarring.

2.1.1 Active and passive forces in the stem cell niche

One of the more exciting and less understood aspects of the stem cell niche, is the effect of physical forces present in the extracellular matrix, such as substrate stiffness and topography.

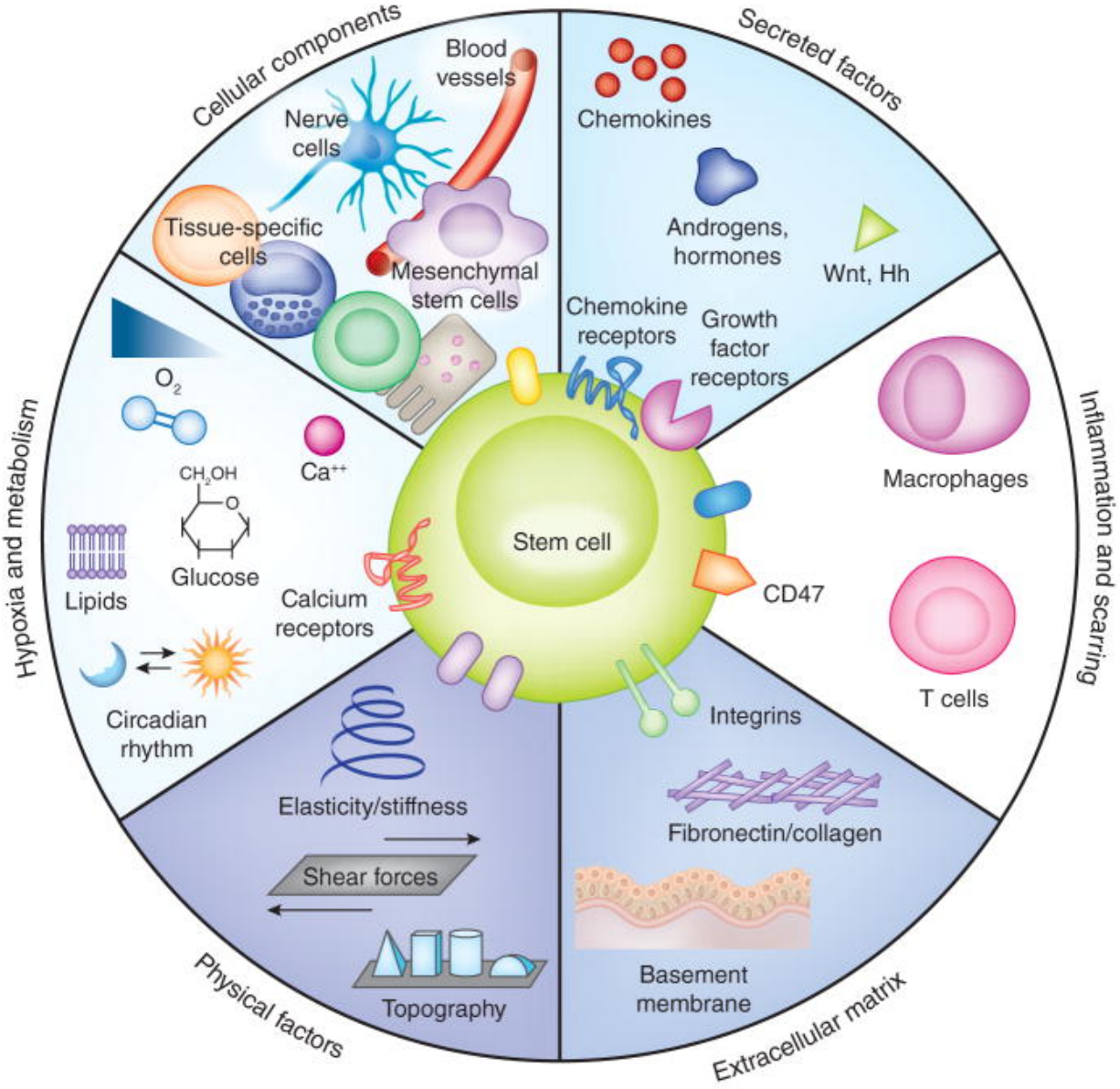

Figure 2.1: Schematic diagram depicting the stem cell niche microenvironment, including the factors that influence and regulate cell fate. Reprinted from [97] with permission from Springer Nature.

Up until recently, the ECM was considered to be an inert supportive scaffold for cells to adhere to. However, it has since been shown that cells can "sense" the elasticity or stiffness of the extracellular matrix and transduce that information into morphological changes in cell structure and directed lineage [120]. One of the most famous experiments in this area was done by Engler in 2006, who demonstrated lineage-specific differentiation of stem cells when cultured on substrates with stiffness corresponding to native tissues [33].

Every extracellular matrix has a characteristic Young's modulus, E, which is a ratio between the tensile stress of a material to its strain and defines the instrinsic elasticity or stiffness of a material, see Equation 2.1.1:

$$E = \frac{\sigma}{\epsilon} = \frac{F/A}{\Delta L/L_0} \tag{2.1}$$

where σ is the stress of a material, defined as the force exerted on an object (F) per cross-sectional area (A), and ϵ is the strain of the material, defined as the change in length (ΔL) divided by the initial length of the object (L_0) . The young's modulus of a material can be found by taking the slope of the stress vs. strain curve for each material.

In Engler's famous experiment, he found that mesenchymal stem cells (MSCs) cultured in identical serum conditions and on substrates with elasticities mimicking brain tissue ($E_{brain} \sim$ 0.1-1 kPa) differentiated toward neurogenic lineages, those cultured on substrates with elasticities mimicking striated muscle tissue ($E_{msucle} \sim$ 8-17 kPa) differentiated toward myogenic lineages, and those cultured on substrates with elasticities similar to bone ($E_{bone} \sim$ 25-40 kPa) differentiated toward osteogenic lineages, see Figure 2.2.

Since this study, there has been a wealth of investigation into the effect of different active and

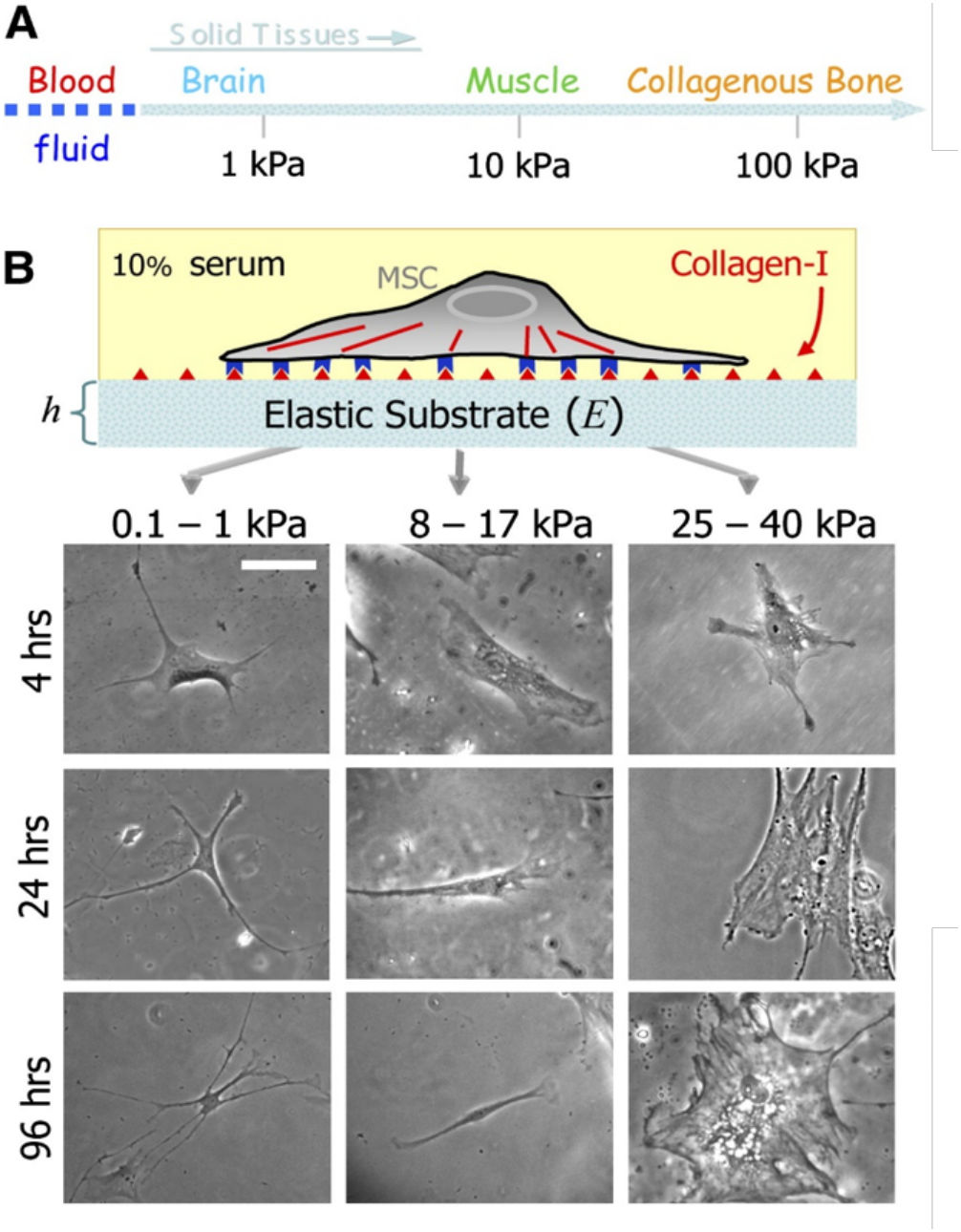

Figure 2.2: a) Schematic diagram depicting elasticities (E) of different tissues. b) Representative light microscopy images of MSCs differentiated on matrices with different Young's moduli. Reprinted from [33] with permission from Elsevier Inc.

passive forces on stem cells using a variety of methods, illustrated in Figure 2.3 [149, 108, 135].

One of the directions by researchers was to mimic morphogenic processes, which often involve cells and tissues undergoing critical deformations such as twisting, bending, and stretching. For example, to mimic forces induced during embryo development, magnetic twisting cytometry was used to apply torque-based deformation to a bead attached to cells. This has been shown to push embryonic stem cells toward cardiomyocyte and smooth muscle cell fates [40]. To mimic the stretching that occurs in blood vessels or the muscle tissues of the beating heart, researchers have used cyclic strain, induced by seeding cells onto a deformable membrane that is periodically stretched using an automated device. This has been shown to induce proliferation of MSCs [103], guide ESC cells toward differentiation into cardiomyacytes [49], and improve maturity and alignment of stem cells in the direction of the stretch [56].

To generate passive forces, where a stem cell simply responds to its surroundings, a number of new scaffold and substrate materials have been developed, similar to the substrates used by Engler with different Young's moduli. Substrate geometry and topography has been shown to encourage alignment of stem cells and differentiation toward different lineages. Researchers developed microprinted islands with different membrane curvatures–MSCs on smaller curvatures differentiated toward adopogenic lineages and MSCs on larger curvatures toward osteogenic lineages [107, 180]. However, even with passive forces, we know that the stem cell niche does not represent a static environment–rather, the properties of the niche change with both space and time. For example, stiffness can vary between three to six orders of magnitude in-vivo in different tissues [28, 189]. This can also vary with the onset of disease. To mimic spatial gradients, researchers have changed gel thickness, crosslinking density, or micropost length, finding that stem cells tended to migrate preferentially toward stiffer regions, even when they were still uncommitted [182, 190]. To mimic temporal gradients, researchers have used sequential crosslinking of biomaterials or have used methods to degrade

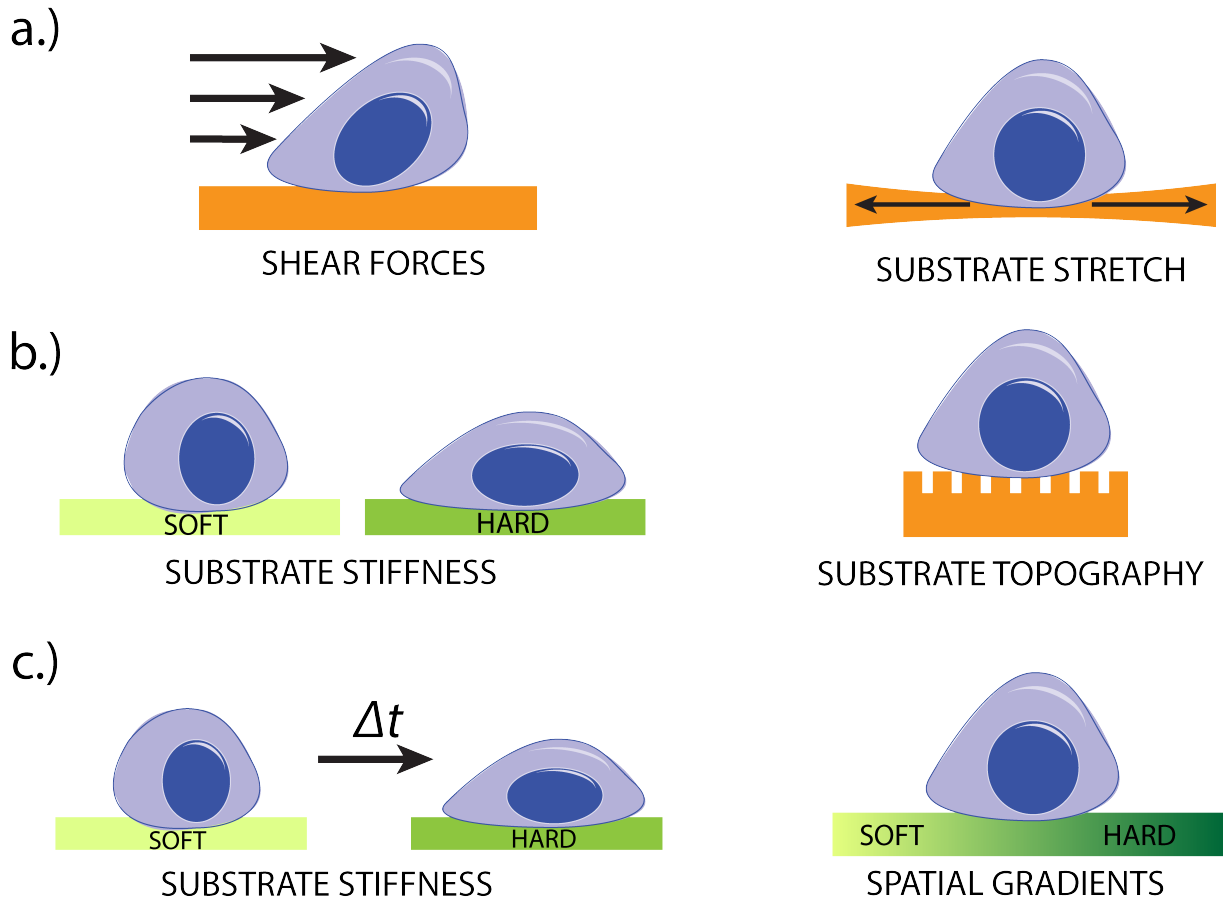

Figure 2.3: Forces can be applied to cells using multiple experimental techniques and through creation of different biomaterial scaffolds. (a) Substrate deformations and external forces, such as shear forces and cyclic stretch, can be used to modulate cell response. (b) Biomaterials can also be used to apply forces to cells by varying substrate stiffness and substrate topography. (c) Biomaterials can also be used to apply temporal and spatial gradients. Temporal gradients can be created by crosslinking scaffolds at different times and spatial gradients can be created by changing the thickness of a material in different locations.

and soften crosslinks to induce stress relaxation [16, 87]. Researchers have found that the effects of these changes are significantly dependent on when during the life cycle of the cells they are introduced. For example, there exists a short window of time in which altering stiffness signalling can dramatically impact neurogenesis [146].

2.1.2 Mechanotransduction: converting physical stimuli into biochemical responses

In order for cells to respond to the different active and passive forces present in the extracellular matrix and subsequently induce morphological changes, two conditions must be met: 1) To sense passive matrix forces, such as elasticity or different topographical gradients, the cell must be able to pull against its substrate at a molecular level, and 2) In order to create a morphological change, a cellular mechano-transducer must exist that sends out signals based on the force the cell generates to deform the matrix material. Once the force felt is converted by the cell into a biochemical signal, the cell can modulate protein expression and enzymes can be triggered to modulate activation energy for reactions to proceed.

Several mechanisms have been investigated as mediators for this mechano-transduction to take place, including:

1. Actin and myosin regulation which creates a contractile force on the cell cytoskeleton. This mechanism was implicated in the case of matrix elasticity and topographical sensing, where it was found that several of the cell's cytoskeletal motors (nonmuscle myosin II isoforms) bind to and create tension along the thin filaments of cortical actin structures in the cytoskeleton [33, 74, 121, 124]. These in turn act on focal adhesions (see mechanism (2) below), and their associated signaling molecules, to transmit forces from inside the cell to the ECM matrix.

2. Focal adhesion proteins, which connect the cytoskeleton of the cell to extracellular matrix receptors, contain transcription factor binding sites that have been shown to modulate cell fate when exposed to ECM stress. Several focal adhesion sensors have been identified, such as vinculin, a tension-based strain sensor [59].

3. ECM binding integrins are heterodimeric transmembrane receptors composed of a combination of α and β subunits. The extracellular head region of the integrin binds different components of the extracellular matrix, such as laminin glycoproteins, fibronectin collagens, and even neighboring cells. The specific combination of α and β subunits that make up each integrin, defines the affinity of the receptor for different ECM components. In the case of mechanosensing, extracellular mechanical stimuli induce a conformational change in the integrin which is then transmitted via the cytoplasmic tail to cytoskeletal actin and couples to intracellular signal cascades [69, 164, 197, 31, 165].

4. Stretch-activated channels, such as Piezo-1, a mechanically sensitive cationic ion channel, transduce physical stimuli through induced changes in the concentration of ions, like Ca^{2+} [137]. Piezo-1, for example, has been found to mediate cell-generated traction forces and influence differentiation towards neuronal and glial lineages [147, 143].

This deeper understanding about the interplay between stem cells and their niche forms the basis for designing functional stem-cell therapeutics. In the early days of stem cell transplantation, it was only possible to transplant cells that could be harvested from tissues such as blood or bone marrow. However, by controlling the forces, signalling molecules, and other factors that influence and guide stem cell fate, it is increasingly possible to direct cells to differentiate into potentially any cell type and with the desired cellular configuration. With the development of induced pluripotent stem cell (iPS) technology, which allows the de-differntiation of adult somatic cells back into pluripotent stem cells, patients can even be treated using their own cells, avoiding issues with immune response [139, 206]. Even more attractive is the possibility to manipulate stem cells in-vivo through the use of implantable,

multi-functional scaffolds that simulate the biochemical cues and both passive and active forces that make up the stem cell niche.

2.2 Carbon as a foundation for stem cell scaffolds

Carbon is one of the fundamental building blocks of life and is the fourth most abundant element in the universe. Its flexibility to form polymers and bond with other elements at temperatures typically encountered on earth enables it to be present in all known living organisms. Due to its ability to hybridize and bond with itself, carbon comes in many versatile forms and allotropes, from diamond, one of the hardest bulk materials and an electrical insulator, to graphite, which has a soft structure and very high electrical conductivity [113]. The widely differing morphologies and crystalline structures of carbon have enabled development of materials and devices with vastly differing chemical, mechanical, and electrical uses. For example, hard carbons like graphite have long been used in lithium-ion battery applications due to their ability to intercalate Lithium, and amorphous, or glassy, carbons have been used frequently as electrochemical sensors due to their ability to form three dimensional shapes from polymer precursors and their wide electrochemical stability windows [123]. Another critical aspect of carbon is its biocompatibility and chemical inertness, making it an ideal material for biological applications, such as biosensors, biomimetic scaffolds, and for the development of implantable devices.

2.2.1 Carbon from polymer precursors

The use of traditional manufacturing processes to shape carbon allotropes into microdevices is difficult due to the hard and brittle nature of most pyrolytic carbons. Similarly, technology derived from integrated circuits, such as the use of focused ion beam milling or reactive ion

etching is expensive and time consuming, making it unpractical for the development of carbon microfeatures. However, rather than machining the final carbon itself, polymers containing carbon can be machined or patterned to create desirable microfeatures and miniature devices and then converted into carbon through a process known as pyrolysis.

During pyrolysis, an organic material or polymer is thermally decomposed in an oxygen-free environment into its carbon backbone. While most polymers change directly into a form of carbon that retains their original morphology without passing through a plastic phase, this process does lead to shrinkage of the polymer due to the decomposition of non-carbon molecules from its structure. This shrinkage is generally isotropic and consistent (repeatable), allowing for reproducible patterning and tight dimensional tolerances in the final product [193].

Typically, carbon derived from pyrolysis is known as "glassy" carbon due to its glass-like appearance when polished [163]. While the exact structure of glassy carbon is still under debate, it is generally believed to have a fullerene-like structure, with discrete fragments of curved carbon sheets interspersed with pentagons and hexagons [53]. This structure translates to its electromechanical properties. For example, glassy carbon exhibits good electrical and thermal conductivity, and has both low porosity and low permeability, making it chemically very inert and able to be etched at high temperatures under an oxygen atmosphere. These properties, combined with the carbon's wide electrochemical stability window and low background noise, makes it excellent for electrochemical applications, especially when the polymer precursor can be patterned into unique three-dimensional and high aspect ratio structures that improve its electrochemical kinetics [60],[123].

One of the most common methods for generating unique three-dimensional glassy carbon structures is through photolithography, or patterning of either a positive or negative polymeric photoresist. Multi-step lithographic processes can also be used to make complex structures and devices, shown in Figure 2.4. By controlling the photoresist composition,

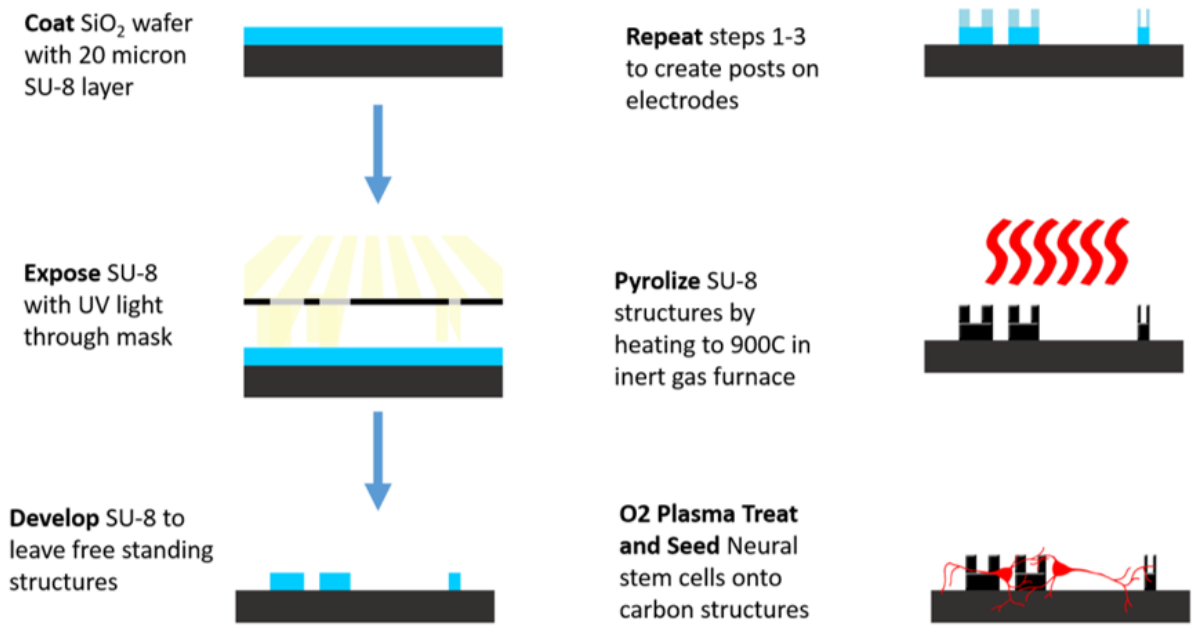

Figure 2.4: A two-step photolithography process for fabrication of carbon micropillars as a stem cell scaffold is shown.

lithography conditions, the soft and hard bake times, and the pyrolysis ramping rates and temperature, a number of unique structures can be fabricated with different geometries, mechanical properties, and chemical properties [118],[192].

Figure 2.5 shows some of the unique structures that have been developed, including high aspect ratio carbon micropillars [6], suspended carbon wires [191], carbon fractals [141], and self-assembled carbon flowers [66]. For example, a two-step photolithography process was used by Wang et. al. to produce high-aspect ratio carbon micropost arrays [191]. The researchers further used the diffraction effect of UV light and different exposure rates to create suspended wires between the carbon posts. This unique structure yielded a high lithium ion charge discharge capacity and proved to have excellent electrochemical properties. Park et. al. created a carbon pillar with a high surface area, biomimetic, fractal-like structure by doping an epoxy-based negative photoresist, SU-8, with carbon nanofibers that include iron catalysts [141]. This growth was retained following pyrolysis.

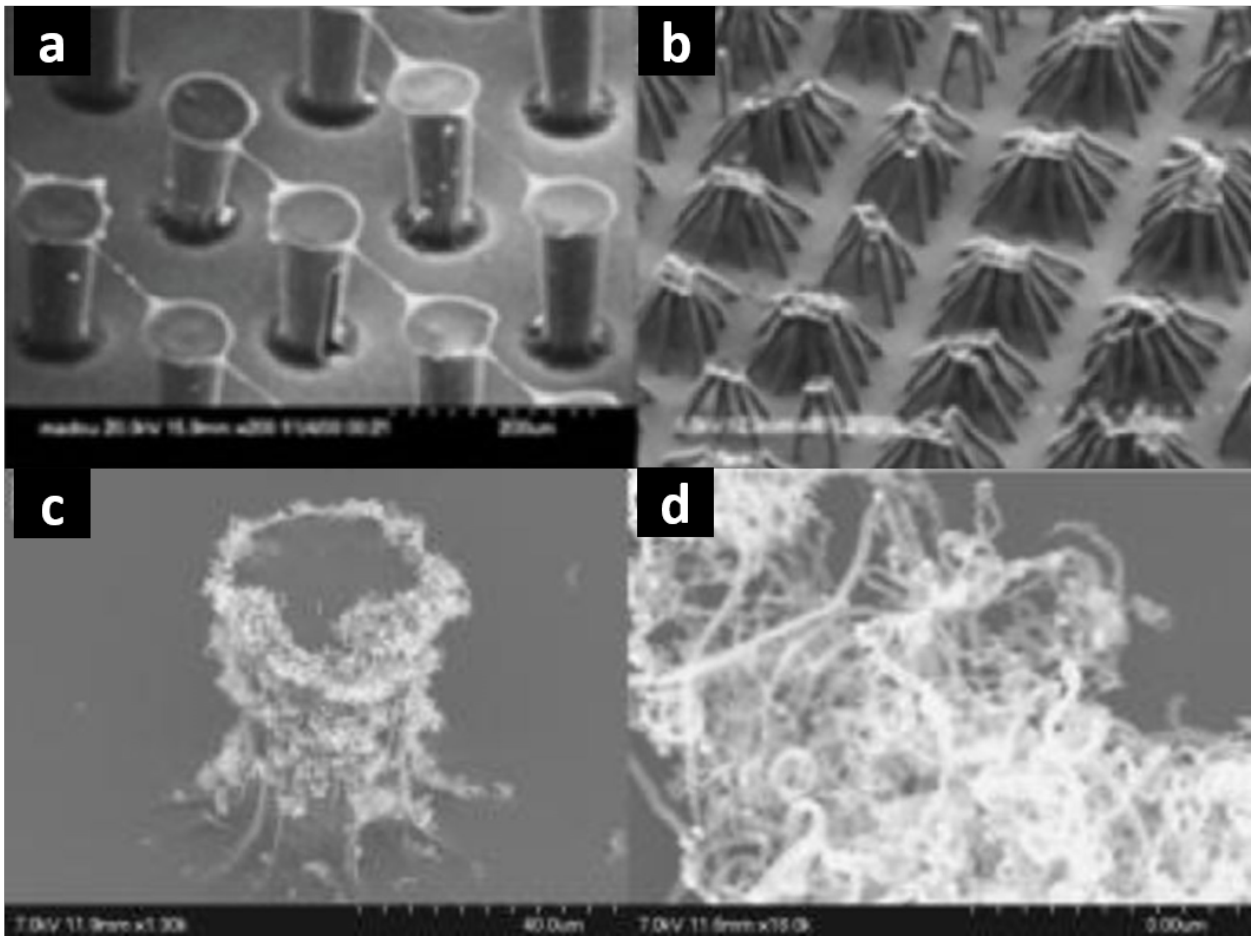

Figure 2.5: Unique MEMS structures created using photolithography: a.) carbon micropillars with suspended nanowires, b.) self-assembled carbon flowers, c.) fractal-like carbon micropillar made with doped photoresist, and d.) close up of fractal structure on micropillar. Reprinted from [111] with permission from Taylor & Francis Group LLC.

2.3 Electrospinning for cell scaffolds

The behavior or liquid jets in electric fields was first observed by Raleigh in 1882 [148] and later studied in detail by Zeleny [208]. Critical contributions to the theoretical framework for electrospinning were made by Taylor, who calculated the conical shape from which a jet leaves the surface of a liquid drop [178] and determined the critical voltage to initiate the jet in the electrospinning process [179]. Since then, increasing interest in the field of nanotechnology and biomimetic structures, has led to the revival of electrospinning for a broad range of applications, including tissue engineering [172, 98], water filtration [63, 115], battery technology [196, 75, 188], sensing [198, 76, 19, 60], and drug delivery [209, 62].

Nanofibers made using electrospinning are one of the most promising substrates for tissue engineering applications due to their ability to mimic the architecture of the natural extracellular matrix (ECM). Nanofibers exhibit high mechanical strength, high porosity, and large surface-to-volume ratio, which increases the contact area between cells and fibers and has been shown to facilitate cellular adhesion. Furthermore, nanofibers can be fabricated from both synthetic and natural ECM mimicking materials and can even be coated with different adhesion proteins, such as laminin or fibronectin, to further improve cell adhesion on the scaffold.

Electrospinning depends on the complex interplay of surface tension, fluid mechanics, and electrical charge, which interact to create electrified jets of polymer solutions [205]. The typical electrospinning setup, shown in Figure 2.6, consists of a (1) high voltage source, which creates an electrical field between the tip of a (2) syringe needle containing a charged solution, and a (3) grounded target onto which the fibers are deposited.

Before electrospinning, a droplet at the tip of the syringe is held together by surface tension forces. As a voltage is applied between the syringe tip and the collector, the metal needle of the syringe electrically charges the polymer solution. At low electric fields, the surface

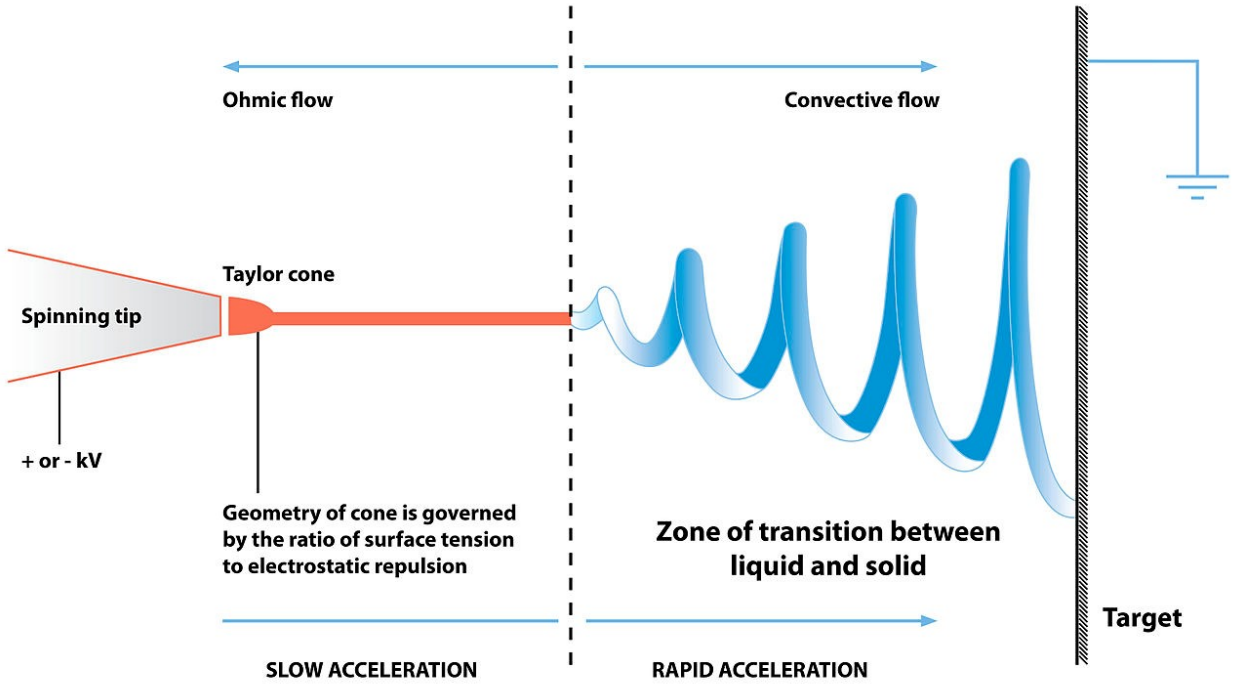

Figure 2.6: Schematic diagram depicting the electrospinning process. Reprinted from [111] with permission from Taylor & Francis Group LLC.

tension forces in the solution are dominant. As the intensity of the electric field is increased, charges induced in the polymer solution repel each other, acting in opposition to the surface tension of the fluid, and create shear stresses. Coulomb repulsion between charged ions in the solution deforms the droplet into a conical shape known as the Taylor cone. At a critical voltage, V_{crit}, the Taylor cone serves as the initiating surface for a charged polymer jet, which emanates from the tip of the conical drop and accelerates toward the collector, see Figure 2.7. As the solvent evaporates during the electrospinning process, electrostatic repulsion elongates the jet and thins it out into a uniform nanofiber, which then gets deposited onto the collector.

To determine at what voltage electrospinning begins to occur, we can look at the critical voltage model developed by Taylor [178]. Taylor suggested jets are formed from the tip of a charged droplet in the nozzle when the sum of the surface forces in the Taylor cone of the droplet equal the sum of the applied electrostatic forces, defined as the derivative of the

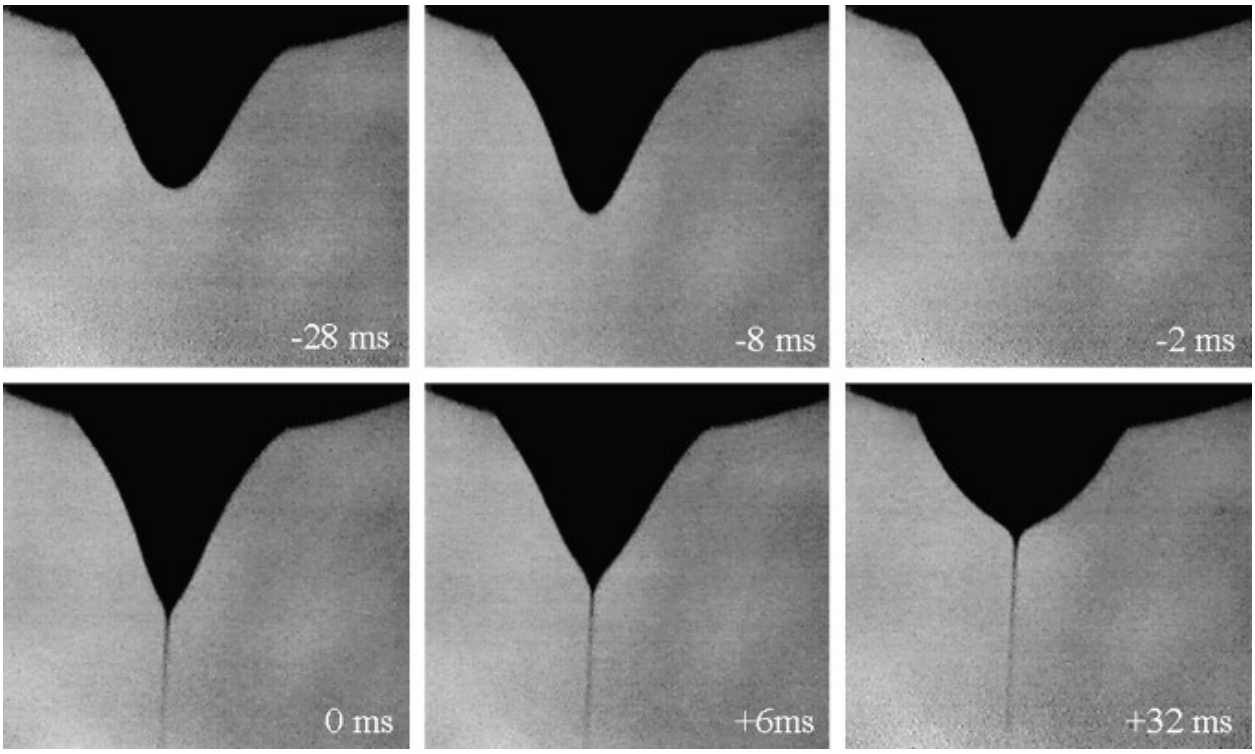

Figure 2.7: Time lapse images showing the formation and structure of the Taylor cone during electrospinning following application of the critical voltage. Reprinted from [151] with permission from Elsevier Ltd.

stored electrical energy in the distance between the nozzle and collector (since the droplet is relatively small, we neglect both the mass of the droplet and any pressure forces).

To calculate the electrostatic force, we utilize the semi-infinite cylinder model developed by Taylor and shown in Figure 2.8. In this case, the surface force can be calculated from the capillary rise method for solution in a cylinder tube and is given in Equation 2.2

$$F_s = 2\pi r\sigma cos(\phi) \tag{2.2}$$

where r is the radius of the nozzle, σ is the surface tension of the drop, and ϕ is the angle the fluid makes with the nozzle as it leaves the rim.

The electrostatic force is based on theoretical and experimental calculations by Van Dyke ([179]), who used the method of images to calculate the attractive force between a needle and a perpendicular plane when a voltage was applied between them. This force is given in Equation 2.3.

$$F_E = \frac{V^2 L^2}{4z^2(ln(\frac{2L}{r}) - \frac{3}{2})} \tag{2.3}$$

where V is the applied voltage, z is the distance between the tip of the nozzle and the collector, and L is the length of the nozzle. Setting the surface and electrostatic forces equation, we obtain Equation 2.4 for the critical voltage required for an electrified jet to

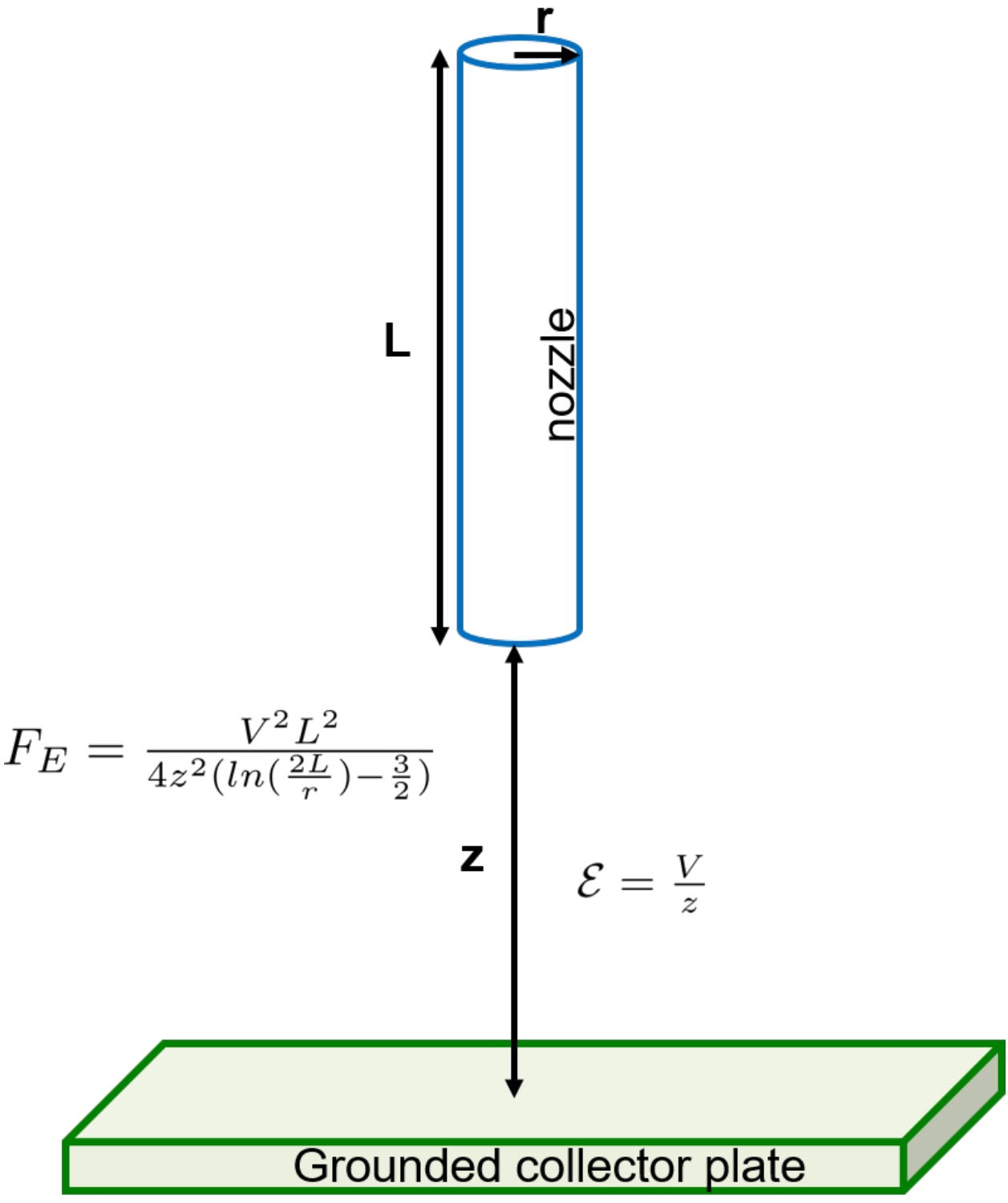

Figure 2.8: A model for approximating the electric field between a needle and a collector. The model assumes the electrospinning setup can be approximated as an infinite cylinder positioned a distance, z, above a grounded parallel plane.

leave the taylor cone.

$$V_{crit} = \left(\frac{4z^2}{L^2}(ln(\frac{2L}{r} - \frac{3}{2})2\pi r\sigma cos(\phi)\right)^{1/2} \tag{2.4}$$

Once the electrospinning process is initiated, it is governed by three polymer instabilities. The first instability, known as the Rayleigh instability, occurs at low electric field strengths or at low solution viscosities. The Rayleigh instability acts axisymmetric to the jet and is governed by surface tension in the solution, which tends to minimize the surface area of the solution by breaking up the jet into individual droplets. This phenomenon, called electrospraying, can be used to create material geometries that include both droplets and nanofibers. Researchers have taken advantage of this instability to create various bead-on-fiber morphologies, whose geometries can be tuned to create scattering and diffraction effects that selectively reflect light and lead to structural colors, such as the colors present on butterfly wings or peacock tail feathers [106, 175].

At high electric fields, or high concentrations of polymer in solution, the Rayleigh instability is suppressed and two other instabilities dominate: the axisymmetric bending instability and the non-axisymmetric whipping instability [204, 169]. These instabilities occur due to the electrostatic charge-charge repulsion present in the jet as the solvent begins to evaporate during the electrospinning process and cause the jet to bend and stretch in an inverse-cone structure, shown in Figure 2.9. At even higher electric fields, the non-axisymmetric whipping instability is enhanced even further, thinning and elongating the jet and depositing micro- to nano-scale fibers onto the conductive ground plate. The application of this process has successfully produced various geometries of electrospun fibers with diameters ranging from a few microns down to tens of nanometers in over 40 different types of organic polymer materials [161, 64, 169].

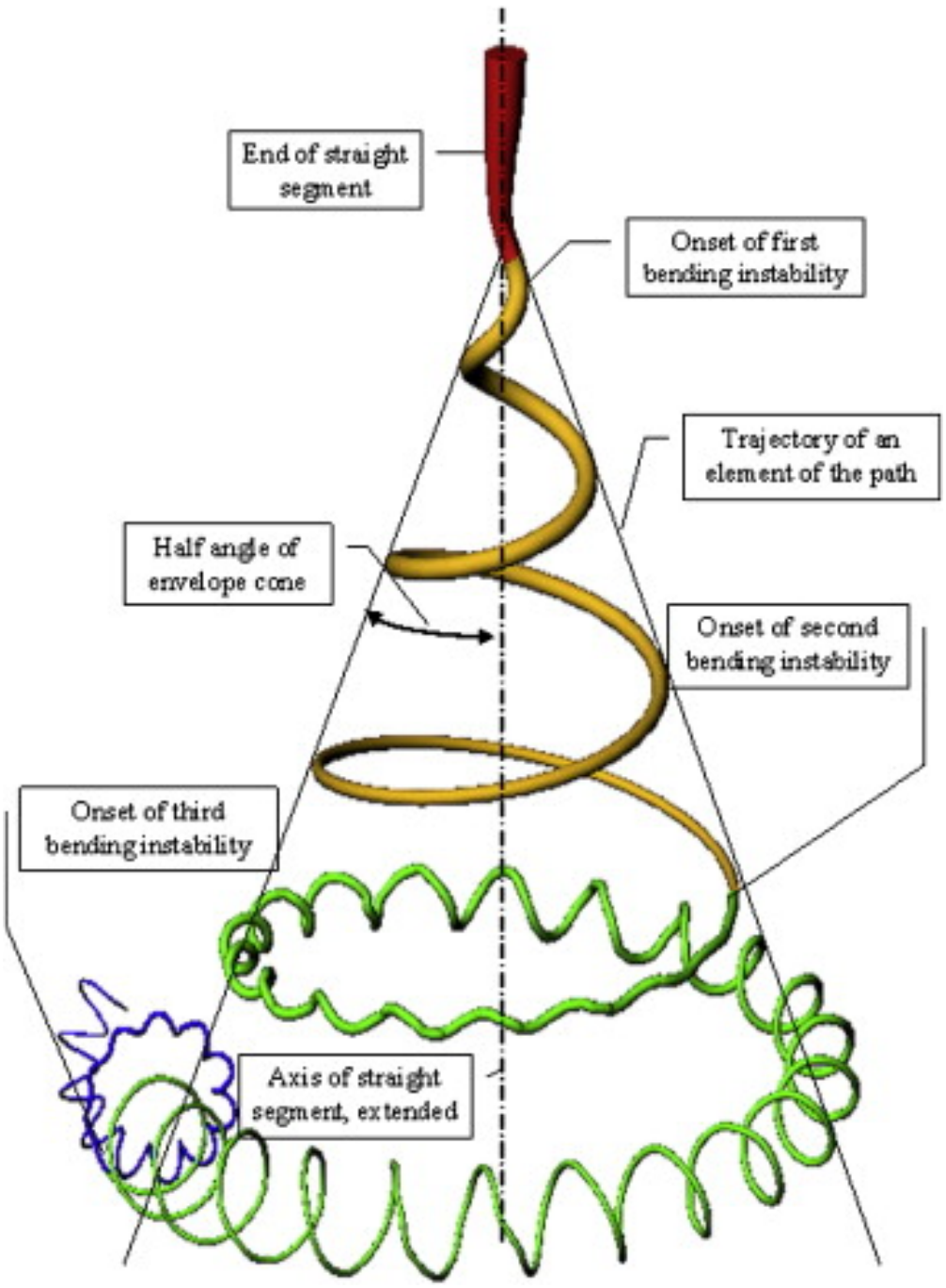

Figure 2.9: Schematic diagram depicting the electrospinning process, including the different instabilities that form at various points of the jet. Reprinted from [151] with permission from Elsevier Ltd.

2.3.1 Electrospinning to influence scaffold microstructure

Despite the simplicity of the electrospinning process, control of fiber diameter varies both temporally and spatially and is based on a number of parameters. In order to understand how to best create electrospun scaffolds with fiber diameters that mimic the extracellular matrix of cells, We will look at the different equations governing control over fiber diameter.

We can look at the main parameters controlling fiber diameter at three different locations in the electrospinning process ([37]): near the nozzle (in a regime known as near-field electrospinning), a terminal fiber diameter attributed to the growth of the whipping instability, and at larger distances from the nozzle (in the regime known as far-field electrospinning).

Near the vicinity of the nozzle, the fiber diameter can be determined by the density and kinematic viscosity of the polymer solution (μ), the distance from the nozzle (z), the polymer flow rate (Q), the electric current (I), and intensity of the external electric field ($\mathcal{E}$), shown in Equation 2.5.

$$d = \left(\frac{6\mu\rho Q^2}{\pi I \mathcal{E} z^2}\right)^{1/2} \tag{2.5}$$

At far distances from the nozzle, Fridrikh et. al. modeled the fiber diameter as a function of the dielectric permittivity and superficial tension of the polymer, the flow rate, and the electric current, see Equation 2.6. This model predicted the existence of a terminal jet diameter achieved during thinning of the jet due to the growth of the whipping instability.

$$d = \left(\gamma\epsilon\frac{Q^2}{I^2}\frac{2}{\pi(2ln\xi - 3)}\right)^{1/3} \tag{2.6}$$

Between these two extremes, the fiber diameter for far-field electrospinning can be expressed as a function of the density of the solution, the flow rate, the electric current, and intensity of the electric field, shown in Equation 2.7.

$$d = \left(\frac{\rho Q^3}{2\pi^2 I \mathcal{E} z} \right)^{1/4} \tag{2.7}$$

Since the current is generally hard to measure, we can modify Equation 2.7 to be a function of the solution conductivity, an easily measured parameter. We express the current, I, in terms of the applied voltage, V, and resistance, R, defined as $R = \frac{z}{\sigma_c S}$, where z is the length of the jet, σ_c is the solution conductivity, and S is the section of the jet ($\pi(\frac{d}{2})^2$). Therefore, $I = \frac{V}{R} = \frac{V \sigma_c \pi d^2}{4z}$. Substituting this into Equation 2.7, and rewriting the electric field in terms of the voltage dropped over a distance, $\mathcal{E} = \frac{V}{z}$, we obtain Equation 2.8 for the fiber diameter:

$$d = \left(\frac{2\rho Q^3 z}{\sigma_c \pi^3 I V^2} \right)^{1/6} \tag{2.8}$$

This theoretical calculation is used in Section 3.1 to electrospin nanofiber mats with desired terminal fiber diameters.

The choice of collector can also be used to influence the final electrospun material. By using a rotating drum as a target [70], and rotating at a high enough RPM, nanofibers can be produced that align parallel to the direction of rotation, shown in Figure 4.1. Rotating at a low rotational speed will produce nanofibers with randomly aligned orientations. By combining photolithography with different electrospinning parameters, structured nanofiber arrays, such as those shown in Figure 2.10 and Figure 2.11 can be fabricated [111].

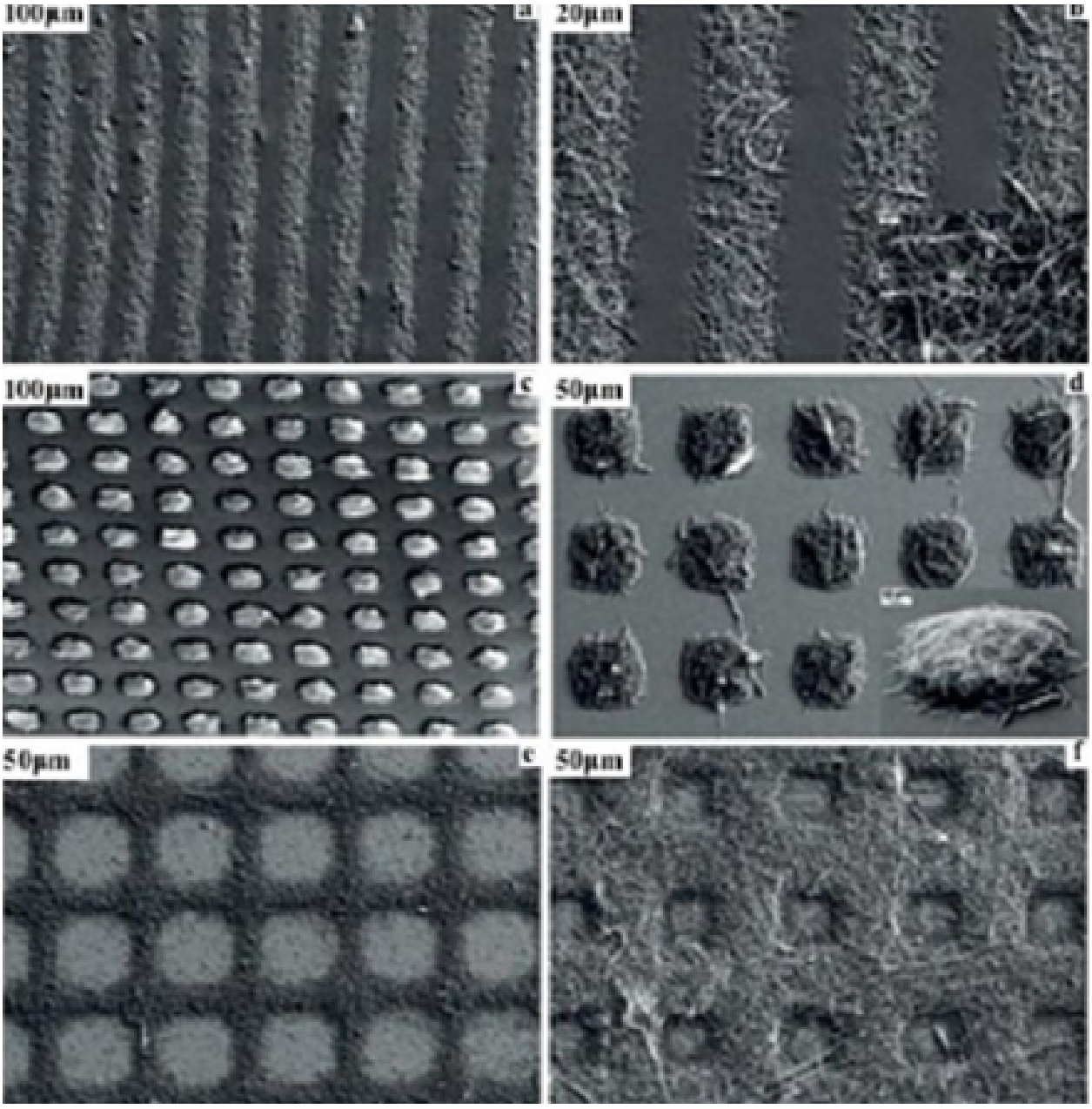

Figure 2.10: Control of electrospinning parameters to create patterned structures: a,b.) electrospun lines, c,d.) patterned nanofiber pillar arrays, and e,f.) connecting nanofiber squares and valleys. Reprinted from [111] with permission from Taylor & Francis Group LLC.

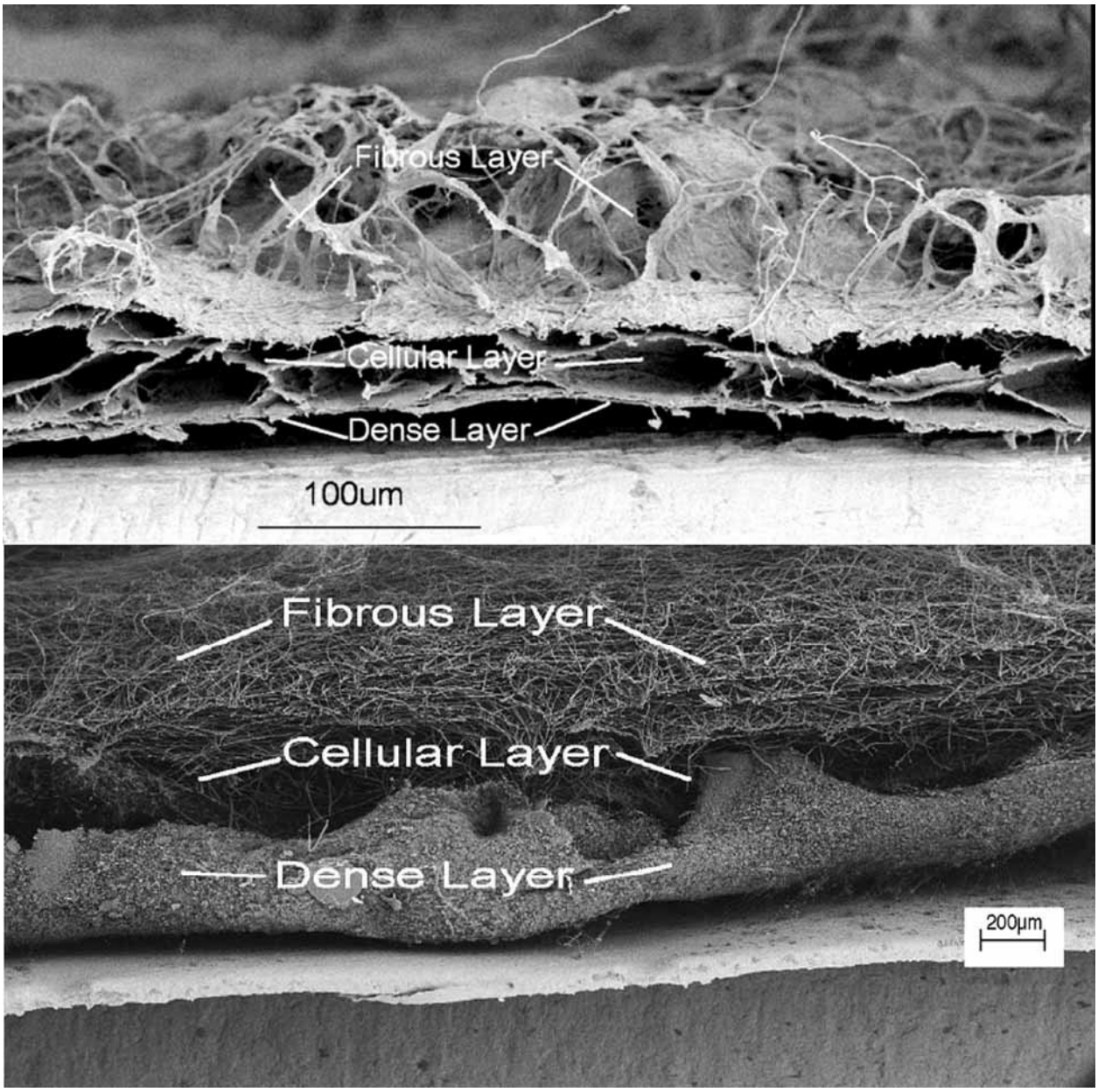

Figure 2.11: Cross-sectional views of a porcine urinary bladder matrix (top) and an electrospun urinary bladder matrix mimicking scaffold composed of cellulose acetate (bottom). (Reprinted from [52] with permission from Elsevier Inc.)

2.3.2 Electrospinning to influence scaffold nanostructure

While tuning the microstructure of electrospun nanofibers is fairly well characterized, some applications can also require the ability to tune the internal polymer structure of the nanofiber mat. This is especially important when the nanofiber mat will be used in sensing applications, such as in electrochemical sensing. In this case, the nanofiber mat is generally made from carbon precursor material and carbonized via pyrolysis (see Section 2.2.1). The final carbon structure is dependant on a number of factors, including pyrolysis ramp rate and temperature, precursor composition, and any kind of mechanical stretching or stress placed onto the polymer prior to or during pyrolysis.

Electrospinning is also able to change the microstructure of the final pyrolized carbon as well, creating more graphitic or electrochemically favorable carbon than that found in photolithography derived glassy carbon [168]. The large shear forces during electrospinning pull on the coiled polymer chains in the jet, orienting them in the outermost diameter of the jet [41]. This process can be enhanced using a rotating drum as the target to physically pull the nanowires following deposition and increas the alignment of the polymer chains within the nanofibers. Another critical way to enhance this mechanical effect is through the addition of carbon nanotubes or similar structures, such as graphene nanoribbons, to the polymer before electrospinning.

The addition of CNTs into polymeric fibers has been shown to affect their physical structures, enhance tensile properties, reduce fiber thermal shrinkage, improve chemical resistance, increase electrical and thermal conductivities, and lead to higher polymer thermal transition temperatures. There are several mechanisms attributed for these improvements in polymer properties.

In non-graphitizable polymer precursors, such as the commonly used precursor, polyacrylonitrile (PAN), polymer chains are generally coiled, as shown in Figure 2.12. Several groups

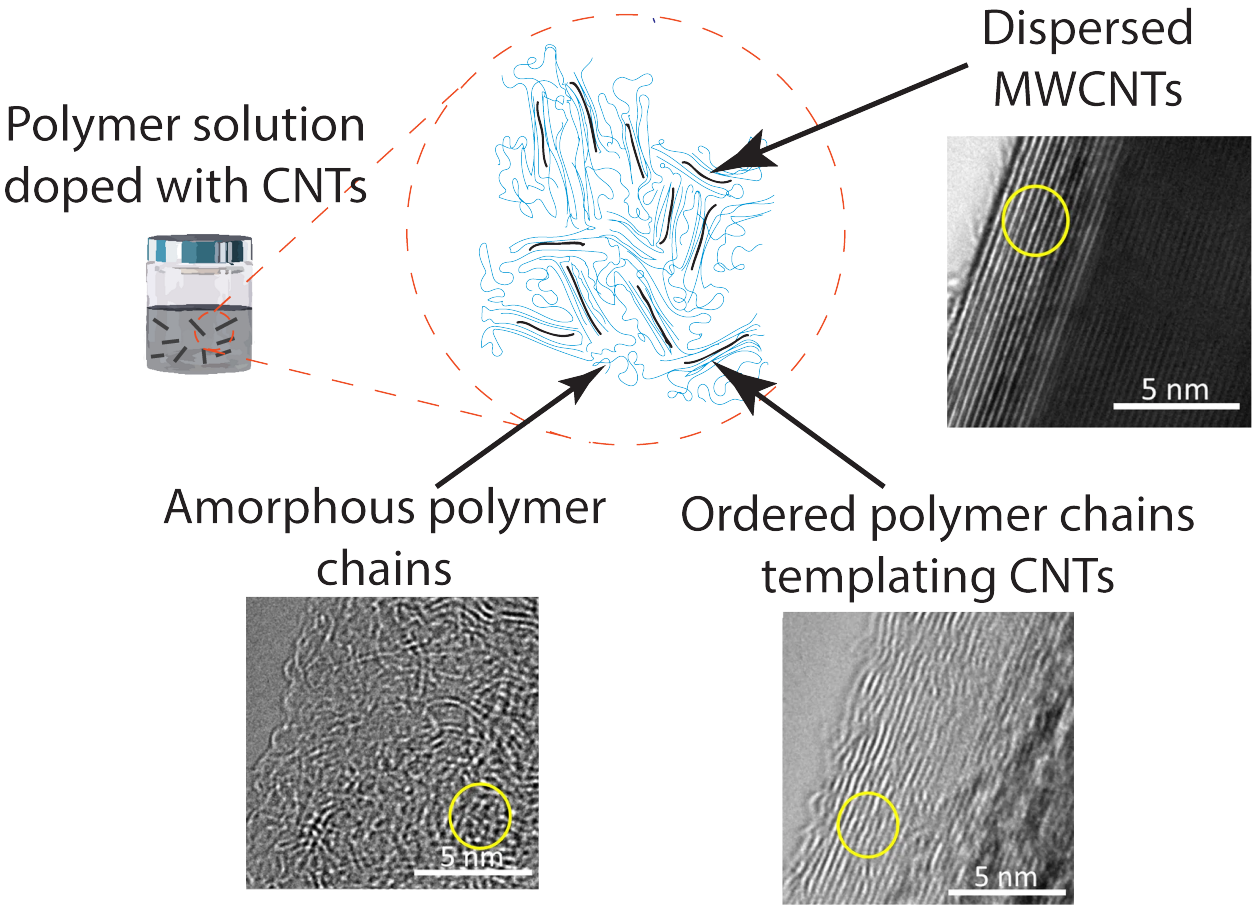

Figure 2.12: Schematic showing different polymer chain configurations in a solution of polyacrylonitrile polymer doped with multi-walled CNTs. TEM image analysis of the final graphitized polymer shows the differences between normal PAN polymer chains, CNTs, and templating along axis of the CNT.

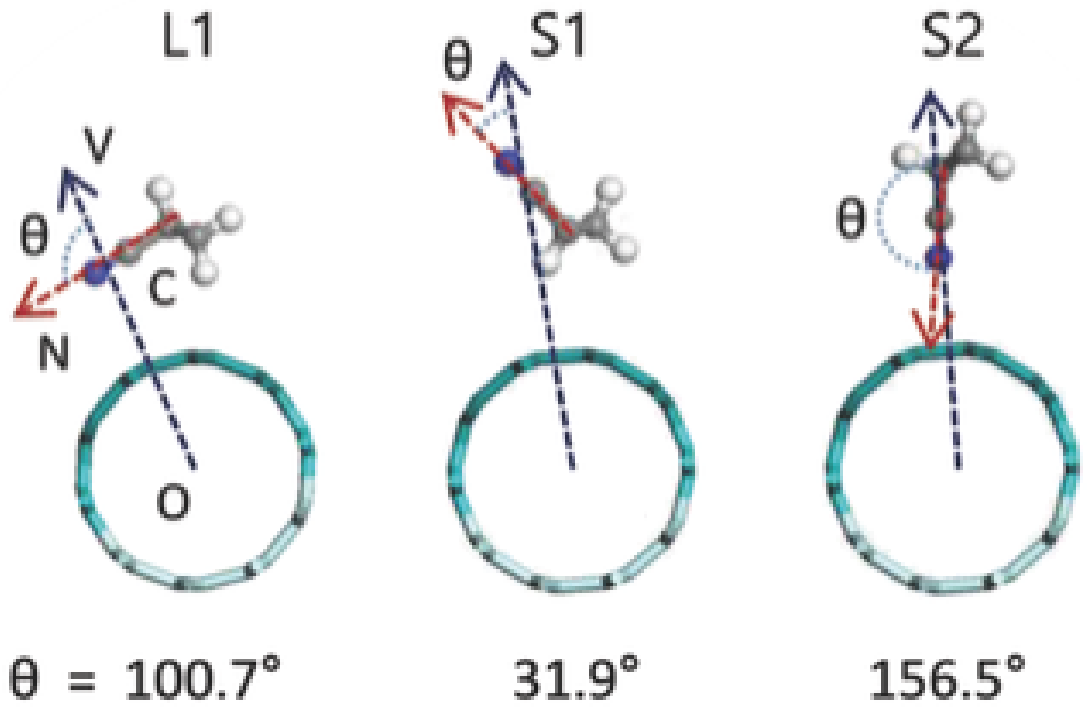

Figure 2.13: Representative configurations of PAN on the surface of (5,5) CNT based on the angle of PAN nitrile groups The configurations show one lying-down (L1) configuration, which was energetically favorable, and two standing-up (S1, and S2) configurations. Reprinted from [101], with permission from Wiley.

have shown both experimentally and using density functional theory calculations that when CNTs are added to the polymer solution, the highly polar PAN nitrile groups tend to linearly align along the axis of the CNT surface in a lying-down configuration (L1 in Figure 2.13) that minimizes interface energetics, even at very low temperatures [101].

This process of uncoiling the PAN polymer chains is further improved through electrospinning with the interplay between molecular drag forces in the polymer and CNTs and the external electrostatic forces. Within the electrospun jet, a dielectrophoretic force exists, which was determined to be negative for PAN molecular chains and is generally positive for CNTs [41]. Therefore, this force will drag CNTs in opposite directions from the PAN moleuclar chains in the flowing jet, generating more shear surfaces and greater interactions between highly polar PAN nitrile groups and CNTs and further enhancing templating of

polymer along the CNT [114],[177]. During pyrolysis, these uncoiled chains are retained, yielding a fragmented graphitic nanofiber structure. This fragmented graphitic structure comes with an abundance of electrochemically active edge planes, which translate directly into the electrical and chemical properties of the nanofiber mats.

2.4 Monitoring neural cell metabolites using electrochemistry

2.4.1 Factors determining electrodes utility toward neurotransmitters

When developing electrode systems for monitoring neurotransmitters in biological environments, there are a number of factors that determine their usefulness in these applications including selectivity, sensitivity, detection limits, stability, and response time [122].

Selectivity is the ability of an electrode to detect an analyte of interest in the presence of other interfering analytes with similar peak potentials. With neurotransmitters like Dopamine, there are a number of interfering ions, including ascorbic acid (AA) and uric acid (UA), and even other interfering neurotransmitters such as Epinephrine. Figure 2.14 shows the peak redox potentials of different neurotransmitters and other important chemicals in the brain. Often, even if the redox potentials are slightly separate, voltammetric peaks can be quite broad, creating overlap from different components and decreasing selectivity. Therefore, one of the best ways to enhance selectivity is by improving the electrochemical kinetics of the electrode for the species in question. A fast heterogenous electron transfer constant, k°, will yield a sharper and larger voltage peak, allowing species with overlapping potentials to be discerned. Another method to enhance selectivity is by taking advantage of adsorption.

Technique	Applied voltage
Cyclic voltammetry	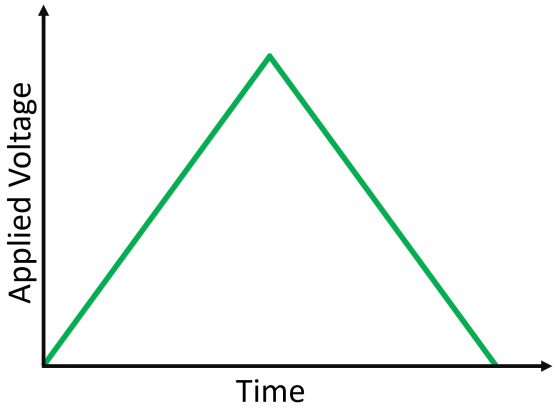
DC Potential Voltammetry	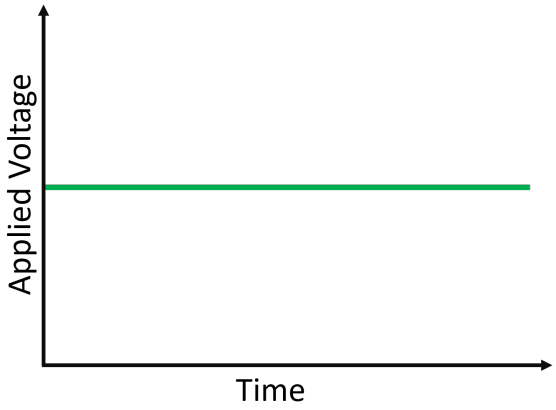
Differential Pulse Voltammetry	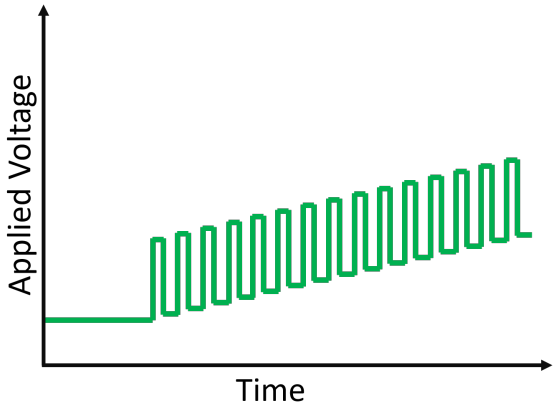

Table 2.1: Applied potentials for different electrochemical methods

Adsorption of certain molecules to the surface preconcentrates them, enhancing signal for the adsorptive species over nonadsorbed species. For example, Dopamine is high adsorptive onto electrode surface, while ascorbic acid, a common interfering substance for Dopamine, is not. Therfore, DA can be selectively detected by allowing it to adsorb onto the surface. Another method researchers have used to enhance selectivity is by coating electrodes selective substrates, like Nafion, a fluoropolymer which selectively allows cations like DA and norepinephrine to pass through while repelling anions like ascorbic acid [91, 154].

Another important aspect for electrochemistry is sensitivity, which is related to the slope of the current versus the concentration of a species near the electrode. One way sensitivity can be improved in neural systems is by increasing adsorption of certain species to the electrode surface. In adsorbed systems, the peak current is related linearly with the scan rate. Meanwhile, in diffusion limited species, current is proportional to the square root of the scan rate. Therefore, by increasing the scan rate, we can increase the peak current significantly more for an adsorbed species over a species dissolved in the solution [85].

Similarly, the limit of detection is critical for neural electrodes and is determined as the lowest detectable concentration level that is at least three times higher than the background noise. To improve detection limits, electrodes should have high sensitivity combined with very low background noise.

Other critical factors for neural electrochemistry are electrode stability over time, particularly since biological systems often contain molecules that can corrode or passivate electrodes, and response time, critical when dealing with biological events with fast time scales [153]. In neural electrochemistry, time scales can range from milliseconds, such as during the release and reuptake of neurotransmitters by synapses, to several seconds, during the conversion of Dopamine-o-quinone to aminochrome (.15/s), to several minutes when dealing with drug response times.

Molecule	Redox-Reaction	Approximate oxidation potential in vivo[30] (vs Ag/AgCl)
Tyrosine derivatives	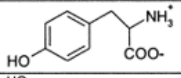	+0.7 V
L-DOPA	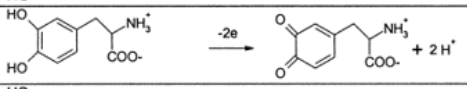	+0.4 V
Dopamine	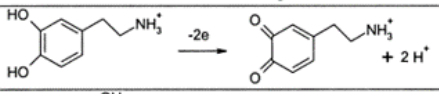	+0.2 V
Norepinephrine	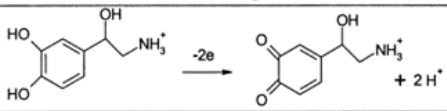	+0.2 V
Epinephrine	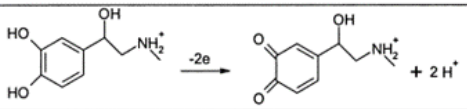	+0.2 V
DOPAC	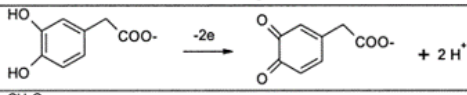	+0.2 V
Homovanilic Acid	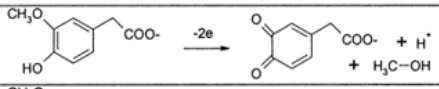	+0.5 V
3-Methoxytyramine	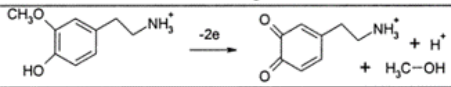	+0.5 V
Tryptophan derivatives	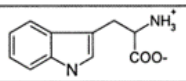	+0.8 V
Serotonin	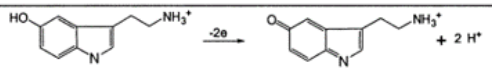	+0.35 V
5-Hydroxyindolacetic acid	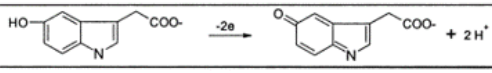	+0.35 V
Other electroactive molecules		
Adenosine[42]	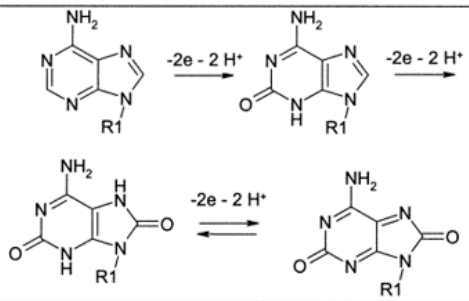	First step +1.2 V
Ascorbic Acid	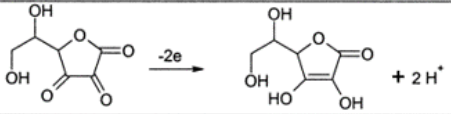	+0.2 V
Uric acid [172]	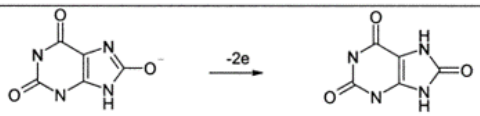	+0.3 V

Figure 2.14

2.4.2 Dopamine electrochemistry on carbon surfaces

Dopamine is a neurotransmitter that modulates critical functions of the central nervous system and its depletion is associated with diseases like Parkinson's, Alzheimer's, and even Depression. It is found in several regions throughout the central nervous system and is also released at the synaptic cleft between two neurons. DA is oxidized in a two-electron oxidation process:

$$\text{Dopamine} \rightleftharpoons \text{Dopamine-o-quinone} + 2\,e^- + 2\,H^+$$

Dopamine electrochemistry on carbon electrode surfaces is complicated by its propensity toward adsorption on these surfaces. Depending on the nature of the carbon, adsorption can occur in different ways. For polished carbon surfaces containing large amounts of oxides, the oxides act as favorable sites for adsorption of cationic species, such as DA, whose amine side chain is protonated at physiological pH. In the case of pyrolized carbon containing H-terminated carbons, DA oxidation is catalyzed through hydrogen bonding of surface carbonyl groups to adsorbed DA molecules. There has also been research looking at adsorption of DA and other catechols onto pristine glassy carbon, absent of surface oxides, due to dispersion interactions between the carbon surface and the phenol ring in catechols [122]. This mechanism yields a certain selectivity for cations over common interferon's like ascorbic acid (AA), where dispersion interactions are suppressed. However, dispersion forces are the same for both anions and cations at carbon surfaces and therefore offere limited selectivity.

For in-vivo electrochemical measurements, adsorption due to oxides is of particular interest because of the enhanced selectivity this mechanism affords in distinguishing DA from other anionic interferon's, such as AA and DOPAC. As described in Section 2.4.1, increasing the scan rate enhances the measurement even further since the response to the adsorbed species begins to dominate even at high concentrations of anionic interferon's.

Chapter 3

Materials and Methods

3.1 Material Fabrication

Polyacrylonitrile (PAN; MW 150,000 u) (Millipore-Sigma, Catalog Number 181315) and multi-walled carbon nanotubes (MWCNTs) (Millipore-Sigma, Catalog Number 659258) were dissolved with anhydrous dimethylformamide (DMF; Fisher Scientific). Briefly, PAN was dissolved in DMF at 60 °C using a stirred-hot plate. Once a homogenous solution was obtained, MWCNTs was added and stirred overnight (∼12 hours) until evenly dispersed. For 8%/1% w/w (PAN/MWCNT), 0.40 g of PAN and 0.05 g of MWCNTs were dissolved in 4.55 g of DMF. For 8%/4% w/w (PAN/MWCNT), 0.4 g of PAN and 0.2 g of MWCNTs were dissolved in 4.4 g of DMF.

A custom-built electrospinning setup with a rotating drum collector was used to produce the nanofibers, see Figure 3.2. The solution was loaded into a 1 mL syringe equipped with a conductive, 21-gauge needle (Jensen Global, Catalog Number: JG21-1.0X). A high potential (+18 kV) was applied at the needle to the grounded collector with a fixed needle-to-collector distance of 15 cm using a commercially available high voltage source (Analog Technologies

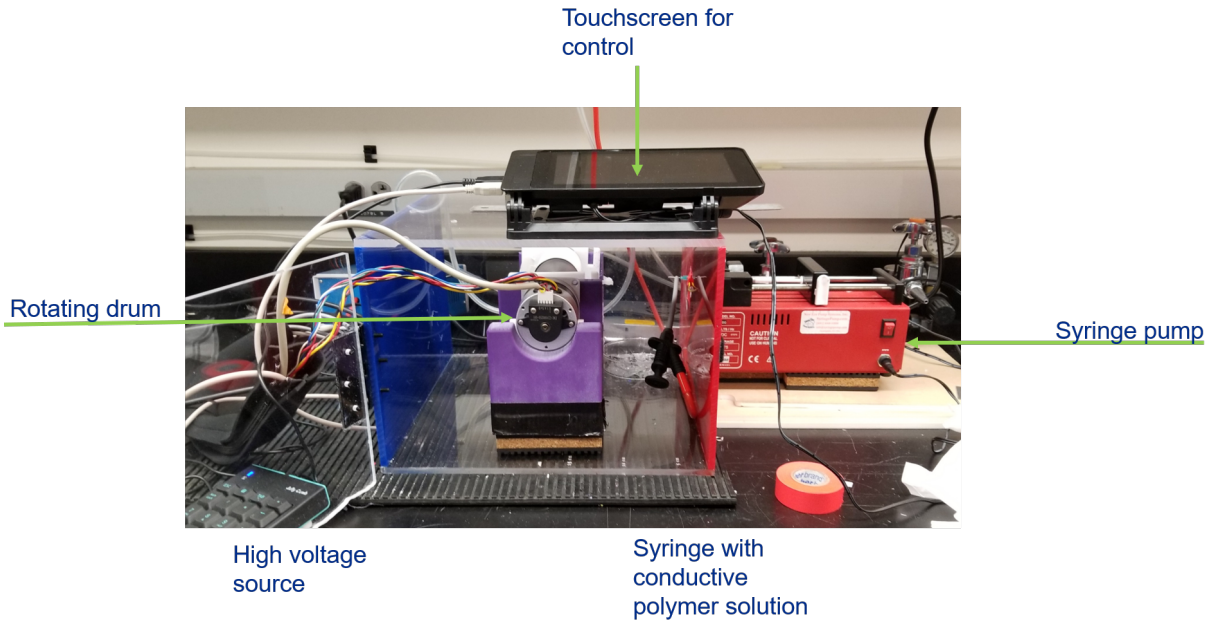

Figure 3.1: The electrospinning setup consists of a high voltage source, which applies a high voltage between the tip of a syringe and a rotating drum collector. The flow rate of the polymer solution is controlled by a programmable syringe pump. The entire setup was automated using a Raspberry Pi and control written in python.

Inc, Catalog Number: AHVAC30KVR5MABT). A syringe pump (New Era, USA) was used to pump the solution (0.5 mL/hr) to maintain the steady Taylor cone. The collector rotation speed was set at 500 rpm to obtain randomly oriented fibers and 3000 rpm to obtain aligned fibers.

The nanofiber mats were mechanically compressed (Dayton's DC Speed Control Roller) five times and stabilized at 280° C in air for 6 h. Following stabilization, the nanofiber mats were pyrolyzed in a tube furnace (Lindberg Blue M1100) with N2 (9,000 SCCM) at 1000° C (ramp rate of $\sim$ 2.5° C/min) for 1 h and allowed to naturally cool to obtain the final carbon nanofiber material.

The resulting carbon nanofiber mats were cut (1 cm x 1 cm) and secured onto glass coverslips (12 mm) using PDMS. For electrically active scaffolds, a small amount of carbon paint was used to join a copper wire to the MSS. The junction was passivated with a sufficient amount

of PDMS ensuring that the carbon paint and copper wire did not contribute to any obtained electrochemical signals.

3.2 Material Characterization

Raman spectroscopy was performed using a Renishaw InVia Raman Microscope. Raman spectra was obtained using a 532 nm excitation laser and fit to Lorentzian peaks for analysis. The I_D/I_G ratio was calculated from the absolute peak intensities of the I_D and I_G Raman bands. SEM analysis was performed using an FEI Magellan 400 SEM.

3.3 Cell Culture and Seeding

Mouse neural stem cells (mNSPCs) were harvested from the medial ganglionic eminance (MGE) and neural cortex (CTX) of 12-day-old mouse embryos (E12). The mNSPCs were proliferated in suspension using Temple (+) consisting of Dulbecco's Modified Eagle Medium (Life Technologies, Cat. 17504) supplemented with 1X B27 (Life Technologies, Cat. 17504), 1X N2 (Life Technologies, Cat. 17502), 1 mM sodium pyruvate (Life Technologies, Cat. 11360070), 2 mM L-glutamine (Life Technologies, Cat. 25030), 1 mM N-acetylcysteine (Millipore-Sigma, Cat. A7250), 10 ng/mL b-FGF (Life Technologies, Cat. PHG0026), 20 ng/mL EGF (Life Technologies, Cat. PHG0311), and 2 ug/mL heparin (Millipore-Sigma, Cat. H3149). Cells were passaged using NeuroCult (Stemcell Technologies, Cat. 05707) dissociation reagent. Prior to cell seeding, the scaffolds were sterilized with 70% ethanol and washed with Ultrapure DI. To coat the scaffolds with Laminin (Life Technologies, Cat. 23017015), PDL (VWR, Cat. IC15017510) dissolved in Ultrapure DI (1:50) was applied to the scaffold for 5 min, washed two times, then incubated with Laminin dissolved in Minimum Essential Medium (Life Technologies, Cat. 11095) overnight. Differentiation media, Temple

(-), consisted of the same formulation without b-FGF, EGF, or heparin. Experiments were conducted using cells between passages 3 to 5.

The MGE and CTX cells were seeded onto the scaffold at a density of 150,000 cells/scaffold and cultured for 6 days with Temple (-) media. The differentiation media was replenished and diluted every 2 days.

PC12 cells (Millipore-Sigma, Cat. 88022401-VL) were proliferated as suspension cultures using RPMI 1640 (Life Technologies, Cat. A1049101) with 10% heat-inactivated DHS (Atlanta Biologicals, Cat. S12150) and 10% FBS (Life Technologies, Cat. 10437010). PC12 cells were passaged using NeuroCult Dissociation reagent. PC12 cells were seeded overnight as adherent cultures using proliferation media to promote growth and adhesion. The proliferation media was replaced with RPMI 1640 with 1% FBS and 100 ng/mL NGF (Millipore-Sigma, Cat. N0513) and replenished every 2 days.

3.4 Cell Viability and Analysis

To assess biocompatibility of mNSCs on the carbon MSS, a Live/Dead Viability/Cytotoxicity assay (Thermo Fisher, Cat. L3224) was performed 1 and 5 days following seeding at the proliferation stage. Live/Dead assays are typically composed of two fluorescent compounds: Calcein acetoxymethyl ester (calcein AM), which is permeable to the cell membrane and Ethidium homodimer-1 (EthD-1), which is impermeable to the cell membrane and fluoresces after entering broken or damaged cell membranes. Cells were first washed with D-PBS and incubated for 30 min with 2 μM calcein AM and 4 μM EthD-1. Coverslips were then inverted onto a glass slide with a drop of fresh calcein AM and EthD-1. Fluorescent imaging was performed using an inverted Nikon Eclipse TI-2.

3.5 Cell Fixation and Processing for Microscopy

For SEM analysis, samples were fixed using 2% paraformaldehyde and 0.01% glutaraldehyde for 10 min and washed three times with PBS. Cells were dehydrated using a series of ethanol washes (10%, 30%, 50%, 70%, 90% and 100%) for 10 minutes each. The 100% ethanol was replaced with 100% acetone and dried using a Leica CO2 critical point dryer. Finally, 4 nm was platinum was sputtered onto the samples using a Leica Sputter Coater 200.

For immunocytochemistry, cells were fixed using 4% paraformaldehyde for 10 min, washed, permeabilized with 0.3% Triton X-100 for 10 min, washed, and blocked with 5% bovine serum albumin (BSA) (RMBio, Cat. BSA-AAF) for 1 h at room temperature. The samples were then incubated overnight with primary antibodies, GFAP (1: 200) (Millipore-Sigma, Cat. G3893), TuJ-1 (1: 200) (Millipore-Sigma, Cat. T2200), and/or MAP2 (1: 200) (Fisher Scientific, Cat. NBP192711SS) diluted in 1% BSA at 4 °C. Primary antibodies were detected with secondary antibodies (Jackson ImmunoResearch, Cat. 715-545-151/711-585-152) diluted in 1% BSA (1: 200) at RT for 2 h. Nuclei were stained with NucBlue^{TM} Live ReadyProbes^{TM} Reagent (Life Technologies, Cat. R37605) for 5 min and mounted with Prolong Antifade Gold Mountant. Fluorescent imaging was performed using the Keyence BZ-X710.

3.6 Immunocytochemistry Analysis

Images obtained from ICC were split into their respective channels (red, blue, and green) for analysis. Neuron angle measurements were obtained by selecting an arbitrary axon in the image and measuring all other angles with respect to that axon. Alignment was measured on a scale from 0 to 1, with 1 indicating highly aligned neuronal axons and 0 being highly unaligned axons. To evaluate astrocyte solidity and circularity, background noise was first removed by thresholding each image, then edges were found and the shape of each astrocyte

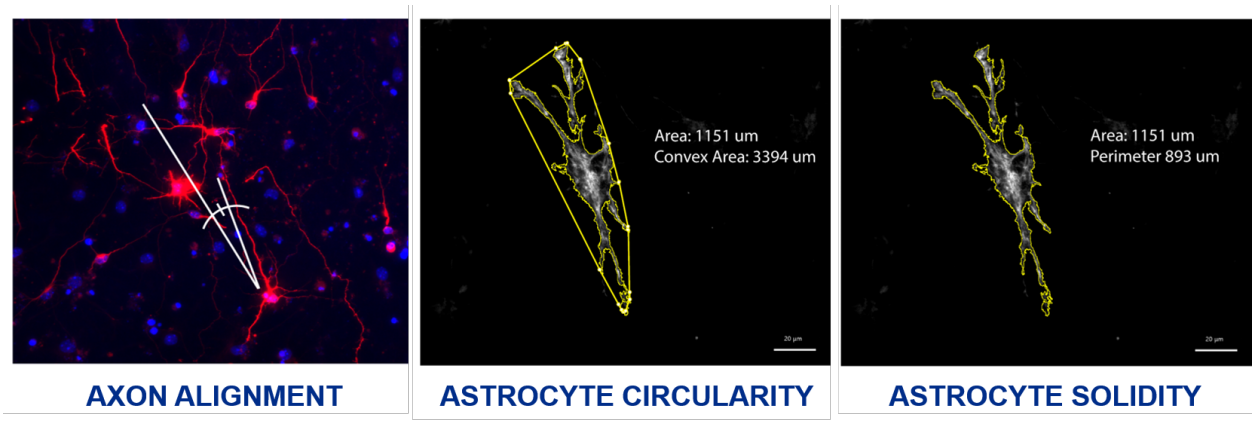

Figure 3.2: Representative images demonstrating how neural axon alignment, astrocyte cytoskeleton circularity, and astrocyte cytoskeleton solidity were calculated.

was outlined. Circularity measures the deviation of each astrocyte from a perfect circle, where 1 represents a perfect circle and values closer to 0 represent more elongated astrocytes. Circularity was evaluated after calculating the area and perimeter of each astrocyte using Equation 3.1, where A is the area and P the perimeter.

$$C = 4\pi \frac{A}{P^2} \tag{3.1}$$

Solidity was measured as the ratio between the area of each astrocyte and the area of the convex hull of each astrocyte, see Equation 3.2, where A is the area and A_C is the convex area. All cells were evaluated and tabulated for each field of view.

$$S = \frac{A}{A_C} \tag{3.2}$$

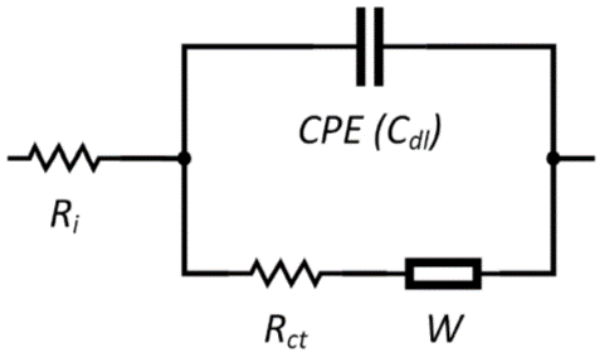

Figure 3.3: The equivalent circuit for three-dimensional carbon nanofiber mats, where a CPE (constant phase element) replaces the double layer capacitance (C_{dl} used in flat electrodes and a Warburg element is added in series to the charge transfer resistance, (R_{CT}), to model the effects of diffusion on the system. The solution resistance is modeled as a resistive element, R_S.

3.7 Electrochemical Detection

Electrochemical tests were carried out using a Princeton Applied Research VersaSTAT 4 Potentiostat. To calibrate electrochemical measurements, the surface area of the electrode must be calculated. For simple, 2-dimensional electrodes, this is typically done using the Randles-Sevick equation [14]. Since the electrospun carbon MSS was a complex, 3-dimensional material, electrochemical impedance spectroscopy (EIS) was used to find the double layer specific capacitance and calculate the electroactive surface area of each electrode using Equation 3.3:

$$S_{active} = \frac{I_c}{C_{dl} \cdot v} \tag{3.3}$$

where C_{dl} is the double layer capacitance [$\mu F cm^{-2}$, I_C is the capacitive current [A], and v is the scan rate [V cm^{-2}] [41, 131, 100]. EIS was performed (10,000 Hz–0.1 Hz) in a blank electrolyte solution (PBS 0.1 M). The EIS Nyquist plot was fit with the equivalent electrical circuit shown in Figure 3.3 and the resulting capacitance was normalized with the geometric surface area of the electrode. I_C and v were found using cyclic voltammetry.

ΔE_p was obtained by measuring the potential separation between the oxidation and reduction peaks at a scan rate of 50 mV/s. After verifying the linearity between the peak current and square root of the scan rate, k_0 was calculated according to the Nicholson method [14, 131, 100] by relating it with a dimensionless kinetic parameter, Φ, using Equation 3.4

$$k^0 = \Phi \left(\frac{\pi D_0 n F v}{RT} \right)^{\frac{1}{2}} \tag{3.4}$$

where Φ is a dimensionless parameter obtained from literature in which the values of Φ were tabulated for various peak-peak separation values in one-electron step processes [131], D_0 is the diffusion coefficient [cm^2 s^{-1}], calculated from the Randles-Sevick equation (Equation 3.5), n is the number of electrons transferred, v is the scan rate [v s^{-1}], F is Faraday's constant (96,485 C mol^{-1}), R is the universal gas constant (8.314 J mol^{-1} K^{-1}), and T is the temperature [K]. The Randles-Sevick equation at 25° C is given below:

$$D_0 = \left(\frac{2.69 \times 10^{-5} i}{n^{\frac{3}{2}} S_A C D v^{\frac{1}{2}}} \right)^2 \tag{3.5}$$

where i is the peak current [A], S_A is the active surface area of the electrode [cm^2] (calculated from Equation 3.3), C is the bulk concentration of the diffusing species [mol cm^{-3}], and D_0 is the diffusion coefficient [cm^2 s^{-1}].

The sensitivity of each electrode was calculated by taking the slope of the DPV calibration

plot and the limit of detection was calculated using Equation 3.6:

$$LOD = \frac{3\sigma}{S} \tag{3.6}$$

where σ is the standard deviation of the background current signal in PBS (0.1 M) and S is the sensitivity of the electrode.

Cells (PC12 and CTX) were seeded on the electrode surface (150,000 cells/cm2) and incubated for 7 days to allow for robust attachment with media replacement every other day. Prior to detection, cell media was removed and the cells were incubated with L-DOPA (100 μM) (Millipore-Sigma, Cat. D9628) dissolved in cell media for 2 h. Following incubation, the electrode with cells was used as the working electrode and directly connected to the potentiostat along with a Pt wire counter electrode and an Ag/AgCl (1M KCl) reference electrode. The L-DOPA medium was replaced with PBS (0.1 M) with KCl (5 mM) to release dopamine from cells. Cyclic voltammetry (CV) was previously optimized and performed (-0.2 V to 0.6 V vs. Ag/AgCl) at four scan rates (0.01 V/s, 0.03 V/s, 0.05 V/s, and 0.5 V/s). DC potential amperometry (DCPA) was performed at the observed oxidation potential of DA from the CVs (200 mV) and monitored for 500 seconds. During DCPA, KCl (100 mM) was injected to obtain the final KCl concentration in order to observe the DA release and subsequent current.

3.8 Mechanical stimulation

For mechanical stimulation, a custom setup was built that applied different surface wave stimulation to cells grown in a 12-well cell culture plate. A 20 mm diameter hole was cut into the

bottom of each well in the 12-well culture plate using a laser cutter. Gold piezoelectrics were attached to the bottom of the culture plate using an adhesive. Finally, polydimethylsiloxane (PDMS) was poured into the top of the culture plate to form a thin, liquid impermeable layer isolating the piezoelectric cell from the culture well. A custom printed circuit board (PCB) was developed that supplied voltage and ground to each piezoelectric cell. The unaligned carbon scaffold was then fixed to the bottom of the PDMS covered culture well using silicon grease. CTX cells were seeded into each well using the procedures described in 3.3. Finally, the whole device was placed into a stem cell incubator.

Mechanical stimulation was accomplished by using a Model 3800 8-Channel Programmable Stimulator (110V, 60Hz) from A-M systems, which was attached to the custom PCB using a flexible ribbon cable. Cells were allowed to adhere to the scaffold for one day before a 25 Hz, 10 V sine wave was applied to the custom PCB for the duration of the culture period (5 days).

Chapter 4

Results and Discussion

4.1 Scaffold Characterization

Unlike other highly sensitive, electrochemical biosensors which require expensive and laborious fabrication techniques, we fabricate carbon MSS by simply electrospinning an inexpensive polymer precursor solution consisting of polyacrylonitrile (PAN) and multi-walled carbon nanotubes (MWCNTs). The resulting polymer nanofibers are then pyrolyzed into carbon, known to be an ideal stem cell scaffold material due to its biocompatibility and macrostructure tunability [6]. While carbon electrodes have a wide electrochemical stability window, their sensitivity and electrochemical performance are highly dependent on their nanostructure. For example, while highly oriented pyrolytic graphitic (HOPG) carbon performs more similar to platinum, glassy carbon obtained from the pyrolysis of polymer precursors (like PAN), generally functions as a poor electrocatalytic, electrochemical sensor [142, 24].

Several key steps in the fabrication process of carbon MSS contribute to its improved electrochemical sensitivity for DA detection. The addition of MWCNTs to PAN templates and

uncoils the PAN polymer chains, leading to a more conductive and fragmented graphitic nanostructure [41, 114, 60]. Stirring the PAN-MWCNT solution further enhances this process by generating microscopic drag forces between the surface-attracted polymer chains and the bulk polymer solution [177, 101]. During the subsequent electrospinning process, shear forces between the MWCNTs and polymer chains, traveling at different velocities within the fiber jet, continue to unwind the polymer. Compression of the material, followed by stabilization at the glass transition temperature (300 °C), preserves the templated PAN molecules in their uncoiled state [41].

Finally, pyrolysis of PAN in an inert environment, at relatively low temperatures (1000 °C), retains native nitrogen within the carbon nanofiber matrix, creating additional electrocatalytic sites for DA-enhanced adsorption and electrochemical activity [10]. The fabrication process permanently embeds the favorable electroactive sites into the carbon nanostructure, an advantage over the typical carbon electrochemical sensor, which requires tedious surface functionalization or mechanical exfoliation to temporarily activate sites for detection. Since carbon MSS does not require any additional activation processes and exhibits an inherent electrochemical detectability, it is naturally advantageous for simultaneous stem cell growth and detection, where an electrode is required to retain active sites following several days or weeks in cell culture.

To tailor the scaffold's macrostructure for neural stem cell growth, we optimized several electrospinning parameters to obtain a post-pyrolysis fiber diameter of 300-500 nm, similar to the diameter of a typical neurite [99]. We also electrospun two different types of carbon MSS geometries (unaligned and aligned, Figure 4.1) to determine the effects of fiber alignment on stem cell differentiation and organization.

To tune the carbon MSS nanostructure, we tested the effect of MWCNT loading on the material properties and electrochemical performance toward DA detection. We fabricated three different carbon scaffolds with varying MWCNT loading amounts: (i) Pure PAN, (ii)

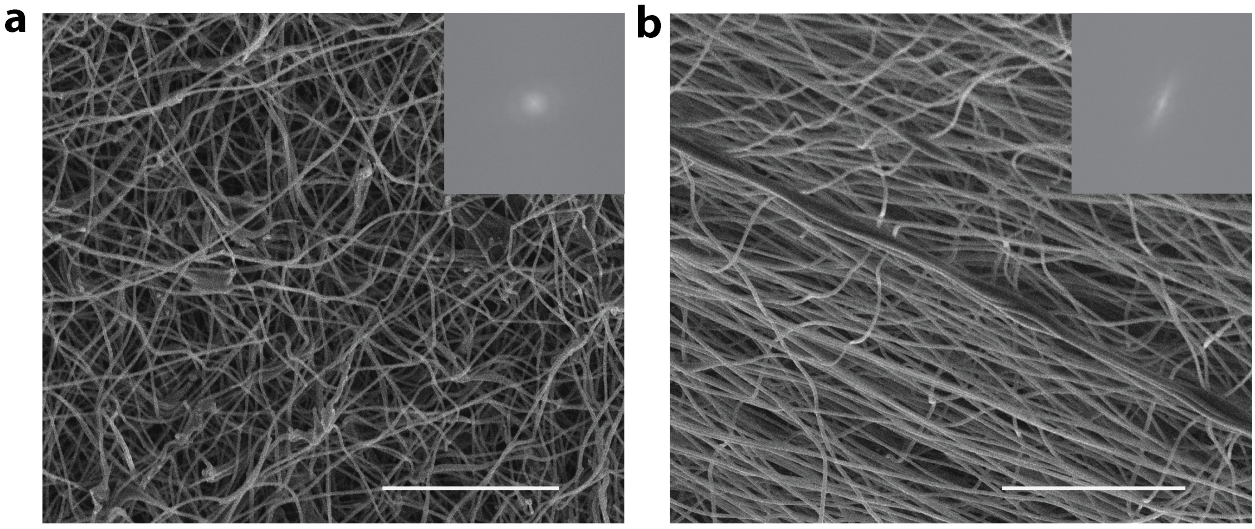

Figure 4.1: SEM images of two macrostructure fiber organizations Unaligned (left) and Aligned (right) with fast Fourier transform (FFT) insets depicting fiber alignment. Scale bar = 10 μm.

1% MWCNT/PAN, and (iii) 4% MWCNT/PAN. X-ray photoelectron spectroscopy (XPS) analysis was performed to verify that a high percentage of nitrogen groups were retained on the surface across all three types of scaffolds (Figure 4.3a). Although nitrogen defects do not directly contribute to the redox activity towards DA, they promote adsorption of DA onto the electrode surface [10].

We used Raman spectroscopy to evaluate the composite carbon nanostructure by comparing the Raman intensity between the D and G band (I_D/I_G). The D band (∼1380 cm-1) in Raman spectra represents defects in sp^2 hybridized carbon, commonly found in amorphous carbon, while the G band (1580 cm-1) is associated with the ordered sp^2 C-C vibrational mode [34]. As shown in Figure 4.3c, an average I_D/I_G ratio of 1.115 +/- 0.077 found for pure PAN indicates an isotropically amorphous carbon (i), while the addition of 1% MWCNT showed an average I_D/I_G ratio to 1.026 +/- 0.109, resulting in a less uniform carbon structure with regions of graphitic carbon embedded in bulk amorphous carbon (ii). Increasing the MWCNT content to 4% further lowered the average I_D/I_G ratio to 0.596 +/- 0.315 indicating a further increase of the graphitic carbon content (iii). Raman mapping of the I_D/I_G ratio

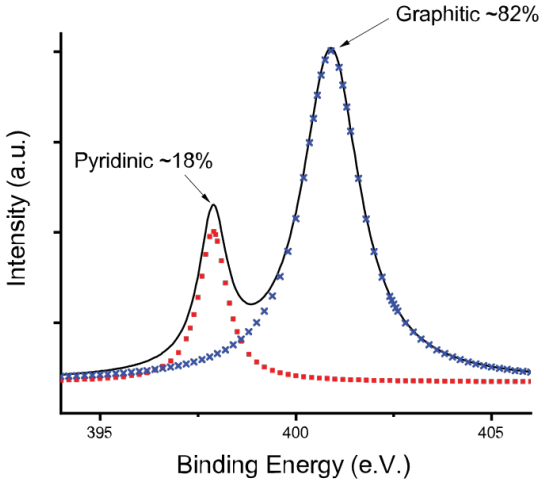

Elements	at. % in scaffold
Carbon	94.5
Oxygen	1
Nitrogen	4.4

Nitrogen Components	at. % in Nitrogen
Pyridinic-N (398.5 eV)	18.2
Pyrrolic-N (400.1 eV)	~0
Graphitic-N (401.3 eV)	81.8

Figure 4.2: Representative XPS distribution of the nitrogen groups found in the pyrolyzed carbon with table listing elemental composition.

	I_D/I_G ratio
Pure PAN	1.22 +/- 0.077
1% MWCNT/PAN	1.026 +/- 0.109
4% MWCNT/PAN	0.315 +/- 0.315

Table 4.1: I_D/I_G ratios for averaged raman spectra of each nanofiber material.

show a highly non-uniform, carbon nanostructure with 4% MWCNT loading (Figure 4.4).

4.2 Carbon MSS as an electrochemical sensor

However, despite their graphitic nature and enhanced electrical properties, pure MWCNTs are generally not suited for electrochemical applications due to the predominance of inactive basal planes over the electrochemically more favorable edge planes [123, 60]. To enhance electrochemical kinetics, one needs sufficient MWCNT loading to unwind PAN polymer chains and to feature enough graphitic edge planes while minimizing MWCNT agglomeration and basal planes. Therefore, we hypothesized that the inherently fragmented graphitic structure of the 1% MWCNT/PAN electrode detects DA more sensitively than either the pure PAN electrode, with little to no graphitic edge planes, and the 4% MWCNT/PAN

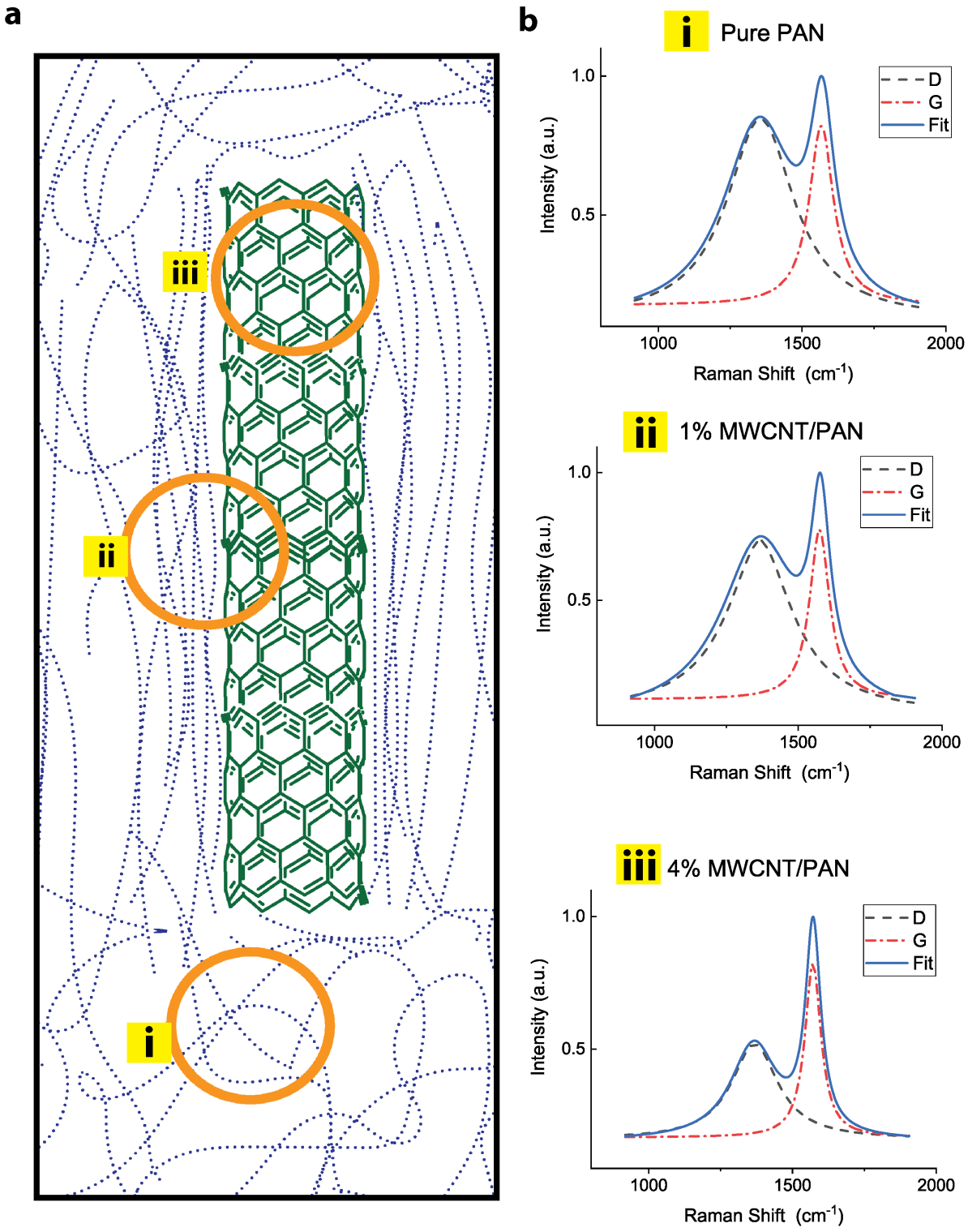

Figure 4.3: (a) Schematic illustrating the corresponding carbon nanostructure obtained from pyrolysis of (i) PAN, (ii) 1% MWCNT/PAN, and (iii) 4% MWCNT/PAN. (b) Average Raman spectra of the resulting carbon structures obtained after pyrolysis of (i) PAN, (ii) 1% MWCNT/PAN, and (iii) 4% MWCNT/PAN.

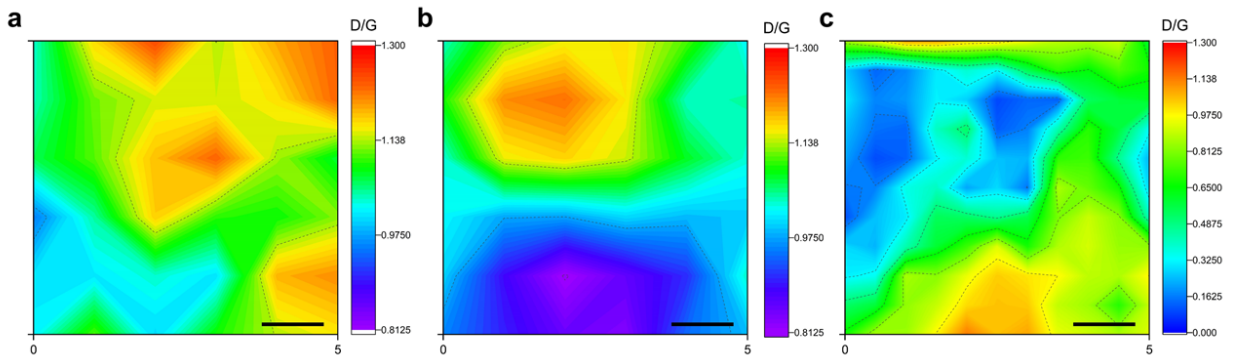

Figure 4.4: Raman map of ID/IG ratio for carbon obtained from (a) Pure PAN, (b) 1%CNT/PAN, and (c) 4%CNT/PAN showing the carbon structure distribution (scale bar = 1 μm).

electrode, that might contain too many basal planes in agglomerated MWCNTs [41, 60].

4.2.1 Electrochemical kinetics

To determine the electrochemical performance of the three different carbon fiber nanostructures, we tested the electrode materials using chemically synthesized DA. Cyclic voltammetry allowed us to determine the reaction kinetics of each material and its response to DA (Figure 4.5 and Figure 4.6). The separation between the reduction and oxidation peaks at different scan rates provides insight into the reversibility and kinetics of our system. In an ideal situation, the peak separation will remain constant regardless of the scan rate. The largest peak separation is observed for the 4% MWCNT and pure PAN electrodes (301 mV and 265 mV separation, respectively) and the lowest is observed for the 1% MWCNT electrode (60 mV separation), indicating more sluggish kinetics for the 4% MWCNT and pure PAN materials over the 1% MWCNT electrode. To quantify the electrode kinetics, the heterogeneous electron transfer rate, k_0, was estimated for each system using the procedure described by Nicholson [131, 100]. As hypothesized, the k_0 for the 1% MWCNT/PAN electrode yielded the most favorable electrochemical kinetics, with k_0 values 4 times that of the pure PAN electrodes and more than 10 times that of the 4% MWCNT/PAN electrodes (Table 4.2).

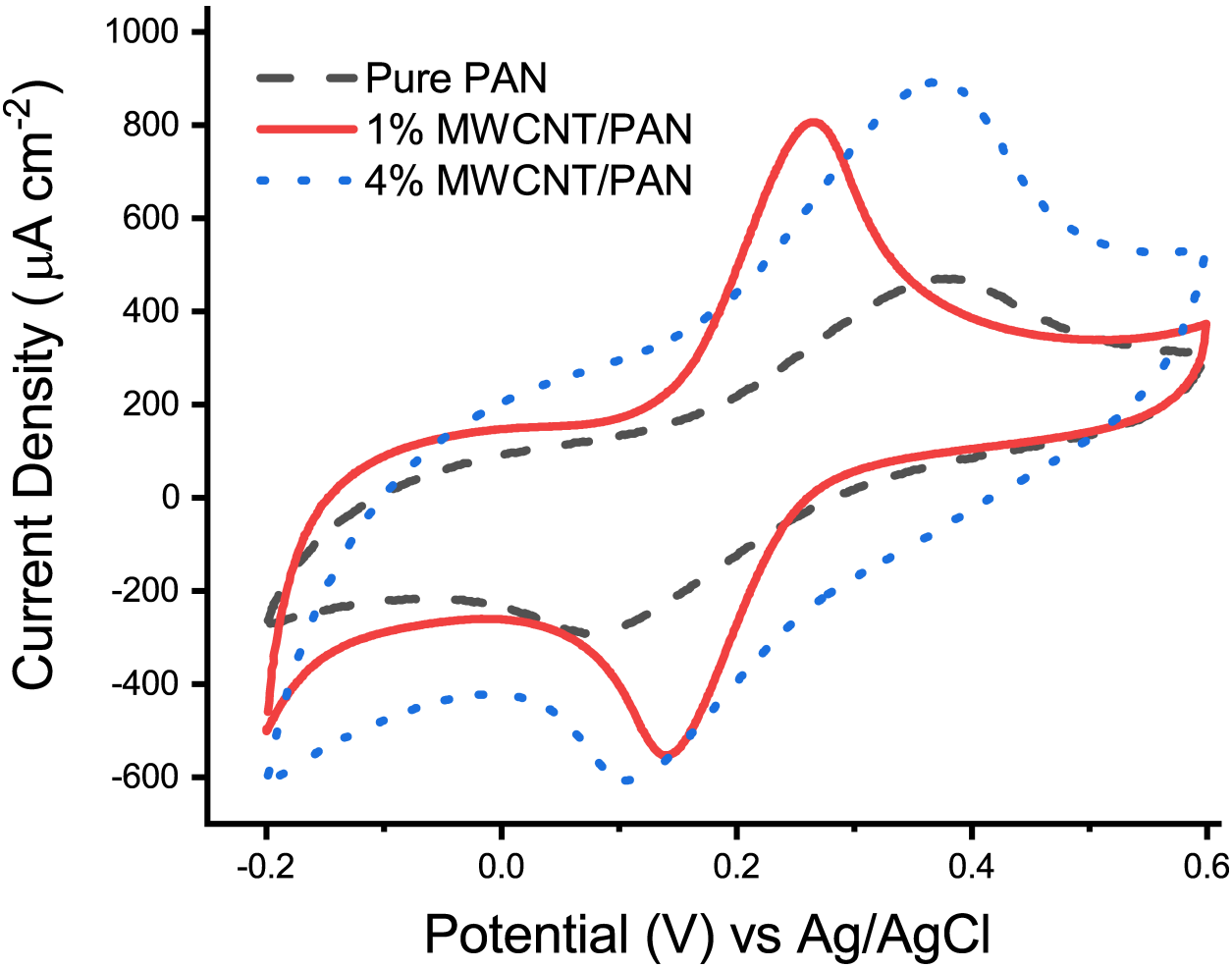

Figure 4.5: CVs of the three electrode materials with 1 mM Dopamine vs Ag/AgCl (50 mV/s). b) DPVs of the electrode material performance. Insets of linear correlations between concentration (x-axis, μM) and current density (y-axis, μA cm-2).

	ΔE_p (mV)	k_0 (cm s^{-}1)	Sensitivity μA cm^{-}2	LOD (μM)
Pure PAN	301	0.00381	1.99	1.17
1% MWCNT/PAN	60	0.0091	5.57	0.393
4% MWCNT/PAN	265	0.0021	9.58	9.7
Pure MWCNT		0.00133		

Table 4.2: Comparison of electrochemical kinetics for four electrode materials.

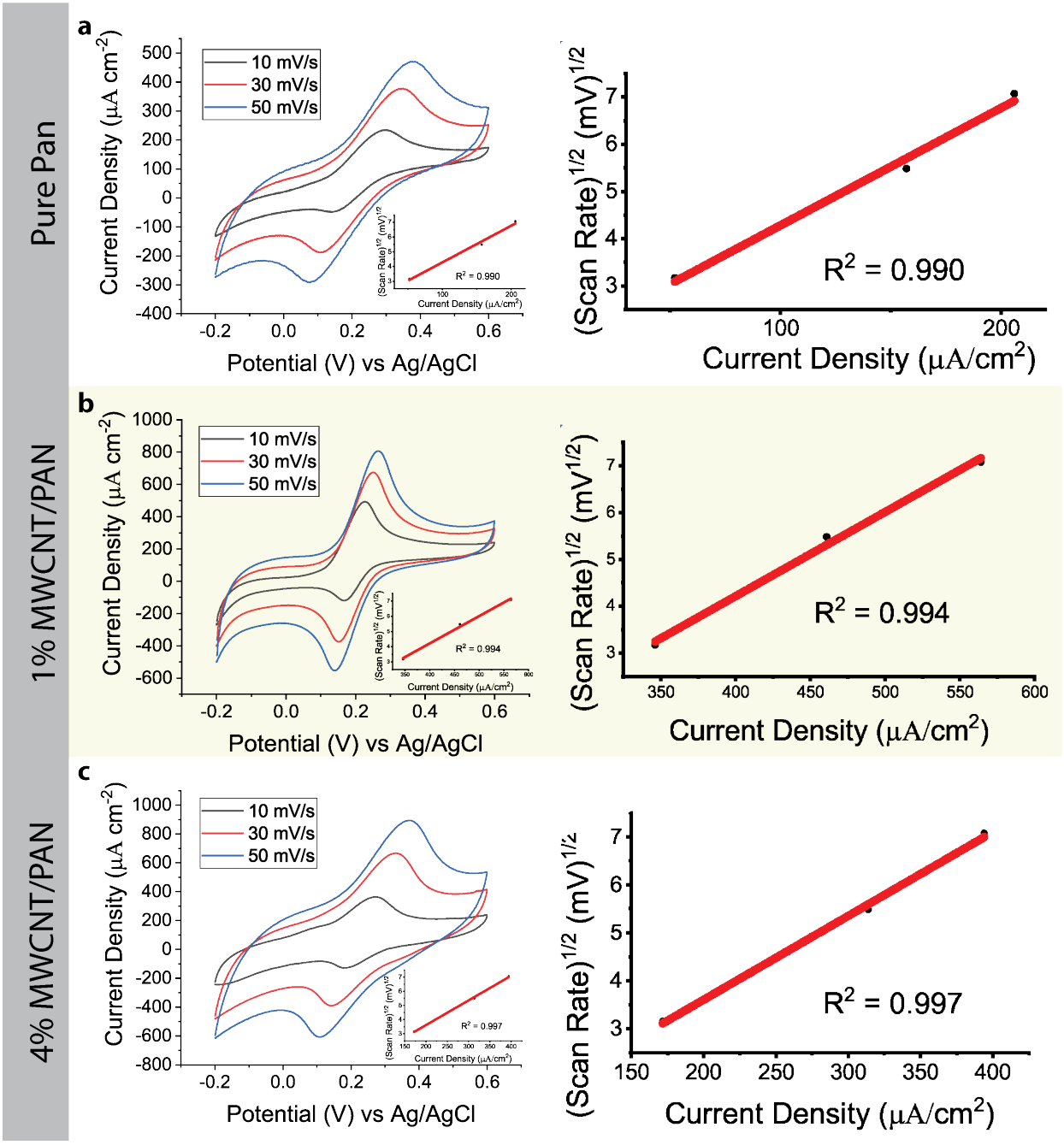

Figure 4.6: Cyclic voltammagrams of three types of electrode materials a) Pure PAN, b) 1% MWCNT/PAN, c) 4% MWCNT/PAN at scan rates ranging from 0.01 V/s − 0.05 V/s. Graphs on the right show the relationship between the peak current and the square root of the scan rate for all CV's. Linear fits for the calibration plots reveal linear response ($R^2 >$ 0.990) for all electrode materials.

Experimental parameter	Range varied	Optimized value
Pulse width	25-100 mV	100 mV
Pulse height	0.025-0.1 s	0.1 s
Step width	0.05-0.2 s	0.2 s
Step height	2.5-20 mV	5 mV

Table 4.3: Optimization of DPV parameters using Taguchi method.

4.2.2 Sensitivity and Limit-of-detection

To quantitatively analyze the sensitivity and limit of detection of each electrode material, we used differential pulse voltammetry (DPV), a highly sensitive voltammetric technique that can yield high signal-to-noise ratios at low concentrations of analyte by decoupling the capacitive, double-layer charging from the faradaic response. DPV was performed while gradually increasing the concentration of dopamine and measuring the resulting peak current (Figure 4.7). To optimize our electrochemical parameters for DPV, we used the Taguchi method to vary the experimental parameters in Table 4.3 over a defined range. A total of 9 separatee experiments were performed at concentrations ranging from 0.1 μM to 500 μM and optimal values for DPV were chosen.

The calibration plots calculated from the DPV (insets Figure **??**b) show a highly linear relationship between analyte concentration and the current peak height (R2 $>$ 0.995 for all electrode materials) allowing us to calculate the sensitivity and limit of detection of each electrode from the slope of the calibration plot and background standard deviation, (Table 4.2). The 1% MWCNT/PAN electrode exhibited a limit-of-detection (LOD) of 0.134 μM (134 nM), comparable to the detection limits observed on highly sensitive electrodes such as graphene nanoflakes (170 nM) [166], nitrogen-doped graphene (930 nM) [105], carbon nanotube-modified gold electrodes (200 nM) [210], and gold nanocup array electrodes (100 nM) [83]. The LOD on the 1% MWCNT/PAN electrode was also an order of magnitude lower than the LOD of pure PAN electrodes and 4% MWCNT/PAN electrodes (1.17 μM and 9.7 μM, respectively). The excellent performance of the 1% MWCNT/PAN electrodes over

the 4% MWCNT/PAN electrodes suggests the 1% loading yields a high ratio of atomic edge planes over basal planes, creating a highly reactive and electrochemically favorable carbon surface. As a result, we used a carbon MSS with 1% MWCNT loading to demonstrate its multi-functional capacity to promote cell growth, adhesion, and metabolite detection.

4.3 Cell adhesion and viability

We utilized mNSPCs derived from both the medial ganglionic eminence (MGE) and dorsal cortex (CTX) of a developing, embryonic mouse brain, see Figure 4.8. We also used PC12 cells, adrenal pheochromocytoma tumor cells, that can be stimulated to generate dopaminergic neuron-like cells [201]. We hypothesized that mNSPCs, which typically require a binding substrate to be either charged or coated with extracellular matrix (ECM) proteins, would not adhere to the fiber surface. We coated the surface of the scaffold with laminin, an ECM protein known to enhance adhesion, growth, and neuron differentiation, to identify whether ECM substrates are necessary for the cells to adhere and integrate to the scaffold. Surprisingly, the mNSPCs adhered well to the scaffold surface both with and without additional protein coating and exhibited a high degree of viability on all carbon MSS surfaces (Figure 4.9 and Figure 4.10).

We believe that the native nitrogen groups, along with the physical characteristics of the carbon MSS macrostructure, promote this improved mNSPC adhesion. SEM images show the topography is similar in size and geometry to the self-assembled fibrils found in the extracellular matrix (ECM) of the mature central nervous system (Figure 4.11 and Figure4.12). However, strong adhesion on the untreated MSS was not observed with PC12 cells, which commonly require a surface coating for adhesion. Consequently, for consistency between experiments, all electrode materials were coated with laminin. Interestingly, PC12s, which typically prefer a collagen coating, showed robust adhesion and spread on the laminin-coated

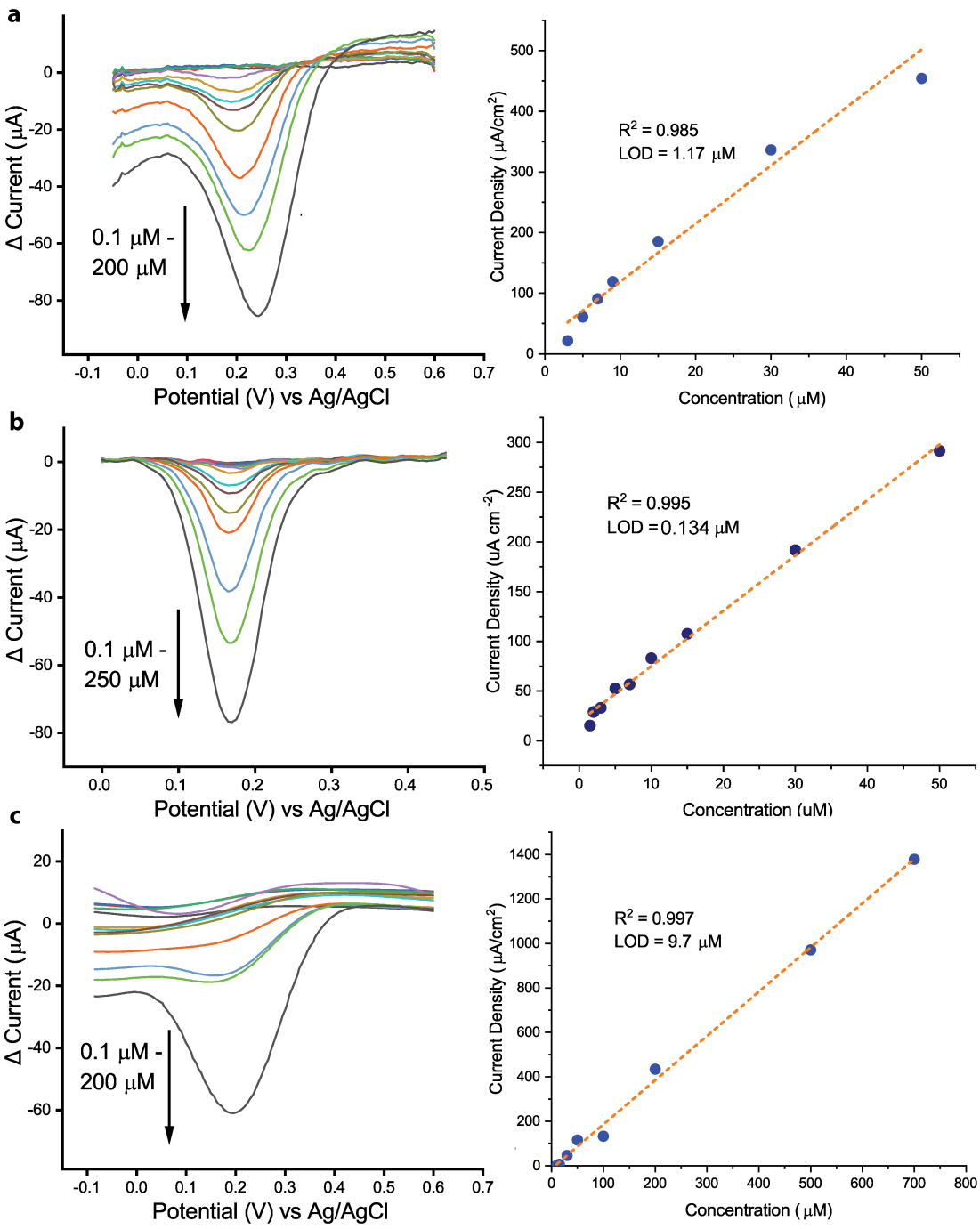

Figure 4.7: DPVs and calibration plots of a) Pure PAN, b) 1% MWCNT/PAN, c) 4% MWCNT/PAN. Linear fits for the calibration plots reveal linear response ($R^2 > 0.990$) between concentration and current peak height for all electrode materials.

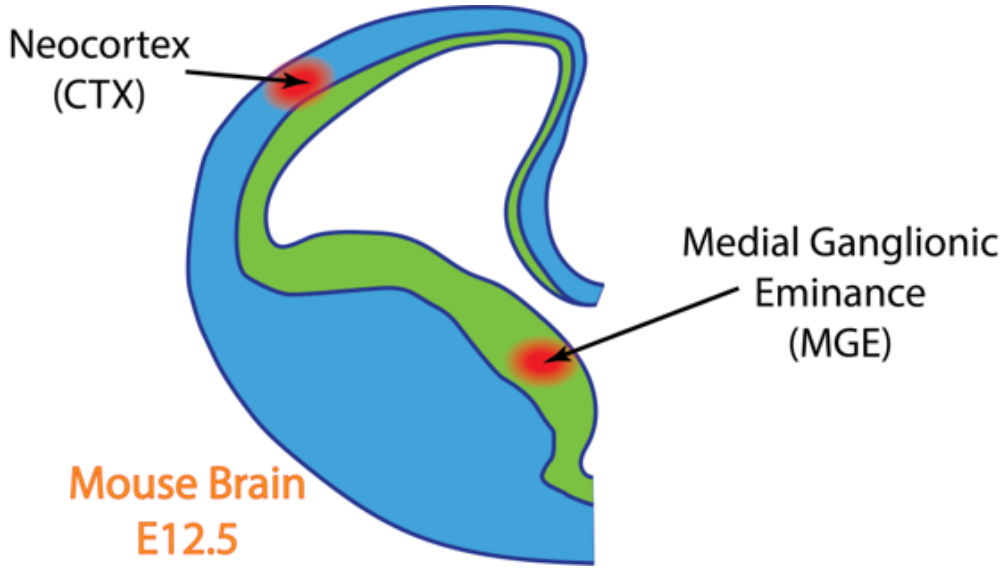

Figure 4.8: Schematic depicting where the two wildy type mNSPCs used in this experiment were derived from in the brain.

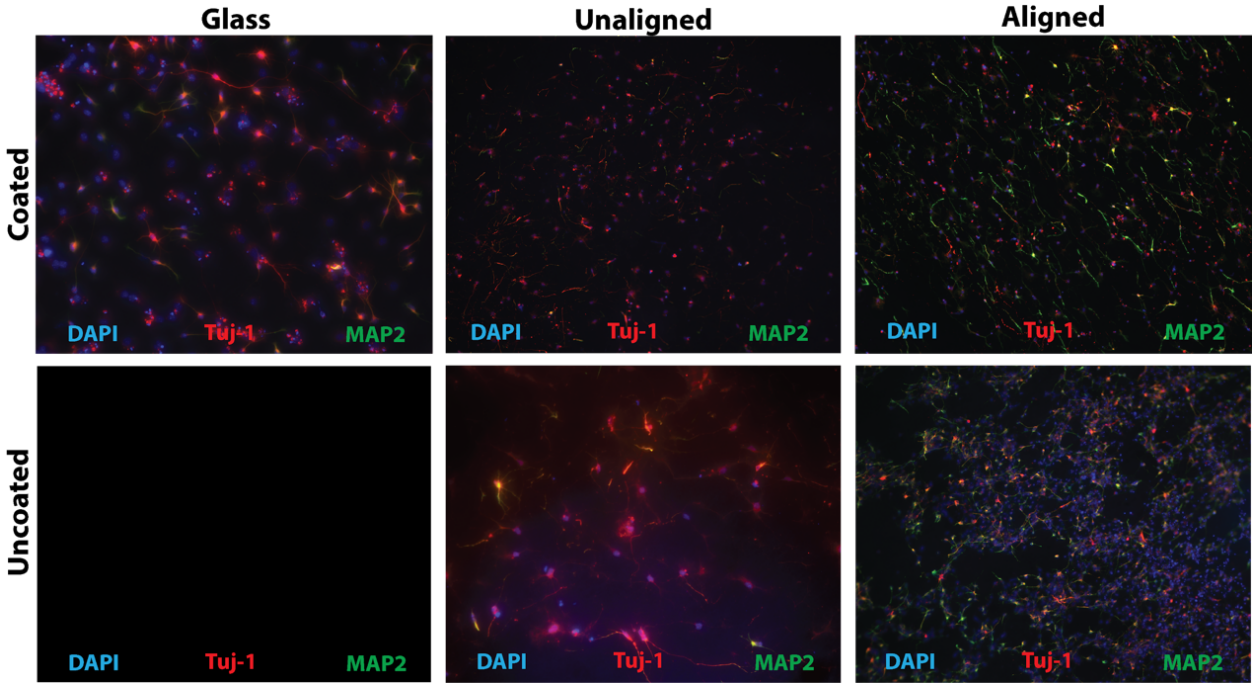

Figure 4.9: Representative fluorescent images of MGE differentiated on coated and uncoated glass, Unaligned MSS, and Aligned MSS. Cells were immunostained for two different neuronal markers, Beta-tubulin III (TuJ-1) and Microtubule Associated Marker 2 (MAP2). There were no visible cells on uncoated glass slides. On the other hand, cells adhered well to both the Unaligned MSS and the Aligned MSS.

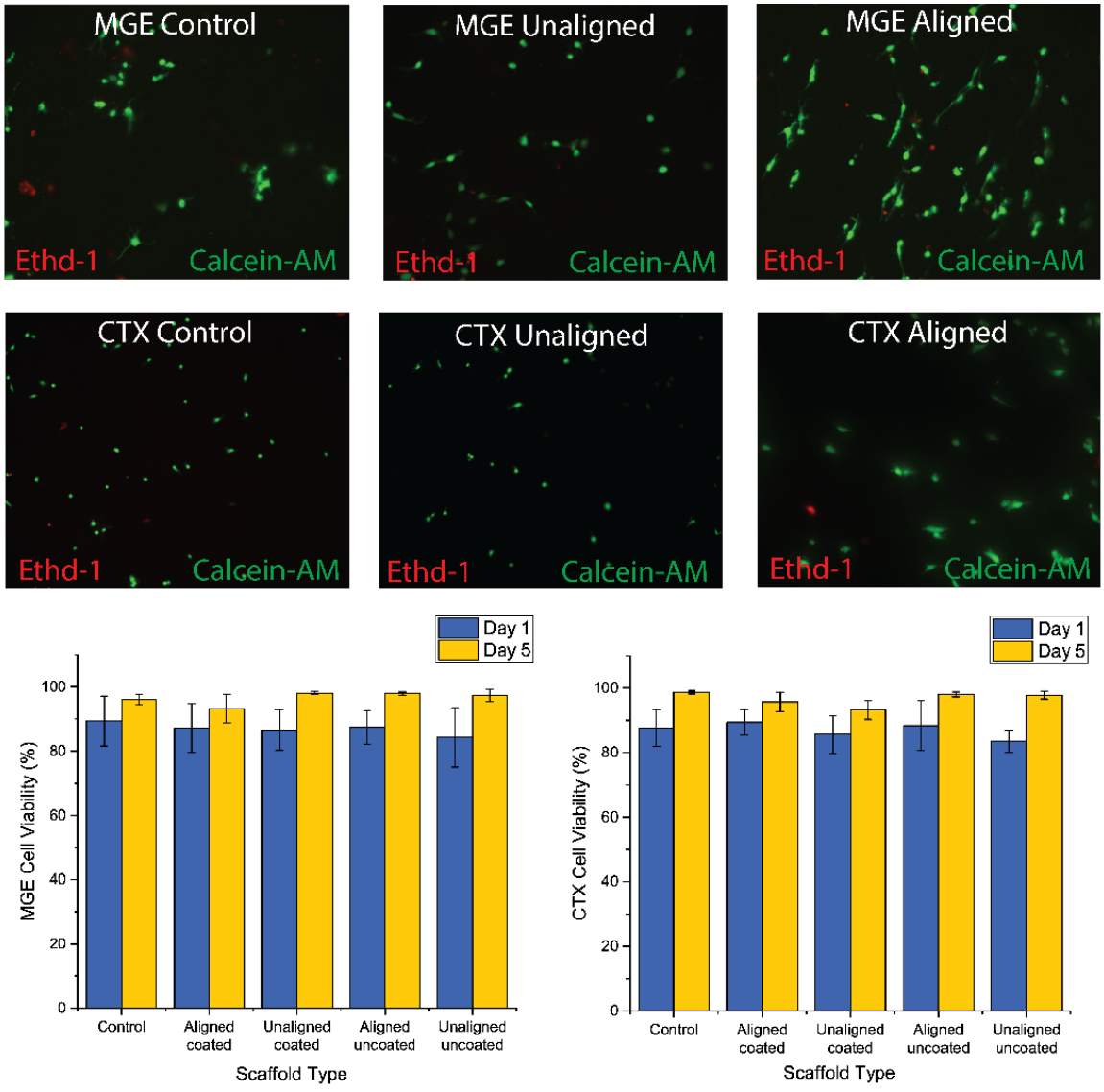

Figure 4.10: Fluorescent images (top) and quantification (bottom) of the Live/Dead assay showing little toxicity on the laminin-coated carbon MSS.

fibers compared to the laminin-coated glass (Figure 4.13), suggesting surface topography plays a critical role in guiding cell adhesion and growth.

4.4 Cell differentiation and morphology

Various biophysical cues have recently been shown to influence neural stem cell growth, behavior, and differentiation, including substrate stiffness and topography. We hypothesized that changing the nanofiber orientation (comparing unaligned and aligned topographies) would significantly alter cell fate and allow us to align cells on the carbon MSS.

4.4.1 Analysis of cell differentiation

To test our hypothesis, MGE and CTX-derived mNSPCs, were spontaneously differentiated by growth factor withdrawal on the carbon MSS for 6 days. We used immunocytochemistry, a technique that utilizes protein/antigen specific antibodies to bind and label a cellular target, to fluorescently visualize these differentiated mNSPCs towards neuronal (beta-tubulin III; TuJ-1) and astrogenic (glial fibrillary acidic protein; GFAP) specific markers [136], see Figure 4.14a. In general, quantification indicated a significant shift in the percent cells that formed astrocytes and neurons (Figure 4.14b) after differentiation on either the carbon MSS compared to the laminin-coated glass surface. For MGE and CTX cells, those grown on aligned and unaligned carbon MSS, showed a significant increase in TuJ-1 expression compared to glass controls (1.5-fold increase on unaligned carbon MSS and 2-fold increase on aligned carbon MSS). More notably, GFAP expression in CTX cells was suppressed more than 2-fold on both aligned and unaligned carbon MSS, while GFAP expression in MGE cells was only significantly suppressed on aligned carbon MSS.

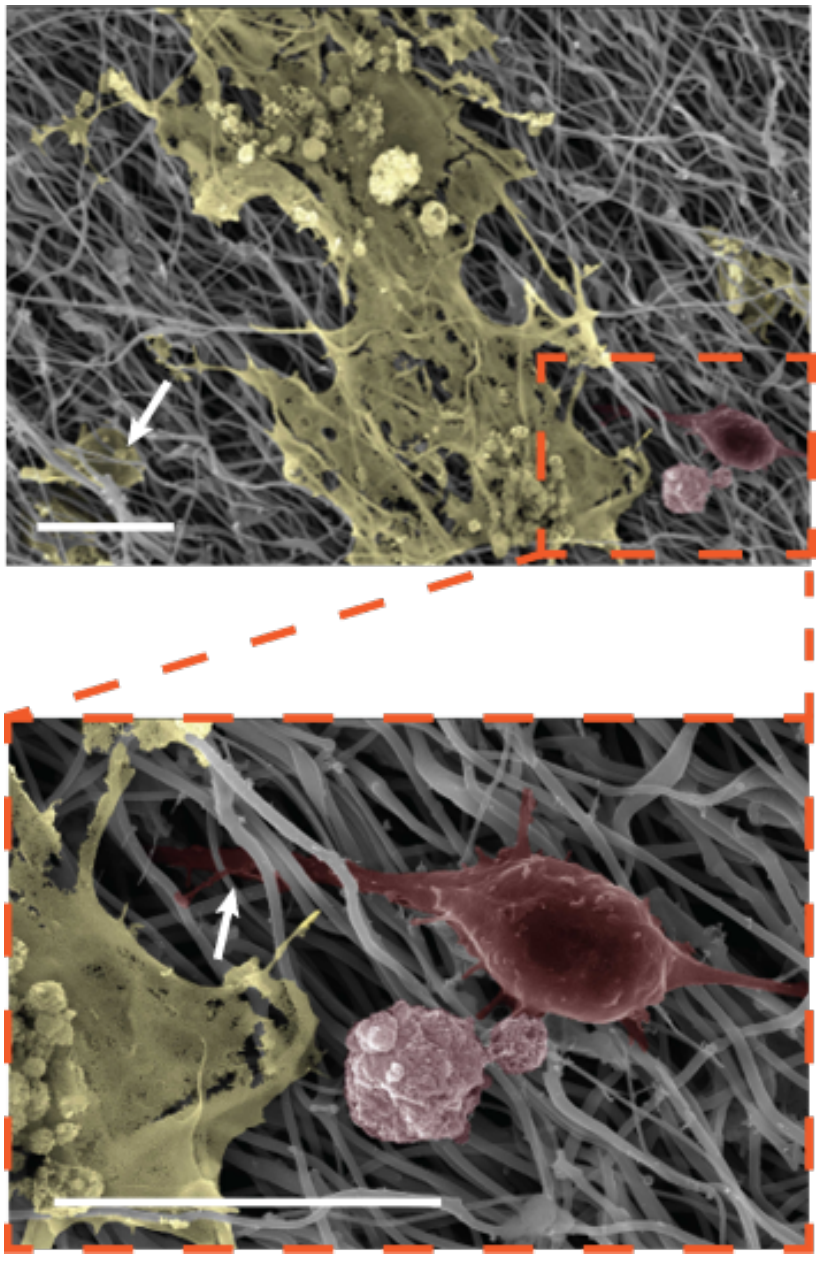

Figure 4.11: Pseudo-colored SEM images of astrocyte and neuron on aligned carbon MSS. Arrow points to axon integration into the MSS. Scale bar = 10 μm.

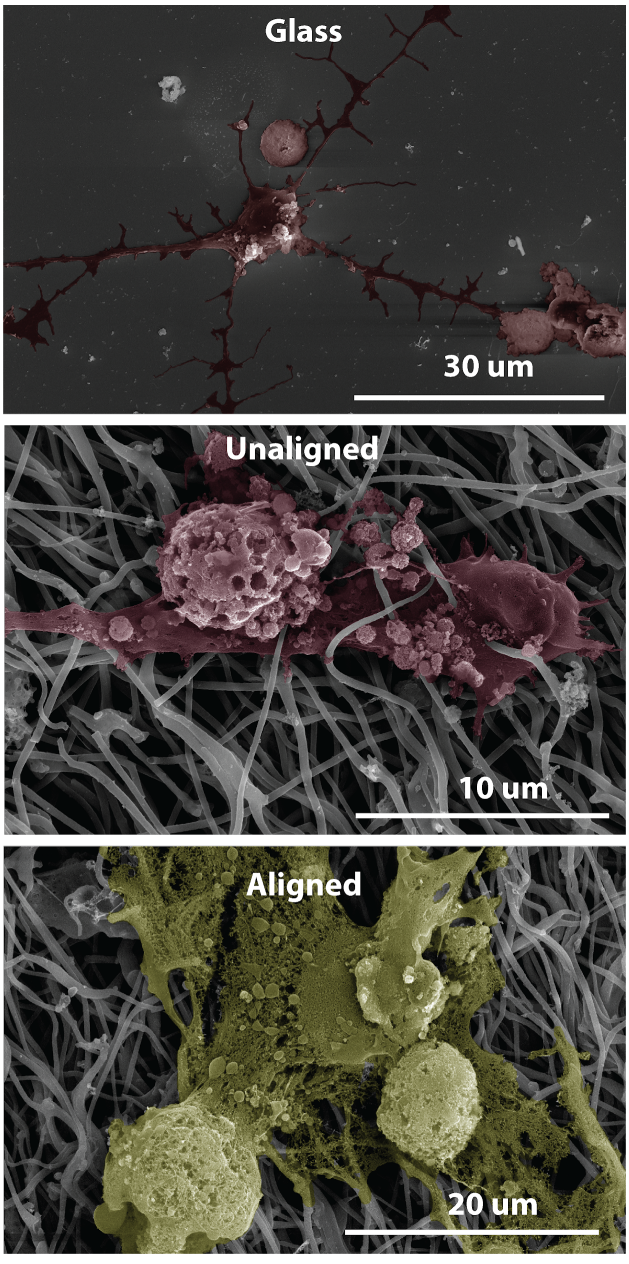

Figure 4.12: Pseudo-colored SEM images of CTX cells differentiated on Glass, Unaligned MSS, and Aligned MSS showing integration of the cytoskeleton into the nanofiber matrix.

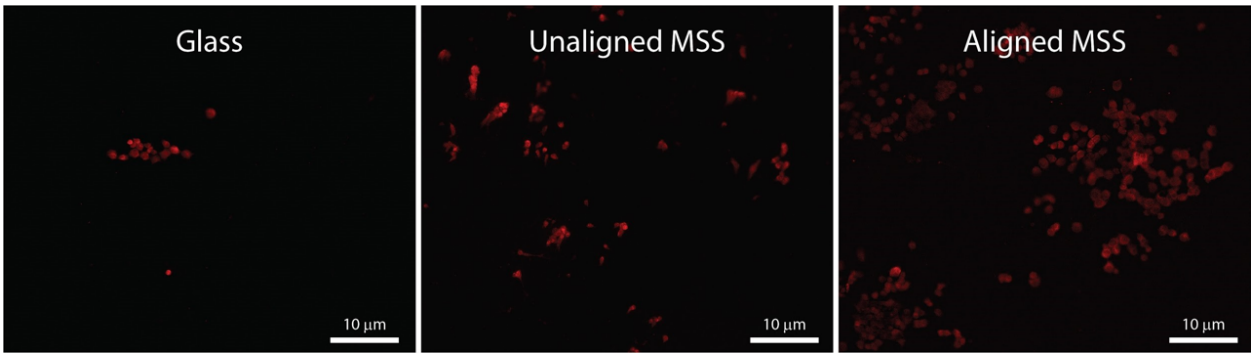

Figure 4.13: F-actin-stained (red) fluorescent images of PC12 cells showing improved adhesion and spread on the MSS surfaces compared to the glass surface.

4.4.2 Analysis of cell morphology

Further analysis revealed differences in differentiated cell morphology. The most apparent difference was observed in the organization of the cellular cytoskeletons for both neurons and astrocytes (Figures 4.15). Fast Fourier Transform (FFT) analysis is used in image processing to convert an image from the space domain to the frequency domain, allowing extraction of valuable information, such as the degree of alignment in an image. FFT analysis of the fluorescent images (inset for Figures 4.15) showed a preferential orientation of cell cytoskeletons along the nanofiber axis, agreeing with the alignment observed in FFT analysis of the SEM images in Figure 4.1 (insets for Figure 4.1).

Neuronal alignment, astrocyte roundness, and astrocyte solidity were used to evaluate cytoskeleton organization in more detail (see Materials and Methods). For both MGE and CTX cells, TuJ-1 expressing neurons exhibited a high degree of axonal alignment on the aligned carbon MSS compared to both glass controls and unaligned carbon MSS ($p < 0.01$, Figure4.16). Astrocyte circularity analysis, illustrating cell spread and coverage, shows similar behavior, where the aligned carbon MSS promoted cytoskeleton organization along the fiber axis, resulting in greater deviations from a circle (perfect circle = 1) when compared to the glass surface and the unaligned carbon MSS (Figure 4.17a and Figure 4.17b).

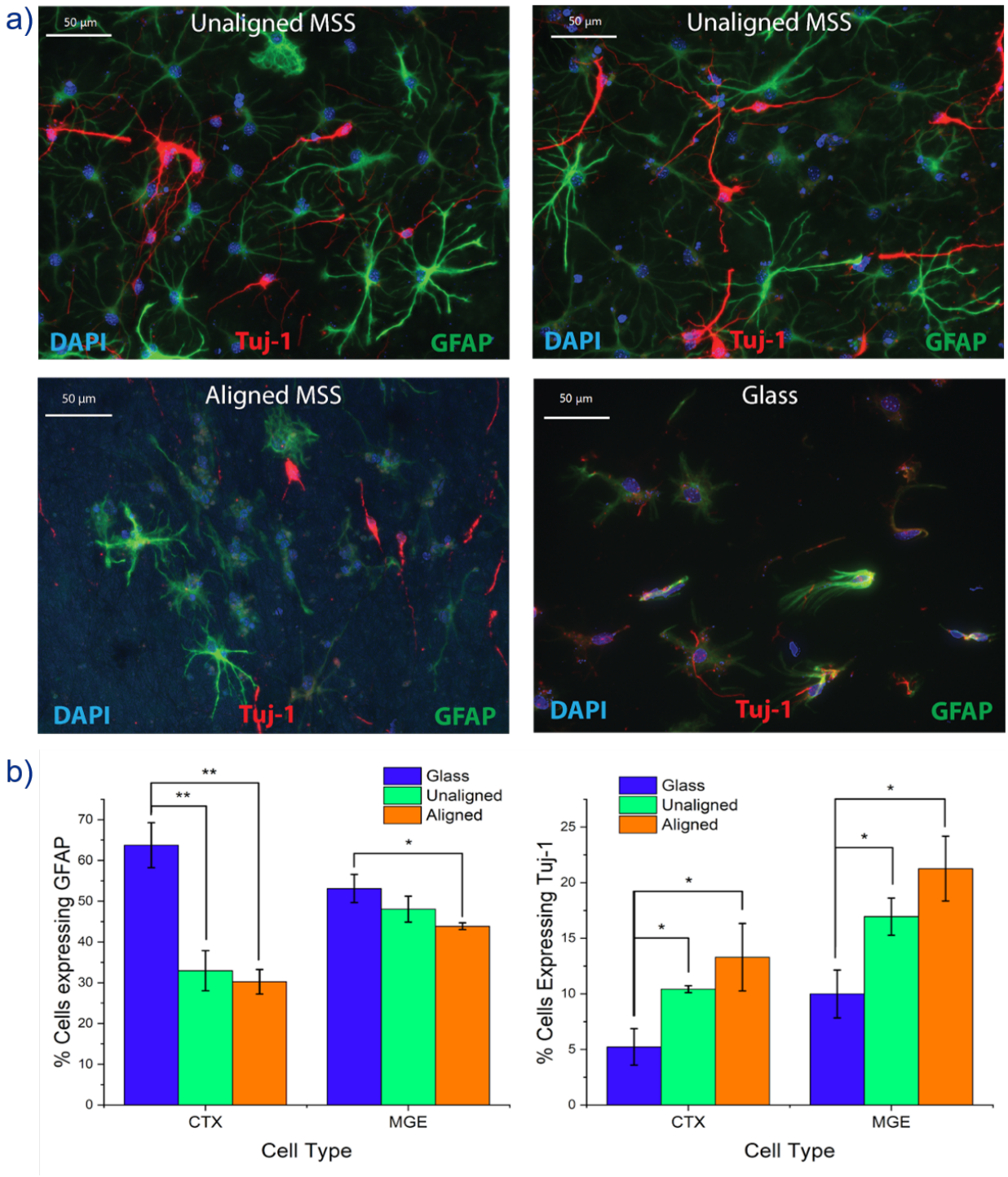

Figure 4.14: (a) Representative fluorescent images of CTX differentiated on the Unaligned MSS, Aligned MSS, and Glass. Distinct morphological observations are apparent between the figures. (b) Quantitative comparison of GFAP (left) and TuJ-1 (right) expression from CTX and MGE mNSPCs differentiated on Glass, Unaligned MSS, and Aligned MSS. (One-way ANOVA and Student's t-test with error bars representing mean +/- s.e.m, n = 3, *p < 0.05, **p < 0.01.)

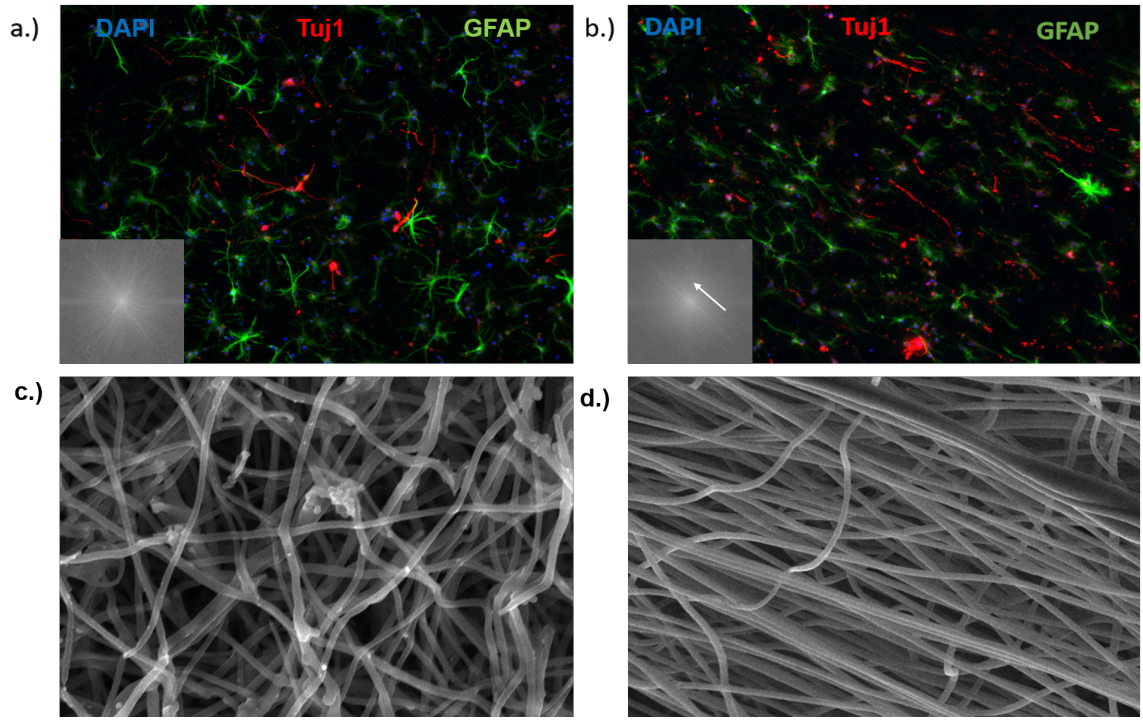

Figure 4.15: (a) Fluorescent images of mNSPCs differentiated on the unaligned MSS (left) and aligned MSS (right) with fast fourier transform (inset, rotated for clarity) performed on the cytoskeletons of astrocytes and neurons. Scale bar = 50 μm. b.) The underlying scaffold geometry, unaligned (c) and aligned (d), is shown below each fluorescent image for clarity.

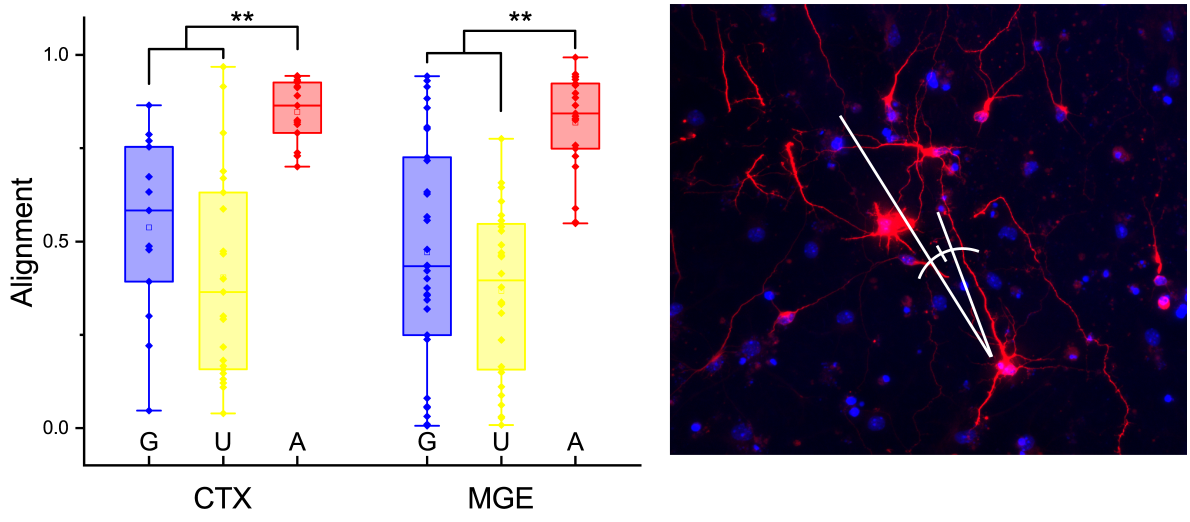

Figure 4.16: Quantitative analysis of (a) neuron axon alignment (One-way ANOVA with Tukey post-hoc test, n > 20, **p < 0.01). (b) Representation of how alignment of neuron axons is calculated in reference to an aribtrary axon.

In addition to morphological differences, astrocyte solidity can be used to evaluate cell development [126]. Astrocyte solidity on the glass surface was highly spread (Figure 4.18a), indicating a large variation of cells at different developmental stages of differentiation from early stage, protoplasmic to late stage, fibrous astrocytes (Figure 4.18c). Interestingly, lower values of astrocyte solidity with a smaller variation on both types of carbon MSSs suggest highly uniform differentiation of fibrous astrocytes ($p < 0.01$, Figure 4.18). This analysis not only illustrates the significance of how biophysical cues can promote cellular organization but also highlights the importance of topography on cell development. Our results indicate that tuning the macrostructure of carbon MSS can play a significant role in stem cell organization and differentiation and can potentially be exploited for more effective cell therapy.

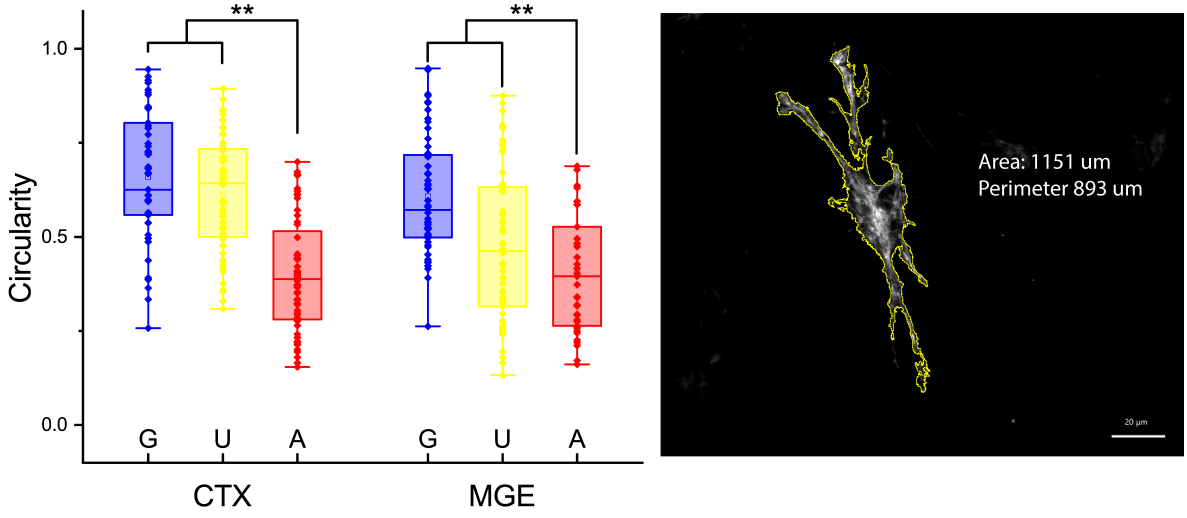

Figure 4.17: Quantitative analysis of (a) astrocyte circularity (One-way ANOVA with Tukey post-hoc test, n > 20, **p < 0.01). (b) Representation of how circularity is calculated by calculating the area and perimeter of each split channel astroctye.

4.5 Cell metabolite detection

Finally, we highlight how the current carbon MSS functions as a simultaneous cell culture platform and sensor by detecting DA from PC12 cells grown directly on the electrode surface for 7 days (Figure 4.20e). Prior to electrochemical experiments, cells were treated with L-DOPA (100 μM), a precursor converted to DA by DOPA decarboxylase in dopaminergic neurons. Following incubation, DA release was triggered by adding KCl (5 mM) for cell exocytosis.

To determine the electrochemical integrity of carbon MSS and an optimal cell seeding density onto the carbon MSS surface, we performed several experiments detecting DA released from four different PC12 cell densities (0 cells cm^{-2}, 50,000 cells cm^{-2}, 150,000 cells cm^{-2}, and 300,000 cells cm^{-2}). A cell density of 150,000 cells per square centimeter was finally chosen since it maximized the current produced (I_{pc}) while preventing cell death from overcrowding.

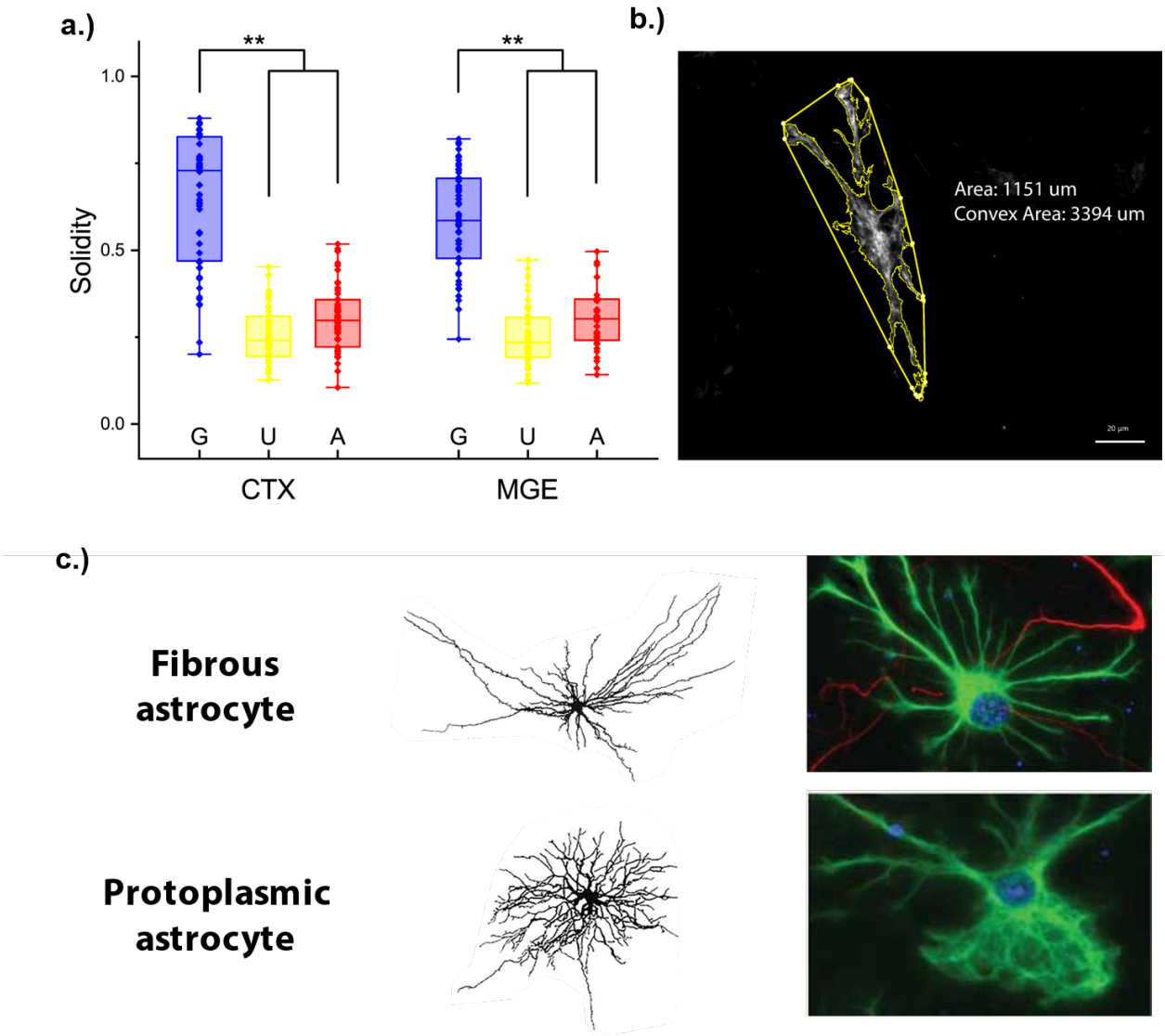

Figure 4.18: Quantitative analysis of (a) astrocyte solidity. (One-way ANOVA with Tukey post-hoc test, n $>$ 20, **p $<$ 0.01). (b) Representation of how solidity is calculated by calculating the ratio between the area and convex hull of each astrocyte. (e) Fibrous and protoplasmic astrocytes depicted schematically side-by-side with corresponding fluorescent images.

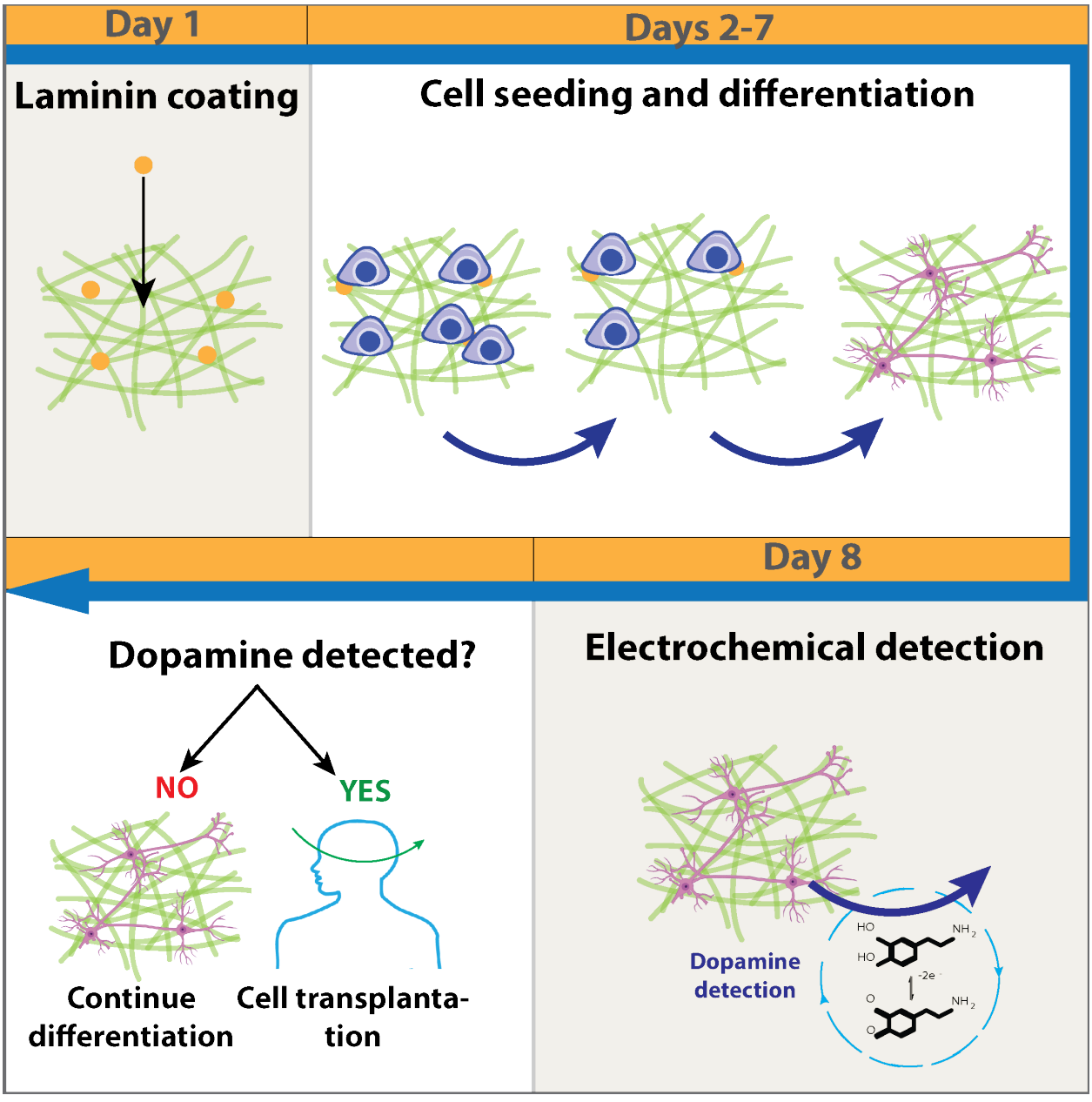

Figure 4.19: Schematic graphic depicting timeline for electrochemical monitoring of dopamine and potential application.

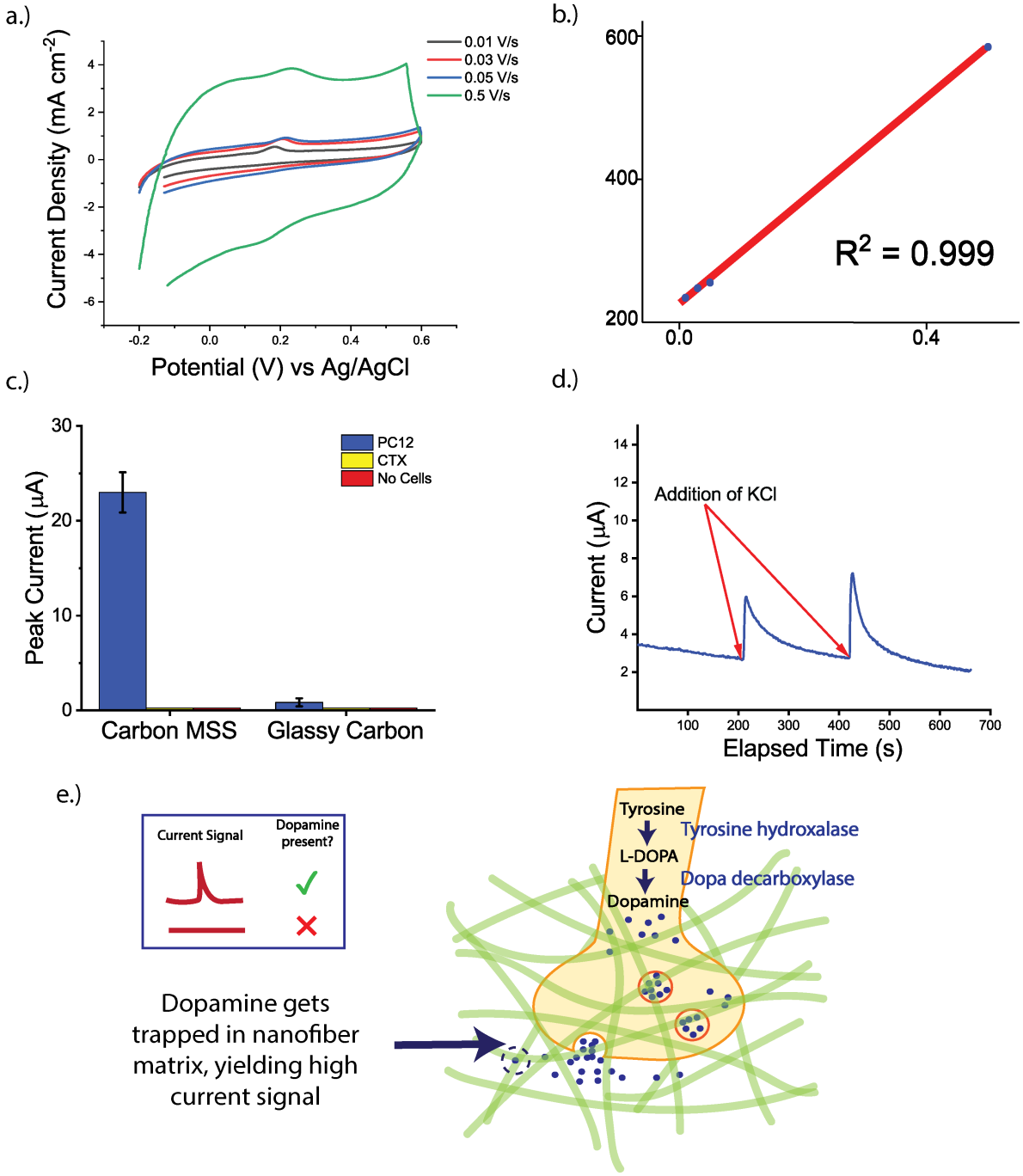

Figure 4.20: Application of the carbon MSS. (a) Cyclic voltammograms for PC12 cells grown on the carbon MSS following L-DOPA pretreatment and depolarization with 5 mM KCl. The reverse peak is not observed at scan rates below 0.5 V/s. b.) Calibration plot of the linear correlation between the scan rate (x-axis, V/s) and current density (y-axis, μA cm^{-2}). (c) DCPA of PC12 cells on carbon MSS following depolarization by 100 mM KCl. (d) Peak currents from cyclic voltammograms of PC12 and CTX cells grown on carbon MSS and GC substrates (n = 3). (e) Schematic diagram depicting how the MSS matrix traps DA preventing diffusion into the bulk medium allowing efficient electrochemical detection.

Following 7 days of culture on the carbon MSS in minimum maintenance media and L-DOPA pretreatment (2 hours), cyclic voltammetry showed distinct oxidation peaks at all scan rates (0.01 V/s - 0.5 V/s). However, no reduction peaks were observed at scan rates below 0.5 V/s, likely due to cellular reabsorption of the oxidized DA (Dopamine-o-quinone) at a rate faster than the reverse sweep [67, 157]. Once the scan rate was increased to 0.5 V/s, a reduction peak was restored, allowing for analysis of the electrochemical kinetics (Figure 4.20a).

We compared ΔE_p values for the carbon MSS when used as a simultaneous cell culture platform versus the bare carbon MSS electrode and surprisingly, only observed a minor increase in ΔE_p, from 60 mV to 74 mV (Figure S2d), significantly less than that observed with other stem cell sensor platforms (e.g. an increase of 100 mV between bare gold and cell-covered gold electrode surfaces) [83]. We compared the CVs of DA released by PC12s grown on carbon MSS versus those grown on glassy carbon electrodes. PC12 cells on the carbon MSS electrode yielded peak current densities of over 20 μA while current densities on glassy carbon electrodes barely reached 1 μA (Figure 4.20c). This peak current was also an order of magnitude higher than current state-of-the-art cell metabolite sensors, such as pyrolyzed 3D glassy carbon scaffolds [6] or large-scale gold nanocup arrays [83]. While the same density of PC12 cells was seeded onto the carbon MSS and GC surface, the clear and detectable signals on the carbon MSS show the efficiency of the nanofiber matrix in capturing, retaining, and preventing DA molecules from diffusing into the bulk solution, schematically illustrated in Figure 4.20d. The linear relationship observed between the scan rate and current density ($R2 > 0.999$, inset for Figure 4.20a) indicates adsorption-based kinetics, verifying that DA is trapped in the nanofiber matrix and potentially increasing the current signal.

To further verify our results, we used DC potential amperometry (DCPA), where a current is continuously monitored at the oxidation voltage of DA, determined from the CV (+200 mV vs Ag/AgCl) (Figure 4.20b). Following membrane depolarization by the addition of KCl (100 mM), a spike in current was observed, indicating the release and immediate oxidation of

DA from PC12 cells grown on the carbon MSS surface. We also compared CVs and DCPAs of CTX cells cultured on both carbon MSS and GC substrates. For both CV and DCPA experiments, we found no detectable current levels compared with no cell controls, indicating no DA was released from these cells (Figure 4.21). The results were corroborated using an ELISA assay (Figure 4.22) which verified that DA was released from PC12 cells and not from CTX cells.

Despite substantial surface coverage by cells, our results show that electrochemical performance is not inhibited on the carbon MSS scaffold, likely due to the abundance of electrochemically active sites deep within the carbon MSS nanofiber matrix. This thorough investigation shows the versatility of carbon MSS as a simultaneous cell scaffold and sensor.

4.6 Mechanisms behind alignment

As discussed in Section 2.1.2, the response a cell has to passive forces in its environment requires a mechano-transducer to transform the force felt by the cell into a biochemical signal. The differences in cytoskeletal morphology associated with cells grown on aligned MSS compared with those grown on unaligned MSS (see Section 4.4) led us to question what mechanotransduction mechanism might be mediating the mNSPCs reaction to the scaffold topography. While there were many potential mechanisms that might contribute to this effect, we hypothesized this effect came from one or both of the following mechanisms:

1. The Piezo1 mechanosensitive ion channel: The Piezo1 mechanosensitive ion channel is a pore-forming membrane proteins that gates in response to mechanical stimuli exerted on the cell membrane. Mechanically sensitive ion channels function by allowing ions or other solutes to flow across cell membranes by switching from open to closed conformations. This channel is considered one of the main molecular force sensors in

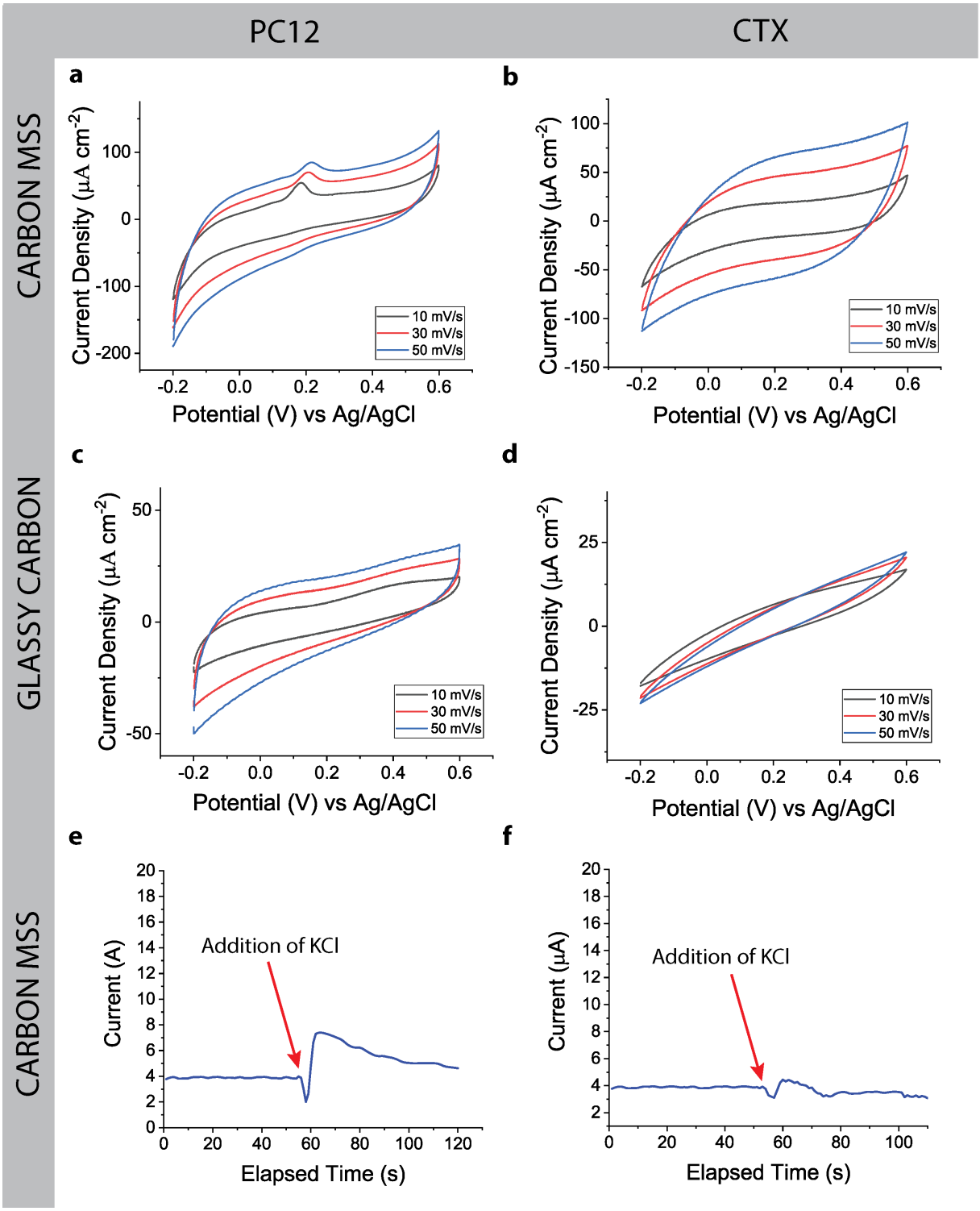

Figure 4.21: a-d) Cyclic voltammagrams obtained following 2 hr L-Dopa pre-treatment and cell exocytosis from CTX and PC12 cells grown for 6 days on the carbon MSS and the Glassy Carbon substrates. e,f) DC amperometry graphs performed on CTX and PC12 cells on the MSS at 200 mV.

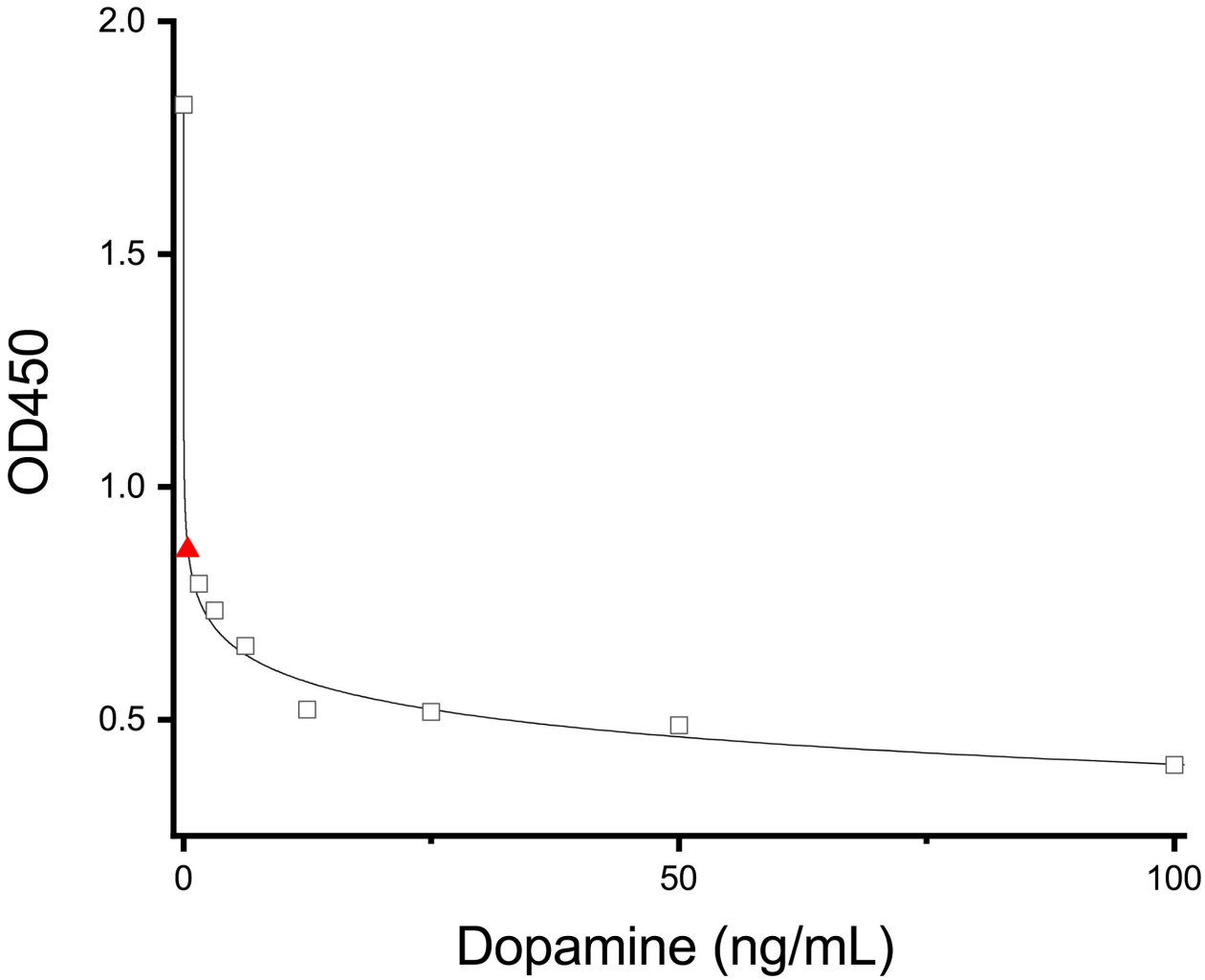

Figure 4.22: ELISA assay to verify dopamine released by PC12 cells (Δ) after 2 h of L-DOPA incubation after dilution (5-fold). ELISA (BioVision, Cat. K4219) was performed to verify dopamine released by PC12 cells and not CTX cells. Prior to electrochemical detection (Experimental Section G), sample (1 mL) was collected to analyze if the L-DOPA pre-treatment and subsequent exocytosis contained dopamine. Dopamine conversion of L-DOPA was verified from the sample collected from PC12 cells grown on the MSS while sample collected from the CTX cells showed no trace of dopamine (OD450 $>>$ 2).

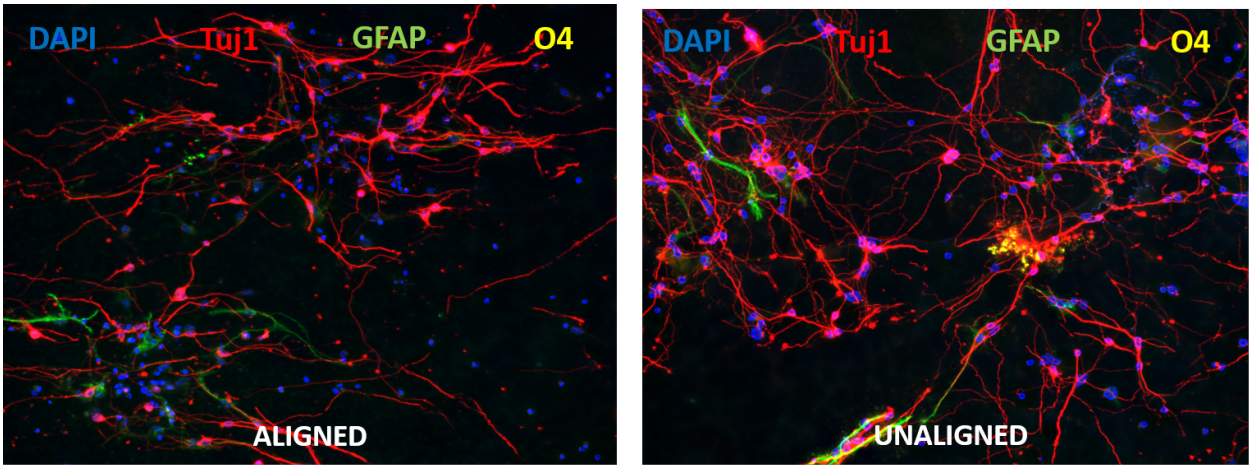

Figure 4.23: Representative fluorescent images of MGE Piezo-1 knockout cells on aligned and unaligned scaffolds.

mammalian cells [156].

2. Laminin-binding integrins: Cells bind to the ECM via integrins, transmembrane proteins that form a bridge between components of the extracellular matrix and intracellular focal adhesions that connect to the cell's actin cytoskeleton. Previous research has shown that laminin ECM coatings play a role in mediating both cyclic forces and migration of mouse NSPCs, suggesting laminin-binding integrins might be mechanotransducers for mouse NSPCs ([8, 36]).

We sought to determine the role of Piezo1 on cell alignment by comparing Piezo1 knockout (KO) to wild type (wt) mNSPCs grown on aligned and unaligned scaffolds, see Figures 4.23 and 4.30. Analysis of neural alignment shows no significant difference between alignment of nueral axons in Piezo1 knockout and wild type mNSPCs grown on aligned scaffolds. However, both Piezo1 KO and WT mNSPCs exhibited significant axonal alignment on aligned scaffolds when compared to alignment on unaligned scaffolds. This indicates that Piezo1 ion channel is not responsible for the alignment we see on the scaffold.

The next thing we wanted to test was the whether the mechanism for mechanotransduction might be due to laminin binding integrins, since most of our scaffolds were coated with

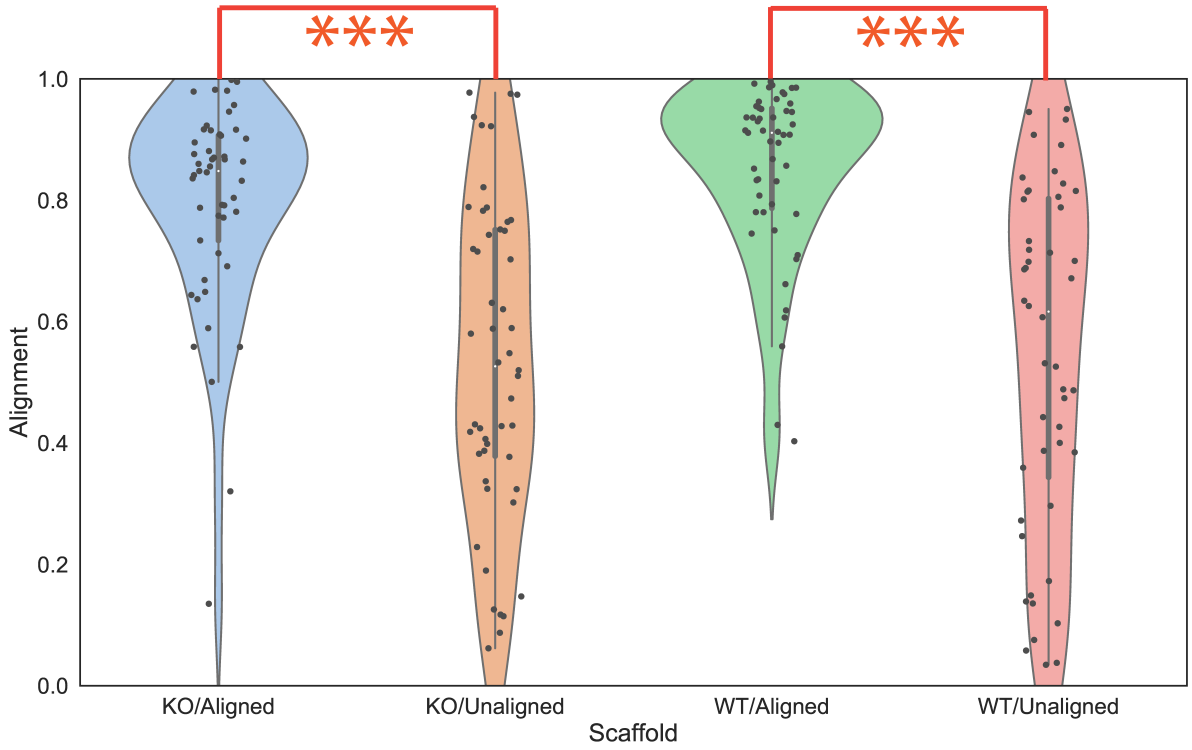

Figure 4.24: Quantitative analysis of alignment of Piezo-1 knockout and wild type MGE mNSPCs. (One-way ANOVA with Tukey post-hoc test, n = 50, ***p $<$ 0.001).

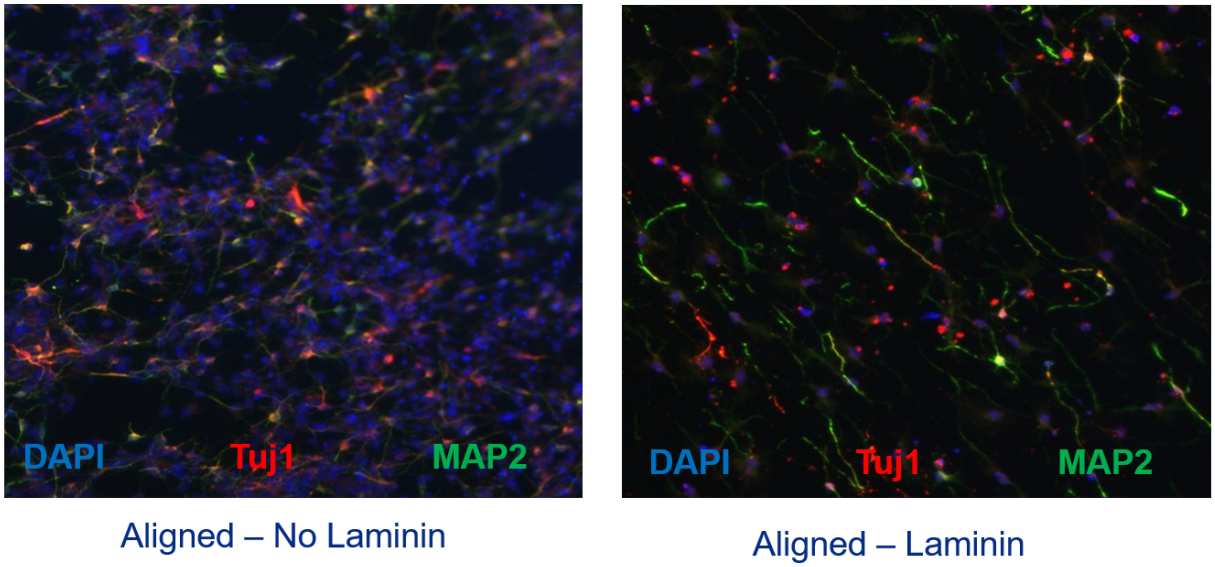

Figure 4.25: Representative flourescent images of mNSPCs grown on aligned scaffolds with and without Laminin coating.

laminin. Before the experiment with laminin, we first ascertained that there was sufficient adhesion even on uncoated scaffolds (see Figure 4.9). We compared growth of mNSPCs on both aligned and unaligned scaffolds coated with and without laminin, see Figures 4.25 and 4.26. While analysis of neural alignment was significantly different on unaligned vs. aligned scaffolds coated with laminin, there was no significant difference in alignment on uncoated scaffolds. These results indicate that laminin binding integrins might play a role in mediating cell alignment on the aligned scaffolds. However, to understand whether this effect is actively due to laminin binding integrins rather than a passive effect from better adhesion on the scaffold, the experiments should be repeated with a different type of coating on the scaffold, such as fibronectin. Since fibronectin similarly facilitates adhesion on the scaffold, it could be used to test whether the lack of alignment on the uncoated aligned scaffold might be due to insufficient adhesion by the cell cytoskeleton.

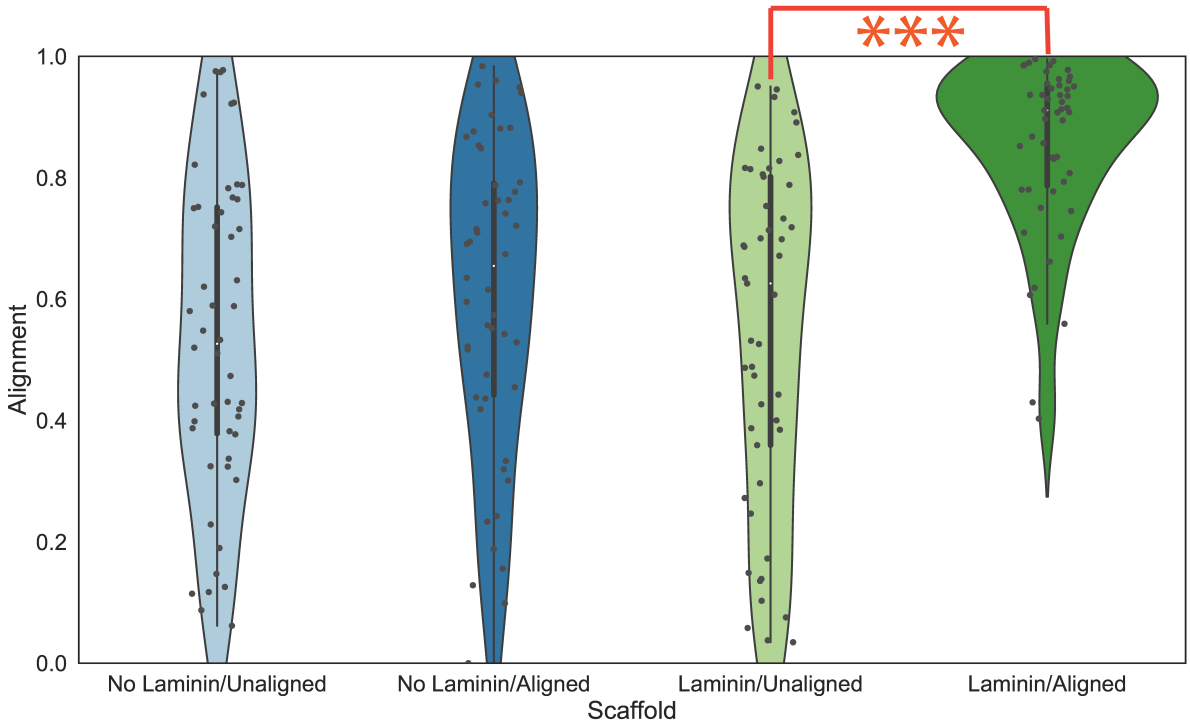

Figure 4.26: Quantitative analysis of mNSPCs grown on aligned scaffolds with and without Laminin coating. (One-way ANOVA with Tukey post-hoc test, n = 50, ***p < 0.001).

Figure 4.27: Image of bending pyrolized carbon MSS.

4.7 Stimulation on the carbon MSS

4.7.1 Mechanical stimulation using piezoelectric effect

One of the goals when developing the nanofibrous carbon MSS was to use the scaffold for mechanical stimulation as well as for electrical stimulation. Generally, conductive materials are not ideal for mechanical stimulation since they tend to be hard and brittle. Electrospinning of polymer nanofibers has the added benefit of creating a flexible, material-like structure that is excellent for applications that require constant mechanical stress, see Figure 4.27.

To show that the scaffold was also able to accomplish mechanical stimulation, we built a piezoelectric stimulation device into a 12-well cell culture plate, see Figure 4.28. To build this, a hole was cut out in the bottom of the culture wells and gold piezoelectric actuators, covered in thin PDMS membrane, were attached. This created a liquid tight barrier while still allowing cells to experience the waveform. The carbon MSS was then attached to the bottom PDMS membrane and cells seeded accordingly. The setup was then rested on a custom fabricated electronic circuit (Figure 4.29 which attached to an 8-channel programmable stimulator via a flat ribbon cable. The stimulation device was placed inside a stem cell incubator while the programmable stimulator remained outside. The circuit was fabricated such that different stimulation conditions could be applied to each set of culture wells.

After seeding, stem cells were allowed to attach onto the scaffold for one day. The second day of culture, a 25 Hz, 10 V sine waveform was applied to the piezoelectric device for the duration of the culture period (5 days).

Figure 4.30 shows representative fluorescent images of the cells on the unaligned scaffolds following 5 days of mechanical stimulation. The images indicate significant morphological differences between cytoskeltons of GFAP and Tuj expressing cells. In particular, astrocyte processes appeared significantly longer and more fibrous on stimulated scaffold. To analyze this more quantitatively we applied similar analysis described in section 4.4 and looked at astrocyte cytokeleton circularity and solidity. Circularity gave an indication of the length of astrocyte processes and solidity gave an indication of astroctyte type.

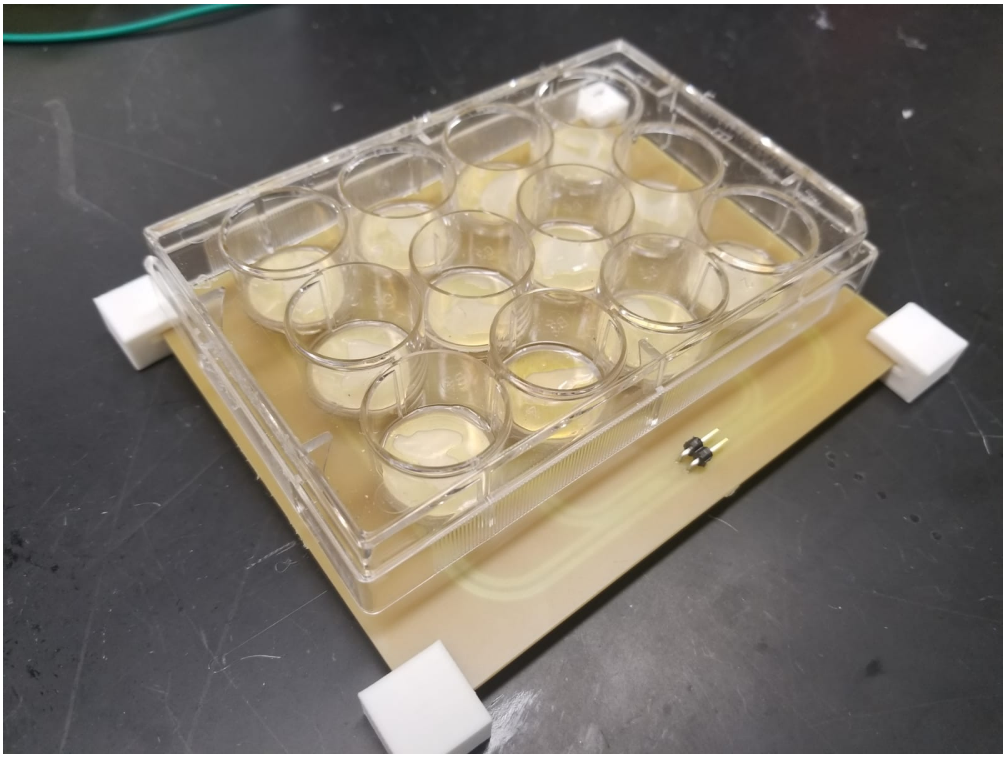

Figure 4.28: Top view of piezoelectric stimulator device with 12-well plate for stem cell culture attached. Each well has a separate gold piezoelectric device attached to the bottom.

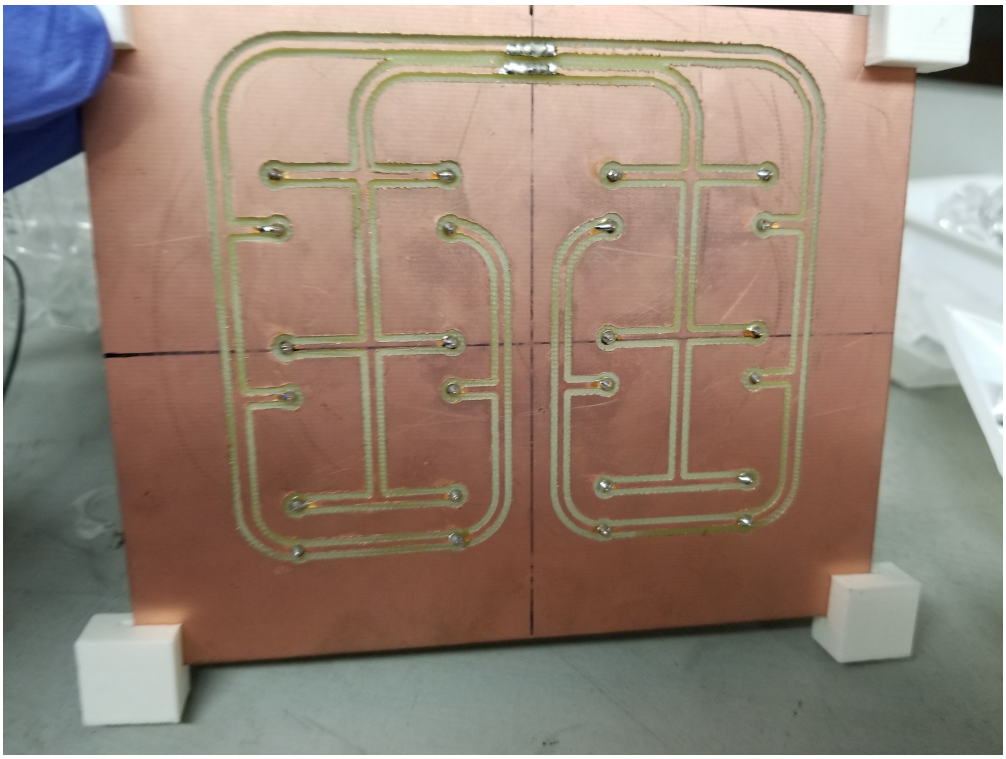

Figure 4.29: Bottom view of the circuit for the piezoelectric stimulator device. Each stimulator for all 12 wells is attached to a single input.

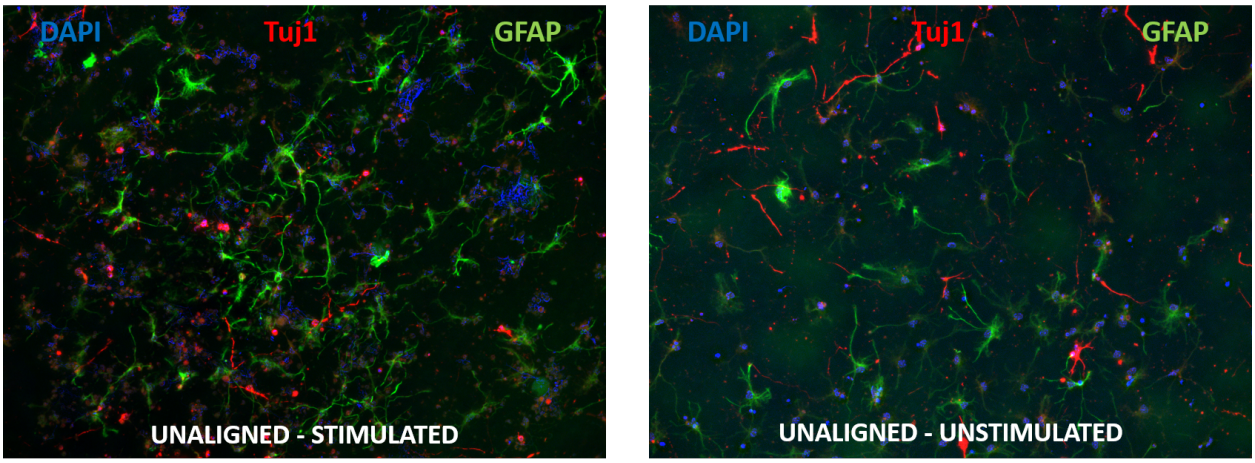

Figure 4.30: Representative fluorescent images of stimulated and unstimulated mNSPCs.

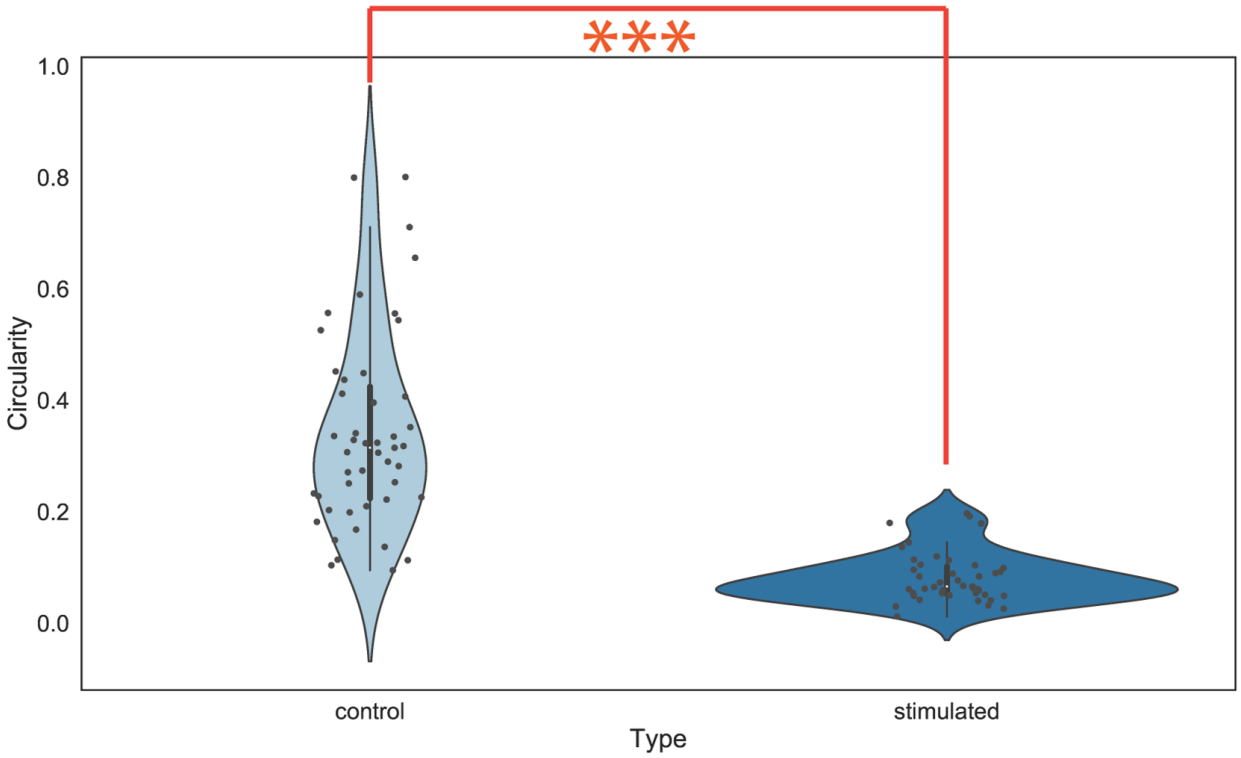

Figure 4.31: Quantitative analysis of cell circularity on stimulated and control mNSPCs. (One-way ANOVA with Tukey post-hoc test, n = 50, ***p < 0.001).

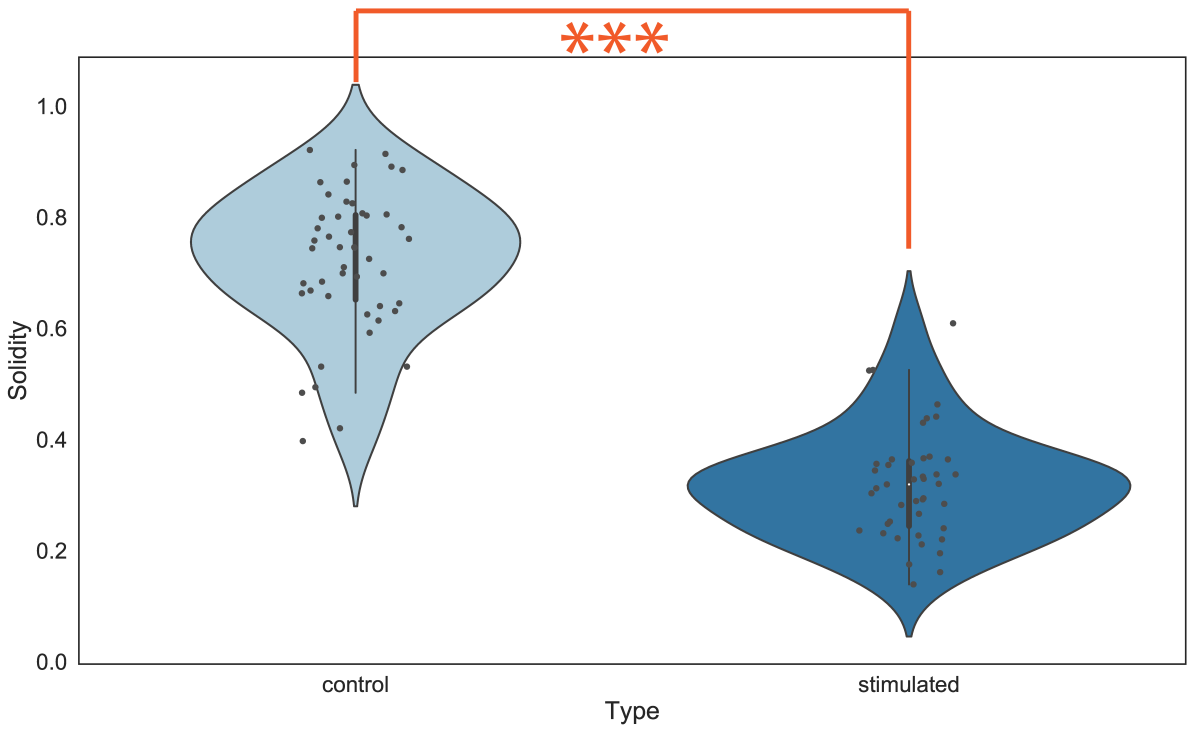

Figure 4.32: Quantitative analysis of cell solidity on stimulated and control mNSPCs. (One-way ANOVA with Tukey post-hoc test, n = 50, ***p $<$ 0.001).

Chapter 5

Conclusion and future work

Developing material solutions for different aspects of stem cell therapy (including cell growth, organization, characterization, and monitoring) is a multifaceted challenge requiring a holistic insight across different areas of science, ranging from materials engineering to cell biology. In this study, we introduce carbon MSS as a tunable, effective, and biocompatible platform with the desired nanofibrous topographies for cell growth and an inherent capability to electrochemically monitor cell metabolites, such as dopamine. Three different cells, including two wild type cells mNSPC and one dopaminergic cell line, were successfully grown on the scaffold. The biophysical cues of the carbon MSS topography, which could be tuned to yield different degrees of fiber alignment and organization, were shown to effectively promote cellular adhesion, cytoskeletal alignment, and astrocyte development in both CTX and MGE wild type mNSPCs. The carbon MSS also demonstrated selective differentiation toward neuronal lineages over glial lineages, important for targeted stem cell therapy. Finally, the carbon MSS was able to sensitively and continuously monitor DA produced from a model dopaminergic cell line grown directly on the scaffold, preserving cell function and integrity while providing valuable information regarding cell phenotype. Carbon MSS not only acts as a traditional scaffold, providing a favorable topography for stem cell growth, but explores

its more practical application as a smart, integrative platform for in situ stem cell characterization and monitoring. The multi-functional carbon platform presented in this study paves the way for developing future integrated stem cell scaffolds, where growth, physical and electrical stimulation, and characterization take place concurrently.

Part III

Centrifugal microfluidic systems for rapid bacteria incubation and antibiotic susceptibility testing

Chapter 6

Introduction

Antibiotics save lives every day by treating severe infections and allowing medical practitioners to perform life-saving surgical and medical procedures. However, antibiotic abuse has contributed to selection pressure and the emergence of new drug resistant and untreatable strains. On top of this, only two new classes of antibiotics have been developed since 1962 [21], resulting in a global healthcare crisis, see Figure 6.1. According to the WHO, antibiotic-resistant infections currently claim at least 50,000 lives each year across Europe and the US, with several hundred thousand more dying in other areas of the world [167]. In the US alone there are currently 23,000 deaths, 2.0 million illnesses, and $20 billion worth of direct extra costs. If antibiotic resistance continues to increase, microbial infections could kill 10 million people every year by 2050 [152].

The immediate solution is proper antibiotic stewardship, which could control antibiotic resistance and prolong the effectiveness of our current antibiotics for generations to come [186]. A critical component to antibiotic stewardship is rapid and effective antibiotic susceptibility testing (AST). Currently, it is estimated that up to 50% of antibiotics prescribed are not needed or are not optimally effective as prescribed. Typically, clinicians use broad spectrum

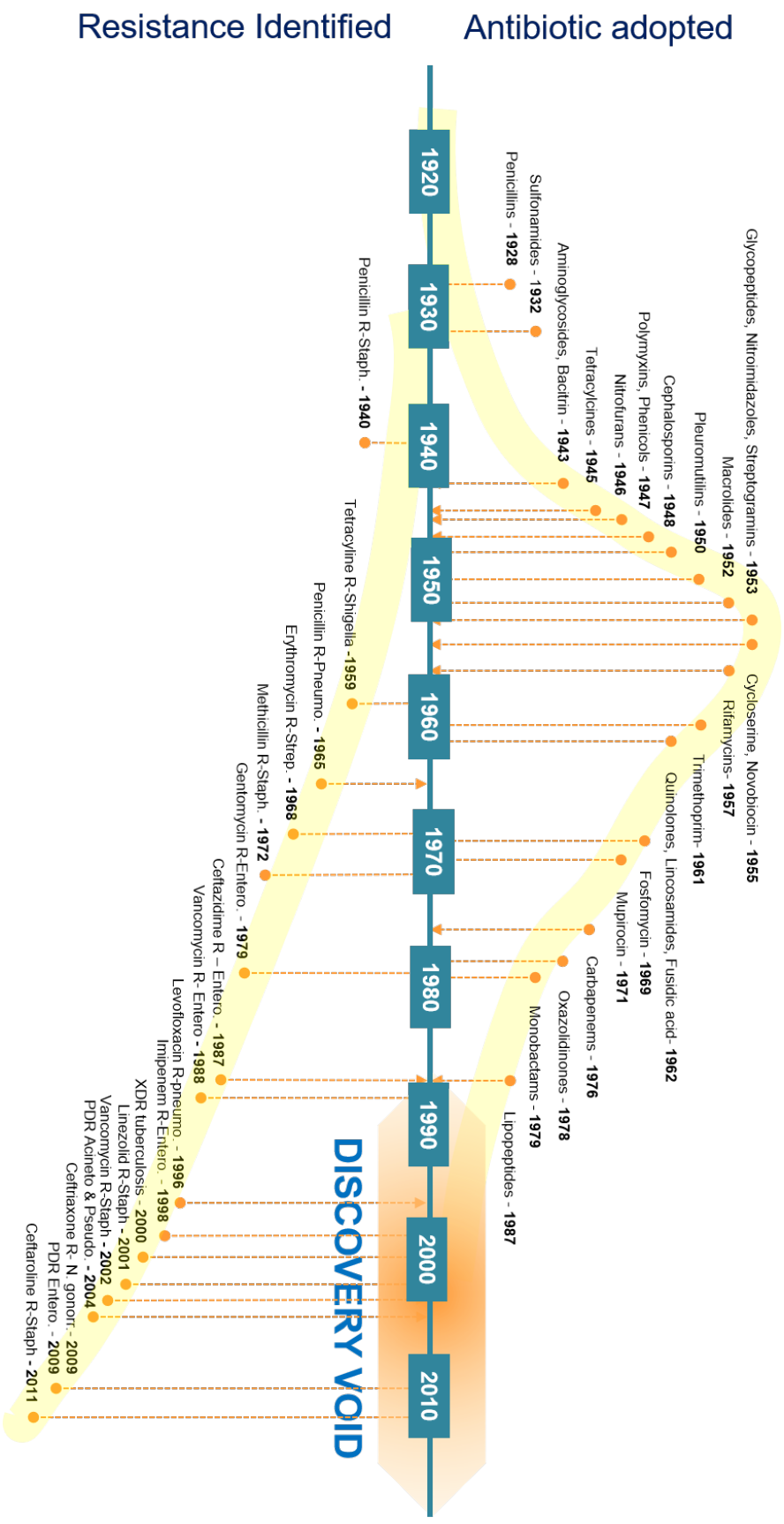

Figure 6.1: Graphic comparing discovery of antibiotics and the development of resistance mechanisms from early 1900s to today.

antibiotics and best guess methods for immediate antibiotic prescription due to the long turnaround times of conventional AST [32].

Traditional phenotypic AST methods, such as broth dilution, agar disc diffusion, or ellipsometer test, are the gold standard in providing relevant diagnostic information on susceptibility since they look at the real-time growth and metabolic response of a bacterial population to an antibiotic. However, these tests are limited by the time it takes for visible colony growth to appear, with incubation times ranging from 18 to 24 hours. Furthermore, they require high starting volumes, involve sample transportation to a central lab, and require several intermediate handling steps performed by trained laboratory technicians, increasing costs and delaying accessibility to diagnostic information for days. State of-the-art genotypic ASTs utilize amplification techniques to create a genome sequence map and identify resistant genes. While they eliminate the need for lengthy bacteria culture and have been implemented commercially, they have not been widely adopted for clinical practice. The main limitations include their inability to identify multi-drug resistance, and predominance of both false positive results, caused by non-pathogenic microorganisms that contaminate the test, and false negative results, caused by new or unknown resistance mechanisms.[176, 26] As a result, phenotypic ASTs remain the most appropriate and reliable diagnostic tests for antibiotic prescription.

While microfluidic, lab-on-a-chip systems have significantly improved accessible diagnostics, successful integration of phenotypic AST in a point-of-care system has remained challenging due to the complex and lengthy nature of the sample preparation. Since the rate limiting step for traditional AST is the incubation of bacteria with antibiotics, many research groups attempt to circumvent this by using techniques such as microfluidic confinement, digital microfluidics, electrokinetics, and agarose microchannels to look at the response of individual cells to an antibiotic within the first few hours of incubation [81, 12, 145, 104]. For example, Pitruzzelo et. al. looked at the morphology and hydrodynamic interactions between single E.

Figure 6.2: The spinbox design and components.

Coli cells and microfluidic traps to determine the bactericidal response to antibiotics within 1-3 hours after the onset of incubation [145]. However their system is only compatible with motile bacteria species and requires traditional off-chip incubation. Furthermore, most single-cell trapping techniques are optimized based on a small number of pathogens and are unable to perform AST on polymicrobial samples [145]. Li et. al. attempted to address these issues by developing a microfluidic chip that can identify and sort individual bacteria species within a complex sample and rapidly incubate bacteria with antibiotics on-chip. However, the system is costly and bulky, requiring an expensive microscope capable of simultaneous incubation, high resolution imaging, and complex image analysis. Furthermore, separating the different bacterial species prior to incubation may provide unreliable AST results that don't account for the codependent interactions among different species in a polymicrobial sample [104] .

To address these issues, we developed a portable, sample-to-answer CD microfluidic cartridge and instrument (SpinBox) that automates all sample processing steps to determine susceptibility results in under 2 hours while maintaining the standard phenotypic-based AST. Unlike other reported microfluidic AST prototypes, the SpinBox provides clinicians

with a completely automated, point-of-care diagnostic tool capable of running the following assay steps: sample dilution and metering, bacteria incubation, cell lysis, sample mixing and neutralization, washing steps, and detection, see Figure 6.2.

By utilizing ribosomal RNA (rRNA) as a unique assay target, the SpinBox is able to process complex, polymicrobial samples much faster than traditional AST methods. There are several advantages of using rRNA over genotypic targets or single cell analysis techniques [26]:

1. rRNA has been shown to be an excellent indicator of bacterial growth and cellular metabolism, and responds rapidly to the presence of antibiotics [127, 51].

2. In ideal incubation conditions, the number of rRNA copies per cell increases significantly (between $10^4 - 10^6$ copies), removing the need for further target amplification and shortening assay time, see Figure 6.3 [211, 51, 140].

3. rRNA has both universal and species-specific sequences that are highly accessible to hybridization by probe pairs, enabling simple bacteria identification and analysis in polymicrobial samples [174, 109].

In order to accommodate the different bacteria found in complex clinical samples, we developed a universal cell lysis method capable of extracting rRNA from both gram-positive and gram-negative microbes. We show lysis on six unique gram- positive and negative species with lysis efficiency comparable to commercial lysis systems, such as the Omnilyse [13, 55]. We also developed a never reported, small-volume bacteria incubation technique in a microfluidic CD that rapidly enhances bacterial growth. By controlling incubation chamber materials, geometry, temperature, and spin protocol, we demonstrate the ability to enhance bacterial incubation (>200% increase in rRNA copies) compared with normal laboratory plate shakers for multiple species of bacteria, including 13 different isolates of E. Coli. Fi-

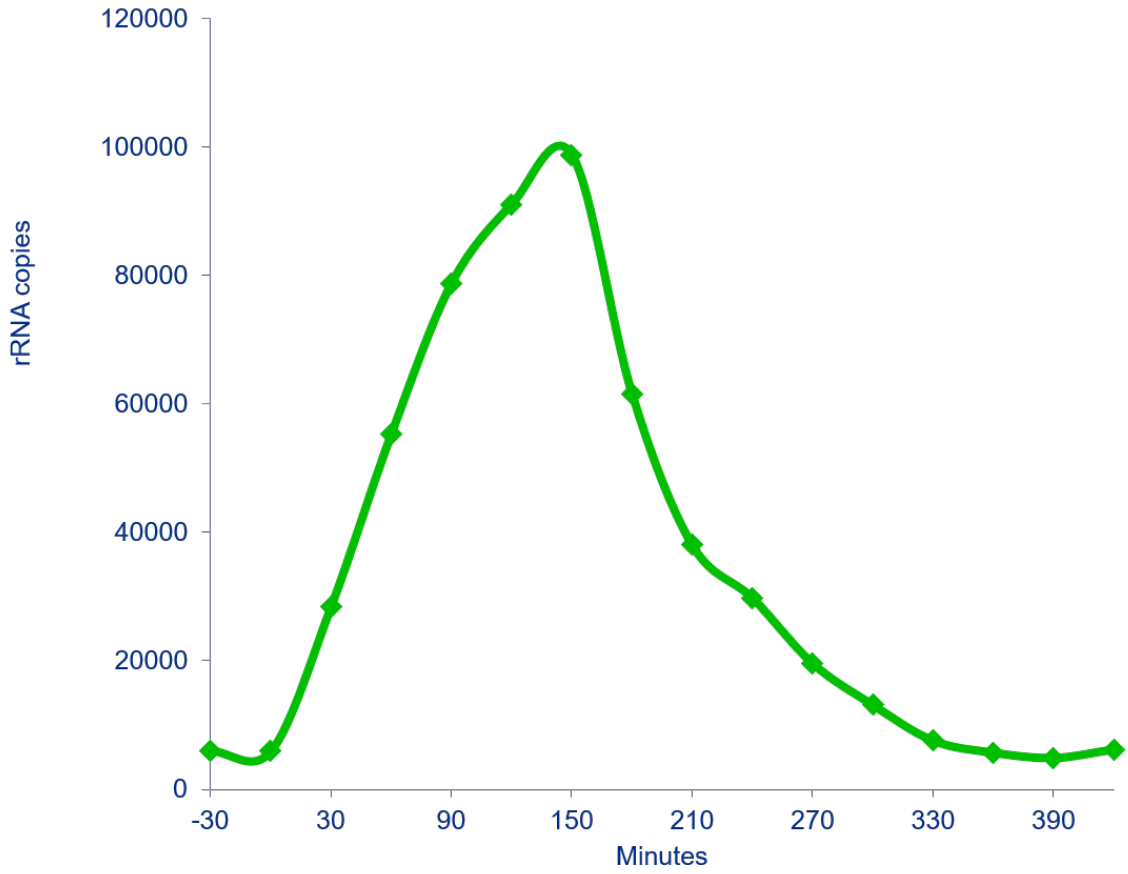

Figure 6.3: Data points show RNA growth as a function of time for a representative bacteria, E. Coli.

nally, we demonstrate the use of our sample preparation system in diagnosing antibiotic resistance in 11 isolates of E. Coli incubated with 5 different antibiotics in under 2 hours.

Chapter 7

Background and Theory

7.1 CD Microfluidics

Over the last decades, centrifugal microfluidics has emerged as an advanced diagnostics platform for point-of-care assays. A centrifugal microfluidic device typically takes the shape of a compact disc (CD) and incorporates interconnecting fluidic channels and chambers that are fabricated into the device. These microfluidic discs are capable of performing complex assays ranging from in-vitro diagnostics to water quality analysis. Furthermore, advancements in microfabrication, optics, and low-cost computers have allowed CD microfluidic technology to become increasingly portable, low cost, and easy to use, making it an ideal system for applications at the point-of-care.

Centrifugal microfluidic devices, also called lab-on-a-disc (LoD) systems, comprise a subcategory of lab-on-a-chip (LoC) devices. The broad category of LoC platforms have advantages such as reduced cost, the use of smaller amounts of materials and reagents, faster reaction times due to small liquid volumes and diffusion distances, portability, and programmability, see full list in Table 4.8. While LoD systems incorporate the same advantages as minia-

Table 7.1: Characteristics of LOC Systems

Advantages	**Disadvantages**
• Reduced material cost	• Difficulty handling large volumes
• Time and labor saving	• External tubing for pumping
• Smaller diffusion distances	• Mixing difficult (Low Reynold's regime)
• Portable and Programmable	• Bubble formation
• Reduced reagent volume and cost	• Difficulty multiplexing

ture chip-based systems, their superiority lies in their inherent simplicity. A simple motor generates several pseudo forces on the platform:

1. The centrifugal force, which acts as a liquid pump and generates a force gradient affecting fluids differently at varying radial positions

2. The Coriolis force, which allows for direction-specific liquid pumping control

3. The Euler force, an inertial force that can be used to create turbulence during mixing or incubation.

The disc rotation facilitates multiplexing of several assays on a single disc, separating components of a sample by density, eliminating trapped bubbles, and allowing liquids to be pumped without direct contact with external hardware (see expanded list in Table 7.2). A single centrifugal disc, combined with a motor for spinning and detection system, can substitute for many aspects of a biomedical laboratory. By using the unique physics available on a rotating platform, along with a small number of active, off-disc components integrated into the spinstand, the CD platform can act as a microscope, a centrifuge, a cell lyser, a sample concentrator, a vortexer/mixer, an x-y positioning stage, a cell incubator, a spectrophotometer, an extractor, and even a PCR thermocycler, see Figure 7.1.

Table 7.2: Characteristics of LOD Systems

Advantages	Disadvantages
• Closed system (motor for pumping)	• unidirectional nature of liquid flow
• Pumps fluids regardless of physical properties	• Difficulty with small volumes (<1 nL)
• Multiplexing ability	
• Handles wide range of fluid volumes	
• Ability to mix and meter	
• Density-based separation	
• Eliminates trapped bubbles	

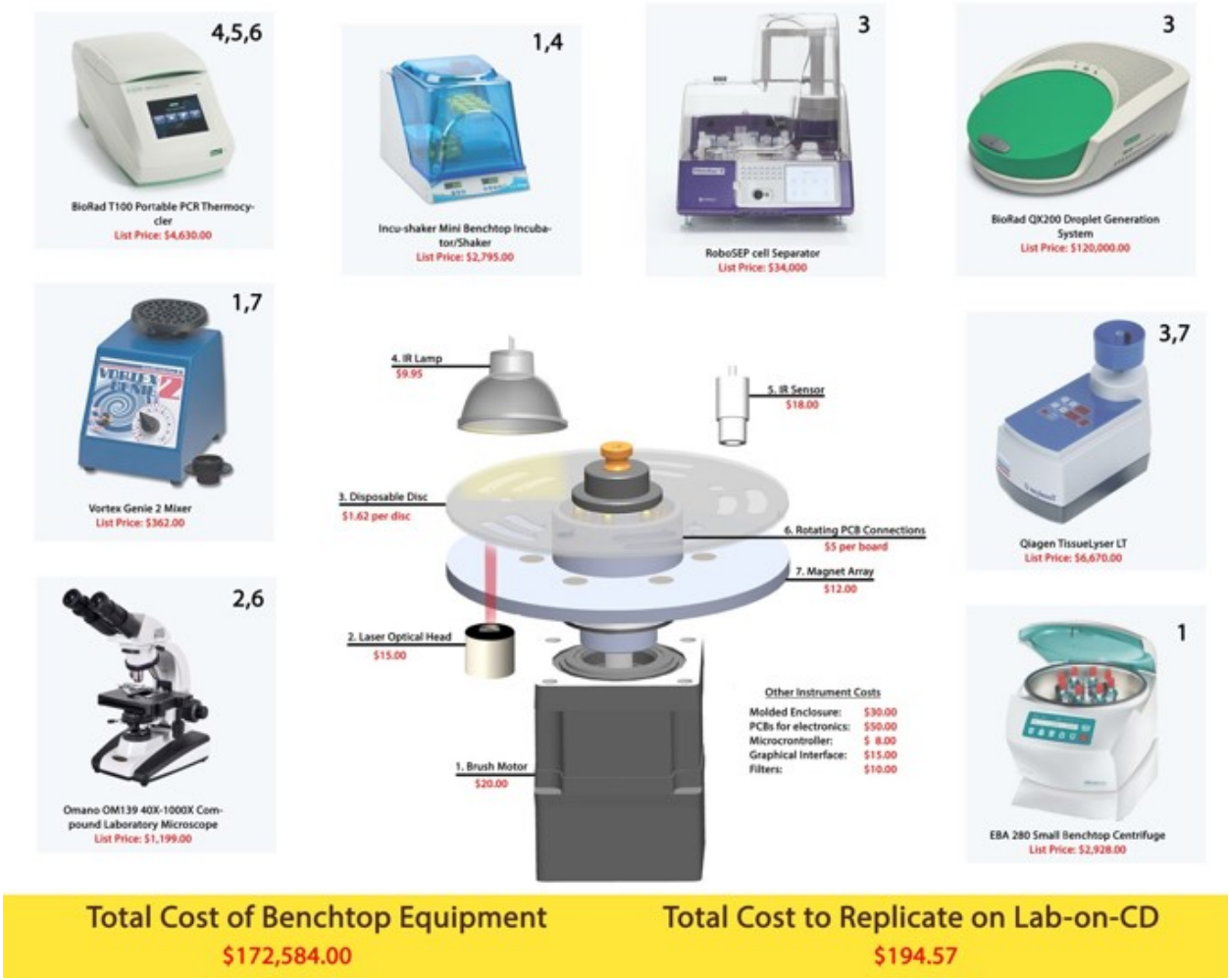

Figure 7.1: The CD as a biomedical laboratory. With only a simple motor and active components, a microfluidic disc can be used to replicate several devices found in a typical biomedical laboratory, for a fraction of the cost. The figure compares the cost of common benchtop equipment versus the components you would need to replicate these systems on a microfluidic platform.

7.1.1 Physical framework for Lab-on-a-Disc

The LoD platform utilizes centrifugal, Coriolis, and Euler forces to manipulate liquid flow on the disc (see Figure 7.2). These three forces are pseudo forces—fictitious forces with respect to a rotating frame of reference and are given in Equation 7.1.1:

$$\vec{F_{tot}} = \vec{F_C} + \vec{F_{Cor}} + \vec{F_E} = \rho\vec{\omega} \times (\vec{\omega} \times r) - 2\rho\vec{\omega} \times \vec{u} - \rho\frac{d\vec{\omega}}{dt} \times \vec{r} \tag{7.1}$$

where ρ is the liquid density, $\vec{r}$ is the average distance of the liquid from the center of the disc, $\vec{\omega}$ is the angular velocity in rad/s, and $\vec{u}$ is the velocity vector of the particle moving on the disc.

Although each of the pseudo forces has its respective characteristics and applications, the main driving force for fluids on a disc is the centrifugal force, which propels liquid radially outward from the center of the disc, forcing it through channels and chambers. The centrifugal force per unit volume acting on a particle is represented by the first term in Equation 7.1.1, $\rho\vec{\omega} \times (\vec{\omega} \times r)$. The Coriolis force is perpendicular to the velocity vector of the moving particle, shown in Figure 7.2. The force per unit volume is given by the second term in Equation 7.1.1, $2\rho\vec{\omega} \times \vec{u}$. The Coriolis force is used in applications for particle separation and in flow-switch techniques [128, 78]. The Euler force is perpendicular to the centrifugal force and opposite to the direction of angular acceleration. This force is only generated when the angular velocity changes with respect to time, and the force per unit volume is given by the third term in Equation 7.1.1, $\rho\frac{d\vec{\omega}}{dt} \times \vec{r}$. The Euler force is mainly used in mixing applications to speed up sample homogenization and is uniquely used in this work for enhancing bacteria incubation.

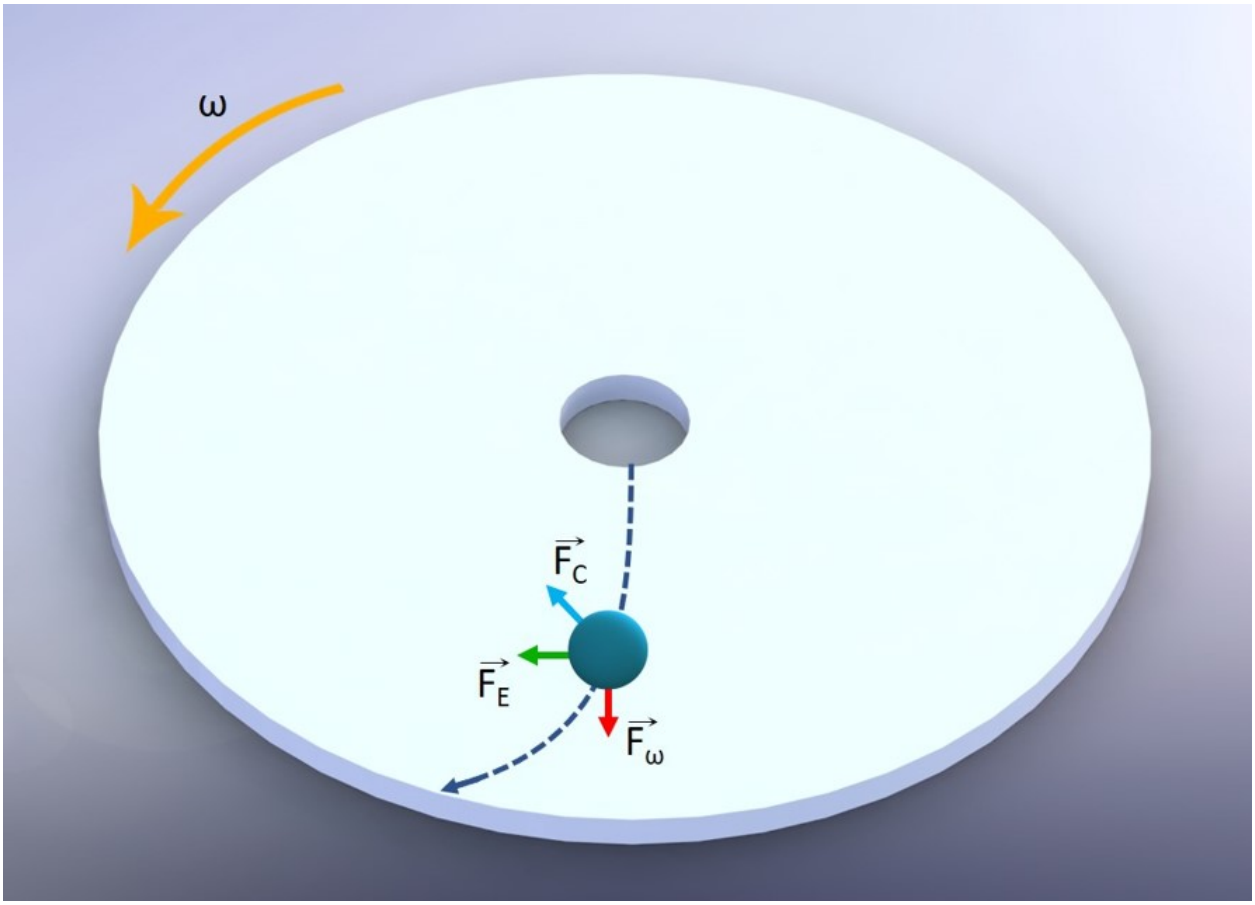

Figure 7.2: Graphic of the psuedo-forces present on a rotating platform, where F_ω is the centrifugal force, F_ω is the coriolis force, and F_E is the Euler force.

Liquid flow characteristics are dependent on the liquid's properties (e.g. density and viscosity), its radial location on the disc, the angular velocity of the disc, and the geometry of the microfluidic features. This flow rate, derived from basic centrifuge theory, was characterized by Madou et al. and Duffy et al. [112, 30]. The average velocity of the liquid on a spinning platform is given by Equation 7.2:

$$\vec{U} = \frac{D_b^2 \rho \vec{\omega^2} \bar{r} \Delta r}{32 \mu L} \tag{7.2}$$

where D_b is the hydraulic diameter of the channel (dened as $4\frac{A}{P}$, where A is the cross-sectional area and P is the wetted perimeter), ρ is the liquid density, $\vec{\omega}$ is the angular velocity of the disc, $\bar{r}$ is the average distance of the liquid in the channels from the center of the disc, Δr is the radial extent of the liquid, μ is the viscosity of the liquid, and L is the characteristic length of the liquid column in the microchannel.

Using this theory, a volumetric flow rate (Q) is defined as $Q = \vec{U} \cdot \vec{A}$. Flow rates achieved experimentally by Duffy et al. had no systematic deviation from the theoretical model and ranged from 5 nl/s to 0.1 ml/s depending on a combination of factors including rotational speeds of the disc (400-1600 rpm), channel widths (20-500 μm), and channel depths (16-340 μm). Since this early work, higher rotation speeds and greater variation in channel width and depth have been used to achieve flow rates that are significantly higher [29]. Furthermore, Duffy et al. tested flow rates for a variety of different liquids to verify the effectiveness of the centrifugal pumping mechanism when pumping liquids with varying physicochemical properties such as pH, ionic strength, and conductivity, demonstrating the CD as a universal pumping mechanism for use with a variety of different chemical and biological samples [30].

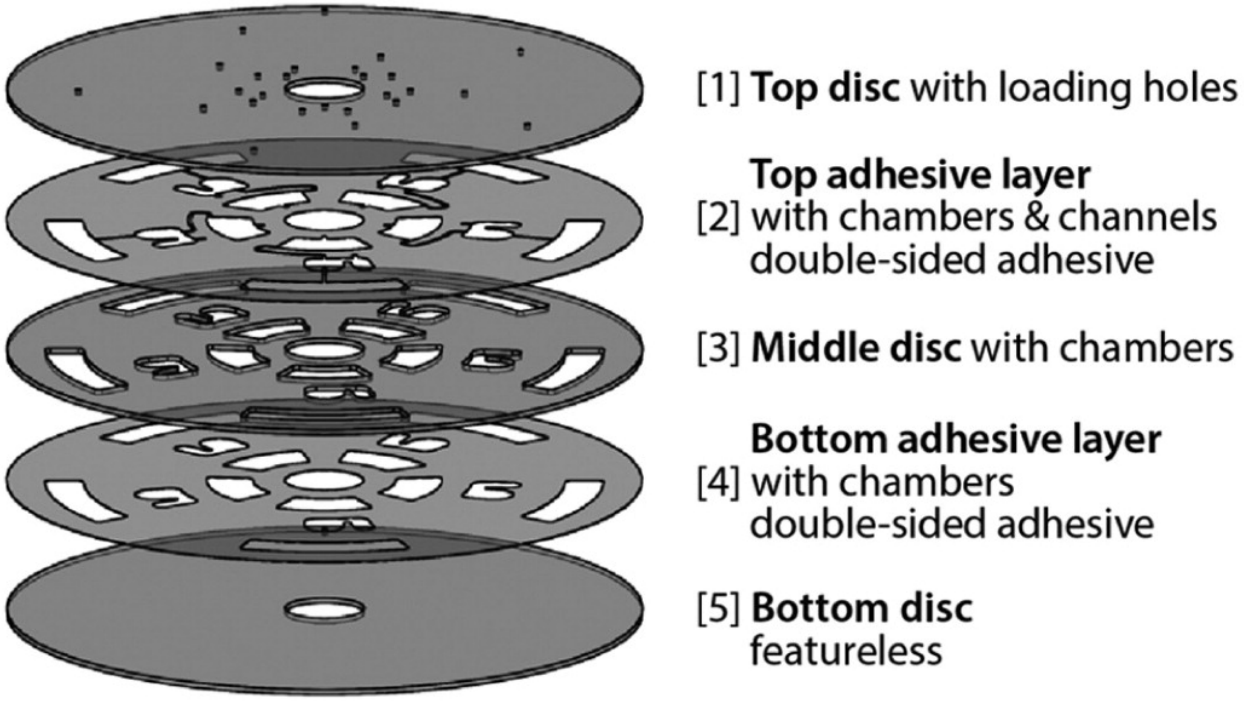

Figure 7.3: The prototype discs used in this work are typically made from several layers of milled plastic and double sided adhesives..

7.1.2 CD Fabrication

Successful adoption and utilization of LoD systems depend on inexpensive and reliable manufacturing solutions for the disposable CD. Common materials used for microfluidic discs include, but are not limited to, polycarbonate, poly(methyl methacrylate) (PMMA), cyclic olefin polymer (COP), polydimethylsiloxane (PDMS), and polyurethane. Often, optical detection requires optical grade materials, which can be costly. These materials can be used for rapid prototyping by molding, 3D printing, laminating, and CNC machining, and some can be injection molded for mass production. For rapid prototyping purposes, microfluidic discs are generally made from layers of adhesives and hard plastics (see Figure 7.3). Features can be cut into polycarbonate, PMMA, or COP sheets using a milling machine [72, 171]. For prototyping, PDMS and polyurethane features can be molded using, for example, a wax or SU-8 mold [30]. PMMA can be cut using a laser, while COP and other polymers in thin sheet form can also be embossed or microthermoformed [171].

Other bonding techniques, such as laser bonding [79], solvent bonding [17], thermal bonding [4], or ultrasonic bonding [181], have been used to bond CD layers together, and these approaches can be scaled up for mass production. Most materials utilized for CD microfluidics are sufficiently hydrophobic for use in hydrophobic burst valves, which are spin frequency controlled valves. In certain cases where the disc surfaces need to be more hydrophilic, the material must be surface treated using oxygen plasma or a surfactant. However, oxygen plasma treatment adds to the cost of fabrication and both plasma or surfactant treatment in general result in devices with short shelf lives [15, 187, 207].

7.1.3 Valving Techniques

Effective valving technologies lie at the heart of sample-to-answer assays, keeping a liquid volume isolated from the rest of the sample handling. Valving techniques on centrifugal microfluidic platforms can be classified into three different categories: passive, active, and semi-active.

Passive valves do not utilize any forces besides those present on the spinning disc, and are actuated by the rotation of the disc itself. The actuation of a passive valve is dependent on the interplay between surface tension and centrifugal force acting on the liquid in the disc. The most common passive valves are burst or capillary valves, see Figure 7.6 [96]. When the angular velocity is sufficiently high, the centrifugal force overcomes the surface tension of the liquid, allowing it to burst into the next chamber. For this reason, the angular frequency at which the valve breaks is called the burst frequency.

Some passive valves are actuated by decreasing the rotational speed of the disc, such as the pneumatic pump or the siphon valve, see Figure 7.6. A siphon valve, connected to a liquid-containing reservoir, again exploits the interplay of capillary forces and centrifugal forces. At initial high angular velocities of the disc, the liquid level in the channel remains below

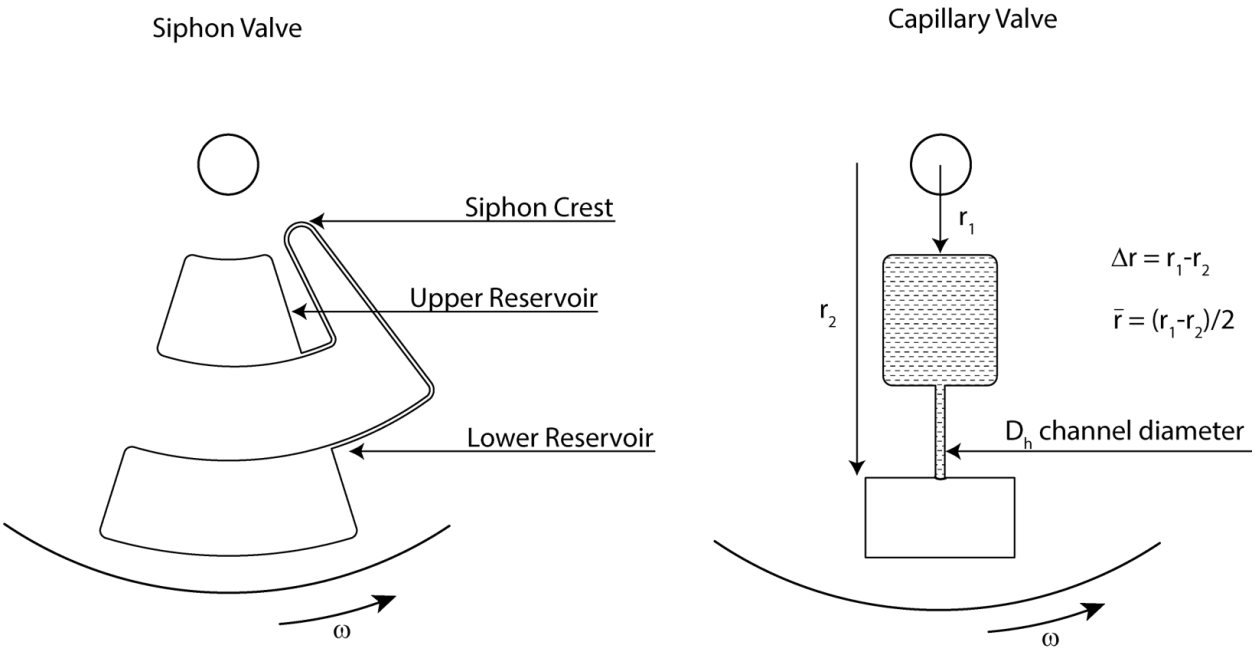

Figure 7.4: Two common passive valves are shown. The siphon valve is actuated at low RPMs, when the capillary force in the siphon is higher than the centrifugal force from rotation. The capillary valve is actuated at high RPM when the centrifugal force overcomes the surface tension in a liquid plug.

the crest of the siphon. When the rotational velocity is sufficiently reduced, capillary forces dominate and the solution fills the siphon, priming the valve. When the angular velocity is increased again, the hydrostatic pressure difference now aids in the complete emptying of the original reservoir.

Another type of passive valve, the Coriolis valve, is actuated by changing the direction of disc rotation [78]. Although passive valves are simple to fabricate, some types require a hydrophilic surface treatment step, usually plasma treatment. This surface treatment is reversible and generally limits the shelf-life of the device to a range of days to weeks [207, 187, 15], while current diagnostic devices remain on the shelf for many months before use. In addition, variations in the manufacturing process can change the burst frequency from device to device, making it difficult to implement a reliable protocol [86].

The complexity of many of today's assays cannot be handled by passive valves alone due

to reliability issues associated with their burst frequencies. Additionally, passive valves are generally not vapor-tight barriers. This characteristic makes the passive valve unsuitable for reagent storage due to the loss or exchange of vapors over time. As a result, active or semi-active liquid-handling techniques must often be used in conjunction with passive valves to achieve a higher level of fluidic control.

Active valves require an external actuation mechanism, resulting in higher reliability and robustness than passive valves. The operation of these valves is independent of or only partially dependent on the angular velocity of the disc. Examples of external actuators include heat sources, lasers, and magnets. The main disadvantage of active valving is the need for additional hardware, adding complexity and cost to the platform.

One of the most famous active valves is the paraffin wax valve, a phase-change valve requiring only a heat source to be turned on to open a paraffin wax valve. Abi-Samra et al. used an infrared lamp to serially open valves made of different temperature paraffin waxes on a CD [2]. The advantage of this technique is that all valves on the same radius of a disc can be actuated at the same time during spinning by positioning the heat source above the desired radial location of the disc.

Another variation on the active valve is the thermo-pneumatic pump valve, which involves heating a ventless chamber of air on a disc. As the air volume thermally expands, it pushes out liquid in an adjacent chamber [1]. The angular velocity of the disc needs to be kept low enough to allow the force generated through thermal expansion to overcome the centrifugal force exerted on the liquid being pumped, while high enough to create a uniform meniscus in the liquid reservoir on which the expanding air can exert pressure. The pumping ability is characterized by the following factors: the amount of temperature change of the air (in accordance with Charles' Law), the size of the ventless chamber, and the location of the liquid on the disc. A heat source, such as an infrared lamp, is the only required piece of external hardware needed for thermo-pneumatic pumping.

We also define another type of valving: semi-active valving. Semi-active valves are RPM-dependent valves that offer a higher level of control than passive valves, yet are simple to fabricate and do not involve surface treatments. They usually integrate additional, inexpensive materials, such as paper, in order to perform valving tasks. Although only a limited number of approaches have been demonstrated in the category of semi-active valves, these valves can be highly practical due to their low cost and ease of implementation. Passive valves, such as capillary valves, may have a spectrum of possible burst frequencies instead of one absolute burst frequency. Semi-active valves reduce the dependence on the reproducibility of the native surfaces of devices by using an alternative material or a delay mechanism. In systems where the fluid-handling tasks become more complex, semi-active valves can be added to achieve more robust control than passive valving techniques alone.

One of the most well researched semi-active valves uses biocompatible dissolvable films [45]. In this approach, two chambers are connected with a pneumatic chamber containing a commercially available dissolvable film tab in between. Under low rotational speeds, a trapped air pocket prevented the liquid in the upstream chamber from entering the pneumatic chamber and wetting the dissolvable film. Once a high enough rotational speed was reached, liquid entered the pneumatic chamber, dissolved the dissolvable film, and passed on to the downstream chamber. The pneumatic chamber equipped with the dissolvable film allowed for more control over the bursting event since the angular frequency of the disc must be sufficiently high for liquid from the upstream chamber to enter the pneumatic chamber and begin the valve-opening process by dissolving the film in that chamber. Although this valve is not vapor tight, it provides considerably more control than capillary valves and is tunable in that films with different dissolution rates can be chosen.

Another type of semi-active valving is established by using paper strips inserted into the CD to perform the function of hydrophilic siphons. Although this type of valving is RPM-controlled, the wicking ability of the paper offers more fluidic control than traditional passive

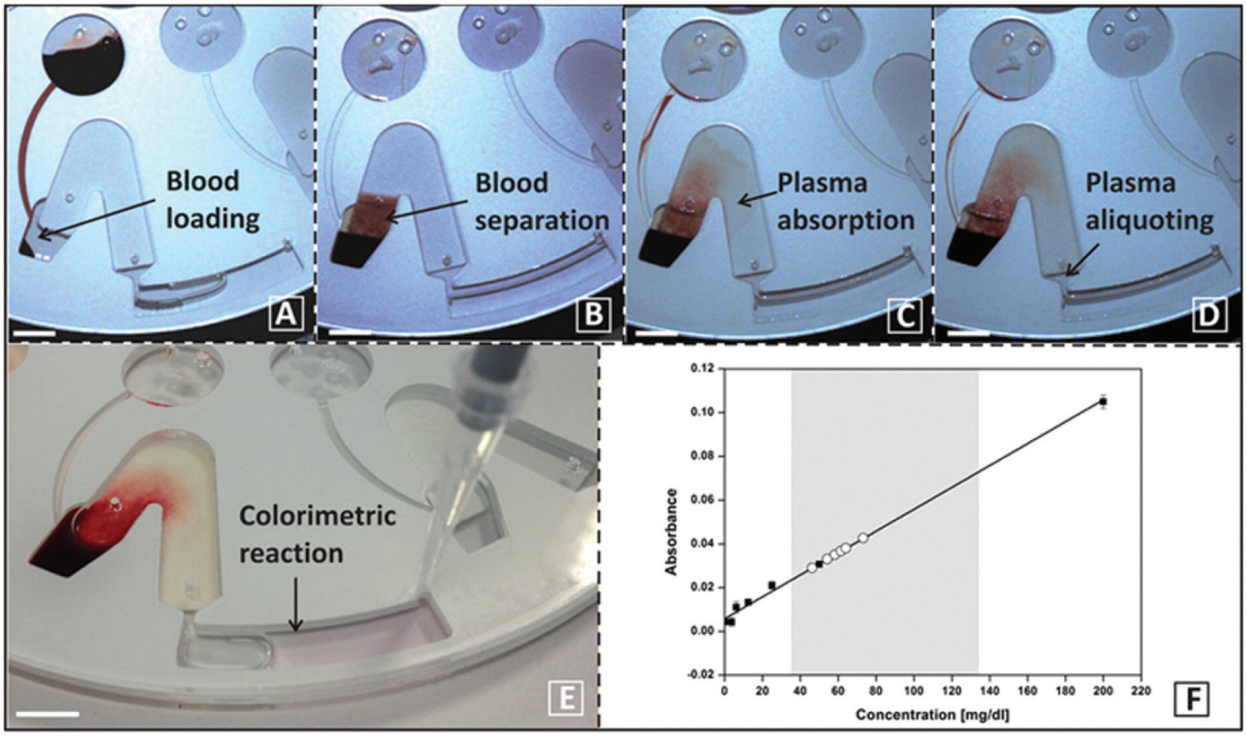

Figure 7.5: (A) The paper siphon was used by Godino et al. to separate blood plasma from red blood cells in whole blood. The blood was aliquoted to minimize contact with the paper. (B) The disc was spun at 6000 rpm for 2min to pellet blood cells and to reduce absorption of blood by the paper. (C) The disc was then spun at 375 rpm to let the paper siphon absorb the blood plasma for 5 minutes until saturation. (D) A spin frequency of 2250 rpm was used to extract plasma from the paper. Then, the two latter steps are repeated until 10 L of plasma has accumulated. (E) The extracted plasma was then used for a colorimetric assay off-disc. (F) The graph shows calibration points as black squares and a patient's triglyceride level as outline circles.

valving. The principle of paper microfluidics on a CD is based on the interplay of capillary forces that allow liquid to wick through the paper and centrifugal forces that push liquid only toward the outer edge of the disc. As shown in Figure 7.5A-E, Godino et al. utilized chromatographic paper in a siphon to achieve a high level of control of blood plasma flow [43].

7.1.4 The CD as a centrifuge

While all three pseudo forces shown in Equation 7.1.1 are proportional to the mass per unit volume of liquid, the centrifugal force is proportional to the square of the angular velocity, making it the strongest acting force in a rotating frame of reference.

Centrifugation takes advantage of this force to rapidly separate a heterogenous mixture into its component parts. In a normal laboratory centrifuge, a sample is placed in a centrifuge tube a certain radial distance and angle from the center of a rotating platform. The sample is spun at a high rpm, separating out components based on their density. The technician decants the supernatant using a pipette. This process is not fully automated and is therefore affected by user error.

The CD has been successfully used to completely automate a centrifuge by using special chambers in which a sample is centrifuged and the supernatant automatically removed by a valve. In 2006, Haeberle et. al. used a rotating CD to separate plasma from whole blood [50]. The setup uses a decanting chamber to sediment whole blood cells in a centrifugal field. A shock interface is created between the blood plasma and whole blood. Once the decanting chamber is completely filled, the plasma overflows into an adjoining chamber.

A further improvement on this design by Amasia, et. al. uses a siphon valve to remove supernatant from the disc [5]. In this design, the disc consists of a primary chamber for large volume blood plasma separation. Hydrophilic surface treatment of the disc allow a separate, siphon valve to transfer the entire plasma supernatant to an adjoining chamber. Siphon valves have an added advantage over volume-dependant chambers since they are actuated by changing the angular velocity of the disc.

Apart from blood-plasma separation, centrifugation has been used on disc to separate cells, clarify lysed samples (see section 7.1.6), and for separation of microscopic particles.

7.1.5 The CD as an Incubator

Incubation uses a combination of growth media, turbulent mixing, temperature and gas control, and other stimuli to trigger growth and metabolic changes in organisms, cells or bacteria. For infectious diseases, phenotypic assays require an incubation step to evaluate the response certain viruses or bacteria to a particular drug or environmental condition. Conventionally, incubation is a several hours to days long process done in petri dishes or agar plates. This long wait time between sample and answer can have drastic consequences in infectious disease diagnostics. For example, with antibiotic susceptibility tests, lack of quick testing leads to overprescription of broad spectrum antibiotics and contributes to overtreatment with broad spectrum antibiotics, one of the contributors to the global antibiotic resistance crisis. Furthermore, while these processes can be high throughput, they are generally slow and complicated, requiring significant sample preparation, transportation to a central lab, and outside instruments such as robotic shakers and microplate readers that tremendously increase cost.

Centrifugal microfluidics is an ideal platform to handle the necessary sample preparation, temperature conditions, and mixing for rapid incubation of bacteria and cells. The disc can be made of biocompatible disposable plastic such as polydimethylsiloxane (PDMS), which is gas permeable for proper aeration and transparent to light for easy detection.

In this work, we utilize the disc for rapid incubation of bacteria with antibiotics in antibiotic susceptibility testing.

7.1.6 The CD as a Mixer

Mixing of reagents and samples is a critical step in many assays. In most microfluidic systems, mixing is challenging due to the low Reynolds numbers and laminar flow regimes present in

microfluidic devices [71, 57]. In microfluidic chips, liquid streams are generally confined to narrow channels, allowing for only diffusive mixing. On the other hand, in microfluidic discs, separate liquid streams are usually flowed into a large chamber, inducing both convective and diffusive mixing. While this phenomenon makes the centrifugal microfluidic platform inherently better for mixing, various passive and active mixing techniques have been developed to further speed up the process.

Researchers have further optimized on-disc mixing by incorporating special micromixers onto microfluidic devices. While passive micromixers utilize special microchannel geometries to induce advection during liquid handling and minimize diffusion times, active micromixers utilize additional hardware or integrated structures to homogenize liquids. One of the simplest passive mixers on a CD is the modified centrifugal force-based serpentine micromixer (CSM) first simulated by La et al. [93] and further optimized by Kuo and Li [92]. A serpentine channel was incorporated into a microfluidic CD design, and the combination of Coriolis force and the channel geometry induced chaotic advection and diffusion in the sample, effectively mixing it. Kuo and Li used the CSM method to mix reagents with plasma after separation by sedimentation, demonstrating the potency of this mixing technique in sample preparation. In Figure 7.6, the 5-second time point from the simulation of this micromixer, with different channel widths, is shown.

Other passive mixing methods utilize droplets as microreaction chambers [3] or bubbles to promote chaotic advection [39]. Droplet formation on a disc, where the small diameter of the microreaction chambers significantly reduces the diffusion distance of any reactants, has been realized by Haeberle et al [50]. Bubble mixing using T-junctions has not yet been integrated on a disc, possibly due to the constraint of the disc's footprint size, but could be implemented in the future.

A more effective passive mixing technique is flow reciprocation, which utilizes less on-disc real estate than serpentine channels and can be used for sample hybridization. In 2009, Noroozi

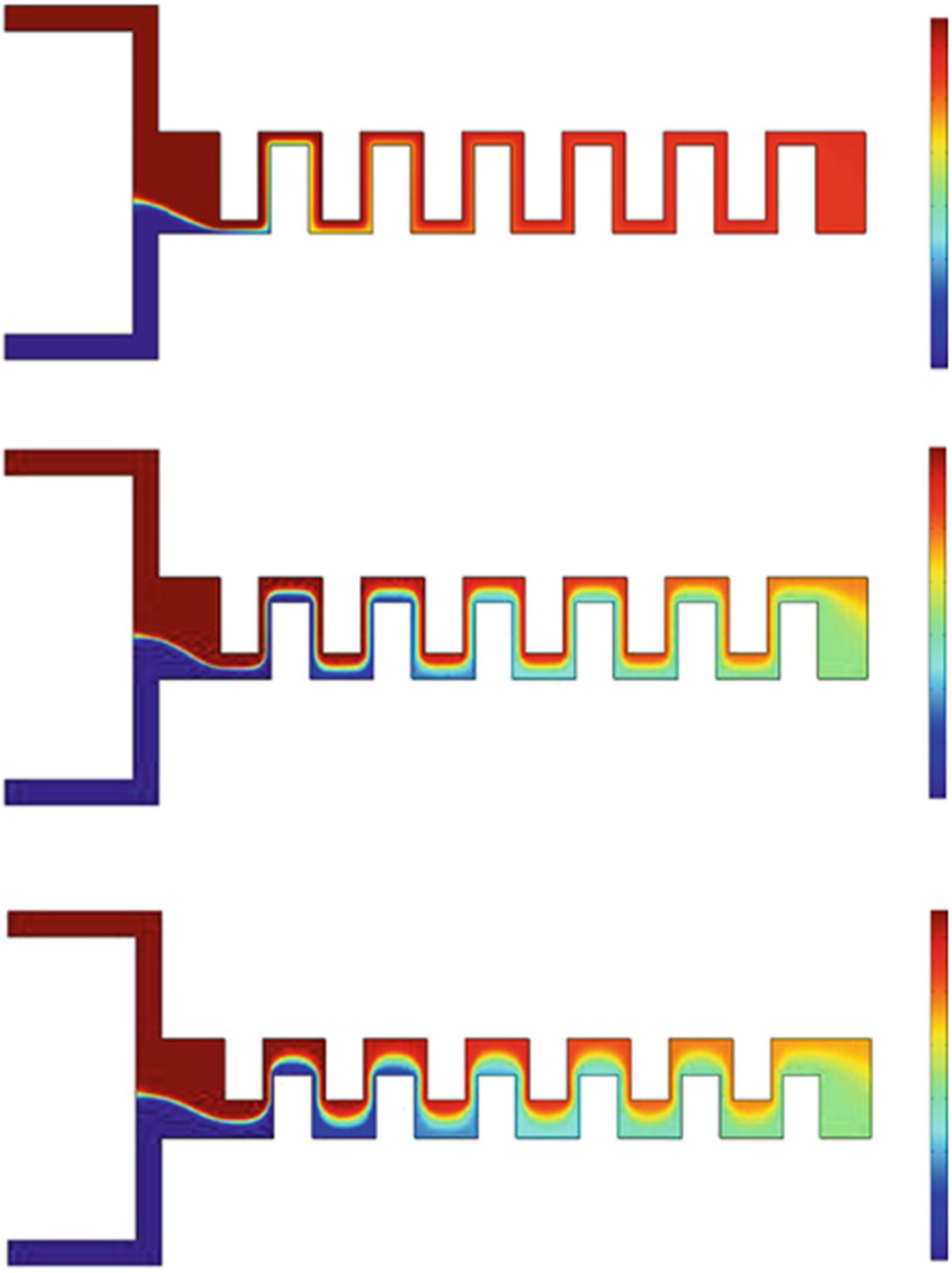

Figure 7.6: Kuo et al. conducted computer-simulated studies on the effects of a serpentine geometry for a microchannel on a microfluidic compact disc (CD). In this model, the CD platform was simulated to spin at 2200 rpm for 5s while mixing plasma and deionized (DI) water. The center of the disc is located to the left, and the liquids flow to the right into a waste chamber. The mixing of plasma (red, top inlets) with DI water (blue, bottom inlets) increases as channel width (around the bends) increases. Best mixing is observed in the third simulation where the final product is an intermediate color, or green, to represent a well-mixed solution.

et al. designed a reciprocating flow mixer which utilized both centrifugal force and the pneumatic pressure generated in a ventless compression chamber to effectively and quickly mix two liquids together [133]. This technique can handle significantly more liquid sample volume than droplet and serpentine mixing. In 2011, Noroozi et al. was able to integrate this technology into a multiplexed LoD immunoassay to improve Burkholderia detection, illustrating the impact this mechanism can have on sample preparation [134].

While effective, some drawbacks to passive mixing for more complicated assays include inefficient use of on-disc real estate, long mixing times, and ineffective mixing of very viscous samples. Active mixing techniques include electro-osmotic mixing, ultrasonic manipulation of a piezoelectric diaphragm, and magnetic mixing. The simplest of these techniques is using magnetic beads as an active mixer [46]. In this technique termed batch-mode mixing, a series of permanent magnets were placed at alternating radial distances underneath the mixing chamber, while magnetic microbeads were placed inside the mixing chamber. As the disc was spun, the beads moved inside the chamber, inducing turbulent mixing by means of the Stokes drag force. To further increase mixing, a shaking protocol was implemented, periodically changing the frequency of rotation to induce phases of acceleration and deceleration. This technique takes advantage of Euler forces to stimulate an advective current during acceleration and deceleration of the disc. This alteration between spinning speeds induces lateral movement of the magnetic beads in the mixing chamber, increasing the mixing area of the beads and drastically reducing mixing time from seven minutes via diffusive mixing to less than one second. The mechanical lysis component of the universal lysis system developed in this work uses the same principle as the batch-mode mixing technique 11. In addition to lysis, it also performs mixing in the same chamber, and has been applied in a nucleic acid extraction system developed by Siegrist et al [170].

The CD as a Particle Separator

Particle sorting is required when there is a low quantity of a target cell type amongst a population of cells. Such cases include separation of fetal cells from the mother's whole blood or rare cancer cells from a tissue sample prior to nucleic acid analysis [64]. The size range of particles that can be separated is inherently limited by the radial size of the disc. Even so, effective particle separation on a disc is possible, and is preferred because motor for rotating the CD uses a small amount of power compared to any benchtop system.

Particle separation can use either passive methods that take advantage of the centrifugal force or active methods that incorporate external components. Aguirre et al. used Dean forces in serial serpentine flow-focusing channels to separate cell-bead complexes from blood [3]. Morijiri et al. separated particles of different densities and sizes using a rotational movement combined with a technique called pinched-flow fractionation. The fluidic structure was filled with a bulk buffer solution before the particles were introduced. As the disc rotated, the pinched segment focused particles onto the upper wall, while the centrifugal force drove the sedimentation of particles by their respective sizes and densities [128].

Besides utilizing pseudo forces present on a rotating platform, additional active components may be integrated for more effective particle separation. Recently, Kirby et al. utilized a set of three magnets on a CD platform to successfully simulate the isolation of rare bioparticles from background tissue cells [84]. A mixed particle suspension, including magnetic and non-magnetic particles of different sizes, was sent through a focusing channel where the centrifugal force, along with three permanent magnets located at different radial distances, separated particles according to their density, size and magnetic properties. Nearly 100 percent separation was achieved. This technique was used to separate MCF-7 cells with as low as 1 target cell in 1 μL of whole blood with capture efficiencies of up to 88% 104. A total of 18 μL of sample was processed on a disc within 10 minutes.

Glynn et al. used geometric designs, termed "size exclusion rail", to separate cells of different sizes [42]. Whole blood, spiked with HL60, colo794 and sk-mel28 cells, was sorted on the microfluidic disc. The different size-gaps in the geometric design allowed the passing of the appropriate sized cells into several bins. Each bin received cells of a certain size range, including components of blood, making this technique a simple and label-free manner for cell sorting.

Schaff et al. demonstrated sedimentation-based particle sorting, where two different beads types (different size and different density), each type functionalized with a different capture antibody, sediment into distinct layers when passing through a density medium. This process also separated the beads from the red blood cells in the case that they are present, and provided a washing step for the beads [160]. Koh et al. performed a similar sedimentation step with only one bead type for the detection of botulinum toxin and achieved a lower limit of detection of 0.09 pg/mL [88].

The CD as a sample concentrator

The detection of low concentration components in many biological or chemical assays may require an initial step to concentrate or isolate the sample. Examples of components that require such a process include proteins, environmental pollutants, and nucleic acids. The method of choice for concentration or purification often involves the use of a solid phase extraction column. We introduce here several methods used to extract compounds: the use of monolith in a micro-column [130], in-situ detection following collection of samples in the column [94, 95], and the use of hydrophobic membranes and dissolvable films for reagent flow control in silica bead-based RNA purification [27].

Moschou et al. discussed the implementation of such a unit on a microfluidic disc for the extraction of proteins [130]. The disc contained a micro-column for separation, a fraction-

ation channel to isolate the proteins from the rest of the sample volume, and an isolation chamber for optical detection of the proteins. The group prepared a monolithic column using in situ polymerization by microwaves for efficient sample extraction. Fluorescent analysis of the isolated analyte showed that at least 80 percent of the original 12.4 pmol sample was recovered.

Works from another group used a different microfluidic disc design to detect and quantify elements in water samples and an environmental pollutant [94, 95]. Instead of elution using organic solvents, the authors analyzed the sample directly in the stationary phase in the column. Direct analysis of the column reduces loss of sample by wall adsorption and the amount of harmful organic solvents used for sample extraction. Using laser ablation, Lafleur and Salin found the limits of detection to be between 0.1 and 12 ng for Ni, Cu, V, and Co [95]. Lafleur et al. analyzed the column for fluorescein by fluorescence and absorbance and for anthracene by fluorescence. The limit of detection of fluorescein was 50 ng using both detection methods, and that of anthracene was 20 ng [94].

Dimov et al. introduced the use of hydrophobic membranes and dissolvable films for liquid reagent control in silica bead-purification of RNA samples [27]. Although the system yielded considerably RNA than benchtop methods, it was capable of purifying both mammalian and bacterial RNA.

Mamaev et al. built a fully contained and fully automated system that performs NA isolation and purification on up to 24 samples. The system incorporates lyophilized reagents, leak-proof inlets for sample input, outlets with standard micro test tubes for sample recovery, and hardware components that deliver heat, pressure, and spinning of the motor to perform valving and pumping. Experiments confirmed that the system was capable of isolating genomic material from Bacillus thuringiensis and Mycobacterium tuberculosis cells that were in the concentration range of 102 to 108 cells/mL and from hepatitis B and C viruses with concentrations of 102 to 107 particles/mL in plasma. Quantitative PCR was performed using

the obtained B. Thuringiensis DNA, and the results amongst the replicates did not vary by more than 10%. The NA obtained from the automated system was compared to those obtained from the manual method, and the two sets of data were almost identical. These experiments confirmed that the platform was reliable for performing NA purification, and the authors project that when integrated with low-density hydrogel microarray technologies, the platform will be capable of analyzing viral and bacterial DNA and detecting genetic point mutations association with cancer or other conditions [116].

Despite the effectiveness of solid phase extraction for sample purification and concentration, a few challenges still prevent its widespread implementation on centrifugal microfluidic systems. One challenge is the requirement for liquid reagent storage for a fully automated assay. In the multi-step elution assays described, the reagents had to be manually introduced into the disc after each step [27, 130]. A second challenge is the incompatibility of the reagents with the materials used to make the disc. For example, Moschou et al. observed that glycidal methacrylate and hexane, components used to create the microcolumn monolith precursor, caused deformation of the disc's PDMS layer [130]. In other cases, organic solvents, such as acetone or methanol, are sometimes the standard reagents for an assay. These solvents etch certain polymers such as polycarbonate or acrylic, limiting material choices.

The CD as a cell lyser

For many biological samples, lysis is necessary for retrieving genomic or proteomic material from cells. The process usually involves breaking the outer membrane of the cells using one of two methods: physical means [77, 72], such as laser-induced thermal shock or sonication [50], or chemical means, which generally involves the use of detergents [45]. Many of these processes can also perform sample homogenization to ensure that the biological sample is uniform in size and texture throughout.

Although a variety of methods can be used for sample lysis on the CD, bead beating, developed by Kido et al., remains the most universally effective method, capable of lysing even the toughest samples [72]. The bead beating setup, shown in Figure 7.7, consists of several permanent magnets located under the disc at alternating radial distances. A small ferromagnetic disc is free to move inside a radial chamber on the CD. As the CD spins, the ferromagnetic small disc moves toward the permanent magnets as it passes them, sliding back and forth in the chamber. Glass beads are added as a grinding media to enhance lysis. This method was used to effectively lyse Saccharomyces cerevisiae cells, considered notoriously difficult to lyse.

7.1.7 The CD as a sensor or detector

Optical detection

The typical CD or DVD optical head contains a number of high-quality, precision components, including a collimated laser, beam splitters, high-quality lenses, and mirrors. A standard CD or DVD player uses the laser optical setup to read a binary series of tiny bumps and pits on a disc. The difference in the scattering angle of the light as the laser bounces off the bumps and pits on a disc is then converted into a code for playing music or video. By adding a minimal number of modifications, this same technology has been adapted into low-cost microscopes and spectrophotometers for imaging of cells and other biological components.

For example, absorbtion measurements, based on changes in optical density, are amongst the most commonly used on the lab-on-a-disc platform. In absorption diagnostics, analyte concentration is determined by measuring the absorbance of specific wavelengths of light through a sample. According to the Beer-Lambert Law ($A = c\epsilon l$), absorbance (A) is linearly proportional to the concentration of an analyte in a solution (c), the molar absorptivity

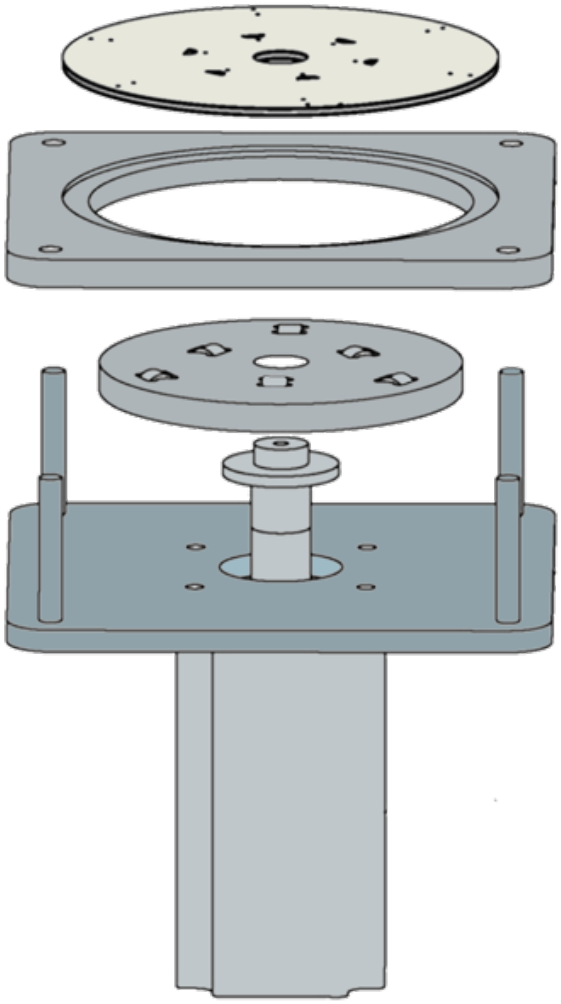

Figure 7.7: A schematic of the bead beating setup is shown. Magnets are placed at two different radial distances. As the disc is spun, a ferromagnetic disc moves back and forth in the disc.

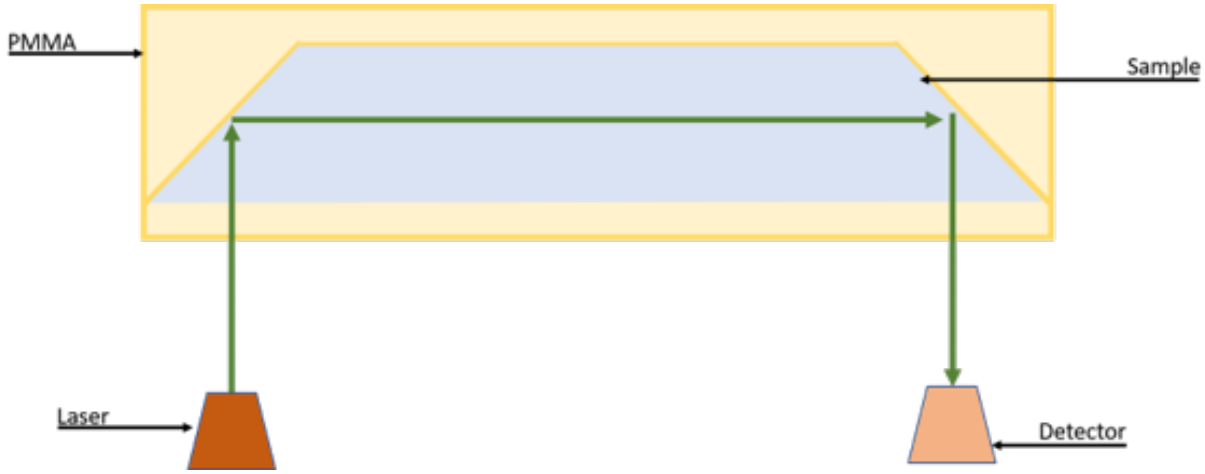

Figure 7.8: A schematic shows how the principle of total internal reflection can be used to increase the path length and enhance absorption in the disc by milling v-shaped grooves in a chamber on the disc.

of the sample (ϵ), and the optical path length through the detection chamber (l). In a microfluidic device, this optical path length is typically very short, and thus the sensitivity of these measurements can be compromised severely.

To account for this, Grumann et al. used a total internal reflection (TIR) mirror-based system to increase the on-disc optical path length to make sensitive glucose measurements from human blood [47]. Figure 7.8 shows a proposed schematic that utilizes a set of parallel milled, angled trenches in the disc which would be covered with a reflective, foil adhesive to bounce laser light through the solution and direct it onto the photodiode. In accordance with Snell's law, the critical angle (α_{crit}, of the milled trench can be calculated to produce total internal reflection throughout the sample ($\alpha_{crit} = sin^{-1}(\frac{n_{air}}{n_{mat}}$. Similarly, Nwankire et al. used a 3D-printed portable spin stand with integrated absorbance measurements to implement a six-parameter liver assay panel from whole blood [138]. Absorbance is also widely used in environmental monitoring [23, 65]. Colorimetric measurements methods have also been used for this application [90].

Fluorescence is amongst the most widely-used detection methods in biomedical diagnostics and has been demonstrated on-disc for applications, such as fluorescent immunoassays [96,

54] by building a low cost fluorescent microscope into the system itself. Fluorescent detection methods, unlike colorimetric detection, do not depend on the optical path length of the sample, contributing to the enhanced lower limit of detection of the method. For example, Duffy et al. used fluorescence to detect 2000 times lower concentration of a substrate, p-nitrophenol phosphate, than using colorimetry in the same sample volume. Fluorescence has been used successfully in conjunction with the centrifugal microfluidic platform for a wide range of applications, including solid phase extraction analysis of PCR assays and immunoassays [82, 173, 61].

Fluorescent detection is generally done with a stationary disc, forcing the user to stop the disc and manually align it to the camera to perform detection. To solve this problem, Ukita and Takayama developed a stroboscopic optical setup to image fluorescent objects on a spinning platform [185].

Electrochemical Detection

Electrochemical detection is an attractive alternative to optical detection because of its low cost, small equipment footprint, high sensitivity, specificity, and portability [111, 195]. The most common type of electrochemical detection used in microfluidic systems is amperometric detection. In amperometric detection, the current produced with either the reduction or oxidation of an electroactive species is monitored.

Amperometric detection has been successfully integrated onto the LoD platform using a slip ring-and-brush setup, shown in Figure 7.9 [132] or a low-noise slip ring with liquid mercury for moving electrical contact [7]. In this detection scheme, three electrodes are typically used: a working electrode, a reference electrode, and an auxiliary electrode. An electrical potential is applied between the working electrode and the reference electrode. At the appropriate potential, a redox reaction occurs, and a current is generated. This current, measured

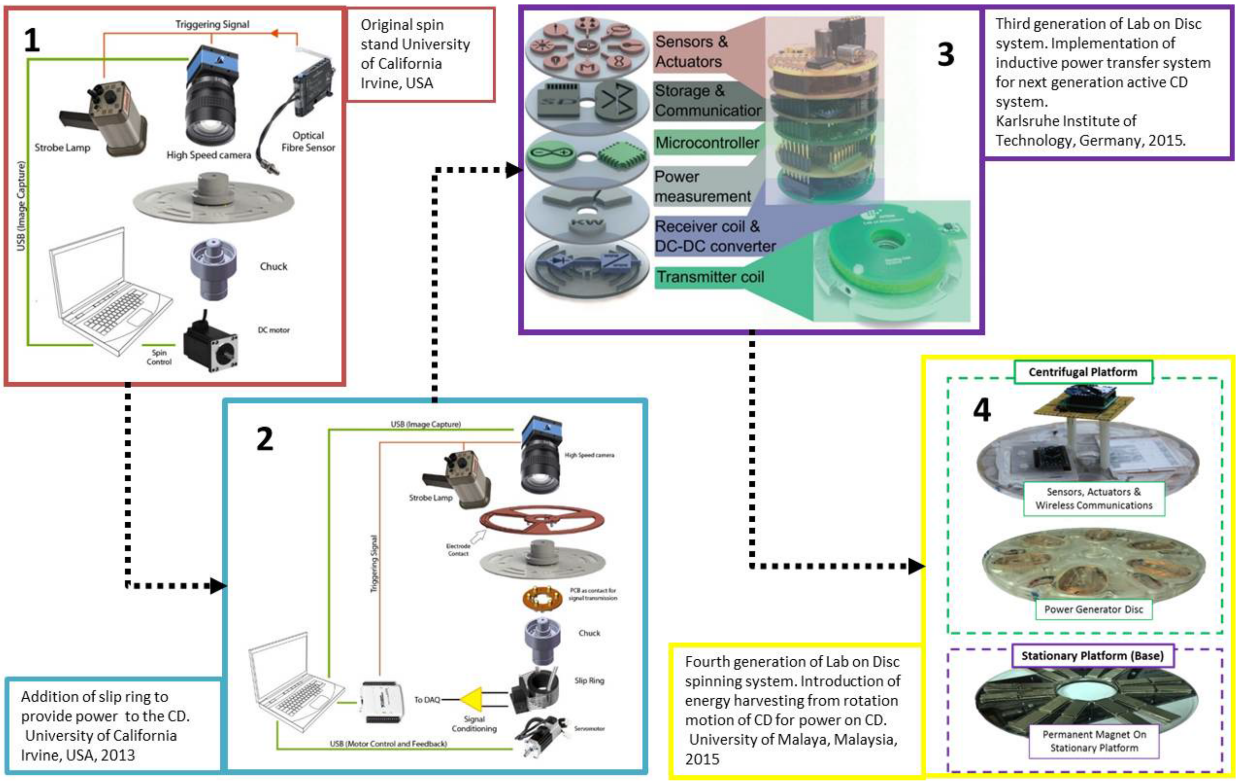

Figure 7.9: Progression of centrifugal microfluidic technology platforms towards stand-alone POC systems from different research groups. System 1 shows the original spin stand structure [110]. System 2 illustrates the addition of a slip ring to the spin stand set-up [119]. System 3 shows the implementation of an inductive power transfer system, reproduced in part from [58] with permission of the Royal Society of Chemistry. System 4 illustrates energy harvesting through the rotating motion of the disc [68].

between the working and auxiliary electrode, is directly proportional to the concentration of analyte being measured, and the voltage potential, measured between the working and reference electrodes, can be used for inferring the presence of a specific analyte in the system [9].

One application of this method is the detection of proteins or antigens in bodily fluid based on the redox reaction of a substrate bound to the target proteins or antigens. Kim et al. recently used this method to detect C-reactive protein (CRP) [82]. This electrochemical method can be used to replace the optical component of standard ELISAs, reducing the footprint of the system.

For POC applications, bulky and expensive external instrumentation is not desirable, limiting some optical set-ups for these applications. Therefore, electrochemical detection methods, which are inexpensive, portable and have a low equipment footprint, are becoming an increasingly favorable option for extreme POC settings. Additionally, fluorescent sensing on CD-based platforms often requires more expensive optical-grade polycarbonate discs, a parameter that does not affect electrochemical detection. The latest electrochemical sensors, such as amperometric sensors featuring redox amplification [184], have sensitivities and very low limits of detection (LODs) that are comparable to optical detection schemes, making them an attractive option for application in future POC systems.

To accomodate this move towards more portable detection methods, centrifugal system set-ups or spin stands have progressed over time in terms of functionality and sophistication. Figure 7.9 illustrates the progression of centrifugal microfluidic technology platforms towards stand-alone devices for extreme POC applications stemming from a number of different research and development institutions. In addition, CD-based systems implementing energy-harvesting techniques have also been developed [68].

Chapter 8

Materials and Methods

8.1 Platform Instrument Fabrication

The portable platform consists of two key components: 1) The spinbox, or instrument (Figure 6.2), and 2) disposable microfluidic cartridges (Figure 8.3). The instrumentation automates the sample processing in the microfluidic cartridge and was assembled primarily from modified off-the-shelf components and 3D-printable parts. The code controlling the various aspects of the instrumentation was written in Python 3, loaded into a Raspberry Pi 3B+ running NOOBS, and interfaced using a 7" Raspberry Pi Touchscreen. An in-house PCB was prototyped to distribute power to various components. The Python repository, CAD assemblies, and PCB drawing can be found at XXX.

The enclosure was assembled from laser-cut PMMA (McMaster Carr) and secured to t-slot extrusions (McMaster Carr). The touchscreen and Raspberry Pi holder were 3D-printed in polycarbonate material on a Stratasys Fortus 450MC material extrusion printer. For experimental testing, a custom spinchuck was machined in aluminum and uses two spring loaded balls to hold the microfluidic cartridge in place. For the portable unit, a world-to-chip

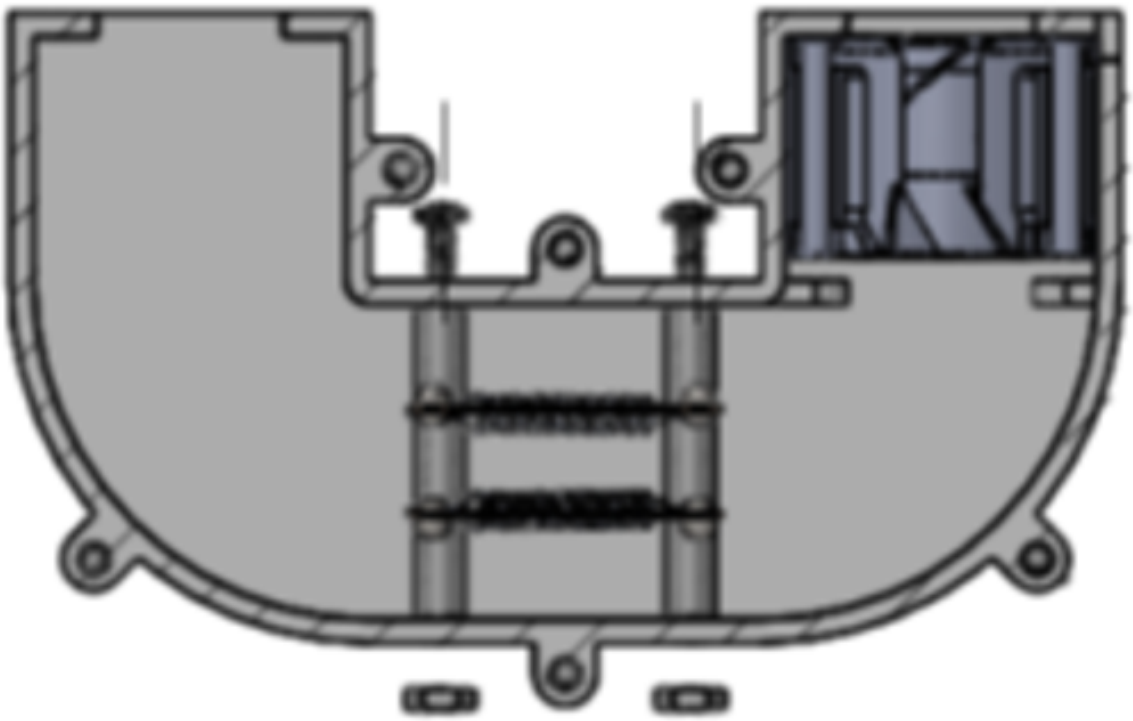

Figure 8.1: The heater consists of a u-shaped, 3D printed housing, resistive coil, and fan.

microfluidic spinchuck was prototyped and 3D printed using a Raise 3D N2 Plus printer.

The environmental control system consisted of a custom fabricated heater and PID temperature controller. The heater was made from a 3D printed, u-shaped housing into which a NiCh resistor coil and micah holder were inserted, see Figure 8.1. A fan was placed on one side of the holder to blow air over the heated resistive element. A thermocouple was placed below the disc and delivered temperature measurements to a PID controller, which regulated the temperature of the resistive element.

Another critical feature of the Spinbox was the development of a fluorescent microscope in the system. The optics component consists of a Mako G-507B monochromatic CMOS camera, an excitation LED, a set of custom arranged filters and focusing lenses, including a

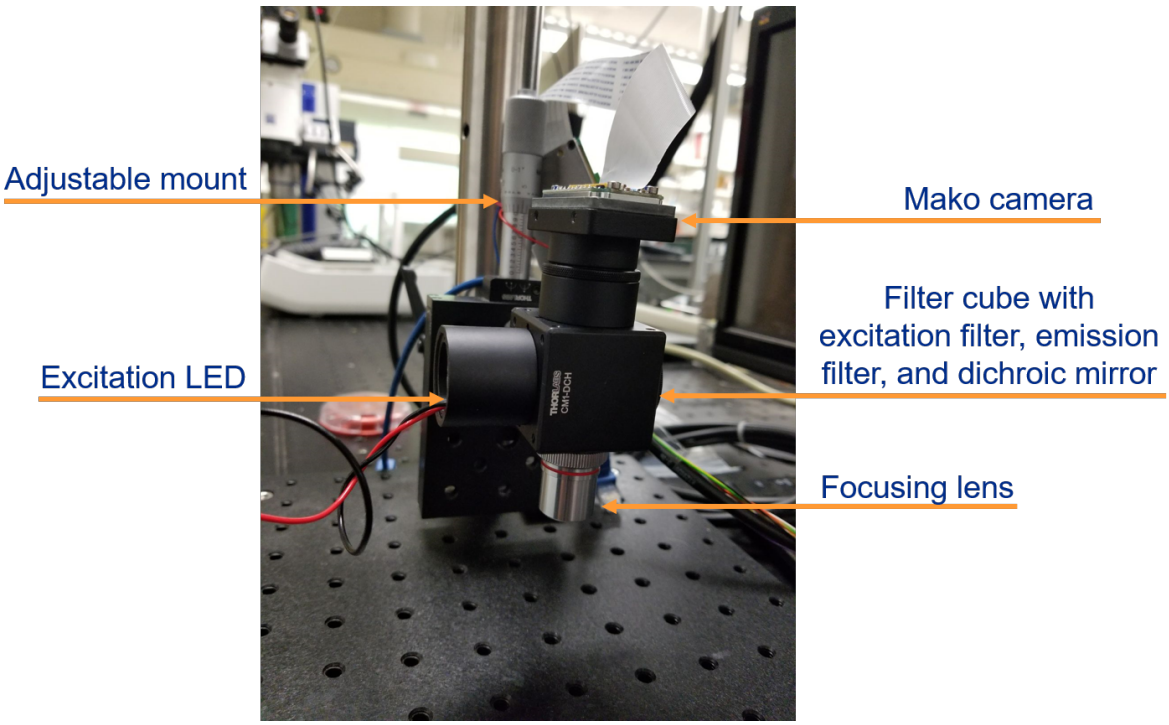

Figure 8.2: The detection system we implemented in the Spinbox includes a monochrome camera, a set of lenses and filters for Cy5 detection, a set of LEDs at 625 nm, a focusing lens, and an adjustable mount.

Cy5 excitation filter, a Cy5 camera emission filter, and a dichroic mirror, and an adjustable camera mount that allows the user to manually change the focal plane of the camera, see Figure 8.2 and Figure A.4.

The camera, combined with an image processing algorithm written using OpenCV was able to take a series of images and perform background subtraction, image smoothing, noise thresholding, spot identification, and intensity quantification, see image processing for representative spots of cy5. The final output was a text file of spot size and intensity.

Details about the rest of the components, assembly, and operation of the platform are included in Appendix A.

8.2 Microfluidic Disc Fabrication

Three different types of microfluidic discs were fabricated in this work: prototype Cyclic Olefin Copolymer (COC, TOPAS) discs manufactured using a CNC machine at microfluidic Chipshop GmbH (Jena, Germany), prototype Poly(methyl methacrylate) (PMMA) discs fabricated using a laser cutter (Trotec Speedy 360), and Cyclic Olefin Copolymer (COC, TOPAS) injection molded discs obtained from microfluidic Chipshop GmbH (Jena, Germany). NaOH was stored in a groove machined in the center of the lysis chamber and sealed using wax. A metal disc that facilitates cell lysis was placed on top of the wax seal to prevent premature release of NaOH. Equal quantities of lysis beads were dispensed into the lysis chambers using a slurry of silica-zirconia beads mixed with polyvinyl alcohol. The disc was then placed into a vacuum heater at 40° C for 30 minutes. Dried down phosphbate buffer (1X) and detector probes were dispensed into the neutralization chamber prior to assembly. Finally, the COC inner feature layer was placed on an alignment jig and sandwiched between two transparent, gas-permeable, single-sided adhesives (MP Biomedicals 097640205) that were cut to shape using a polyvinyl cutter (Silhouette Cameo 2). A double-sided adhesive (3M 300 LSE) was affixed to the cutout on the bottom of the detection chamber of the disc, creating a fluidic seal between an optional, modular microarray and the detection chamber of the disc.

8.3 Bacteria, antibiotics, and media

E. coli clinical urine isolates were obtained from the University of California, Los Angeles (UCLA) Clinical Microbiology Laboratory with approval from the UCLA and Veterans Affairs Institutional Review Boards and appropriate Health Insurance Portability and Accountability Act exemptions. Bacteria was inoculated into Mueller-Hinton (MH) broth with

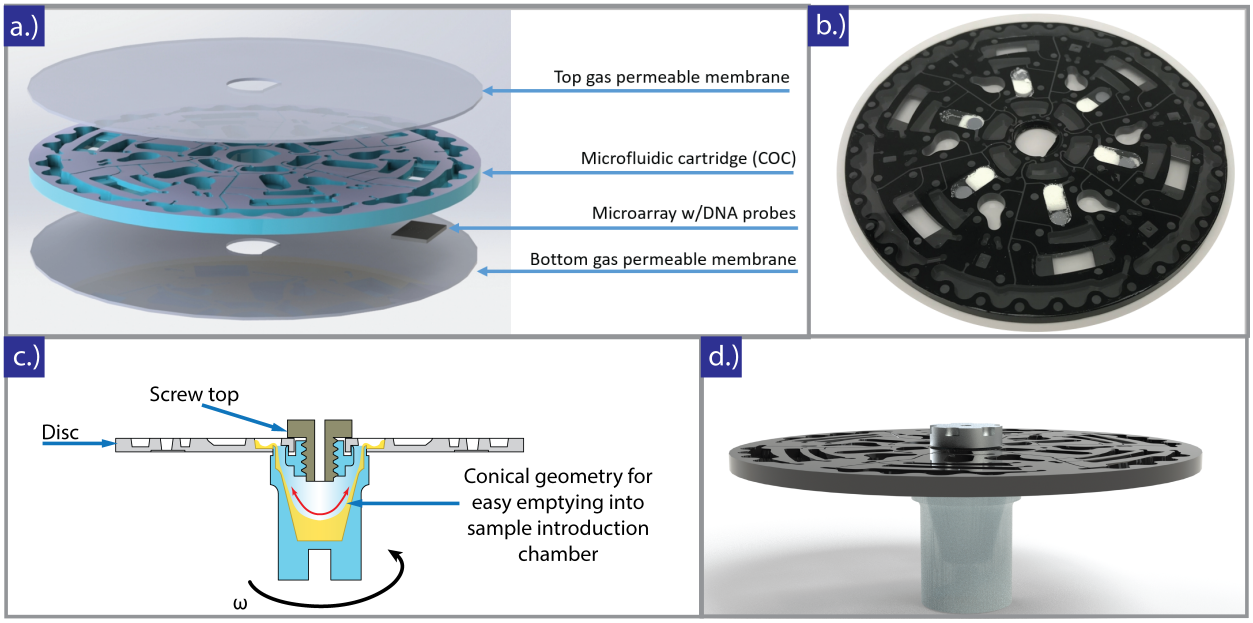

Figure 8.3: The microfluidic disc design. a) The disc consists of 3 layers: an inner feature disc made from COC with disc chambers and channels milled on both sides, and 2 laminating, gas-permeable adhesives that seal in the features. An optional microarray can be inserted for hybridization of rRNA with capture probes, b) A photo of the assembled disc, with all components inside, is shown, c) A cross section schematic of the world-to-chip interface is shown, d) The fully assembled cartridge, including the disc and world-to-chip interface.

12% glycerol (Becton, Dickinson, Sparks, MD) and stored at -80° C.

Experiments were conducted from the frozen isolates. Bacteria was defrosted and cultured overnight by inoculating 5 μL of freezer stock bacteria into 5 mL of cation-adjusted Mueller Hinton (MH_2) broth (Sigma, St. Louis, MO) and incubating in a shaker incubator at 37 C. The following day, working samples were prepared by diluting the overnight culture with MH_2 broth to $\sim 6 \times 10^5$ cfu/mL. The prepared cultures were pipetted into the incubation chamber on the disc or 96-well plate and immediately sealed. Bacteria was also plated on LB agar (MOBIO Laboratories Inc., Carlsbad, CA) to verify the colony forming units (cfu).

For rapid incubation experiments, either 75 μL or 200 μL of prepared cultures were pipetted into each chamber of the disc or 96-well plate and placed in the appropriate spinstand incubator or shaker incubator. Bacteria was incubated at 37 C and oscillated at 1 Hz through an angle of 180 on the spinstand or 400 rpm on the tabletop shaker. After the designated incubation period, sample was collected for plating or lysed for Luminex analysis. Serial dilutions (10^{-6}) were performed prior to triplicate plating and were incubated overnight prior to counting the following day. For Luminex readings, 70 μL of sample was removed from the chambers and mixed with 35 μL of 1M NaOH for 5 minutes. The sample was neutralized by adding 105 μL of phosphate buffer solution. 150 μL of neutralized lysate was collected and characterized using a Luminex MagPix assay instrument with custom capture probes designed to hybridize with oligonucleotides on Luminex MagPlex-TAG microspheres.

In certain growth experiments, cultures were spiked with one of the following antibiotics diluted in (MH_2) broth before incubation in the disc: 4 μg/ml ciprofloxacin (Sigma, St. Louis, MO), 32 μg/ml ceftriaxone, 512 μg/ml ampicillin, g/ml nitrofurantoine, or μg/ml cefazolin.

For cell lysis experiments, bacteria was spun down from the incubation chamber into the cell lysis chamber following sample entry.

Chapter 9

Results and Discussion

9.1 Microfluidic CD design and operation

9.1.1 CD forces and principle of operation

We take advantage of the psuedo-forces present on a rotating platform to tackle challenges in laminar flow systems that have limited their use in AST microfluidics. There are three main psuedo-forces on rotating platforms: the Euler force, Coriolis force, and Centrifugal force.[89] The SpinBox predominantly takes advantage of the Euler and Centrifugal forces to guide sample through the multiple assay steps in the microfluidic disc.

The Centrifugal force, shown in Equation 9.1, acts radially outward, providing unidirectional liquid pumping. The many chambers and channels milled into the disc create barriers to fluid flow. A narrow channel coming out of a chamber creates a pressure barrier that must be overcome before fluid can pass. By rotating the disc above a critical speed, the centrifugal

force can overcome the pressure force and the fluid is free to burst to the next chamber.

$$\vec{F_c} = \rho\vec{\omega}(\vec{\omega} \times \vec{r}) \tag{9.1}$$

The Euler force, perpendicular to the Centrifugal force, is proportional to the change in angular velocity per unit time and can be used to generate vortical flow and provide uniform mixing within a microfluidic chamber. The Euler force, per unit volume, is expressed in Equation 9.2

$$\vec{F_E} = -\rho\frac{d\vec{\omega}}{dt} \times \vec{r} \tag{9.2}$$

where s is the liquid density, $\frac{d\vec{\omega}}{dt}$ is the change in the angular velocity per unit time, and $\vec{r}$ is the mean distance of the liquid from the center of the disc.

This force dominates when the disc is subject to changes in velocity, such as cycles of unidirectional acceleration-and-deceleration or changes in the direction of rotation. Turbulent mixing, and bacterial incubation, is thus dependent on chamber geometry (height and inner and outer chamber radii, r_1 and r_2 in Figure 9.1), acceleration/deceleration rate, and angular span of the mixing chamber [150]. Oscillation is accomplished by cycling between two angles of the disc at a specific frequency. This motion takes advantage of the Euler force to create chaotic advection within the sample, effectively mixing it.

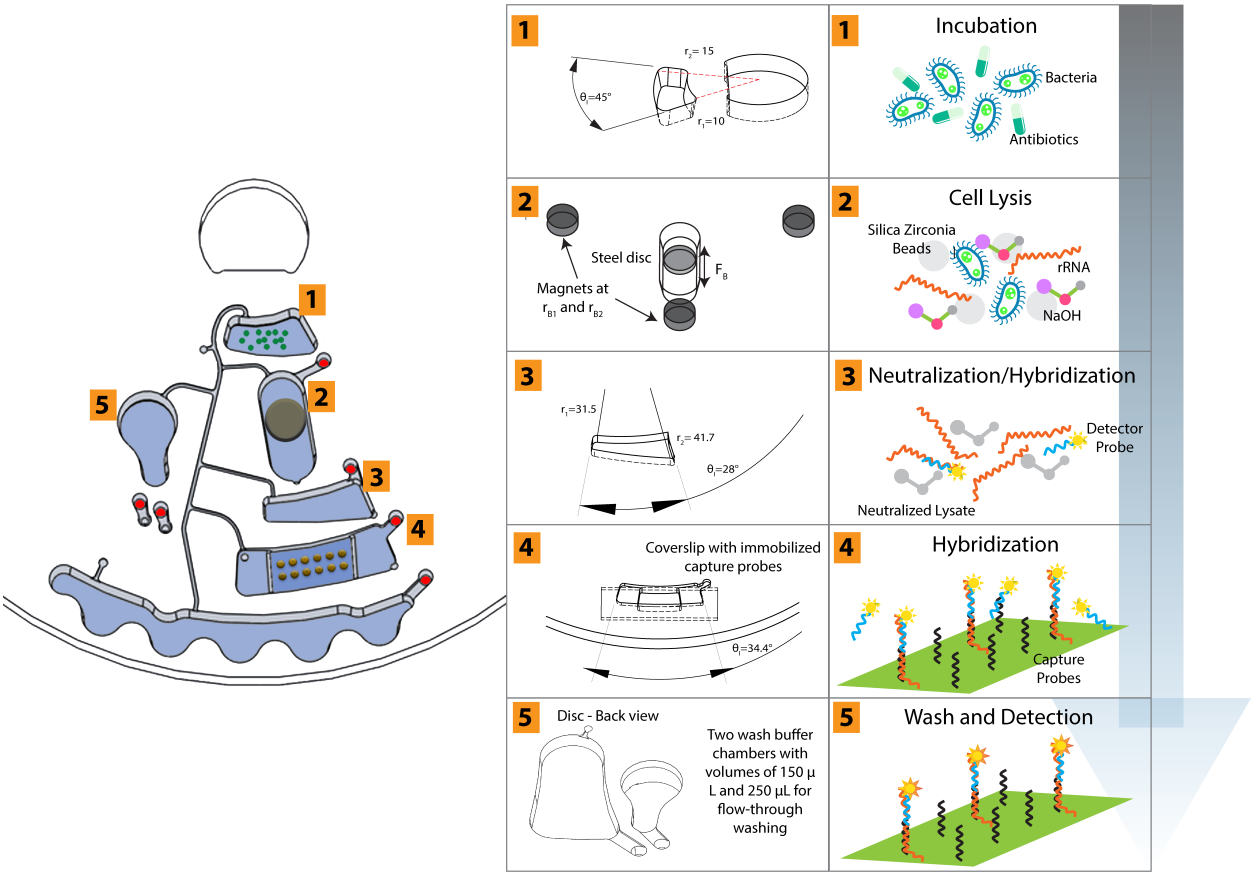

Figure 9.1: The microfluidic disc design is shown with assay steps on right corresponding to fluidic chambers labeled on the disc. The middle column highlights critical features of important fluidic geometries on the disc.

9.1.2 CD design and fluidic steps

To take advantage of the multiplexing capacity of the microfluidic disc, each disc consists of 6 multiplexed, fluidically identical, but separate sections of the disc. Each section was used to test a different bacteria and antibiotic combination. In practice, each section would be used to test the patient sample for susceptibility of different antibiotics. The testing sequence begins with sample loading into the first chamber of the microfluidic disk.

Table 9.1 demonstrates the fluidic sequence for the microfluidic disc. To simplify sample loading, we prototyped a world-to-chip (WTC) interface to dispense liquid into the first chamber of each section of the disk simultaneously. The sample is loaded into the main

Table 9.1: Microfluidic Disc Sequence

Step	Protocol	Details
Incubation	Oscillation	2 Hz, 180°
Valve 1	Laser+Spin	2000 RPM
Cell Lysis	Spin	200 RPM
Valve 2	Laser+Spin	2000 RPM
Neutralization	Oscillation	1 Hz, 180°
Valve 3	Laser+Spin	2000 RPM
Hybridization	Oscillation	1 Hz, 180°
Valve 4	Laser+Spin	4000 RPM
Wash 1	Spin	1000 RPM
Wash 2	Spin	1000 RPM
Detection	Position + Camera	0 RPM

compartment, designed to store liquid buffer, and the centrifugal disk is secured using the self-sealing "top-piece". Baffles were incorporated at the bottom of the WTC to improve mixing during oscillation. By spinning at a critical RPM (¿5000), the centrifugal force drives the mixed sample up the inner walls of the WTC and through the outlet holes connected to each incubation chamber. Metering is accomplished by taking advantage of chamber geometry and having overflow channels, shown in Figure 9.1. The volume of the sample entry chamber dictates the amount of sample used in the disc and the rest runs off to the waste chamber via an overflow channel on the bottom of the disc.

An oscillation protocol is used to incubate bacteria once in the incubation chamber (Figure 9.1). The incubation chamber is subject to cycles of rapid acceleration/deceleration at an angular span of 45° to generate vigorous mixing. The robust mixing provides even distribution of macromolecules (e.g. antibiotics and nutrients) and ensures sufficient sample aeration, required for bacterial growth. Oscillation is also used in the neutralization chamber to resuspend dried down phosphate buffer.

The lysis chamber utilizes a combination of mechanical and chemical lysis to effectively release genomic data from a number of bacterial pathogens. As the microfluidic disc is rotated at a low angular velocity (¡500 RPM), the metal disc interacts with the array of

permanent magnets, moving back and forth in the lysis chamber and mixing the sample with the silica-zirconia beads and the chemical lysis reagent (1 M NaOH). The mechanical forces generated between the metal disc and beads provide shear forces that break open cell walls.

The neutralization chamber contains dried down PBS and fluorescently labeled detector probes, which are resuspended during oscillation of the disc. The PBS neutralizes the NaOH from the lysis chamber, preventing degradation of rRNA sequences. At this point, the sample can be either removed from the disc, for detection on a separate system (e.g. Luminex Mag-Pix or other fluorescent microscope), or can continue on for hybridization and detection directly in the disc if a microarray is inserted into the detection chamber.

The hybridization and detection chamber contains a sticky adhesive on one side, allowing a glass or polymer slide functionalized with detector probes (microarray) to snap into the back of the disc. A 9 x 5 mm window exposes the detector probes to the rest of the chamber. Following neutralization, neutralized lysate slowly and completely fills up the chamber. Diffusion, combined with oscillatory mixing, allows rRNA to hybridize and bind with the complementary detector probes. Following hybridization, two wash buffers are released, flowing through the chamber to wash away any unbound rRNA into a waste chamber, eliminating false positive results. After these washing steps, the detection chamber is imaged using the camera and fluorescent lenses present in the SpinBox.

A series of active valves are used as gates between different chambers connected by narrow fluidic channels, see Figure 9.2. Since the inner feature disc is fabricated from a black COC polymer, these valves are made by milling half of a channel on one side of the feature disc, and the subsequent half on the other side of the disc, leaving a 0.25 mm thick piece of COC overlapping the two half-channels, see Figure 9.2a. To open a valve, a laser is focused on the valve position (Figure 9.2b), melting away the plastic covering (Figure 9.2c and allowing free flow of liquid between the adjacent half-channels (Figure 9.2d). The energy required for

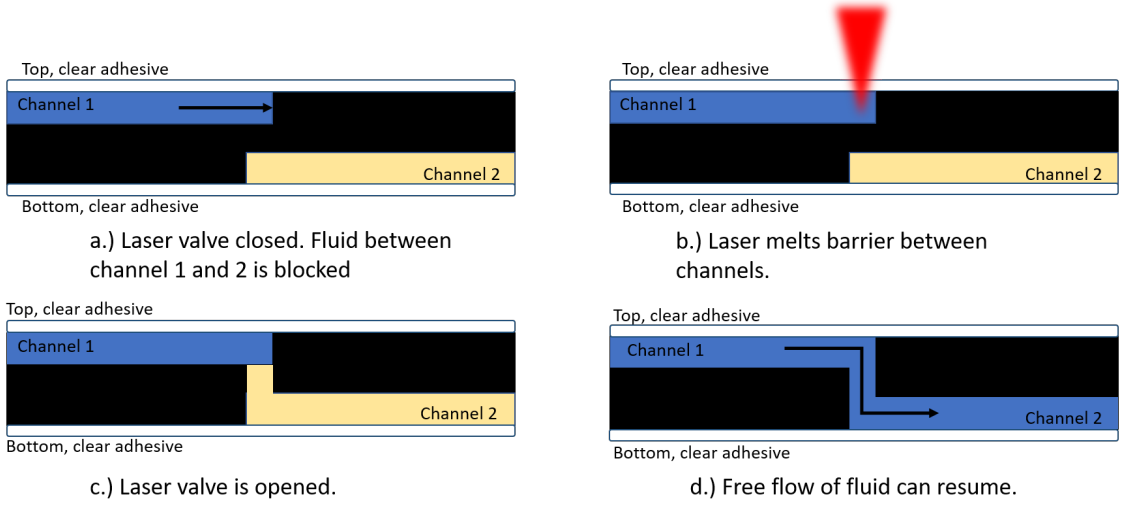

Figure 9.2: The sequence for opening one of the six laser valves on the disc is shown: a) Liquid in channel 1 (top side of disc and located at smaller radius than channel 2) is blocked from passing to channel 2 (bottom side of disc and located at larger radius than channel 1) by the black COC polymer, b) A laser is focused on the valve location, c) the COC polymer melts, creating an opening between channel 1 and 2, and d) Liquid is free to flow from channel 1 to channel 2.

opening each valve is nearly 1 Joule, estimated using equation 9.3.

$$Q_{tot} = Q_T + Q_F + Q_V = mc_p\Delta T + mL_F + mL_V \tag{9.3}$$

where c_p is the specific heat of our material, ΔT is the change in temperature needed to melt the material, m is the mass of the valve, L_F is the latent heat of fusion for our material, and L_V is the latent heat of vaporization for our material. With our 1 W laser, and an estimated efficiency of 20%, we require 5 seconds to open each valve. Positioning of the laser is accomplished in two ways: 1.) the radial position is set by a servo motor and linear rail onto which the laser is mounted and 2.) the angular position is set by moving the motor to a specified angular position.

9.2 Universal Cell Lysis

The bacteria cell wall has evolved to become one of the most resilient barriers against harsh environmental conditions filled with toxic contaminants. In fact, the origin of antibiotic resistance stems from this evolutionary response. For example, gram-negative bacteria are naturally more resilient to antibiotics than gram-positive bacteria due to their dual-layered cell envelope. The additional outer-layer, absent in gram-positives, consists of an asymmetric lipid membrane formed by exterior-facing lipopolysaccharides and interior-facing phospholipids.

Due to the thicker cell wall of gram-positive bacteria, a combination of mechanical and alkaline chemical lysis is needed to release rRNA from cells. The mechanical component of our lysis system helps puncture and tear open the tough outer cell membrane of gram-positive bacteria by causing shear and friction forces between the cell wall and 100 μm sized silica/zirconia beads (Figure 9.3b). Once the cell wall is obliterated, NaOH denatures the ribosomal complex, allowing the 16s rRNA fragment to be recovered (Figure 9.3c). Finally, the sample is neutralized with PBS to prevent rRNA hydrolysis by prolonged NaOH exposure (Figure 9.3d).

To optimize the lysis protocol for bacteria, we varied a number of parameters, including lysis time, spin speed of the disc (which determined the oscillation of the metal disc in the lysis chamber), silica/zirconia bead slurry amount (which determined the amount of grinding material for mechanical lysis), and lysis puck geometry. The results are shown for gram positive isolate Staphylococcus aureus (SA15-21-08) in Figure 8 and expressed as a percentage of the Luminex signal obtained using the Omnilyse commercial lysis system. As a control, chemical lysis (1 M NaOH) is shown as well. The results of the optimization experiments were used to determine an optimal universal lysis system, with characteristics summarized in Table 9.2.

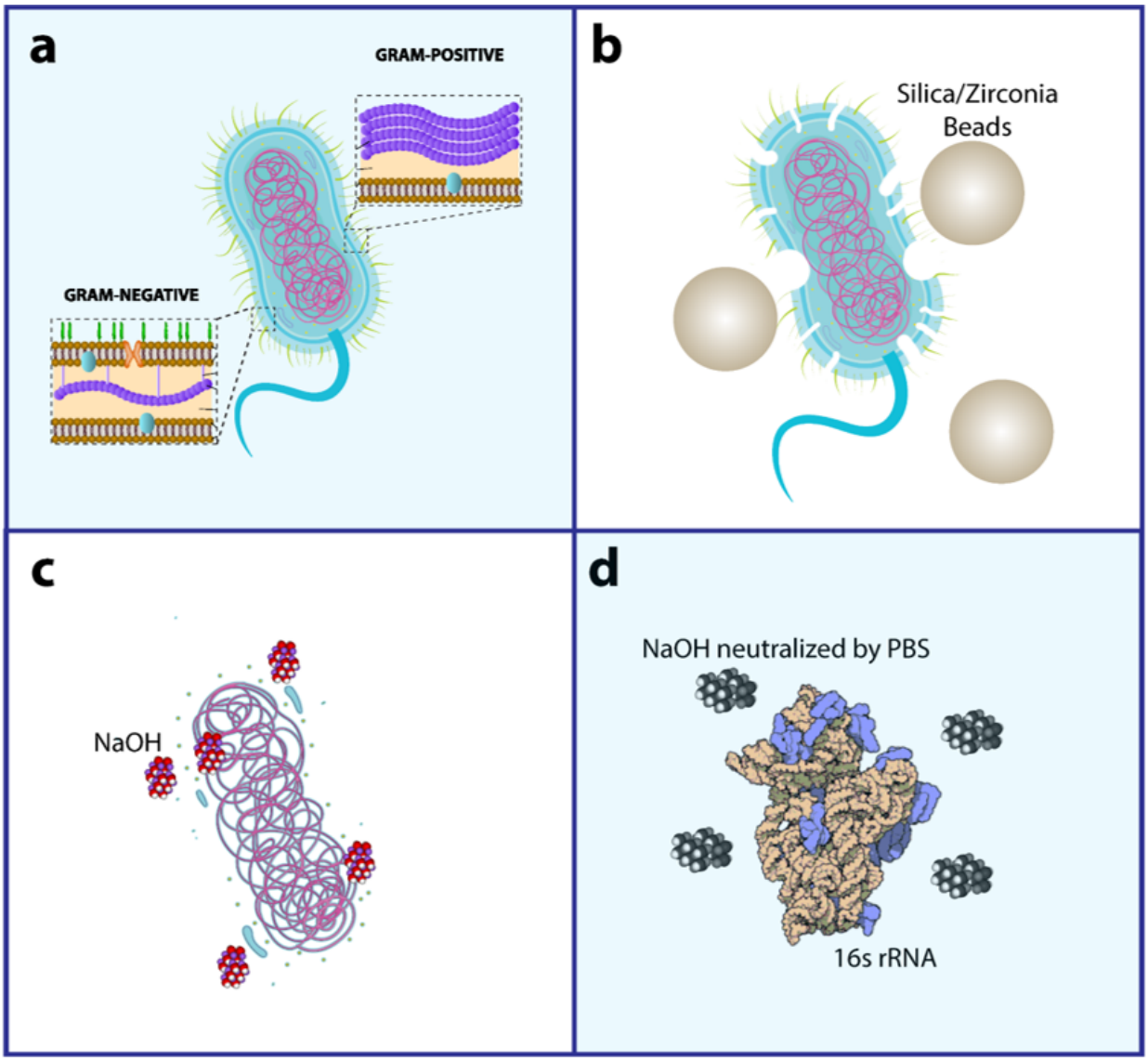

Figure 9.3: Universal lysis schematic: a) The thick cell wall of gram-positive bacteria means both chemical and mechanical lysis are required, b) Mechanical lysis with metal discs and silica/zirconia beads punctures cell walls, releasing genomic data, c) Alkaline lysis (1M NaOH) denatures ribosomal complex, allowing target rRNA fragmets to be recovered, d) PBS neutralizes NaOH, preventing further RNA hydrolysis.

Table 9.2: Lysis Characteristics

Characteristic	Optimal Value
Lysis Time	6 min
Spin Speed	100 RPM
Bead Amount	120 μL
Puck Geometry	Double

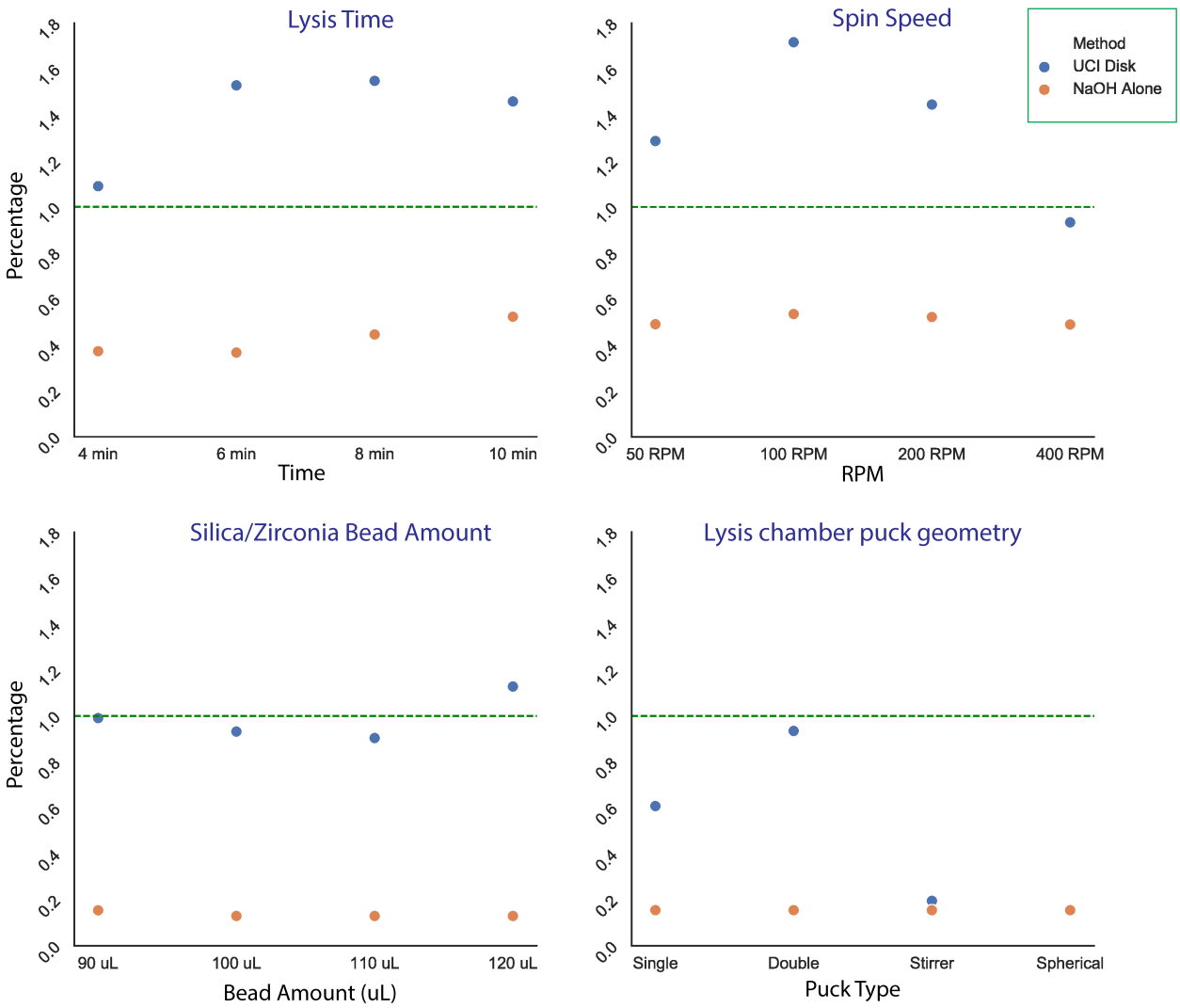

Figure 9.4: Optmizing lysis efficiency. Both chemical lysis and chemical+mechanical lysis of E. Coli were tested against the Omnilyse cartridge for a series of parameters. All measurements are shown as a percentage of the omnilyse cartridge signal, which has been normalized to 100% (dotted green line). a) Total lysis time was varied from 4-10 minutes. b) Total spin RPM was varied from 50-400 RPM. c) Total Silica/Zirconia bead slurry was varied from 90-120 μL pipetted into the lysis chamber. d) Several puck geometries were tested, including a single or double thin steel disc, a magnetic stir bar, or a spherical steel disc.

Finally, to demonstrate our universal lysis system, we lysed several gram-positive bacteria, including 2 strains of Staphylococcus aureus (SA), a strain of Coagulas negative staphylococcus (CNS), a strain of Streptococcus agalactiae (Sagal), and a strain of Enterococcus (EFs), see Figure 9.5. While lysis efficiency on the disc varied, all strains showed lysis efficiency at least 75% of the Omnilyse system.

9.3 Rapid Bacteria Incubation

For liquid bacterial cultures, rapid and healthy growth depends on three main parameters: 1.) Sample aeration: A bacteria sample needs to have plenty of access to fresh oxygen for growth, 2.) Nutrient availability: A sample needs to be thoroughly mixed in order to provide nutrients equally to all parts of the culture, and 3.) Prevention of biofilms and clumping: Shaking and agitation can prevent bacteria culture from settling to the bottom of a chamber and forming biofilms or clumps that hinder reproduction.

The low Reynold numbers in microfluidic systems exhibit laminar flow regimes, which are dominated by viscous, rather than inertial forces. The absence of turbulence makes healthy and rapid bacterial growth particularly challenging and forces microfluidic devices to rely on either passive molecular diffusion or external energy sources for mixing [200, 125]. Furthermore, the small enclosed volumes characteristic of microfluidic systems restricts access to fresh oxygen, making sample aeration difficult without bulky or complex external pumps that bubble oxygen through a sample [25].

To optimize incubation, while keeping within the available real estate of the portable disc, the incubation chamber characteristics in Table 9.3 were chosen. The angular span was maximized while still keeping 6 multiplexed sections on the disc, and r_1 and r_2 were restricted by the need for fitting all assay steps onto the chosen disc radius of 60 mm. The incubation

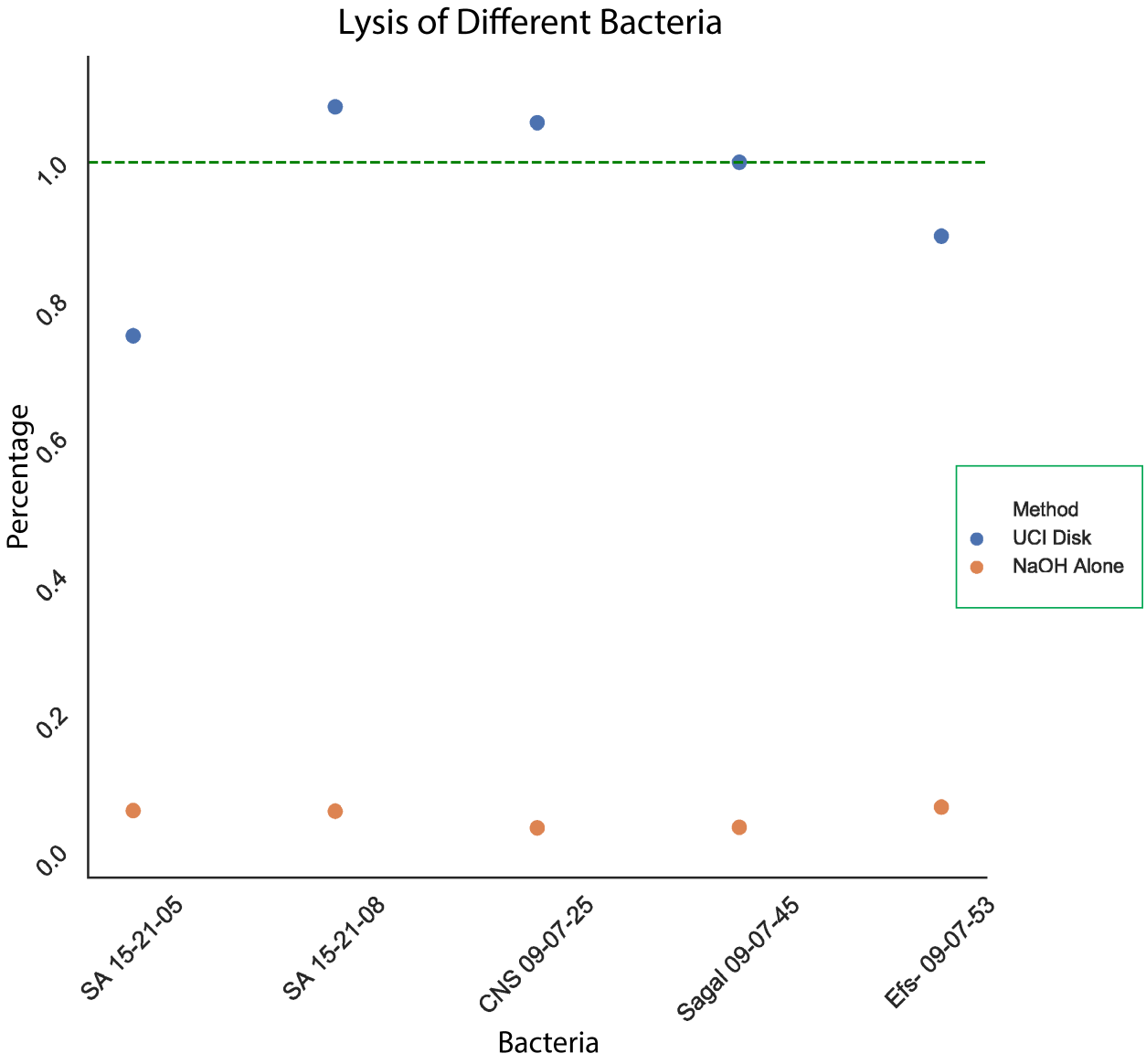

Figure 9.5: 6 gram positive isolates were compared with chemical lysis alone and chemical+mechanical lysis, including 2 Staph. aureus (SA), 1 Coagulas negative staphylococcus (CNS), 1 Strep. agalactiae (Sagal), and 1 Enterococcus (EFs). All measurements are shown as a percentage of the omnilyse cartridge signal, which has been normalized to 100% (dotted green line).

Table 9.3: Incubation Chamber Characteristics

Characteristic	Value
Inner radius (r_1)	10 mm
Outer radius (r_2)	15 mm
Acceleration/deceleration rate	240 rad/s
Angular span (θ_I)	45°

chamber was also milled completely through the inner feature disc, allowing for a large surface area of the chamber to be covered by a gas-permeable membrane.

9.3.1 Optimizing incubation time

We compared the growth using our chosen CD chamber design and oscillation protocol to cultures grown in a 96−well plate and CD placed into a standard incubator shaker (BRAND HERE) at 400 RPM. Observation of fluid within the different configurations showed more turbulence and advection in the disc in the Spinbox than in either the 96-well plate or disc in the SpinBox. Figure 9.6 shows a significant increase in rRNA growth of the disc on the spinstand at both 60 and 90 minutes compared with the other configurations. At 90 minutes, an average 162% increase in rRNA was observed in the incubator spinstand compared with a 96−well plate on the plate shaker incubator. The incubator disc in the SpinBox showed an average 122% increase in rRNA after 90 minutes compared to the 96 well plate, demonstrating that both the type of mixing and aeration have an effect on bacterial growth.

9.3.2 Incubation of multiple species of bacteria

To ascertain that the effect was not isolated to a single E. Coli strain, we compared growth on the disc and the 96−well plate in 14 different strains of E. coli, see Figure 9.7. The graph compares cfu/mL on the disc (y-axis) vs. the 96−well plate (x-axis). The red dotted line

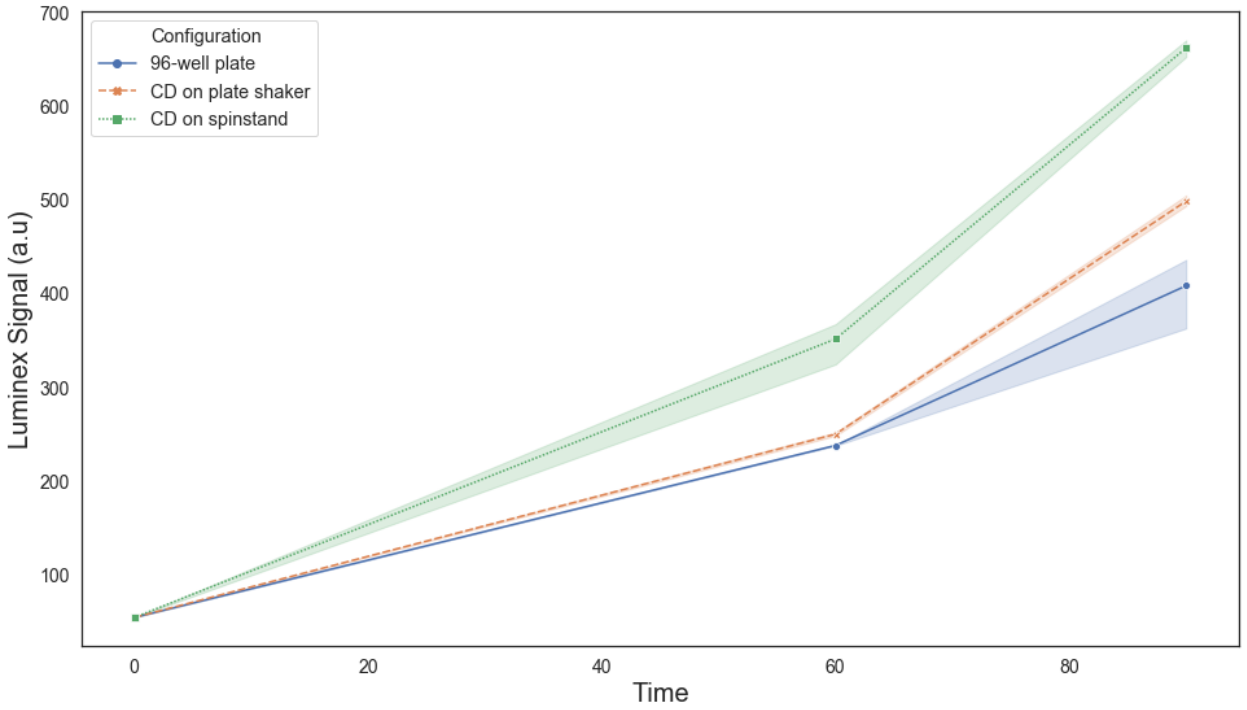

Figure 9.6: Comparing E. Coli growth on the 96-well plate in the plate shaker incubator, the disc in the plate shaker incubator, and the disc on the incubator spinstand. Growth is shown as luminex signal intensity. Shading represents error bars.

has a slope of 1 (y = x) and represents bacteria growing equally on the plate and on the disc. All data points above the red dotted line represent strains that grew better on the disc and data points below the red dotted line represent strains that grew better on the 96-well plate. The majority of the isolates tested showed more than 2x better growth on the disc than the 96-well plate. There were 2 strains of E. Coli that showed worse growth on the disc than on the 96-well plate. This might be either an outlier or might represent bacterial strains that favor alternative growth conditions. However, despite the growth characteristics of these E. coli strains, the measured cfu/mL, compared with the 0 minute time point, is sufficient to test antibiotic susceptibility.

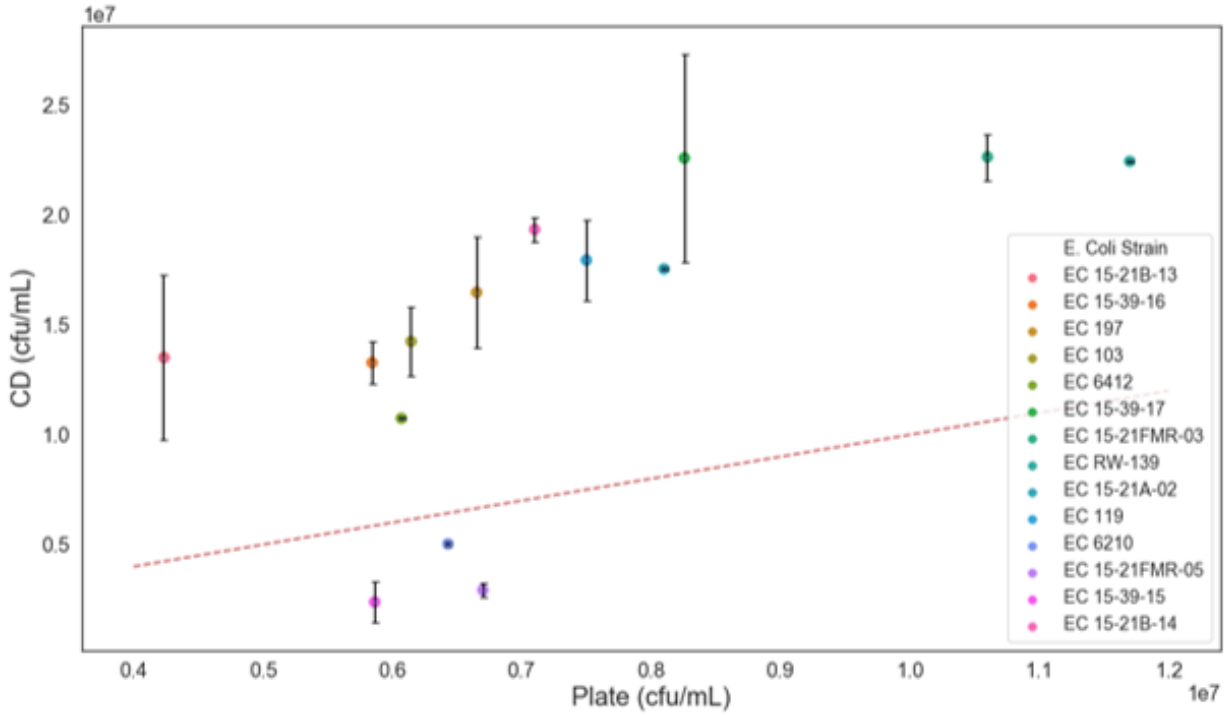

Figure 9.7: Growth for 14 different strains of E. coli in the disc on the incubator spinstand are compared with growth on the 96−well plate in the plate shaker incubator. The dotted red line ($y = x$) has a slope of 1, with data points above it showing greater growth on the disc and data points below it showing greater growth on the plate. Growth is shown in colony forming units per milliliter (cfu/mL).

9.3.3 Effects of the gas-permeable membrane

To isolate the effect of the gas-permeable membrane on growth, we looked at incubation with and without a gas-permeable membrane. Figure 9.9 compares the disc in the spinstand and 96-well plate in the plate shaker covered with either a gas-permeable membrane or a gas impermeable foil. To make sure variability only came from the type of membrane used, a prototype disc was used that isolated the incubation chamber. Half of each disc or plate was covered with the gas permeable membrane and half was covered with an impermeable membrane, see Figure 9.8. Therefore, the bacteria strain, shaking protocol, and material conditions were the same for all chambers. As seen in the graph in Figure 9.9, the gas permeable membrane allowed for significantly more growth than the nonpermeable foil for both the disc and 96-well plate (¿2x more growth for the 96-well plate, and ¿4x more growth

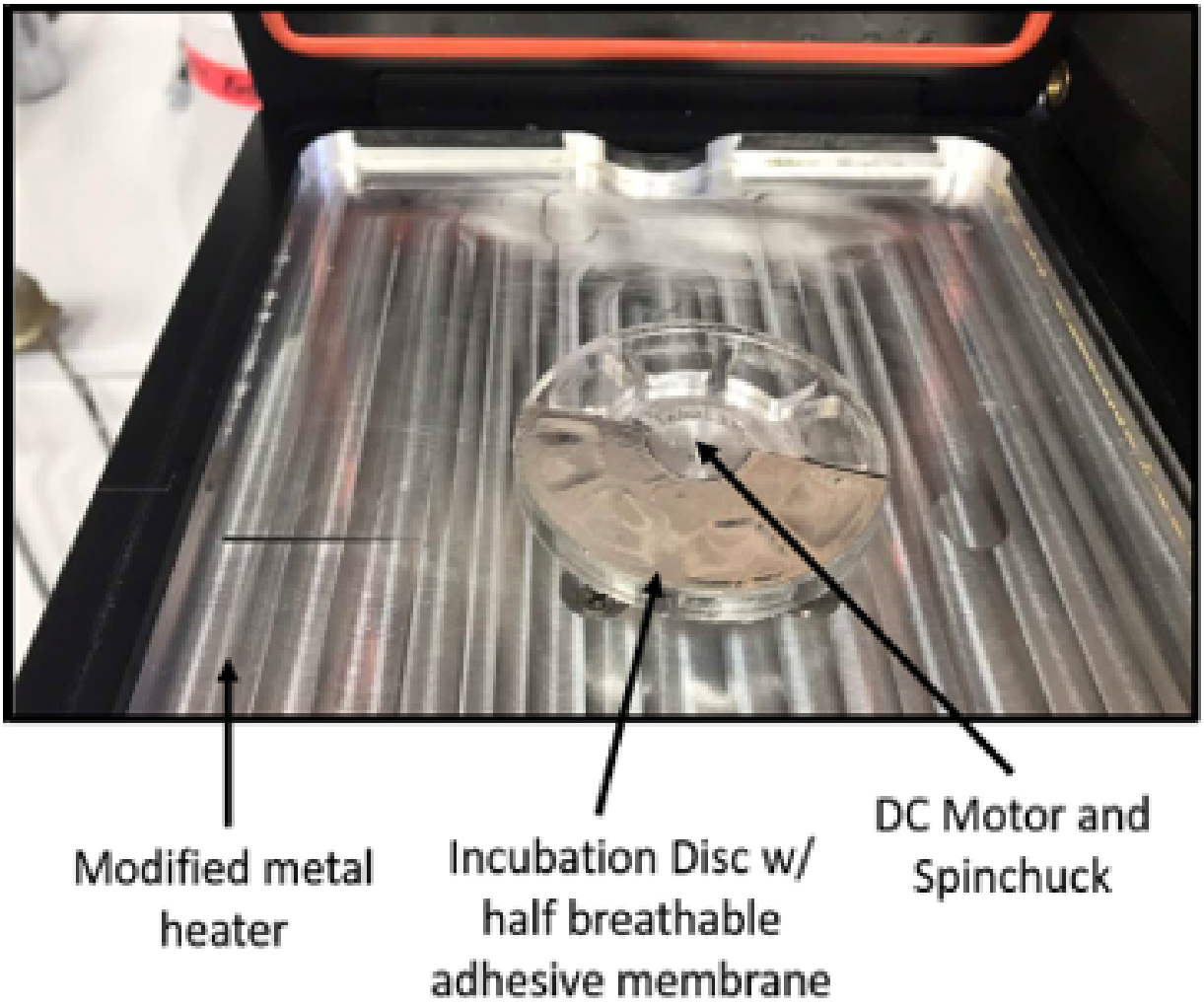

Figure 9.8: A prototype disc was fabricated that isolates the incubation chamber for testing the breathable membrane. Half of the disc is covered with a non-permeable foil adhesive and half is covered with the gas-permeable membrane.

for the disc).

9.4 Antibiotic Susceptibility Testing

To demonstrate our system was efficient in determining antibiotic susceptibility, 11 different E. coli isolates were incubated with a total of five commonly prescribed, broad-spectrum antibiotics using the microfluidic disc and compared to the 96-well plate. We chose three

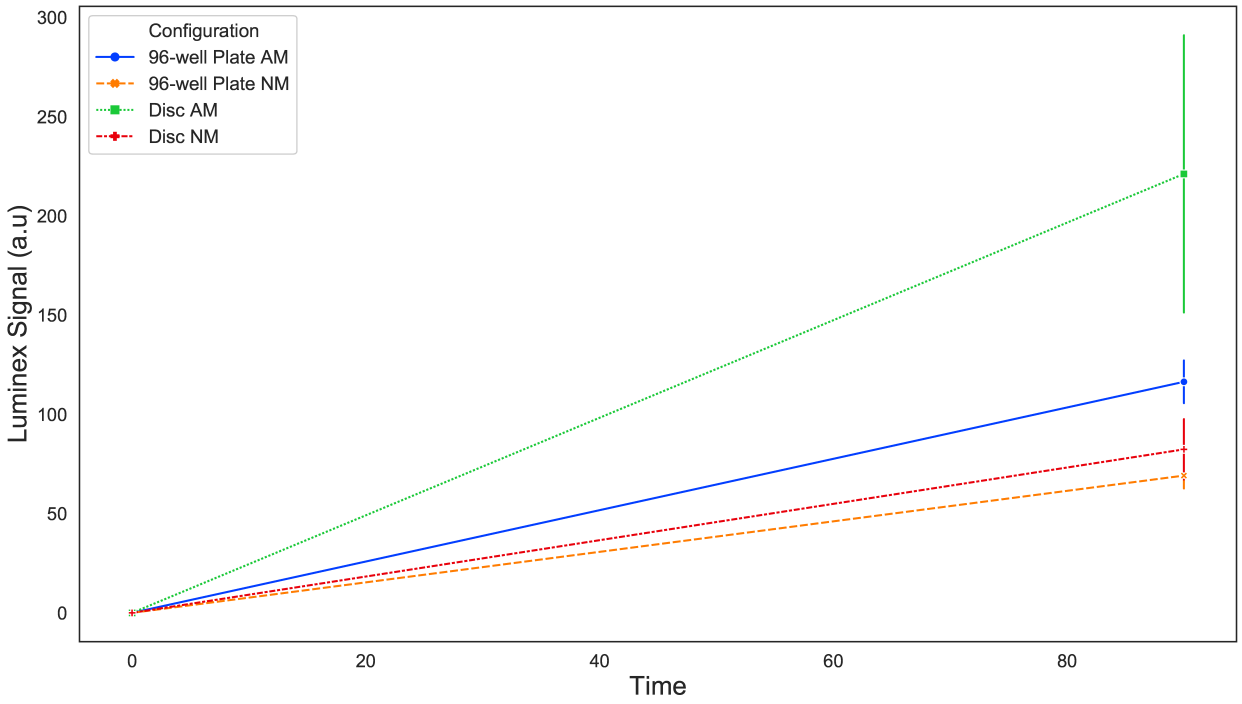

Figure 9.9: Results for growth of E. Coli in both the 96-well plate and disc both with and without an air permeable membrane.

antibiotics whose mechanism of action inhibits the bacterial cell wall (ampicillin, cefazolin, and ceftriaxone) and two antibiotics that target bacteria DNA functions, thereby preventing replication (nitrofurantoin and ciprofloxacin).

Figure 9.11 shows the ratio from the rRNA signals of bacteria incubated with and without antibiotics (Abx/No Abx) for both the disc (Figure 9.11a) and the plate (Figure 9.11b). If the ratio is large (near or above 1), the bacteria is resistant since its growth is similar to the no antibiotic control, see Figure 9.10. If the ratio is small (closer to or below 0), the bacteria is susceptible since its growth is suppressed by the antibiotic and much less than the no antibiotic control, see Figure 9.10. The red and blue lines in Figure 9.11 show the average of all resistant or susceptible bacteria on either the disc or plate (error shown as a gradient). While both the plate and the disc showed significant differences in average ratios between the resistant and susceptible bacteria ($p<0.01$), the resistant bacteria showed higher average ratios on the disc than the plate ($p<0.05$) indicating an improved ability to

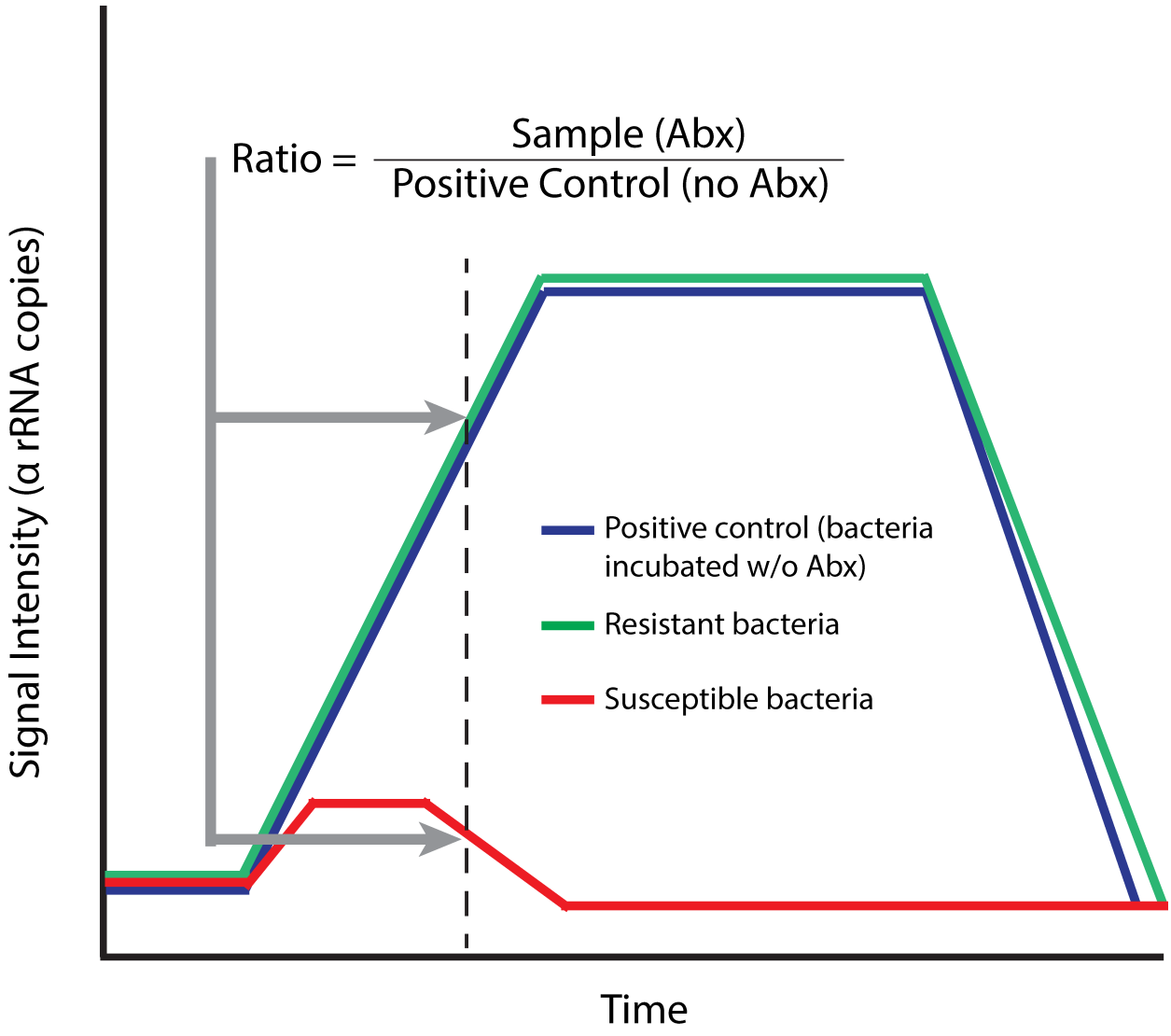

Figure 9.10: Conceptual drawing showing how the ratio is calculated for each signal. The ratio of the signal from the bacteria incubated with antibiotics to the positive control, where the same bacteria is incubated without antibiotics, is close to one for resistant bacteria and close to 0 for susceptible bacteria.

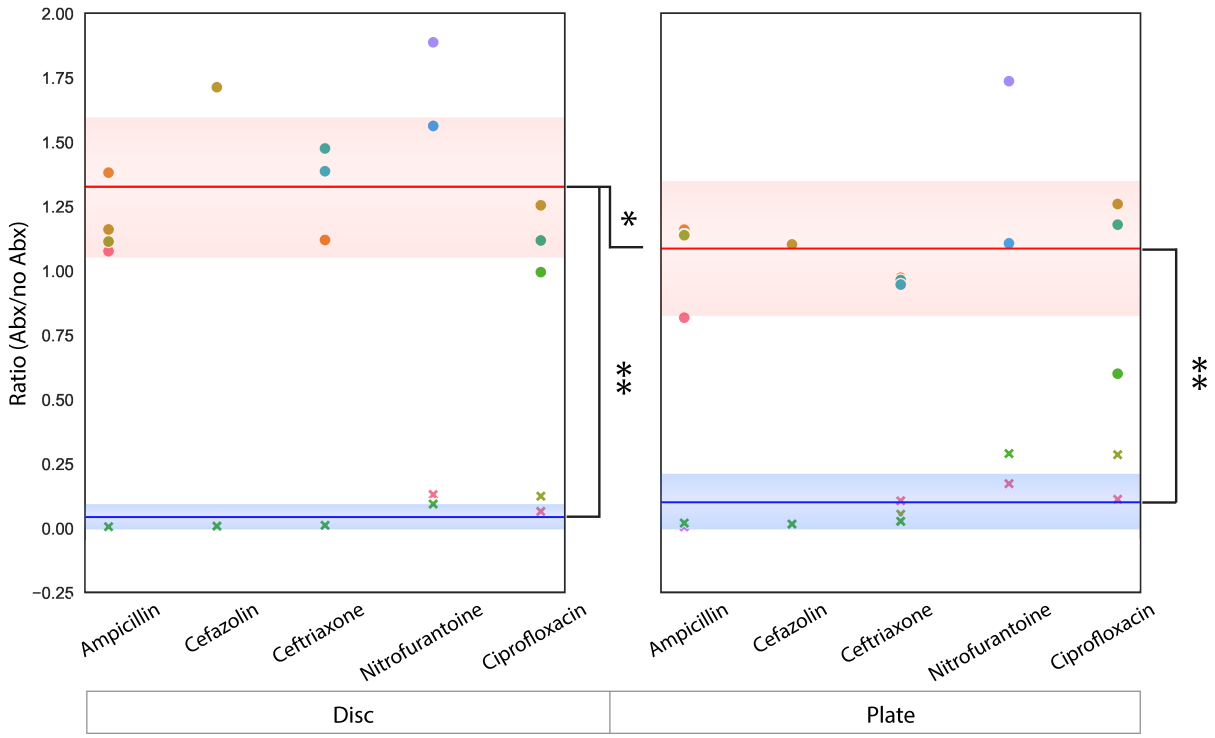

Figure 9.11: Ratios of signal intensity of each bacteria incubated with and without antibiotics for the disc (a) and the plate (b). The blue and red lines represent the average of all ratios for resistant (red) and susceptible (blue) bacteria.

distinguish antibiotic susceptibility on the disc.

In Figure 9.12, an average ratio for the response of multiple bacteria to each antibiotic was determined. In all bacteria/antibiotic combinations, the average ratios from the disc incubation were comparable to those on the 96-well plate. However, on the disc, susceptible bacteria incubated with antibiotics showed very low uniform average ratios, with no statistically significant differences between antibiotic effectiveness. Interestingly, on the plate, susceptible bacteria exposed to the three antibiotics that target the cell wall (ampicillin, cefazolin, and ceftriaxone), showed a lower average ratio than those exposed to antibiotics that target bacterial DNA functions (nitrofurantoin and ciprofloxacin) (<0.05). This uncertainty could contribute to false positives when interpreting susceptibility data. Therefore, results from the disc incubation provide clinicians more confidence in their prescription of antibiotics.

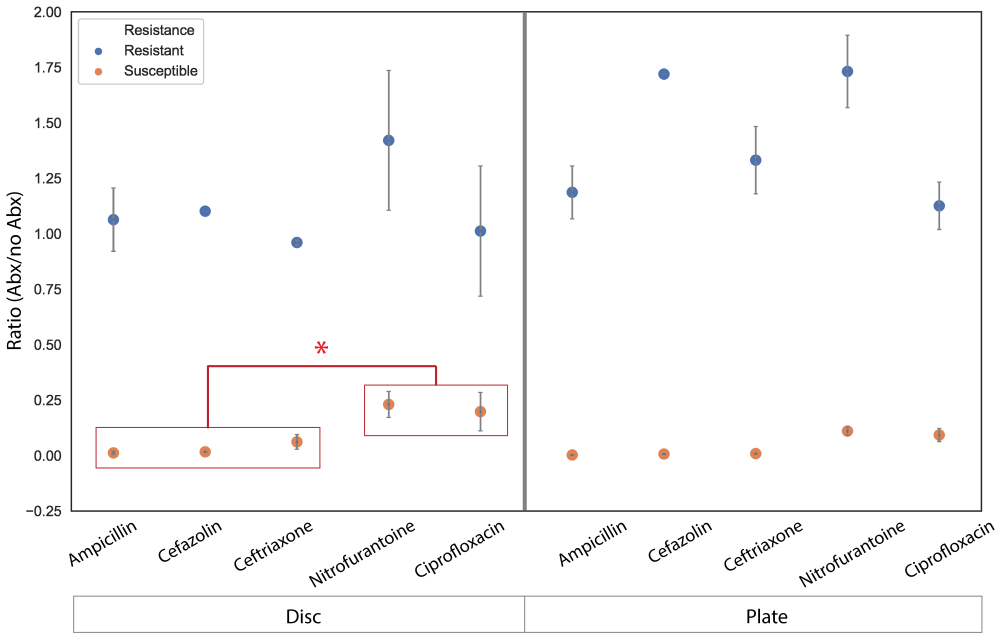

Figure 9.12: Average ratio of signal intensity of E. coli strains incubated with and without each antibiotic. The graph on the right shows ratios for resistant and susceptible bacteria grown on the plate and the left shows resistant and susceptible bacteria grown on the disc.

Chapter 10

Conclusion

We demonstrated a never reported method for enhancing bacteria incubation on a microfluidic platform capable of determining bacterial response in the presence of five antibiotics. Robust mixing of a liquid bacteria sample in the microfluidic chamber on the CD provides rapid growth by ensuring adequate sample aeration, nutrient dispersion, and prevention of biofilm formation. The well mixed sample is capable of determining bacterial response to antibiotics quicker compared to the off-chip incubation when using rRNA as the detection mechanism. The design of the incubation chamber on the CD was optimized to include further downstream sample processing, including a universal gram positive and negative cell lysis system, capable of lysing 6 different types of gram positive and negative bacteria, interchangeable microarray detection chamber, two washing chambers, and waste chamber. The CD was integrated with a custom designed SpinBox capable of automating all sample processing steps after the initial sample dilution in the world-to-chip interface. The system serves as a powerful step towards improving rapid AST PoC diagnostics by minimizing sample handling. In reality, the rapid incubation on a microfluidic CD can be adapted and combined with a variety of unexplored detection mechanisms to further improve AST.

Part IV

Concluding remarks and future work

In this thesis I describe the development of two bioMEMS platforms and their use as tools to study and control biological organisms.

In Part II, I describe the development of a nanomaterial scaffold that can be used for studying stem cells. This scaffold has important properties that make it ideal for the study and control of neural stem cells including its biocompatibility, 3D microstructure tunability, and its excellence as an electrochemical sensor. The scaffold is used to grow, stimulate, and differentiate mouse neural stem cells. It is also used successfully as a sensor to monitor Dopamine produced directly from cells growing on the scaffold.

In Part III, I describe the development of a centrifugal microfluidic platform that is used for studying microorganisms like bacteria. This platform is able to significantly improve bacterial incubation compared with incubation in a 96-well plate in typical plate shaker incubators. This system is then used to develop a phenotypic antibiotic susceptibility test that can rapidly identify resistance in 11 different species of E. Coli in under 2 hours.

After completing the projects outlined in this work, it begs the question: can these two BioMEMS platforms be combined and used to study a variety of cells and microorganisms? I am hopeful that my future work, or that of my colleagues, can accomplish this task.

One of the important things the microfludic platform can add is the addition of different fluidic and mechanical forces. For example, by adding the nanofiber scaffold into a microfluidic disc, stem cells can be studied under different flow conditions. One experiment that can be done is to use the disc to simulate the flow encountered in blood vessels to study how this environment might effect stem cell differentiation toward lineages found in the lining of blood vessel or arterial walls.

Another important force that can be simulated on the centrifugal platform is gravity. Research from the Kepler Space Observatory suggests that there may be up to two billion planets in our galaxy with Earth-like characteristics, yet the unanswered question remains:

can these planets support life and if so, what would that life look like? Though these planets are deemed "Earth-like", actual conditions may drastically differ. One of the most unique, unexplored aspects of these planets are its gravity, which can be several times larger than earth's one g. The centrifugal force can be used to create the synthetic conditions, such as temperature, pressure, and hypergravity found on some of these Kepler planets on organisms in the disc. The viability, growth, and stress response of these organisms to these different conditions can then be evaluated. This setup can further be extended to organized communities of cells, stem cells, bacteria, or to model organisms such as C. elegans, which have previously been cultured on a spinning microfluidic disc to study the effects of gravity on aging [80].

The microfluidic disc can also be used as a sample preparation system to automate delivery of nutrients to stem cells, bacteria, or other organisms, simplifying their incubation and making experiments more reproducible. By integrating electricity onto the spinning system, we can even use the nanofiber mat as an embedded electrochemical sensor during incubation. The combination of these two MEMS platforms can allow for critical research and study of organisms at the stem cell, bacteria, and whole organism level.

Bibliography

[1] K. Abi-Samra, L. Clime, L. Kong, R. Gorkin, T.-H. Kim, Y.-K. Cho, and M. Madou. Thermo-pneumatic pumping in centrifugal microfluidic platforms. *Microfluidics and nanofluidics*, 11(5):643–652, 2011.

[2] K. Abi-Samra, R. Hanson, M. Madou, and R. A. Gorkin III. Infrared controlled waxes for liquid handling and storage on a cd-microfluidic platform. *Lab on a Chip*, 11(4):723–726, 2011.

[3] G. R. Aguirre, V. Efremov, M. Kitsara, and J. Ducrée. Integrated micromixer for incubation and separation of cancer cells on a centrifugal platform using inertial and dean forces. *Microfluidics and Nanofluidics*, 18(3):513–526, 2015.

[4] M. Amasia, M. Cozzens, and M. J. Madou. Centrifugal microfluidic platform for rapid pcr amplification using integrated thermoelectric heating and ice-valving. *Sensors and Actuators B: Chemical*, 161(1):1191–1197, 2012.

[5] M. Amasia and M. Madou. Large-volume centrifugal microfluidic device for blood plasma separation. *Bioanalysis*, 2(10):1701–1710, 2010.

[6] L. Amato, A. Heiskanen, C. Caviglia, F. Shah, K. Zór, M. Skolimowski, M. Madou, L. Gammelgaard, R. Hansen, E. G. Seiz, M. Ramos, T. R. Moreno, A. Martínez-Serrano, S. S. Keller, and J. Emnéus. Pyrolysed 3d-Carbon Scaffolds Induce Spontaneous Differentiation of Human Neural Stem Cells and Facilitate Real-Time Dopamine Detection. *Advanced Functional Materials*, 24(44):7042–7052, 2014.

[7] S. Z. Andreasen, D. Kwasny, L. Amato, A. L. Brøgger, F. G. Bosco, K. B. Andersen, W. E. Svendsen, and A. Boisen. Integrating electrochemical detection with centrifugal microfluidics for real-time and fully automated sample testing. *RSC Adv.*, 5(22):17187–17193, 2015.

[8] J. Arulmoli, M. M. Pathak, L. P. McDonnell, J. L. Nourse, F. Tombola, J. C. Earthman, and L. A. Flanagan. Static stretch affects neural stem cell differentiation in an extracellular matrix-dependent manner. *Scientific reports*, 5(1):1–8, 2015.

[9] A. J. Bard, L. R. Faulkner, J. Leddy, and C. G. Zoski. *Electrochemical methods: fundamentals and applications*, volume 2. wiley New York, 1980.

[10] J. A. Behan, M. K. Hoque, S. N. Stamatin, T. S. Perova, L. Vilella-Arribas, M. García-Melchor, and P. E. Colavita. Experimental and Computational Study of Dopamine as an Electrochemical Probe of the Surface Nanostructure of Graphitized N-Doped Carbon. *The Journal of Physical Chemistry C*, 122(36):20763–20773, Sept. 2018.

[11] H. Bernheimer, W. Birkmayer, O. Hornykiewicz, K. Jellinger, and F. Seitelberger. Brain dopamine and the syndromes of Parkinson and Huntington Clinical, morphological and neurochemical correlations. *Journal of the Neurological Sciences*, 20(4):415–455, Dec. 1973.

[12] S. Brosel-Oliu, O. Mergel, N. Uria, N. Abramova, P. v. Rijn, and A. Bratov. 3d impedimetric sensors as a tool for monitoring bacterial response to antibiotics. *Lab on a Chip*, 19(8):1436–1447, Apr. 2019.

[13] M. Brown, R. Doebler, B. Irvine, T. Ferguson, and G. Blackburn. Compositions and methods for capture and elution of biological materials via particulates, Oct. 2012.

[14] D. A. C. Brownson and C. E. Banks. *The Handbook of Graphene Electrochemistry*. Springer-Verlag, London, 2014.

[15] C. Canal, R. Molina, E. Bertran, and P. Erra. Wettability, ageing and recovery process of plasma-treated polyamide 6. *Journal of adhesion science and technology*, 18(9):1077–1089, 2004.

[16] O. Chaudhuri, L. Gu, D. Klumpers, M. Darnell, S. A. Bencherif, J. C. Weaver, N. Huebsch, H.-p. Lee, E. Lippens, G. N. Duda, and D. J. Mooney. Hydrogels with tunable stress relaxation regulate stem cell fate and activity. *Nature Materials*, 15(3):326–334, Mar. 2016.

[17] D. Chen, M. Mauk, X. Qiu, C. Liu, J. Kim, S. Ramprasad, S. Ongagna, W. R. Abrams, D. Malamud, P. L. Corstjens, et al. An integrated, self-contained microfluidic cassette for isolation, amplification, and detection of nucleic acids. *Biomedical microdevices*, 12(4):705–719, 2010.

[18] G. Y. Chen, D. W. P. Pang, S. M. Hwang, H. Y. Tuan, and Y. C. Hu. A graphene-based platform for induced pluripotent stem cells culture and differentiation. *Biomaterials*, 33(2):418–427, Jan. 2012.

[19] E. Cho, A. Perebikovsky, O. Benice, S. Holmberg, M. Madou, and M. Ghazinejad. Rapid iodine sensing on mechanically treated carbon nanofibers. *Sensors*, 18(5):1486, 2018.

[20] J. Clarke, H.-C. Wu, L. Jayasinghe, A. Patel, S. Reid, and H. Bayley. Continuous base identification for single-molecule nanopore dna sequencing. *Nature nanotechnology*, 4(4):265, 2009.

[21] A. R. Coates, G. Halls, and Y. Hu. Novel classes of antibiotics or more of the same? *British Journal of Pharmacology*, 163(1):184–194, May 2011.

[22] S. L. Crittenden, D. S. Bernstein, J. L. Bachorik, B. E. Thompson, M. Gallegos, A. G. Petcherski, G. Moulder, R. Barstead, M. Wickens, and J. Kimble. A conserved rna-binding protein controls germline stem cells in caenorhabditis elegans. *Nature*, 417(6889):660–663, 2002.

[23] M. Czugala, D. Maher, F. Collins, R. Burger, F. Hopfgartner, Y. Yang, J. Zhaou, J. Ducrée, A. Smeaton, K. J. Fraser, et al. Cmas: fully integrated portable centrifugal microfluidic analysis system for on-site colorimetric analysis. *RSC advances*, 3(36):15928–15938, 2013.

[24] D. A. C. Brownson, D. K. Kampouris, and C. E. Banks. Graphene electrochemistry: fundamental concepts through to prominent applications. *Chemical Society Reviews*, 41(21):6944–6976, 2012.

[25] M. D. Brennan, M. L. Rexius-Hall, L. Jane Elgass, and D. T. Eddington. Oxygen control with microfluidics. *Lab on a Chip*, 14(22):4305–4318, 2014.

[26] M. Davenport, K. E. Mach, L. M. D. Shortliffe, N. Banaei, T.-H. Wang, and J. C. Liao. New and developing diagnostic technologies for urinary tract infections. *Nature Reviews Urology*, 14(5):296–310, May 2017.

[27] N. Dimov, E. Clancy, J. Gaughran, D. Boyle, D. Mc Auley, M. T. Glynn, R. M. Dwyer, H. Coughlan, T. Barry, L. M. Barrett, et al. Solvent-selective routing for centrifugally automated solid-phase purification of rna. *Microfluidics and Nanofluidics*, 18(5-6):859–871, 2015.

[28] D. E. Discher, D. J. Mooney, and P. W. Zandstra. Growth Factors, Matrices, and Forces Combine and Control Stem Cells. *Science*, 324(5935):1673–1677, June 2009.

[29] J. Ducrée, S. Haeberle, S. Lutz, S. Pausch, F. v. Stetten, and R. Zengerle. The centrifugal microfluidic Bio-Disk platform. *Journal of Micromechanics and Microengineering*, 17(7):S103–S115, June 2007.

[30] D. C. Duffy, H. L. Gillis, J. Lin, N. F. Sheppard, and G. J. Kellogg. Microfabricated Centrifugal Microfluidic Systems: Characterization and Multiple Enzymatic Assays. *Analytical Chemistry*, 71(20):4669–4678, Oct. 1999.

[31] P. Dwayne G. Stupack. The Biology of Integrins, Aug. 2007.

[32] T. P. M. Editors. Antimicrobial resistance: Is the world unprepared? *PLOS Medicine*, 13(9):1–3, 09 2016.

[33] A. J. Engler, S. Sen, H. L. Sweeney, and D. E. Discher. Matrix elasticity directs stem cell lineage specification. *Cell*, 126(4):677–689, 2006.

[34] A. C. Ferrari and J. Robertson. Interpretation of Raman spectra of disordered and amorphous carbon. *Physical Review B*, 61(20):14095–14107, May 2000.

[35] R. P. Feynman. There's plenty of room at the bottom. *California Institute of Technology, Engineering and Science magazine*, 1960.

[36] L. A. Flanagan, L. M. Rebaza, S. Derzic, P. H. Schwartz, and E. S. Monuki. Regulation of human neural precursor cells by laminin and integrins. *Journal of neuroscience research*, 83(5):845–856, 2006.

[37] S. V. Fridrikh, H. Y. Jian, M. P. Brenner, and G. C. Rutledge. Controlling the fiber diameter during electrospinning. *Physical review letters*, 90(14):144502, 2003.

[38] E. Fuhrer, A. Bäcker, S. Kraft, F. J. Gruhl, M. Kirsch, N. MacKinnon, J. G. Korvink, and S. Sharma. 3d Carbon Scaffolds for Neural Stem Cell Culture and Magnetic Resonance Imaging. *Advanced Healthcare Materials*, 7(4):1700915, 2018.

[39] P. Garstecki, M. J. Fuerstman, M. A. Fischbach, S. K. Sia, and G. M. Whitesides. Mixing with bubbles: a practical technology for use with portable microfluidic devices. *Lab on a Chip*, 6(2):207–212, 2006.

[40] L. R. Geuss and L. J. Suggs. Making cardiomyocytes: How mechanical stimulation can influence differentiation of pluripotent stem cells. *Biotechnology Progress*, 29(5):1089–1096, 2013.

[41] M. Ghazinejad, S. Holmberg, O. Pilloni, L. Oropeza-Ramos, and M. Madou. Graphitizing Non-graphitizable Carbons by Stress-induced Routes. *Scientific Reports*, 7(1):16551, Nov. 2017.

[42] M. Glynn, C. Nwankire, D. Kinahan, and J. Ducrée. Cluster sizing of cancer cells by rail-based serial gap filtration in stopped-flow, continuous sedimentation mode. In *2015 28th IEEE International Conference on Micro Electro Mechanical Systems (MEMS)*, pages 192–195. IEEE, 2015.

[43] N. Godino, E. Vereshchagina, R. Gorkin, and J. Ducrée. Centrifugal automation of a triglyceride bioassay on a low-cost hybrid paper-polymer device. *Microfluidics and nanofluidics*, 16(5):895–905, 2014.

[44] H. H. Goldstine and A. Goldstine. The electronic numerical integrator and computer (eniac). *Mathematical Tables and Other Aids to Computation*, 2(15):97–110, 1946.

[45] R. Gorkin III, C. E. Nwankire, J. Gaughran, X. Zhang, G. G. Donohoe, M. Rook, R. O'Kennedy, and J. Ducrée. Centrifugo-pneumatic valving utilizing dissolvable films. *Lab on a Chip*, 12(16):2894–2902, 2012.

[46] M. Grumann, A. Geipel, L. Riegger, R. Zengerle, and J. Ducrée. Magneto-hydrodynamic micromixing for centrifugal lab-on-a-disk platforms. *SPECIAL PUBLICATION-ROYAL SOCIETY OF CHEMISTRY*, 296:593–595, 2004.

[47] M. Grumann, J. Steigert, L. Riegger, I. Moser, B. Enderle, K. Riebeseel, G. Urban, R. Zengerle, and J. Ducrée. Sensitivity enhancement for colorimetric glucose assays on whole blood by on-chip beam-guidance. *Biomedical microdevices*, 8(3):209–214, 2006.

[48] R. Guo, S. Zhang, M. Xiao, F. Qian, Z. He, D. Li, X. Zhang, H. Li, X. Yang, M. Wang, R. Chai, and M. Tang. Accelerating bioelectric functional development of neural stem cells by graphene coupling: Implications for neural interfacing with conductive materials. *Biomaterials*, 106:193–204, Nov. 2016.

[49] S.-J. Gwak, S. H. Bhang, I.-K. Kim, S.-S. Kim, S.-W. Cho, O. Jeon, K. J. Yoo, A. J. Putnam, and B.-S. Kim. The effect of cyclic strain on embryonic stem cell-derived cardiomyocytes. *Biomaterials*, 29(7):844–856, Mar. 2008.

[50] S. Haeberle, T. Brenner, R. Zengerle, and J. Ducrée. Centrifugal extraction of plasma from whole blood on a rotating disk. *Lab on a Chip*, 6(6):776–781, 2006.

[51] C. Halford, R. Gonzalez, S. Campuzano, B. Hu, J. T. Babbitt, J. Liu, J. Wang, B. M. Churchill, and D. A. Haake. Rapid antimicrobial susceptibility testing by sensitive detection of precursor rRNA using a novel electrochemical biosensing platform. *Antimicrobial agents and chemotherapy*, 57(2):936–943, 2013.

[52] D. Han and P.-I. Gouma. Electrospun bioscaffolds that mimic the topology of extracellular matrix. *Nanomedicine: Nanotechnology, Biology and Medicine*, 2(1):37–41, 2006.

[53] P. J. F. Harris. Fullerene-related structure of commercial glassy carbons. *Philosophical Magazine*, 84(29):3159–3167, 2004.

[54] H. He, Y. Yuan, W. Wang, N.-R. Chiou, A. J. Epstein, and L. J. Lee. Design and testing of a microfluidic biochip for cytokine enzyme-linked immunosorbent assay. *Biomicrofluidics*, 3(2):022401, 2009.

[55] E. K. Heiniger, J. R. Buser, L. Mireles, X. Zhang, P. D. Ladd, B. R. Lutz, and P. Yager. Comparison of point-of-care-compatible lysis methods for bacteria and viruses. *Journal of Microbiological Methods*, 128:80–87, Sept. 2016.

[56] J. S. Heo and J.-C. Lee. -catenin mediates cyclic strain-stimulated cardiomyogenesis in mouse embryonic stem cells through ROS-dependent and integrin-mediated PI3K/Akt pathways. *Journal of Cellular Biochemistry*, 112(7):1880–1889, 2011.

[57] V. Hessel, H. Löwe, and F. Schönfeld. Micromixers—a review on passive and active mixing principles. *Chemical Engineering Science*, 60(8-9):2479–2501, 2005.

[58] J. Höfflin, S. M. T. Delgado, F. S. Sandoval, J. G. Korvink, and D. Mager. Electrifying the disk: a modular rotating platform for wireless power and data transmission for lab on a disk application. *Lab on a Chip*, 15(12):2584–2587, 2015.

[59] A. W. Holle and A. J. Engler. More than a feeling: discovering, understanding, and influencing mechanosensing pathways. *Current Opinion in Biotechnology*, 22(5):648–654, Oct. 2011.

[60] S. Holmberg, M. Ghazinejad, E. Cho, D. George, B. Pollack, A. Perebikovsky, R. Ragan, and M. Madou. Stress-activated pyrolytic carbon nanofibers for electrochemical platforms. *Electrochimica Acta*, 290:639–648, Nov. 2018.

[61] N. P. Horrocks, F. Vollrath, and C. Dicko. The silkmoth cocoon as humidity trap and waterproof barrier. *Comparative Biochemistry and Physiology Part A: Molecular & Integrative Physiology*, 164(4):645–652, 2013.

[62] X. Hu, S. Liu, G. Zhou, Y. Huang, Z. Xie, and X. Jing. Electrospinning of polymeric nanofibers for drug delivery applications. *Journal of controlled release*, 185:12–21, 2014.

[63] L. Huang, S. S. Manickam, and J. R. McCutcheon. Increasing strength of electrospun nanofiber membranes for water filtration using solvent vapor. *Journal of membrane science*, 436:213–220, 2013.

[64] Y. Huang, E. L. Mather, J. L. Bell, and M. Madou. Mems-based sample preparation for molecular diagnostics. *Analytical and bioanalytical chemistry*, 372(1):49–65, 2002.

[65] H. Hwang, Y. Kim, J. Cho, J.-y. Lee, M.-S. Choi, and Y.-K. Cho. Lab-on-a-disc for simultaneous determination of nutrients in water. *Analytical chemistry*, 85(5):2954–2960, 2013.

[66] S. Jin, H. Deng, D. Long, X. Liu, L. Zhan, X. Liang, W. Qiao, and L. Ling. Facile synthesis of hierarchically structured Fe3o4/carbon micro-flowers and their application to lithium-ion battery anodes. *Journal of Power Sources*, 196(8):3887–3893, Apr. 2011.

[67] C. E. John and S. R. Jones. Fast Scan Cyclic Voltammetry of Dopamine and Serotonin in Mouse Brain Slices. In A. C. Michael and L. M. Borland, editors, *Electrochemical Methods for Neuroscience*, Frontiers in Neuroengineering. CRC Press/Taylor & Francis, Boca Raton (FL), 2007.

[68] K. Joseph, F. Ibrahim, J. Cho, T. H. G. Thio, W. Al-Faqheri, and M. Madou. Design and development of micro-power generating device for biomedical applications of lab-on-a-disc. *PLoS One*, 10(9), 2015.

[69] A. Katsumi, A. W. Orr, E. Tzima, and M. A. Schwartz. Integrins in Mechanotransduction. *Journal of Biological Chemistry*, 279(13):12001–12004, Mar. 2004.

[70] P. Katta, M. Alessandro, R. Ramsier, and G. Chase. Continuous electrospinning of aligned polymer nanofibers onto a wire drum collector. *Nano letters*, 4(11):2215–2218, 2004.

[71] M. Keller, J. Naue, P. P. Vinayaka, O. Strohmeier, D. Mark, U. Schmidt, R. Zengerle, and F. von Stetten. Microfluidic app featuring nested pcr for forensic screening assay on off-the-shelf thermocycler. In *17th International Conference on Miniaturized Systems for Chemistry and Life Sciences, no. October*, pages 320–322, 2013.

[72] H. Kido, M. Micic, D. Smith, J. Zoval, J. Norton, and M. Madou. A novel, compact disk-like centrifugal microfluidics system for cell lysis and sample homogenization. *Colloids and Surfaces. B, Biointerfaces*, 58(1):44–51, July 2007.

[73] A. A. Kiger, D. L. Jones, C. Schulz, M. B. Rogers, and M. T. Fuller. Stem cell self-renewal specified by jak-stat activation in response to a support cell cue. *Science*, 294(5551):2542–2545, 2001.

[74] K. A. Kilian, B. Bugarija, B. T. Lahn, and M. Mrksich. Geometric cues for directing the differentiation of mesenchymal stem cells. *Proceedings of the National Academy of Sciences*, 107(11):4872–4877, Mar. 2010.

[75] C. Kim, K. S. Yang, M. Kojima, K. Yoshida, Y. J. Kim, Y. A. Kim, and M. Endo. Fabrication of electrospinning-derived carbon nanofiber webs for the anode material of lithium-ion secondary batteries. *Advanced Functional Materials*, 16(18):2393–2397, 2006.

[76] I.-D. Kim and A. Rothschild. Nanostructured metal oxide gas sensors prepared by electrospinning. *Polymers for Advanced Technologies*, 22(3):318–325, 2011.

[77] J. Kim, S. H. Jang, G. Jia, J. V. Zoval, N. A. Da Silva, and M. J. Madou. Cell lysis on a microfluidic cd (compact disc). *Lab on a Chip*, 4(5):516–522, 2004.

[78] J. Kim, H. Kido, R. H. Rangel, and M. J. Madou. Passive flow switching valves on a centrifugal microfluidic platform. *Sensors and Actuators B: Chemical*, 128(2):613–621, Jan. 2008.

[79] J. Kim and X. Xu. Excimer laser fabrication of polymer microfluidic devices. *Journal of Laser Applications*, 15(4):255–260, 2003.

[80] N. Kim, C. M. Dempsey, C.-J. Kuan, J. V. Zoval, E. O'Rourke, G. Ruvkun, M. J. Madou, and J. Y. Sze. Gravity force transduced by the mec-4/mec-10 deg/enac channel modulates daf-16/foxo activity in caenorhabditis elegans. *Genetics*, 177(2):835–845, 2007.

[81] S. Kim, F. Masum, J.-K. Kim, H. J. Chung, and J. S. Jeon. On-chip phenotypic investigation of combinatory antibiotic effects by generating orthogonal concentration gradients. 19(6):959–973.

[82] T.-H. Kim, K. Abi-Samra, V. Sunkara, D.-K. Park, M. Amasia, N. Kim, J. Kim, H. Kim, M. Madou, and Y.-K. Cho. Flow-enhanced electrochemical immunosensors on centrifugal microfluidic platforms. *Lab on a Chip*, 13(18):3747, 2013.

[83] T.-H. Kim, C.-H. Yea, S.-T. D. Chueng, P. T.-T. Yin, B. Conley, K. Dardir, Y. Pak, G. Y. Jung, J.-W. Choi, and K.-B. Lee. Large-Scale Nanoelectrode Arrays to Monitor the Dopaminergic Differentiation of Human Neural Stem Cells. *Advanced Materials*, 27(41):6356–6362, 2015.

[84] D. Kirby, J. Siegrist, G. Kijanka, L. Zavattoni, O. Sheils, J. O'Leary, R. Burger, and J. Ducrée. Centrifugo-magnetophoretic particle separation. *Microfluidics and Nanofluidics*, 13(6):899–908, July 2012.

[85] P. T. Kissinger, J. B. Hart, and R. N. Adams. Voltammetry in brain tissue—a new neurophysiological measurement. *Brain research*, 55(1):209–213, 1973.

[86] M. Kitsara, C. E. Nwankire, L. Walsh, G. Hughes, M. Somers, D. Kurzbuch, X. Zhang, G. G. Donohoe, R. O'Kennedy, and J. Ducrée. Spin coating of hydrophilic polymeric films for enhanced centrifugal flow control by serial siphoning. *Microfluidics and nanofluidics*, 16(4):691–699, 2014.

[87] A. M. Kloxin, A. M. Kasko, C. N. Salinas, and K. S. Anseth. Photodegradable Hydrogels for Dynamic Tuning of Physical and Chemical Properties. *Science*, 324(5923):59–63, Apr. 2009.

[88] C.-Y. Koh, U. Y. Schaff, M. E. Piccini, L. H. Stanker, L. W. Cheng, E. Ravichandran, B.-R. Singh, G. J. Sommer, and A. K. Singh. Centrifugal microfluidic platform for ultrasensitive detection of botulinum toxin. *Analytical Chemistry*, 87(2):922–928, Jan. 2015.

[89] L. X. Kong, A. Perebikovsky, J. Moebius, L. Kulinsky, and M. Madou. Lab-on-a-cd: A fully integrated molecular diagnostic system. *Journal of Laboratory Automation*, 21(3):323–355, 2016. PMID: 26082453.

[90] M. C. Kong and E. D. Salin. Spectrophotometric determination of aqueous sulfide on a pneumatically enhanced centrifugal microfluidic platform. *Analytical chemistry*, 84(22):10038–10043, 2012.

[91] E. W. Kristensen, W. G. Kuhr, and R. M. Wightman. Temporal characterization of perfluorinated ion exchange coated microvoltammetric electrodes for in vivo use. *Analytical chemistry*, 59(14):1752–1757, 1987.

[92] J.-N. Kuo and B.-S. Li. Lab-on-cd microfluidic platform for rapid separation and mixing of plasma from whole blood. *Biomedical microdevices*, 16(4):549–558, 2014.

[93] M. La, S. J. Park, H. W. Kim, J. J. Park, K. T. Ahn, S. M. Ryew, and D. S. Kim. A centrifugal force-based serpentine micromixer (csm) on a plastic lab-on-a-disk for biochemical assays. *Microfluidics and nanofluidics*, 15(1):87–98, 2013.

[94] J. P. Lafleur, A. A. Rackov, S. McAuley, and E. D. Salin. Miniaturised centrifugal solid phase extraction platforms for in-field sampling, pre-concentration and spectrometric detection of organic pollutants in aqueous samples. *Talanta*, 81(1-2):722–726, 2010.

[95] J. P. Lafleur and E. D. Salin. Pre-concentration of trace metals on centrifugal microfluidic discs with direct determination by laser ablation inductively coupled plasma mass spectrometry. *Journal of Analytical Atomic Spectrometry*, 24(11):1511–1516, 2009.

[96] S. Lai, S. Wang, J. Luo, L. J. Lee, S.-T. Yang, and M. J. Madou. Design of a compact disk-like microfluidic platform for enzyme-linked immunosorbent assay. *Analytical chemistry*, 76(7):1832–1837, 2004.

[97] S. W. Lane, D. A. Williams, and F. M. Watt. Modulating the stem cell niche for tissue regeneration. *Nature biotechnology*, 32(8):795, 2014.

[98] J. Lannutti, D. Reneker, T. Ma, D. Tomasko, and D. Farson. Electrospinning for tissue engineering scaffolds. *Materials Science and Engineering: C*, 27(3):504–509, 2007.

[99] K. Larsson, H. Brisby, B. R. Johansson, E. Runesson, and B. Rydevik. Electron microscopy analysis of neurites extending from dorsal root ganglia in vitro following exposure to intervertebral disc cells. *Cells Tissues Organs*, 196(1):82–89, 2012.

[100] I. Lavagnini, R. Antiochia, and F. Magno. An Extended Method for the Practical Evaluation of the Standard Rate Constant from Cyclic Voltammetric Data. *Electroanalysis*, 16(6):505–506, Apr. 2004.

[101] J. Lee, J. I. Choi, A. E. Cho, S. Kumar, S. S. Jang, and Y.-H. Kim. Origin and Control of Polyacrylonitrile Alignments on Carbon Nanotubes and Graphene Nanoribbons. *Advanced Functional Materials*, 28(15):1706970, 2018.

[102] J.-H. Lee, H. K. Choi, L. Yang, S.-T. D. Chueng, J.-W. Choi, and K.-B. Lee. Nondestructive Real-Time Monitoring of Enhanced Stem Cell Differentiation Using a Graphene-Au Hybrid Nanoelectrode Array. *Advanced Materials*, 30(39):1802762, 2018.

[103] W.-C. C. Lee, T. M. Maul, D. A. Vorp, J. P. Rubin, and K. G. Marra. Effects of uniaxial cyclic strain on adipose-derived stem cell morphology, proliferation, and differentiation. *Biomechanics and Modeling in Mechanobiology*, 6(4):265–273, July 2007.

[104] H. Li, P. Torab, K. E. Mach, C. Surrette, M. R. England, D. W. Craft, N. J. Thomas, J. C. Liao, C. Puleo, and P. K. Wong. Adaptable microfluidic system for single-cell pathogen classification and antimicrobial susceptibility testing. *Proceedings of the National Academy of Sciences*, 116(21):10270–10279, 2019.

[105] S.-M. Li, S.-Y. Yang, Y.-S. Wang, C.-H. Lien, H.-W. Tien, S.-T. Hsiao, W.-H. Liao, H.-P. Tsai, C.-L. Chang, C.-C. M. Ma, and C.-C. Hu. Controllable synthesis of nitrogen-doped graphene and its effect on the simultaneous electrochemical determination of ascorbic acid, dopamine, and uric acid. *Carbon*, 59:418–429, Aug. 2013.

[106] J. Lin, X. Wang, B. Ding, J. Yu, G. Sun, and M. Wang. Biomimicry via Electrospinning. *Critical Reviews in Solid State and Materials Sciences*, 37(2):94–114, Apr. 2012.

[107] W. F. Liu, C. M. Nelson, D. M. Pirone, and C. S. Chen. E-cadherin engagement stimulates proliferation via Rac1. *Journal of Cell Biology*, 173(3):431–441, May 2006.

[108] Y. K. Luu, J. E. Pessin, S. Judex, J. Rubin, and C. T. Rubin. Mechanical signals as a non-invasive means to influence mesenchymal stem cell fate, promoting bone and suppressing the fat phenotype. *BoneKEy osteovision*, 6(4):132, 2009.

[109] K. E. Mach, C. B. Du, H. Phull, D. A. Haake, M.-C. Shih, E. J. Baron, and J. C. Liao. Multiplex Pathogen Identification for Polymicrobial Urinary Tract Infections Using Biosensor Technology: A Prospective Clinical Study. *Journal of Urology*, 182(6):2735–2741, Dec. 2009.

[110] M. Madou, J. Zoval, G. Jia, H. Kido, J. Kim, and N. Kim. Lab on a cd. *Annu. Rev. Biomed. Eng.*, 8:601–628, 2006.

[111] M. J. Madou. *Fundamentals of microfabrication: the science of miniaturization*. CRC press, 2002.

[112] M. J. Madou and G. J. Kellogg. LabCD: a centrifuge-based microfluidic platform for diagnostics. volume 3259, pages 80–93, 1998.

[113] M. J. Madou, V. H. Perez-Gonzalez, and B. Pramanick. *Carbon: The Next Silicon?: Book 1 - Fundamentals*. Momentum Press, Jan. 2016. Google-Books-ID: IPxdCwAAQBAJ.

[114] T. Maitra, S. Sharma, A. Srivastava, Y.-K. Cho, M. Madou, and A. Sharma. Improved graphitization and electrical conductivity of suspended carbon nanofibers derived from carbon nanotube/polyacrylonitrile composites by directed electrospinning. *Carbon*, 50(5):1753–1761, Apr. 2012.

[115] M. Makaremi, R. T. De Silva, and P. Pasbakhsh. Electrospun nanofibrous membranes of polyacrylonitrile/halloysite with superior water filtration ability. *The Journal of Physical Chemistry C*, 119(14):7949–7958, 2015.

[116] D. Mamaev, B. Shaskolskiy, E. Dementieva, D. Khodakov, D. Yurasov, R. Yurasov, D. Zimenkov, V. Mikhailovich, A. Zasedatelev, and D. Gryadunov. Rotary-based platform with disposable fluidic modules for automated isolation of nucleic acids. *Biomedical microdevices*, 17(1):18, 2015.

[117] S. E. Marsh and M. Blurton-Jones. Neural stem cell therapy for neurodegenerative disorders: The role of neurotrophic support. *Neurochemistry International*, 106:94–100, June 2017.

[118] R. Martinez-Duarte. SU-8 Photolithography as a Toolbox for Carbon MEMS. *Micromachines*, 5(3):766–782, Sept. 2014.

[119] R. Martinez-Duarte, R. A. Gorkin III, K. Abi-Samra, and M. J. Madou. The integration of 3d carbon-electrode dielectrophoresis on a cd-like centrifugal microfluidic platform. *Lab on a Chip*, 10(8):1030–1043, 2010.

[120] F. Martino, A. R. Perestrelo, V. Vinarskỳ, S. Pagliari, and G. Forte. Cellular mechanotransduction: from tension to function. *Frontiers in physiology*, 9:824, 2018.

[121] R. McBeath, D. M. Pirone, C. M. Nelson, K. Bhadriraju, and C. S. Chen. Cell Shape, Cytoskeletal Tension, and RhoA Regulate Stem Cell Lineage Commitment. *Developmental Cell*, 6(4):483–495, Apr. 2004.

[122] R. L. McCreery. Carbon electrode surface chemistry. In *Voltammetric Methods in Brain Systems*, pages 1–26. Springer, 1995.

[123] R. L. McCreery. Advanced Carbon Electrode Materials for Molecular Electrochemistry. *Chemical Reviews*, 108(7):2646–2687, July 2008.

[124] R. J. McMurray, M. J. Dalby, and P. M. Tsimbouri. Using biomaterials to study stem cell mechanotransduction, growth and differentiation. *Journal of Tissue Engineering and Regenerative Medicine*, 9(5):528–539, 2015.

[125] H. E. H. Meijer, M. K. Singh, T. G. Kang, J. M. J. d. Toonder, and P. D. Anderson. Passive and Active Mixing in Microfluidic Devices. *Macromolecular Symposia*, 279(1):201–209, 2009.

[126] R. H. Miller and M. C. Raff. Fibrous and protoplasmic astrocytes are biochemically and developmentally distinct. *The Journal of Neuroscience: The Official Journal of the Society for Neuroscience*, 4(2):585–592, Feb. 1984.

[127] R. Mohan, K. E. Mach, M. Bercovici, Y. Pan, L. Dhulipala, P. K. Wong, and J. C. Liao. Clinical Validation of Integrated Nucleic Acid and Protein Detection on an Electrochemical Biosensor Array for Urinary Tract Infection Diagnosis. *PLOS ONE*, 6(10):e26846, Oct. 2011.

[128] T. Morijiri, S. Sunahiro, M. Senaha, M. Yamada, and M. Seki. Sedimentation pinched-flow fractionation for size- and density-based particle sorting in microchannels. *Microfluidics and Nanofluidics*, 11(1):105–110, Mar. 2011.

[129] S. J. Morrison and A. C. Spradling. Stem cells and niches: mechanisms that promote stem cell maintenance throughout life. *Cell*, 132(4):598–611, 2008.

[130] E. A. Moschou, A. D. Nicholson, G. Jia, J. V. Zoval, M. J. Madou, L. G. Bachas, and S. Daunert. Integration of microcolumns and microfluidic fractionators on multitasking centrifugal microfluidic platforms for the analysis of biomolecules. *Analytical and bioanalytical chemistry*, 385(3):596, 2006.

[131] R. S. Nicholson. Theory and Application of Cyclic Voltammetry for Measurement of Electrode Reaction Kinetics. *Analytical Chemistry*, 37(11):1351–1355, Oct. 1965.

[132] Z. Noroozi, H. Kido, and M. J. Madou. Electrolysis-Induced Pneumatic Pressure for Control of Liquids in a Centrifugal System. *Journal of The Electrochemical Society*, 158(11):P130–P135, Jan. 2011.

[133] Z. Noroozi, H. Kido, M. Micic, H. Pan, C. Bartolome, M. Princevac, J. Zoval, and M. Madou. Reciprocating flow-based centrifugal microfluidics mixer. *Review of Scientific Instruments*, 80(7):075102, 2009.

[134] Z. Noroozi, H. Kido, R. Peytavi, R. Nakajima-Sasaki, A. Jasinskas, M. Micic, P. L. Felgner, and M. J. Madou. A multiplexed immunoassay system based upon reciprocating centrifugal microfluidics. *The Review of Scientific Instruments*, 82(6):064303, June 2011.

[135] T. E. North, W. Goessling, M. Peeters, P. Li, C. Ceol, A. M. Lord, G. J. Weber, J. Harris, C. C. Cutting, P. Huang, et al. Hematopoietic stem cell development is dependent on blood flow. *Cell*, 137(4):736–748, 2009.

[136] J. Nourse, J. Prieto, A. Dickson, J. Lu, M. Pathak, F. Tombola, M. Demetriou, A. Lee, and L. Flanagan. Membrane Biophysics Define Neuron and Astrocyte Progenitors in the Neural Lineage. *STEM CELLS*, 32(3):706–716, Mar. 2014.

[137] J. L. Nourse and M. M. Pathak. How cells channel their stress: Interplay between Piezo1 and the cytoskeleton. *Seminars in Cell & Developmental Biology*, 71:3–12, Nov. 2017.

[138] C. E. Nwankire, M. Czugala, R. Burger, K. J. Fraser, T. Glennon, B. E. Onwuliri, I. E. Nduaguibe, D. Diamond, J. Ducrée, et al. A portable centrifugal analyser for liver function screening. *Biosensors and Bioelectronics*, 56:352–358, 2014.

[139] Okano Hideyuki, Nakamura Masaya, Yoshida Kenji, Okada Yohei, Tsuji Osahiko, Nori Satoshi, Ikeda Eiji, Yamanaka Shinya, and Miura Kyoko. Steps Toward Safe Cell Therapy Using Induced Pluripotent Stem Cells. *Circulation Research*, 112(3):523–533, Feb. 2013.

[140] M. Ouyang, R. Mohan, Y. Lu, T. Liu, K. E. Mach, M. L. Y. Sin, M. McComb, J. Joshi, V. Gau, P. K. Wong, and J. C. Liao. An AC electrokinetics facilitated biosensor cassette for rapid pathogen identification. *Analyst*, 138(13):3660–3666, June 2013.

[141] B. Y. Park, R. Zaouk, C. Wang, and M. J. Madou. A Case for Fractal Electrodes in Electrochemical Applications. *Journal of The Electrochemical Society*, 154(2):P1–P5, Feb. 2007.

[142] A. N. Patel, S.-y. Tan, T. S. Miller, J. V. Macpherson, and P. R. Unwin. Comparison and Reappraisal of Carbon Electrodes for the Voltammetric Detection of Dopamine. *Analytical Chemistry*, 85(24):11755–11764, Dec. 2013.

[143] M. M. Pathak, J. L. Nourse, T. Tran, J. Hwe, J. Arulmoli, D. T. T. Le, E. Bernardis, L. A. Flanagan, and F. Tombola. Stretch-activated ion channel Piezo1 directs lineage choice in human neural stem cells. *Proceedings of the National Academy of Sciences*, 111(45):16148–16153, Nov. 2014.

[144] A. Perebikovsky, A. Hwu, A. Yale, M. Ghazinejad, and M. J. Madou. Nanofibrous Carbon Multi-functional Smart Scaffolds for Simultaneous Cell Differentiation and Dopamine Detection. *ACS Biomaterials Science & Engineering*, Dec. 2019.

[145] G. Pitruzzello, S. Thorpe, S. Johnson, A. Evans, H. Gadêlha, and T. F. Krauss. Multiparameter antibiotic resistance detection based on hydrodynamic trapping of individual E. coli. *Lab on a Chip*, 19(8):1417–1426, Apr. 2019.

[146] S. Rammensee, M. S. Kang, K. Georgiou, S. Kumar, and D. V. Schaffer. Dynamics of Mechanosensitive Neural Stem Cell Differentiation. *STEM CELLS*, 35(2):497–506, 2017.

[147] S. Ranade, R. Syeda, and A. Patapoutian. Mechanically Activated Ion Channels. *Neuron*, 87(6):1162–1179, Sept. 2015.

[148] L. Rayleigh. Xx. on the equilibrium of liquid conducting masses charged with electricity. *The London, Edinburgh, and Dublin Philosophical Magazine and Journal of Science*, 14(87):184–186, 1882.

[149] G. C. Reilly and A. J. Engler. Intrinsic extracellular matrix properties regulate stem cell differentiation. *Journal of biomechanics*, 43(1):55–62, 2010.

[150] Y. Ren and W. W.-F. Leung. Numerical and experimental investigation on flow and mixing in batch-mode centrifugal microfluidics. *International Journal of Heat and Mass Transfer*, 60:95–104, 2013.

[151] D. H. Reneker and A. L. Yarin. Electrospinning jets and polymer nanofibers. *Polymer*, 49(10):2387–2425, 2008.

[152] R. o. A. Resistance. *Antimicrobial resistance: tackling a crisis for the health and wealth of nations*. Review on Antimicrobial Resistance, 2014.

[153] J. A. Ribeiro, P. M. Fernandes, C. M. Pereira, and F. Silva. Electrochemical sensors and biosensors for determination of catecholamine neurotransmitters: a review. *Talanta*, 160:653–679, 2016.

[154] M. E. Rice and C. Nicholson. Measurement of nanomolar dopamine diffusion using low-noise perfluorinated ionomer-coated carbon fiber microelectrodes and high-speed cyclic voltammetry. *Analytical chemistry*, 61(17):1805–1810, 1989.

[155] R. J. Rice, N. M. Pontikos, and R. L. McCreery. Quantitative correlations of heterogeneous electron-transfer kinetics with surface properties of glassy carbon electrodes. *Journal of the American Chemical Society*, 112(12):4617–4622, June 1990.

[156] P. Ridone, M. Vassalli, and B. Martinac. Piezo1 mechanosensitive channels: what are they and why are they important. *Biophysical reviews*, pages 1–11, 2019.

[157] D. L. Robinson, B. J. Venton, M. L. A. V. Heien, and R. M. Wightman. Detecting Subsecond Dopamine Release with Fast-Scan Cyclic Voltammetry in Vivo. *Clinical Chemistry*, 49(10):1763–1773, Oct. 2003.

[158] M. Ronaghi, S. Erceg, V. Moreno-Manzano, and M. Stojkovic. Challenges of Stem Cell Therapy for Spinal Cord Injury: Human Embryonic Stem Cells, Endogenous Neural Stem Cells, or Induced Pluripotent Stem Cells? *STEM CELLS*, 28(1):93–99, 2010.

[159] D. T. Scadden. Nice neighborhood: emerging concepts of the stem cell niche. *Cell*, 157(1):41–50, 2014.

[160] U. Y. Schaff and G. J. Sommer. Whole blood immunoassay based on centrifugal bead sedimentation. *Clinical chemistry*, 57(5):753–761, 2011.

[161] J. D. Schiffman and C. L. Schauer. A review: electrospinning of biopolymer nanofibers and their applications. *Polymer reviews*, 48(2):317–352, 2008.

[162] R. Schofield. The relationship between the spleen colony-forming cell and the haemopoietic stem cell. *Blood cells*, 4(1-2):7–25, 1978.

[163] O. J. A. Schueller, S. T. Brittain, C. Marzolin, and G. M. Whitesides. Fabrication and Characterization of Glassy Carbon MEMS. *Chemistry of Materials*, 9(6):1399–1406, June 1997.

[164] M. A. Schwartz, M. D. Schaller, and M. H. Ginsberg. Integrins: Emerging Paradigms of Signal Transduction. *Annual Review of Cell and Developmental Biology*, 11(1):549–599, 1995.

[165] S. Seetharaman and S. Etienne-Manneville. Integrin diversity brings specificity in mechanotransduction. *Biology of the Cell*, 110(3):49–64, 2018.

[166] N. G. Shang, P. Papakonstantinou, M. McMullan, M. Chu, A. Stamboulis, A. Potenza, S. S. Dhesi, and H. Marchetto. Catalyst-Free Efficient Growth, Orientation and Biosensing Properties of Multilayer Graphene Nanoflake Films with Sharp Edge Planes. *Advanced Functional Materials*, 18(21):3506–3514, 2008.

[167] P. R. Shankar and R. Balasubramanium. Antimicrobial resistance: global report on surveillance 2014. *Australasian Medical Journal (Online)*, 7(5):237, 2014.

[168] S. Sharma, A. Sharma, Y.-K. Cho, and M. Madou. Increased graphitization in electrospun single suspended carbon nanowires integrated with carbon-MEMS and carbon-NEMS platforms. *ACS applied materials & interfaces*, 4(1):34–39, 2012.

[169] Y. Shin, M. Hohman, M. P. Brenner, and G. Rutledge. Electrospinning: A whipping fluid jet generates submicron polymer fibers. *Applied physics letters*, 78(8):1149–1151, 2001.

[170] J. Siegrist, R. Gorkin, M. Bastien, G. Stewart, R. Peytavi, H. Kido, M. Bergeron, and M. Madou. Validation of a centrifugal microfluidic sample lysis and homogenization platform for nucleic acid extraction with clinical samples. *Lab on a Chip*, 10(3):363–371, 2010.

[171] J. Siegrist, R. Gorkin, L. Clime, E. Roy, R. Peytavi, H. Kido, M. Bergeron, T. Veres, and M. Madou. Serial siphon valving for centrifugal microfluidic platforms. *Microfluidics and Nanofluidics*, 9(1):55–63, July 2010.

[172] T. J. Sill and H. A. von Recum. Electrospinning: applications in drug delivery and tissue engineering. *Biomaterials*, 29(13):1989–2006, 2008.

[173] J. Steigert, M. Grumann, M. Dube, W. Streule, L. Riegger, T. Brenner, P. Koltay, K. Mittmann, R. Zengerle, and J. Ducrée. Direct hemoglobin measurement on a centrifugal microfluidic platform for point-of-care diagnostics. *Sensors and Actuators A: Physical*, 130:228–233, 2006.

[174] H. Stender, M. Fiandaca, J. J. Hyldig-Nielsen, and J. Coull. PNA for rapid microbiology. *Journal of Microbiological Methods*, 48(1):1–17, Jan. 2002.

[175] J. Sun, B. Bhushan, and J. Tong. Structural coloration in nature. *RSC Advances*, 3(35):14862–14889, Aug. 2013.

[176] A. Sundsfjord, G. S. Simonsen, B. C. Haldorsen, H. Haaheim, S.-O. Hjelmevoll, P. Littauer, and K. H. Dahl. Genetic methods for detection of antimicrobial resistance. *APMIS*, 112(11-12):815–837, 2004.

[177] N. Tajaddod, H. Li, and M. L. Minus. Low-temperature graphitic formation promoted by confined interphase structures in polyacrylonitrile/carbon nanotube materials. *Polymer*, 137:346–357, Feb. 2018.

[178] G. I. Taylor. Disintegration of water drops in an electric field. *Proceedings of the Royal Society of London. Series A. Mathematical and Physical Sciences*, 280(1382):383–397, 1964.

[179] G. I. Taylor. Electrically driven jets. *Proceedings of the Royal Society of London. A. Mathematical and Physical Sciences*, 313(1515):453–475, 1969.

[180] A. Totaro, M. Castellan, G. Battilana, F. Zanconato, L. Azzolin, S. Giulitti, M. Cordenonsi, and S. Piccolo. YAP/TAZ link cell mechanics to Notch signalling to control epidermal stem cell fate. *Nature Communications*, 8(1):1–13, May 2017.

[181] R. Truckenmüller, Y. Cheng, R. Ahrens, H. Bahrs, G. Fischer, and J. Lehmann. Micro ultrasonic welding: joining of chemically inert polymer microparts for single material fluidic components and systems. *Microsystem Technologies*, 12(10-11):1027–1029, 2006.

[182] J. R. Tse and A. J. Engler. Stiffness Gradients Mimicking In Vivo Tissue Variation Regulate Mesenchymal Stem Cell Fate. *PLoS ONE*, 6(1), Jan. 2011.

[183] O. Tsuji, K. Miura, Y. Okada, K. Fujiyoshi, M. Mukaino, N. Nagoshi, K. Kitamura, G. Kumagai, M. Nishino, S. Tomisato, H. Higashi, T. Nagai, H. Katoh, K. Kohda, Y. Matsuzaki, M. Yuzaki, E. Ikeda, Y. Toyama, M. Nakamura, S. Yamanaka, and H. Okano. Therapeutic potential of appropriately evaluated safe-induced pluripotent stem cells for spinal cord injury. *Proceedings of the National Academy of Sciences*, 107(28):12704–12709, July 2010.

[184] Y. Ukita, S. Kondo, T. Azeta, M. Ishizawa, C. Kataoka, M. Takeo, and Y. Utsumi. Stacked centrifugal microfluidic device with three-dimensional microchannel networks and multifunctional capillary bundle structures for immunoassay. *Sensors and Actuators B: Chemical*, 166:898–906, 2012.

[185] Y. Ukita and Y. Takamura. A new stroboscopic technique for the observation of microscale fluorescent objects on a spinning platform in centrifugal microfluidics. *Microfluidics and Nanofluidics*, 18(2):245–252, 2015.

[186] C. L. Ventola. The Antibiotic Resistance Crisis. *Pharmacy and Therapeutics*, 40(4):277–283, Apr. 2015.

[187] A. Vesel and M. Mozetic. Surface modification and ageing of pmma polymer by oxygen plasma treatment. *Vacuum*, 86(6):634–637, 2012.

[188] A. L. Viet, M. Reddy, R. Jose, B. Chowdari, and S. Ramakrishna. Nanostructured nb2o5 polymorphs by electrospinning for rechargeable lithium batteries. *The Journal of Physical Chemistry C*, 114(1):664–671, 2010.

[189] L. G. Vincent, Y. S. Choi, B. Alonso-Latorre, J. C. d. Álamo, and A. J. Engler. Mesenchymal stem cell durotaxis depends on substrate stiffness gradient strength. *Biotechnology Journal*, 8(4):472–484, 2013.

[190] L. G. Vincent and A. J. Engler. Post-degradation forces kick in. *Nature Materials*, 12(5):384–386, May 2013.

[191] C. Wang, G. Jia, L. Taherabadi, and M. Madou. A novel method for the fabrication of high-aspect ratio C-MEMS structures. *Journal of Microelectromechanical Systems*, 14(2):348–358, Apr. 2005.

[192] C. Wang and M. Madou. From MEMS to NEMS with carbon. *Biosensors and Bioelectronics*, 20(10):2181–2187, Apr. 2005.

[193] C. Wang, R. Zaouk, B. Y. Park, and M. J. Madou. Carbon as a MEMS material: micro and nanofabrication of pyrolysed photoresist carbon. *International Journal of Manufacturing Technology and Management*, 13(2-4):360–375, Jan. 2008.

[194] H. Wang, T. Maiyalagan, and X. Wang. Review on Recent Progress in Nitrogen-Doped Graphene: Synthesis, Characterization, and Its Potential Applications. *ACS Catalysis*, 2(5):781–794, May 2012.

[195] J. Wang. Electrochemical biosensors: towards point-of-care cancer diagnostics. *Biosensors and Bioelectronics*, 21(10):1887–1892, 2006.

[196] L. Wang, Y. Yu, P. Chen, D. Zhang, and C. Chen. Electrospinning synthesis of c/fe3o4 composite nanofibers and their application for high performance lithium-ion batteries. *Journal of Power Sources*, 183(2):717–723, 2008.

[197] N. Wang, J. P. Butler, and D. E. Ingber. Mechanotransduction across the cell surface and through the cytoskeleton. *Science*, 260(5111):1124–1127, May 1993.

[198] W. Wang, H. Huang, Z. Li, H. Zhang, Y. Wang, W. Zheng, and C. Wang. Zinc oxide nanofiber gas sensors via electrospinning. *Journal of the American Ceramic Society*, 91(11):3817–3819, 2008.

[199] Z. Wang, R. Samanipour, and K. Kim. Organ-on-a-chip platforms for drug screening and tissue engineering. In *Biomedical engineering: frontier research and converging technologies*, pages 209–233. Springer, 2016.

[200] K. Ward and Z. H. Fan. Mixing in microfluidic devices and enhancement methods. *Journal of Micromechanics and Microengineering*, 25(9):094001, Aug. 2015.

[201] R. H. S. Westerink and A. G. Ewing. The PC12 cell as model for neurosecretion. *Acta Physiologica*, 192(2):273–285, 2008.

[202] J. Xie, S. M. Willerth, X. Li, M. R. Macewan, A. Rader, S. E. Sakiyama-Elbert, and Y. Xia. The differentiation of embryonic stem cells seeded on electrospun nanofibers into neural lineages. *Biomaterials*, 30(3):354–362, Jan. 2009.

[203] T. Xie and A. C. Spradling. A niche maintaining germ line stem cells in the drosophila ovary. *Science*, 290(5490):328–330, 2000.

[204] A. L. Yarin, S. Koombhongse, and D. H. Reneker. Bending instability in electrospinning of nanofibers. *Journal of applied physics*, 89(5):3018–3026, 2001.

[205] A. L. Yarin, S. Koombhongse, and D. H. Reneker. Taylor cone and jetting from liquid droplets in electrospinning of nanofibers. *Journal of applied physics*, 90(9):4836–4846, 2001.

[206] J. Yu, M. A. Vodyanik, K. Smuga-Otto, J. Antosiewicz-Bourget, J. L. Frane, S. Tian, J. Nie, G. A. Jonsdottir, V. Ruotti, R. Stewart, I. I. Slukvin, and J. A. Thomson. Induced Pluripotent Stem Cell Lines Derived from Human Somatic Cells. *Science*, 318(5858):1917–1920, Dec. 2007.

[207] Y. I. Yun, K. S. Kim, S.-J. Uhm, B. B. Khatua, K. Cho, J. K. Kim, and C. E. Park. Aging behavior of oxygen plasma-treated polypropylene with different crystallinities. *Journal of adhesion science and technology*, 18(11):1279–1291, 2004.

[208] J. Zeleny. The electrical discharge from liquid points, and a hydrostatic method of measuring the electric intensity at their surfaces. *Physical Review*, 3(2):69, 1914.

[209] J. Zeng, X. Xu, X. Chen, Q. Liang, X. Bian, L. Yang, and X. Jing. Biodegradable electrospun fibers for drug delivery. *Journal of controlled release*, 92(3):227–231, 2003.

[210] P. Zhang, F.-H. Wu, G.-C. Zhao, and X.-W. Wei. Selective response of dopamine in the presence of ascorbic acid at multi-walled carbon nanotube modified gold electrode. *Bioelectrochemistry*, 67(1):109–114, Sept. 2005.

[211] K. Zwirglmaier, W. Ludwig, and K.-H. Schleifer. Recognition of individual genes in a single bacterial cell by fluorescence in situ hybridization – RING-FISH. *Molecular Microbiology*, 51(1):89–96, 2004.

Appendix A

Spinbox Design

The main mechanical assemblies of the spinbox are shown below, including the full list of materials needed to build each assembly. The outer housing (not shown) is made from laser-cut PMMA and is affixed to the outer shell. The touchscreen user interface, raspberry pi, and electronics are also not shown below.

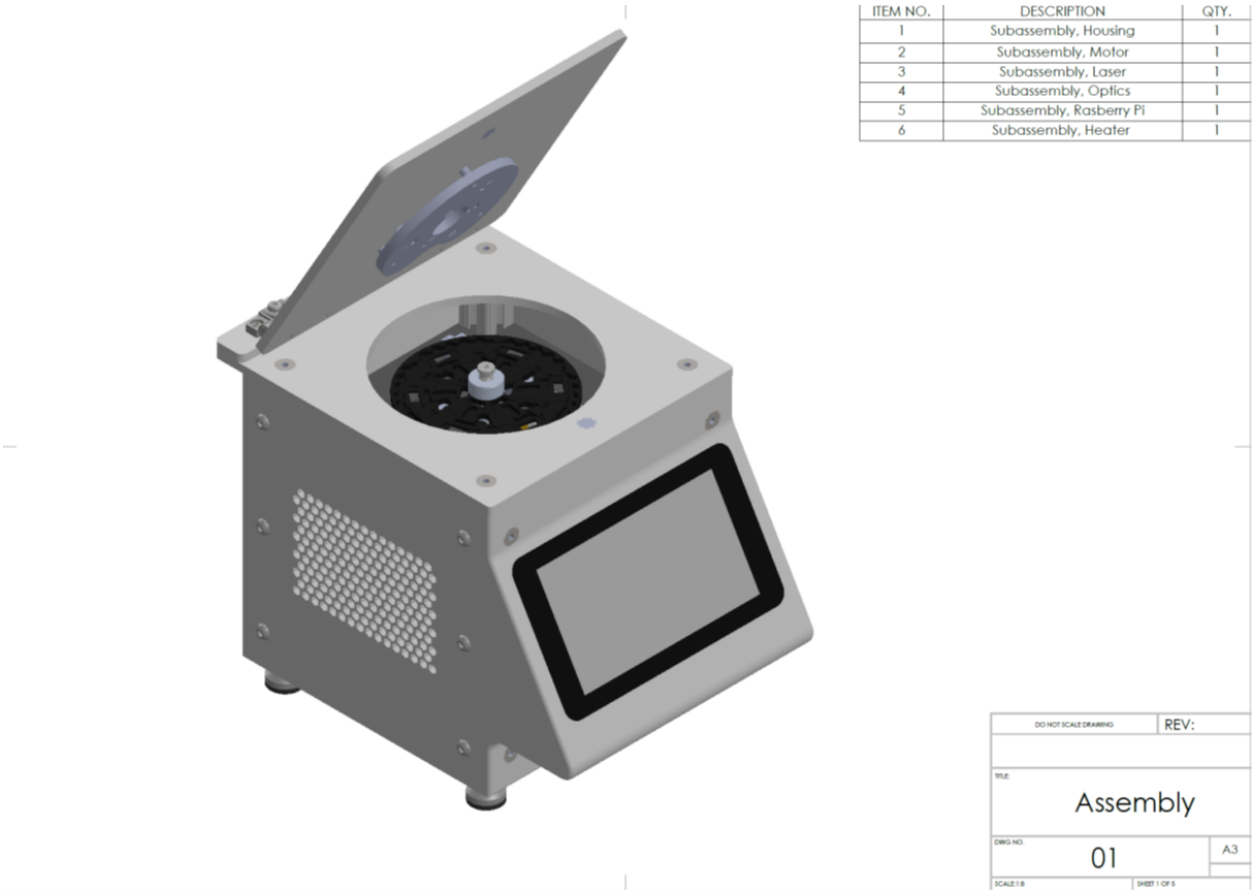

Figure A.1: Full assembly of entire spinbox.

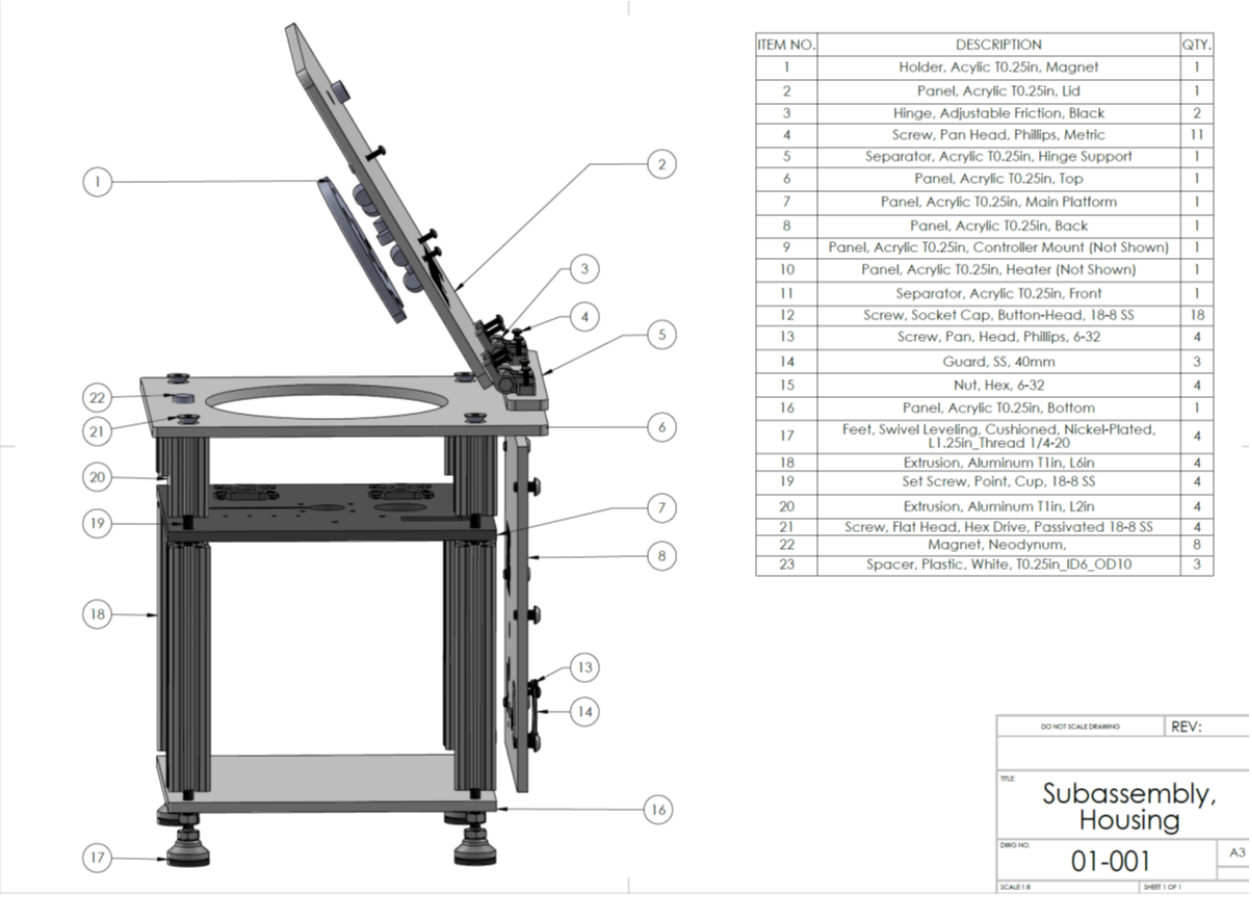

ITEM NO.	DESCRIPTION	QTY.
1	Holder, Acylic T0.25in, Magnet	1
2	Panel, Acrylic T0.25in, Lid	1
3	Hinge, Adjustable Friction, Black	2
4	Screw, Pan Head, Phillips, Metric	11
5	Separator, Acrylic T0.25in, Hinge Support	1
6	Panel, Acrylic T0.25in, Top	1
7	Panel, Acrylic T0.25in, Main Platform	1
8	Panel, Acrylic T0.25in, Back	1
9	Panel, Acrylic T0.25in, Controller Mount (Not Shown)	1
10	Panel, Acrylic T0.25in, Heater (Not Shown)	1
11	Separator, Acrylic T0.25in, Front	1
12	Screw, Socket Cap, Button-Head, 18-8 SS	18
13	Screw, Pan, Head, Phillips, 6-32	4
14	Guard, SS, 40mm	3
15	Nut, Hex, 6-32	4
16	Panel, Acrylic T0.25in, Bottom	1
17	Feet, Swivel Leveling, Cushioned, Nickel-Plated, L1.25in_Thread 1/4-20	4
18	Extrusion, Aluminum T1in, L6in	4
19	Set Screw, Point, Cup, 18-8 SS	4
20	Extrusion, Aluminum T1in, L2in	4
21	Screw, Flat Head, Hex Drive, Passivated 18-8 SS	4
22	Magnet, Neodynum,	8
23	Spacer, Plastic, White, T0.25in_ID6_OD10	3

Figure A.2: Components of Spinbox housing.

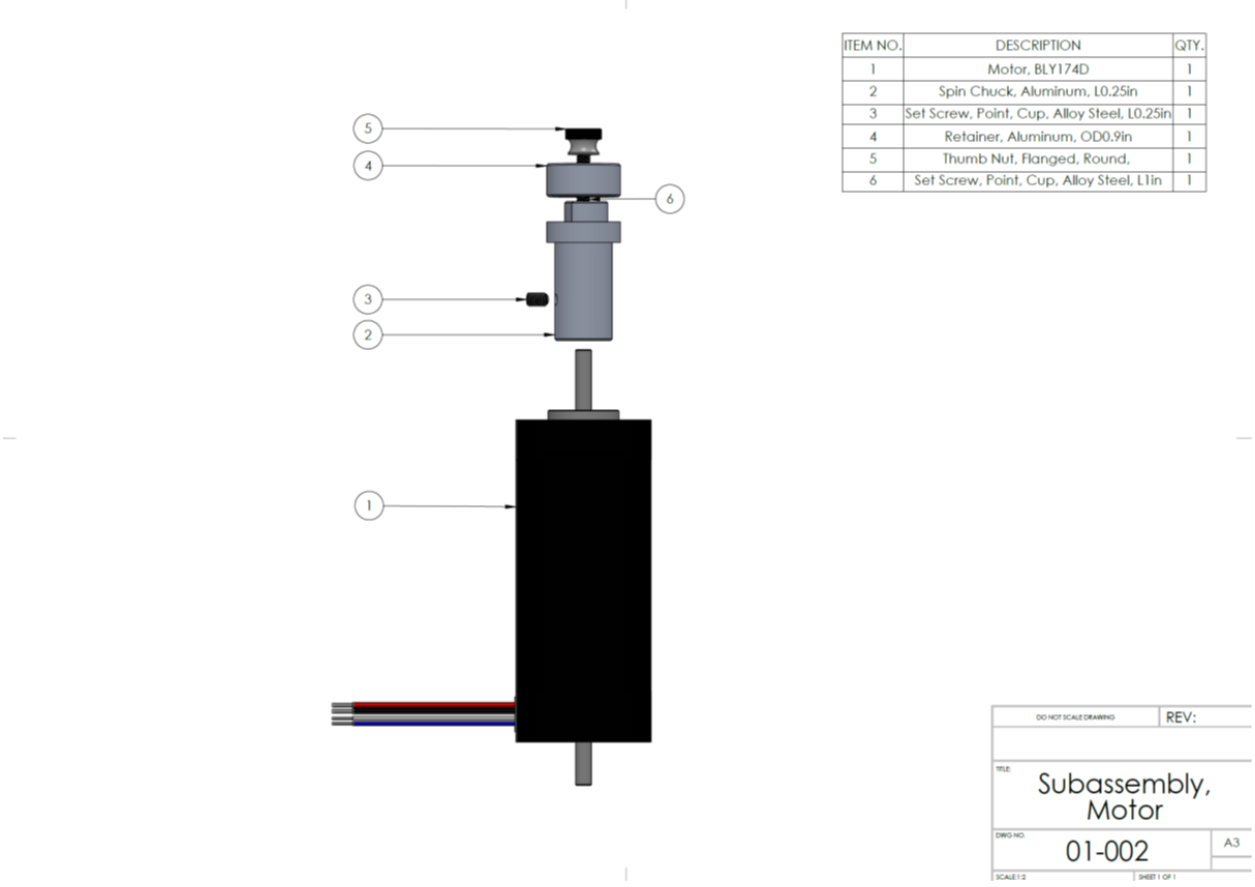

Figure A.3: Spinbox motor design and interface with the disc.

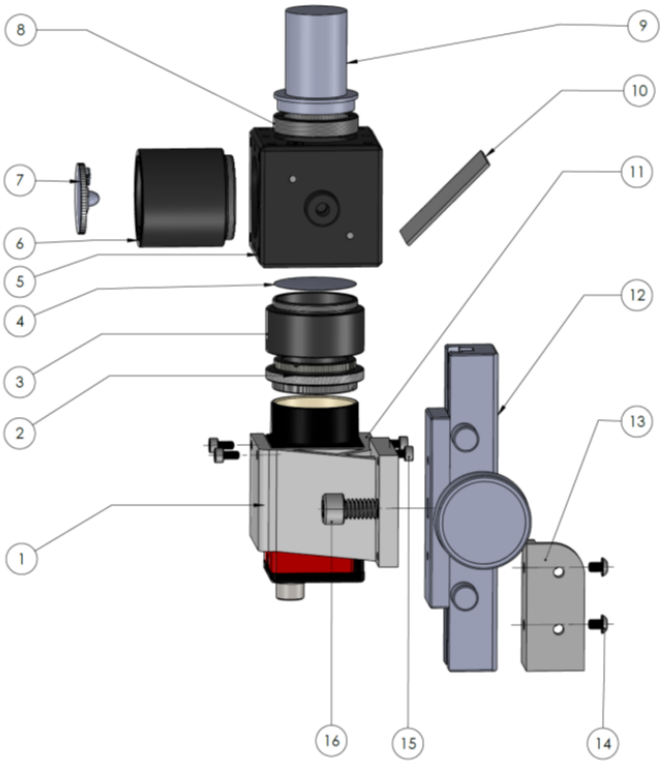

ITEM NO.	DESCRIPTION	QTY.
1	Camera, Mako-G, C-Mount	1
2	Adapter, Camera	1
3	Adapter, Filter Cube	1
4	Lens, Filter	1
5	Cube, Filter Holder	1
6	Adapter, Filter Cube to LED	1
7	PCB, LED, Excitation	1
8	Adapter, Filter Cube to Lens	1
9	Lens, Magnification	1
10	Holder, Camera, Mako	1
11	Holder, Camera, Mako	1
12	Mount, Holder, Camera, Adjustable	1
13	Mount, Panel, Holder, Camera	1
14	Screw, Socket Cap, Button Head	5
15	Screw, Head Cap, Socket, M2.5	4
16	Screw, Head Cap, Socket, 1/4-20	1

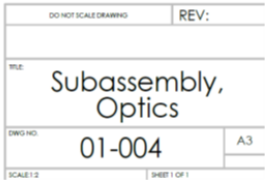

Figure A.4: Custom made fluorescent microscope in the Spinbox.

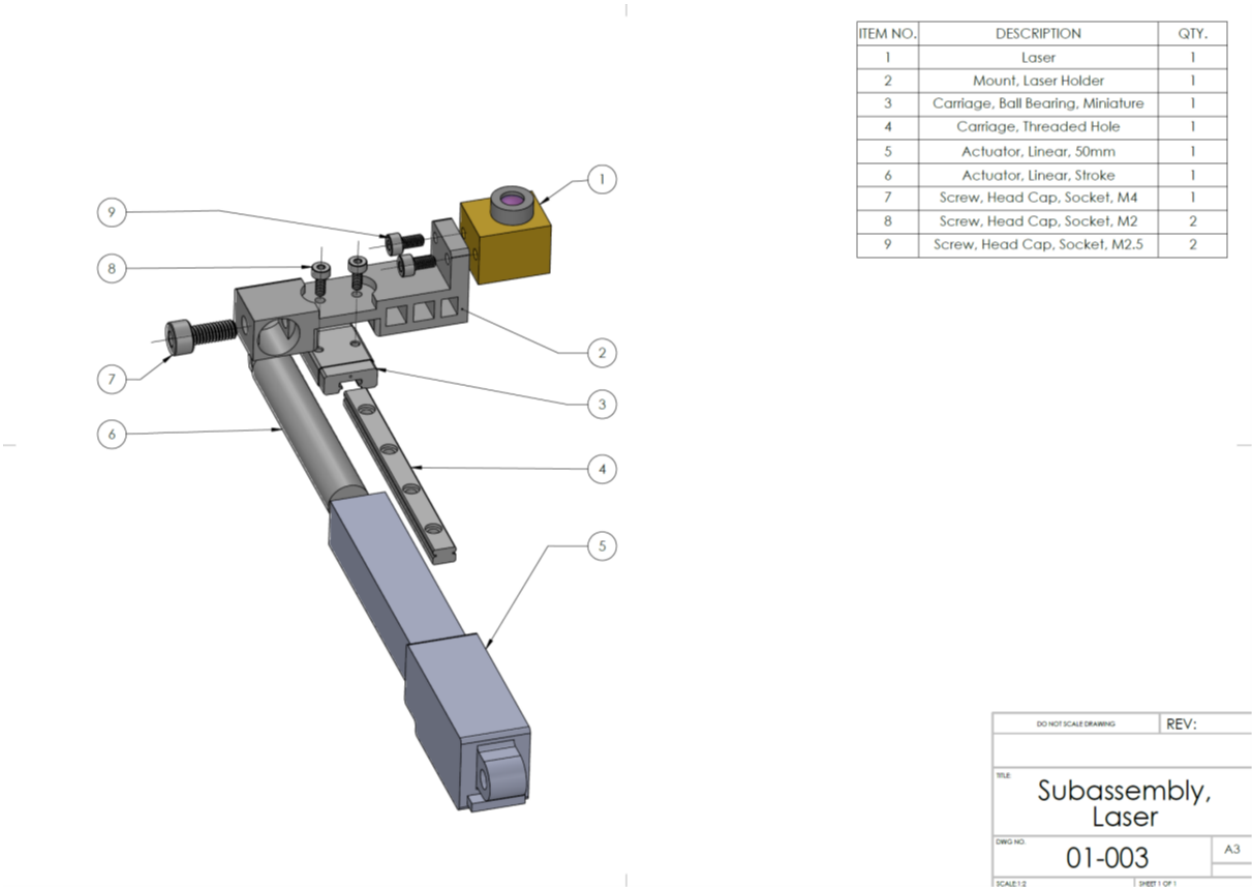

Figure A.5: Components of laser and linear rail used to open valves on the microfluidic disc.

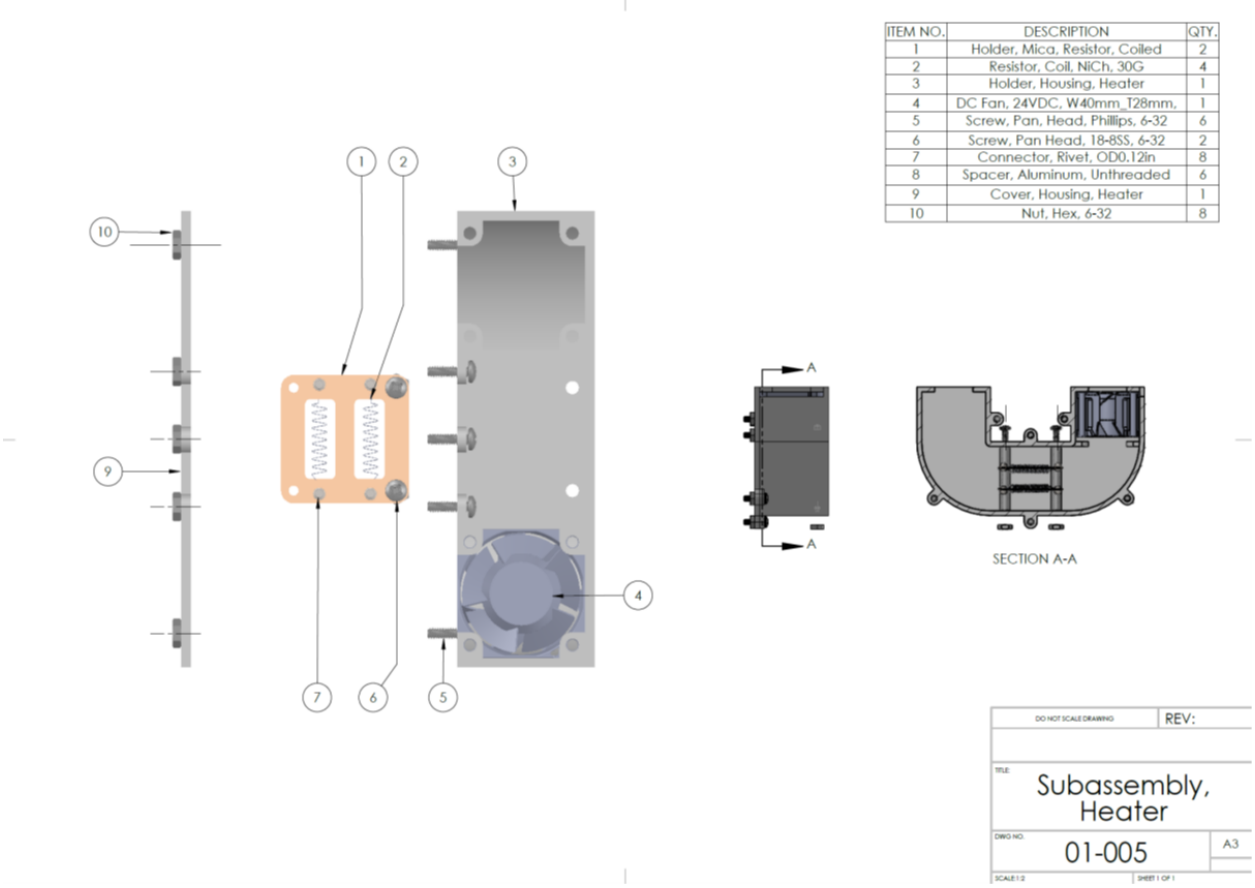

Figure A.6: Components of heater subsytem used to create an environmental, temperature control system in the Spinbox.

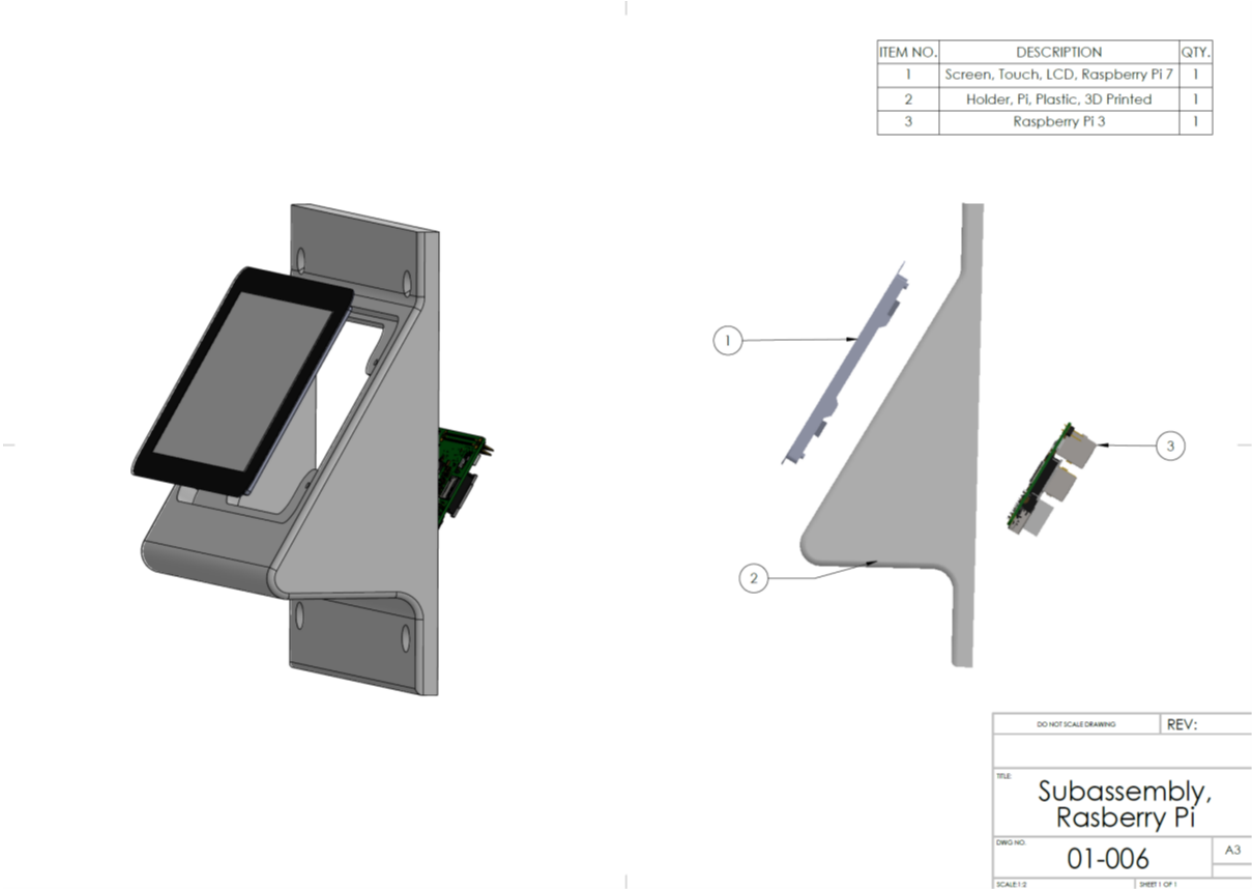

Figure A.7: Components of Spinbox user interface. This includes the touchscreen, raspberry pi, and 3D printed ergonomic housing.

Appendix B

Software and programming for SpinBox

The software that controls the Spinbox in Section III is based on a python3 program with a set of libraries including pyqt4 as the graphical user interface. It has the following functions:

1. Controlling the movement of the main, brushless DC motor. This includes spinning at a specified RPM, acceleration/deceleration (RPM/s), oscillation at a specified angle and frequency (Hz), and angular positioning.

2. Controlling the linear actuator to move the laser to a certain radial position. A linear actuator is used here to carry a 5W blue light laser diode. A PWM code is sent from the raspberry pi to the actuator through GPIO pins on the Raspberry Pi. The motor and linear actuator are moved correspondingly to target the laser at specific valving position.

3. Controlling the laser with desired power. The laser is controlled by an PWM code to adjust the power for fast and accurate actuation of the valve.

4. Controlling the excitation led to light up the detection area. A GPIO code is integrated to control a 1W led excitation source for the integrated fluorescent microscope.

5. Controlling the custom-built fluorescent microscope to take picture. Through an ethernet cable, the camera is controlled through Pymba (https://github.com/morefigs/pymba), a python wrapper for Allied Vision's Vimba C API. The library enables control over camera parameters such as exposure and gain.

6. Processing the image with OpenCV code. OpenCV-python is an open source computer vision library that was used to detect and measure the fluorescence intensity of each probe binding area. Pictures of the detection area before and after hybridization are taken by the custom built fluorescence microscope camera for comparison. To process the fluorescent image, each image is first background subtracted. Then the resulting image is smoothed with a gaussian blurry algorithm. A threshold is then applied to remove any spikes from the picture which may be falsely recognized as detection spots. Finally, the findContours function is used to outline the perimeter of the fluorescent spots and the intensity of each pixel is summed up as the total fluorescence intensity.